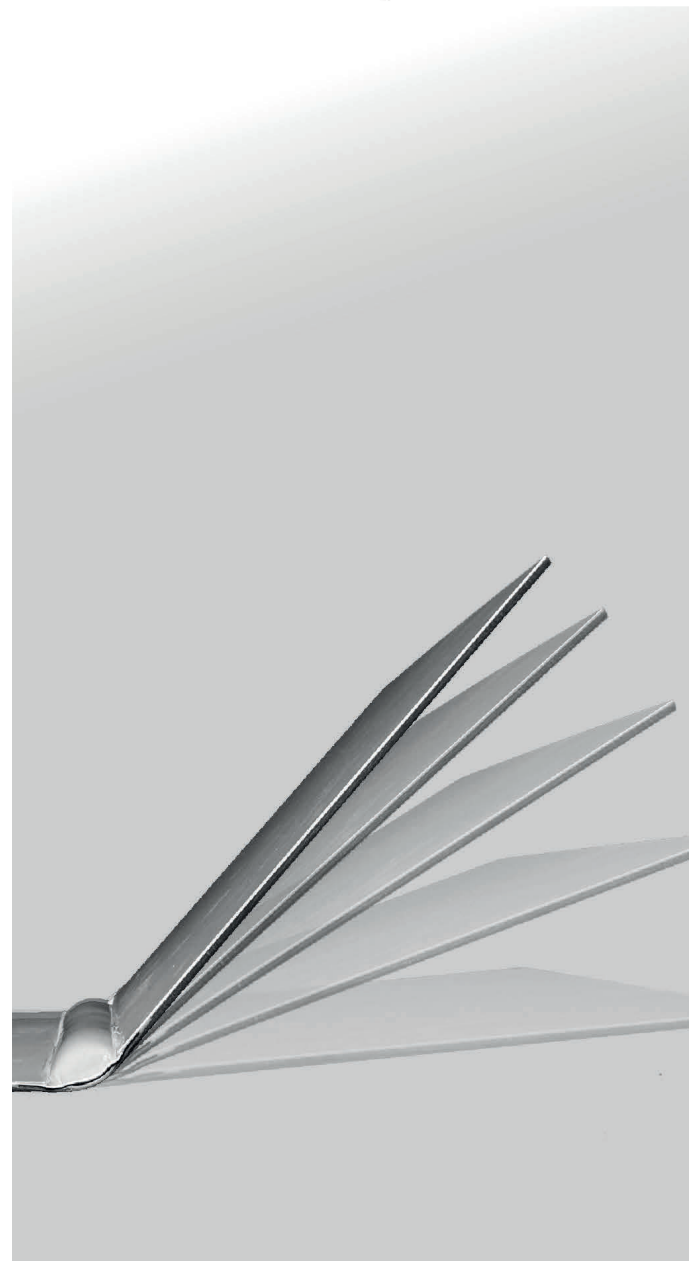
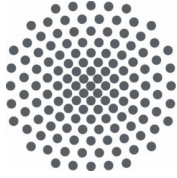


Anja Mader

Bio-inspired
Integrated Actuation
and Variable Stiffness for
Compliant Mechanisms





Forschungsberichte

itke

aus dem Institut für Tragkonstruktionen
und Konstruktives Entwerfen,
Universität Stuttgart

Herausgeber:
Professor Dr.-Ing. Jan Knippers

Institut für Tragkonstruktionen und Konstruktives Entwerfen:
Forschungsbericht 48

Anja Mader:
Bio-inspired Integrated Actuation and Variable Stiffness
for Compliant Mechanisms

Stuttgart, Juni 2022

ISBN 978-3-922302-48-3

D 93

© Institut für Tragkonstruktionen
und Konstruktives Entwerfen
Universität Stuttgart
Keplerstraße 11
D-70174 Stuttgart



Alle Rechte, insbesondere der Übersetzung, bleiben vorbehalten.
Vervielfältigung jeglicher Art, auch auszugsweise, ist nicht
gestattet.

BIO-INSPIRED INTEGRATED ACTUATION AND
VARIABLE STIFFNESS FOR COMPLIANT
MECHANISMS



von der Fakultät Architektur und Stadtplanung
der Universität Stuttgart zur Erlangung der Würde eines
Doktor-Ingenieurs (Dr.-Ing.) genehmigte Abhandlung

Vorgelegt von

Anja Mader

aus Ulm

Hauptberichter: Prof. Dr.-Ing. Jan Knippers

Mitberichter: Prof. Dr. rer. nat. Thomas Speck

Tag der mündlichen Prüfung: 10.02.2022

Institut für Tragkonstruktionen und Konstruktives
Entwerfen der Universität Stuttgart, 2022

'Probleme kann man niemals mit derselben Denkweise lösen, durch die sie entstanden sind.' - *Albert Einstein*

ACKNOWLEDGEMENTS

I would like to express my sincere gratitude to all those who helped me along the path to this thesis. In the first place, I am deeply grateful for my supervisor and head of the ITKE Prof. Dr.-Ing. Jan Knippers, for giving me the opportunity to conduct this research. Throughout my time at the ITKE and forwards, I had the privilege to experience his trust and support. Further, I would like to extend my gratitude to my co-advisor, Prof. Thomas Speck, for investing the time to review and correct my thesis. Both also took a great part in initializing and leading the Collaborative Research Center SFB-TRR 141: Biological Design and Integrative Structures funded by the DFG. Without this framework and funding, big parts of this research would not have been possible. Apart from that, I would like to thank the Baden-Württemberg foundation for also funding this research through the NaBau 4 (BIAG) project.

During my time as a doctoral candidate at the University of Stuttgart, I was very fortunate to work with exceptional colleagues at my side. I thank them wholeheartedly for the fruitful and enjoyable cooperation: Dr. Axel Körner, Dr. Larissa Born, Gundula Schieber and Saman Saffarian. This biomimetic research was also only possible thanks to our interdisciplinary partners. Here I would like to thank the Plant Biomechanics Group (PBG) Freiburg, especially Dr. Olga Speck, Dr. Marco Caliaro and Max Langer for their valuable insights and collaboration in identifying and investigating the biological role model. Equally, I thank Prof. Dr. Oliver Betz and Dr. Paavo Bergmann, from the Institute of Evolution and Ecology (EvE) at the University of Tübingen. Further, I thank the German Institute for Textile and Fibre Research Denkendorf (DITF) and Institute for Textile and Fiber Technologies (ITFT) at the University of Stuttgart, both under the direction of Prof. Dr.-Ing. Götz T. Gresser, for the support in the materialization of the developed concepts.

A big thank you also to my former students and interns Pierre-Alexandre Masset, Sandie Kate Fenton; William Whitmore and Emily Kliewer, that have helped me so much in the development of this work. I also want to thank the student assistants Mariia Chumak, Fatemeh Karegar, Ahmad Razavi, Tessa Rudolph, Gesche Falkenburg and Natasha Neera Nathan for their support during prototyping.

Finally, I would like to express my gratitude also to everybody else that supported me along the path. Thank you to my family for believing in me and having supported me for all these years; to Dr. Anaëlle Dumas for her proofreading of this thesis; and a sincere thanks also to all my colleagues and friends at the University of Stuttgart for these wonderful years together.

ZUSAMMENFASSUNG

Aufgrund von Vorteilen, wie einer geringen mechanischen Komplexität, geringem Gewicht und der Abwesenheit von Reibung oder Verschleiß, werden nachgiebige kinetische Systeme zunehmend auch für großflächige Anwendungen, wie zur Fassadenverschattung, eingesetzt. Um die Vorteile nachgiebiger Systeme auch für die Aktuierung zu nutzen, wurden in zwei Fallstudien bioinspirierte gelenkfreie Aktuierungsprinzipien entwickelt. Beide konnten in physikalischen Prototypen 2-dimensionalen nachgiebigen Systemen erfolgreich aktuieren. Zusätzlich wurde ein adaptives Steifigkeitskonzept entwickelt, um die Tragfähigkeit temporär steigern zu können.

In einem bionischen Top-Down-Ansatz wurden zunächst die Blattfaltung durch Turgorschwankungen in den vergrößerten bulliformen Zellen der Modellpflanze *Sesleria nitida* mit Hilfe einer FEA untersucht. Die Experimente zeigen, dass der Turgordruck das Blatt gegen eine vorhandene Vorspannung öffnet. In den bulliformen Zellen vorkommende Turgor- und Volumenschwankungen erzeugen Kräfte, die hoch genug sind, um das Blatt zu öffnen und passiv zu schließen. Dieses auf Druck basierende Antriebsprinzip wird zu einer technischen Zellstruktur abstrahiert, die aus mehreren, aus glasfaserverstärktem Kunststoff (GFK) hergestellten, Zellen mit nachgiebigen Gelenken besteht. Eine Erhöhung des Zellinnendrucks bewirkt eine Rekonfiguration der technischen Zelle, was zur Biegung des Aktuators führt. Gleichzeitig weisen dünnwandige Pflanzengewebe eine starke turgorabhängige Steifigkeit auf. Auch im technischen Aktuator steigt die Steifigkeit proportional mit dem Zellinnendruck. Durch das Hinzufügen einer zweiten, entgegengerichteten Zellreihe kann die Steifigkeit des Aktuators unabhängig von der Biegung gesteuert werden. In dieser Konstellation wird die Biegung durch das Verhältnis der Zellinnendrucke in den beiden Zellreihen bestimmt. In physikalischen und numerischen Experimenten steigt die Steifigkeit eines zellulären Aktuators bei einer Druckerhöhung um 1 bar um den Faktor 2,5.

Im Rahmen des zweiten bionischen Entwicklungsprozesses wurde ein pneumatischer Aktuator entwickelt, der vollständig in das Laminat eines GFKs integriert ist. Dieser Ansatz ermöglicht eine einfache Herstellung und ein schlankes, homogenes Erscheinungsbild. Als Vorbild für den Laminataufbau des GFKs diente die Ultrastruktur der Flügeladern der Streifenwanze (*Graphosoma lineatum italicum*). Wird die pneumatische Kammer, analog zu der Resilin-enthaltenden Endocuticula im biologischen Vorbild, mit einer elastomeren Schicht umgeben, verhindert dies die Delamination der Laminatschichten. Bei einer Erhöhung des Innendrucks führen die exzentrische Platzierung

der pneumatischen Kammer und die größere Nachgiebigkeit der dünneren Lagen zu einer Rotation in diese Richtung. Auf diese Weise wird bei der Platzierung in einer Gelenkzone mit größerer Nachgiebigkeit eine Faltbewegung erzeugt. Eine quasi-uniforme Biegung wird durch die Platzierung einer großflächigen pneumatischen Kammer in einer Platte, mit verteilter Nachgiebigkeit, erreicht. Die adaptive Steifigkeit wird durch eine antagonistische Aktuatoranordnung realisiert. Diese ist inspiriert von antagonistischen Muskeln, die für die Versteifung von Skelettgelenken notwendig sind. Ein Innendruck von 1,8 bar in beiden antagonistischen Aktuatoren erhöht die Steifigkeit einer GFK-Platte um 60% im Vergleich zum druckfreien Zustand.

ABSTRACT

Due to advantages, such as a low mechanical complexity, low weight, and the absence of friction or wear, compliant kinetic systems are increasingly used, including for large-scale applications like facade shading. To exploit the advantages also for the actuation, bio-inspired joint-free actuators were developed within two case studies. Both actuation principles proved their potential to actuate 2-dimensional compliant devices within physical prototypes. Additionally, adaptive stiffness concepts were developed to potentially increase the load bearing capability temporarily.

Following a biomimetic top-down approach, the leaf folding of the model plant *Sesleria nitida* caused by turgor variations within large bulliform cells was investigated using a FEA. The turgor pressure opens the leaf against a present pre-stress. Turgor and volume variation within the bulliform cells that result from fluctuations in water availability generate forces high enough to fold and unfold the leaf. This pressurize-based actuation principle is abstracted to a technical cellular structure constructed from GFRP (glass fibre-reinforced plastic) cells with compliant hinges. An increase in inner cell pressure causes a reconfiguration of the cell and an overall bending motion of the actuator. At the same time, thin-walled plant tissues show a strong turgor dependent stiffness. By adding a second, counteracting cell row that decouples deformation from absolute pressure, this can be realized also in the technical actuator. The bending motion is now determined by the pressure ratio, and the stiffness by the pressure magnitude. Within physical and numerical experiments, the stiffness of a cellular actuator increases by a factor of 2.5 at a pressure increase of 1 bar.

Within the second case study, a pneumatic actuation that is fully integrated into a GFRP laminate was developed. The wing vein ultrastructure of *Graphosoma lineatum italicum* inspired the laminate built-up of the GFRP with an integrated pneumatic pouch. By surrounding the pouch with an elastomeric layer, analogous to the resilin bearing endocuticle within the biological model, a delamination of the laminate layers is prohibited. The approach allows a simple fabrication, and slender, homogenous appearance. Upon an internal pressure increase, the eccentric placement of the pneumatic pouch and the greater compliance of the thinner layer results in a rotation into that direction. This way a folding motion is realized by a pouch placed in a hinge zone of greater compliance. A quasi-uniform bending is created by placing a segmented large-surface pouch integrated in a plate of distributed compliance. The adaptive stiffness is added by an antagonistic actuator set-up inspired by opposing muscles used to control and stiffen skeletal joints. For a GFRP plate an increase in stiffness of 60% was achieved at 1.8 bar internal pressure.

CONTENT

1	Introduction	1
1.1	Motivation	1
1.2	Kinetic Systems	2
1.2.1	Conventional kinetic systems.....	2
1.2.2	Kinetic systems in architecture	4
1.2.3	Compliant mechanisms	6
1.3	Actuation.....	14
1.4	Biomimetics	16
1.5	Research Hypothesis and Aim.....	19
2	Background	25
2.1	Actuation in Engineering.....	25
2.1.1	Introduction to actuators	25
2.1.2	Conventional actuation systems	26
2.1.3	Unconventional actuators	29
2.1.4	Comparison of different actuators.....	33
2.1.5	Conclusions	35
2.2	Actuation in Biology	37
2.2.1	Definition	37
2.2.2	Actuation in plant movements	37
2.2.3	Actuation in animal movement.....	42
2.2.4	Conclusions	46
2.3	Bio-inspired Actuation	48
2.4	Variable Stiffness	50
2.4.1	Definition of stiffness	50
2.4.2	Variable stiffness concepts.....	52
2.4.3	Material properties	53
2.4.4	Second moment of area	57
2.4.5	Boundary conditions	59
2.4.6	Non-linear effects	61
2.4.7	Conclusions	66
3	Case Studies	69
3.1	Case Study I: Plant-inspired Actuation and Adaptive Stiffness.....	70
3.1.1	Plant-inspired cellular actuation	71
3.1.2	Variable stiffness of cellular structures	86

3.1.3	Further considerations & outlook	98
3.1.4	Conclusions	100
3.2	Case Study II: Integrated Pneumatic Actuation and Adaptive Stiffness	103
3.2.1	Bio-inspired integrated pneumatic actuation	104
3.2.2	Variable stiffness through integrated pneumatic actuation.....	123
3.2.3	Further considerations & outlook	134
3.2.4	Conclusions	137
4	Conclusive Comparison & Final Considerations.....	139
4.1	Comparison of Case Studies	139
4.1.1	Strengths and weaknesses	139
4.2	Reflection of Research Hypothesis and Aim.....	144
4.3	Future Directions	145
5	Appendix	148
6	References	162
6.1	Online Images.....	178

NOMENCLATURE

Geometric

A	Area	[m ²]
b	Width of a cross-section	[m]
h	Height of a cross-section	[m]
L	Length	[m]
r	Radius	[m]
t	Thickness	[m]
V	Volume	[m ³]
α	Sidewall tilting angle of technical cell	[°]
θ	Actuation angle of GFRP plate	[°]

Mechanic

C	Material stiffness matrix	
C^*	Stiffening factor	
E	Modulus of elasticity	[Pa]
E_{ft}	Young's modulus of fresh tissue	
E_i	Initial Young's modulus	
E_t	Apparent tissue Young's modulus	
E^*	Stiffening factor	
ε	Strain	
F	Force	[N]
f	Force vector	
G	Shear modulus	[Pa]
G'	Shear storage modulus	[Pa]
J	Second moment of area	[m ⁴]
k	Stiffness	
k_b	Bending stiffness	
K	Global stiffness matrix	
K_e	Elastic stiffness matrix	
K_g	Geometric stiffness matrix	
K_T	Tangent stiffness matrix	
K_u	Initial displacement stiffness matrix	
m	Mass	[kg]
M	Bending moment	[Nm]
P	Absolute pressure	[Pa]
P_i/P_o	Inner / outer pressure	
P_u/P_l	Upper / lower cell pressure	
P_{ft}	Turgor pressure of fresh tissue	
ρ	Density	[g/m ³]
R	Specific gas constant for dry air	[J/(kg·K)]
σ	Stress	[Pa]
σ_{rad}	Radial stress of a pressure vessel	
σ_θ	Circumferential stress of a pressure vessel	
s	Stress vector	
T	Absolute temperature	[K]
τ_{stall}	Stall torque	[Nm]
u	Displacement vector	
ν	Poisson's ratio	

W	Mechanical work	[J]
W_{el}	Elastic energy	
W_p	Work potential of pressure	
W_{use}	Work to alter volume (of a pressurized cell)	

1 INTRODUCTION

1.1 MOTIVATION

Kinetic systems allow the adaptation to changing environmental conditions and user requirements. This holds true for numerous application scenarios. Correspondingly broad is the range of designs and scales of kinetic systems. The starting point for this investigation is their use in architectural shading systems. Existing kinetic systems are based on standardized forms. This results in many limitations and complicates the applications to architectural geometries departing from planar and parallel configurations. In these cases, the ability of adaptation comes with the cost of additional mechanical complexity. This further increases the maintenance and proneness to failure (Körner et al. 2018; Lienhard et al. 2011; Schleicher et al. 2015). A potential solution to overcome the high mechanical complexity and maintenance intensity of such movable building structures, are compliant kinetic systems. These enable motion based on elastic deformation. The consequent monolithic construction principle allows for a reduced number of parts, weight, cost, and maintenance requirements due to the absence of friction or wear. The compliant design was derived from nature (Howell et al. 2013). Many plant organs and body parts of animals move without specific mechanical elements such as joints or hinges. The ability for motion arises from locally adapted stiffness of their components (Howell et al. 2013; Knippers and Speck 2012).

However, large-scale compliant kinetic systems materialized so far are driven by conventional actuators, such as electric motors or pneumatic pistons. This contradicts the fundamental idea of compliant construction principle to avoid sliding elements and therefore friction and wear. Consequently, the next developmental step is the integration of the actuation into the compliant system, following the actuation principle of natural compliant systems. This offers additional advantages such as a further reduction of the mechanical complexity, weight, and size of the overall system. Further, the embedment of the actuator not only potentially makes it less visible, but also protects it from environmental influences. In addition to high demands in quantifiable terms such as durability, robustness, and reliability, qualitative aspects such as aesthetic demands must be fulfilled as well, to be used in architecture. As the focus on application here lies in the realm of shading devices, an active actuation that can be triggered by the user is defined as a prerequisite. This excludes the use of passive, material-based systems responding autonomously and solely to a change in environmental conditions. Between the active actuation principles, the fluidic actuation is a promising alternative to conventional actuators. This is also due to the high forces it can generate, as well as the broad application temperature range and rapid response times.

A second aspect that is considered in the following work is the development of adaptive stiffness concepts. The necessity arises from the conflict inherent to compliant mechanisms, to be on the one hand soft enough to allow the required deformation and on the other hand to be able to bear external loads. During high wind loads, the compliant systems that have been implemented in architecture so far require to be moved to a safety position to withstand the loads. This limits their functionality during this time. An adaptive stiffness could ideally stiffen the kinetic systems temporarily against high external loads when needed. Ideally, this stiffness variation can be achieved with the same principles and devices used for actuation.

In the subsequent introductory chapters, the starting point for this investigation will be described in more detail. These topics include conventional kinetic systems, compliant systems, examples for compliant systems in architecture as well as material considerations and an introduction to biomimetics. Based on the information gained from these insights, the *problem statement*, *research question*, *objectives* as well as *methodology* of this thesis will be delivered.

1.2 KINETIC SYSTEMS

1.2.1 Conventional kinetic systems

Kinetic systems in engineering are manifold. They exist in countless variations and scales, everywhere in our daily lives. The necessity for motion arises from different needs. Usually, fulfilling a certain motion is associated with fulfilling a certain task. This may include positioning or the need to adapt to user-requirements. Kinetic systems are realized as mechanisms and machines. In mechanical engineering, a mechanism is defined as a device consisting of connected mechanical elements working together to transfer or transform energy, force or motion from an input to an output. A machine differs from a mechanism by its purpose. A machine fulfills a specific task or performs a defined work (Schleicher 2015).

Both, machines and mechanisms, are kinetic systems. The underlying construction principles, which are the basis for how these kinetic systems are designed, are widely used since the Industrial Revolution (years 1760-1820/40). The increased accessibility of coal eased the production of iron and steel. These improved in quality and therefore became a widespread construction material. The age of the Industrial Revolution was also characterized by the transition from hand to machine-based production. A new design paradigm rooted in this period. It is based on the assemblage of mass-produced, mono-functional, rigid parts, and is still common practice today. As these parts are

produced from stiff materials, their deflections are negligible. This allows for a convenient, linear planning process. Widely known examples following this construction principle are the automobile or locomotives (Schleicher 2015). This construction principle is also referred to as rigid body dynamics or rigid body kinetics. It describes the motion of interconnected bodies caused by external forces (Paul 1979; Tsai 1999). To change the magnitude, point of application or direction of an applied force, mechanical devices are put together from so-called Simple Machines (see FIG. 1.1).

These four basic principles of machines were discovered already in ancient times: rigid objects pushed or pulled by a rod or rope, change the point of where the force is exerted. By passing a rope around a pulley, the direction of the force is changed, defining the second Simple Machine. Another well-known representative is the lever, which changes the magnitude of a force. The fourth Simple Machine is the inclined plane that also changes the magnitude of a force. The angle of its inclination controls the force and travelling distance needed to elevate an object. These simple basic principles can be combined and expanded to convert the applied forces as efficiently and as targeted as possible to the desired outcome. Complex machines as we know them today are designed as such (Schumacher et al. 2010). Simple Machines can be categorized into two groups, based on whether the movement happens along a line (vector resolution of forces) or around a pivot (characterized by the equilibrium of torques) (Schleicher 2015). This also defines the two kinds of movement one can differentiate: translation and rotation. The first one appears if an object changes its position in parallel to a coordinate axis, while the second one describes the change of orientation of an object in space by rotating around an axis (Schumacher et al. 2010). The different kinds of movement and the associated primary elements of a machine require for different types of hinged connections. Four different joints, namely the rotary-, sliding-, cam-, and gear joint (see FIG. 1.2) (Heling et al. 2017). Together with related connections as cables and belts, they interconnect the assembly of solid parts and together form a machine (Schleicher 2015).

The use of these basic tools of design elements expanded during the past centuries. While it is an efficient and appropriate solution for many problems, it is not suitable for all application scenarios. However, instead of questioning the fundamental way of designing, the described approach of using basic building blocks was also pursued in these unsuitable cases. By sticking to the concept of connecting rigid bodies with movable links, more and more complex machines were created, with an increasing number of parts, well into the hundreds and thousands (see FIG. 1.3). This poses increased planning and manufacturing expenses and makes it difficult to integrate new materials, apply new design methods or address new functional demands (Schleicher 2015).

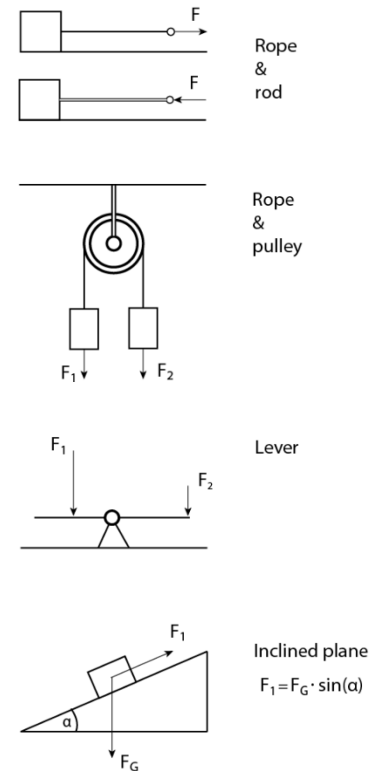


FIG. 1.1: Four Simple Machines changing the direction or magnitude of a force as building blocks for kinetic mechanisms based on rigid body dynamics. Based on (Schumacher et al. 2010).

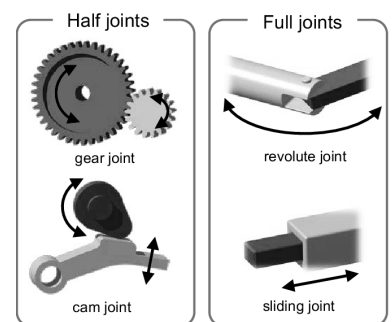


FIG. 1.2: The four joint types: rotary-, sliding-, cam-, and gear joint. (Heling et al. 2017)



FIG. 1.3: Complex structure of the control surface of an airplane wing. (Photo by Annom / CC0)

1.2.2 Kinetic systems in architecture

Despite the widespread notion of buildings as rigid immovable structures, associated with stability and safety, a closer look reveals that there are a considerable number of moving pieces in today's living spaces. They are a response to the need for adaptation and enable spatial adjustments to changing functional requirements that are triggered by internal as well as external factors. Examples are widespread and range from small-scale, valves or flaps, over medium-scale objects like windows, doors, shutters or sun louvers, up to large-scale devices including escalators, elevators, adaptable facades, retractable roofs, or folding bridges (Schleicher 2015; Schumacher et al. 2010). Some large-scale examples are listed in FIG. 1.4. These movable elements are often a prerequisite for the building's durability and help buildings to be more sustainable and energy efficient. At the same time, they contribute towards a richer and more aesthetic experience (Schumacher et al. 2010).

Kinetic systems in architecture can be classified by their field of application. *Spatial applications* provide flexibility by adaptation to changing needs and enable the creation of different atmospheres, contributing to the user's well-being. Parts of the interior or the envelope of a building can be movable (displacement) or variable (deformation) to create changing spatial configurations. Examples include variable room elements as movable walls, platforms, or cells, as well as variable building envelopes. The construction of these elements that needs to ensure an efficient and easy use, as well as the costs, pose a challenge to these systems. *Visual applications* aim to make a building more attractive by the usage of dynamic design. Therefore, this field covers the symbolization as well as staging of movement. Kinetic systems in architecture might use factors as equilibrium and imbalance or speed, form, mass, and sound to compose the way a building is experienced and used. As a third category, the *energetic applications* are defined. They form a broad field with many examples in place in most of the houses already today. As the building sector is a major factor in the global energy consumption, this field of application is of special

importance. Movement is utilized to regulate energy flows within a building to increase the building's energetic performance. Movable systems have a high potential in the optimization of renewable energy harvesting and the thermal regulation of buildings. Adaptive façades can provide an advantage in terms of sunlight and heat regulation (Schumacher et al. 2010).

Independent of the fields of application, motion in architecture can potentially happen at every scale. Whole cities and houses might move as a reaction to changing environmental conditions. This can be seen with nomads. However, also stationary buildings can move to follow the direction of the sun. Parts of houses or their envelope can move for example to enlarge the inner space. However, the most common moving elements are individual elements on comparably small scale. These are usually mass-produced and arrive at the construction site pre-assembled with limited possibilities of individual adjustments (Schumacher et al. 2010). Due to the great number of moving systems already present in buildings, one might argue that the border between building and machine has already been crossed (Schleicher 2015). Consequently, the same design principles as for engineering mechanics are applied. Therefore, mainly stiff



FIG. 1.4: Examples for kinetic systems in architecture:

(A) The Rolling Bridge by Thomas Heatherwick, Paddington Basin. (Photos (left & right) by Loz Pycock / CC BY-SA 2.0)

(B) Kinetic façade Al Bahar Towers by AEDAS. (Photo by Inhabitat / CC BY-NC-ND 2.0)

(C) Milwaukee Art Museum by Santiago Calatrava. (Upper photo by Dasparag / CC BY-SA 4.0; lower photo by gillfoto / CC BY-SA 4.0)

(D) Kinetic façade Syddansk Universitet by Henning Larsen Architects. (Photo by S.Juhl / CC0 1.0)

(E) Responsive façade Institut du Monde Arabe by Enrique Jan + Jean Nouvel + Architecture-Studio. (Photo by Rory Hyde / CC BY-SA 2.0)

(F) Retractable roof National Stadium Narodowy. (Photo by Tadeusz Rudzki / CC BY-SA 3.0)

(G) Umbrellas in Al-Masjid al-Nabawi. (Upper photo by Najamuddin Shahwani / CC BY 3.0; lower photo by Soly1907 / CC BY 3.0)



FIG. 1.5: Shading system inside the double-curved façade of the Peek & Cloppenburg Flagship store Cologne. (Photo by © Raimond Spekking / CC BY-SA 3.0 (via Wikimedia Commons))



FIG. 1.6: Examples for the proneness to failure of conventional shading systems such as external blinds.

materials are used, and kinetic mechanisms are put together of rigid bodies usually connected by hinged joints to create moveable elements. However, for the design of the kinetic structures in architecture, different underlying conditions apply. Besides the mentioned standardized applications as windows and doors, movable structures in architecture usually are designed, constructed, and manufactured only in small quantities or as single pieces. Because of the small quantities produced and the large scale, extensive test runs do not take place at the building scale. This makes these custom-made architectural devices prototypes that need to function on the first attempt (Knippers and Speck 2012; Schleicher 2015; Schumacher et al. 2010).

Caused by the ease of design and fabrication, the conventional design favors linear motions along a grid of orthogonal axes. This limits their application to planar and parallel configurations. A complete adaptation to other than planar surfaces is not always possible (see FIG. 1.5) or comes with the drawback of increased mechanical complexity and cost. The additional mechanical complexity is associated with an increased weight, and results in maintenance-intensive structures prone to failure (see FIG. 1.6). Due to the delicacy of these shading systems, they often have to be placed inside the building envelope, reducing their effectiveness (Nasrollahi 2009). Alternative systems such as membrane structures can take up only two distinct positions; open and closed. Due to the non-existent bending stiffness of membranes, no stable in-between state can be achieved with them. In architecture, elements utilizing elastic deformation are used only at a small scale, such as springs or dampers. Due to the load-bearing capacity required, their use at larger scales is rare (Schumacher et al. 2010).

1.2.3 Compliant mechanisms

1.2.3.1 Definition

Compliant mechanisms follow different constructional principles to create motion than conventional mechanisms. As mentioned above these consist of rigid bodies connected by hinges or sliding joints. Therefore, they generally suffer from a high mechanical complexity and a high number of parts. This comes with a high weight and further tribological aspects need to be considered. Compliance offers itself as a possible solution to overcome these problems. It is defined as deformability that relies on reversible strains (Kuder et al. 2013). In nature, most moving things are flexible, and the bending of these flexible parts enables motion. For mankind, generating motions through elastic strains is not an entirely new concept. Some of the earliest man-made machines were compliant mechanisms. A famous example is the bow, which has been in use since ancient times (Howell et al. 2013).

Compliant mechanisms are kinetic systems built as monolithic single piece. More precisely, compliant mechanisms are defined as mechanisms in which at least one component is sensibly deformable in respect to the other rigid links involved. A graphical and physical comparison of the conventional and compliant design is given in FIG. 1.7 and FIG. 1.8. As conventional kinetic systems, compliant mechanisms transform an input energy, which can be of mechanical, thermal, electric or of other nature, into a desired output motion (see FIG. 1.9) (Lobontiu 2003). That means that, due to the elastic deformation, some of the input energy is stored in the deflected members in the form of strain energy. This allows them to be used as tools and machines. From the perspective of actuation, the spring-like behavior that stores and releases energy is also interesting, as it implies that actuation is only necessary in one direction. The unbent state will be restored by the elastic energy stored within the system.

While in the traditional design one function is assigned to one part, in compliant mechanisms the same overall function needs to be achieved with fewer parts. Subsequently, each part usually fulfills several functions. A dramatic reduction in the number of parts reduces not only weight but also the assembly costs and simplifies the manufacturing (Howell et al. 2013). Ideally, depending on the design, compliant mechanisms can be manufactured as one monolithic piece e.g. by injection moulding or using 3D printing or other additive manufacturing techniques (Schleicher 2015). The reduced number of parts and the monolithic construction principle also eliminates friction and wear. This erases in the need for lubrication and reduces maintenance in general (Lobontiu 2003). This predestines compliant mechanisms for applications under harsh environments or locations that are difficult to access. Mechanisms used in such environments have to work reliable, as maintenance is hardly possible. Another advantage of compliant mechanisms is their potential to be miniaturized. They show an increased performance in terms of precision, especially in small-scale applications. Drawbacks of mechanical systems, such as backlash, vibration or noise, are reduced or eliminated, in contrast to mechanical systems where friction occurs. The most sophisticated compliant mechanisms can therefore be found in microsystems (Howell et al. 2013; Schleicher 2015). Probably, the most important benefit of using compliant mechanisms is the possible weight savings. This is interesting also in aerospace applications. Here, the largest examples for compliant mechanisms can be found. These include solar panels, antennas or reflectors (FIG. 1.10) (Fowler et al. 2011).

However, there are also challenges associated with the design of compliant mechanisms. The possible range of motion is limited as due to the monolithic character, only a low level of rotation can be realized. It is not possible to achieve a pure and continuous rotation. Moreover, the systems are usually sensitive

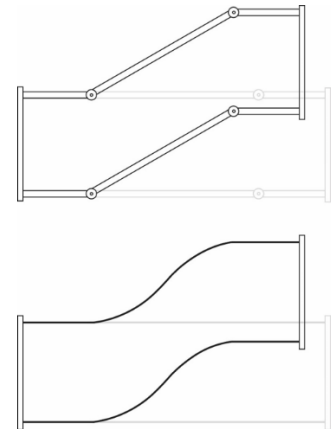


FIG. 1.7: Rigid body (upper) and compliant (lower) mechanism.

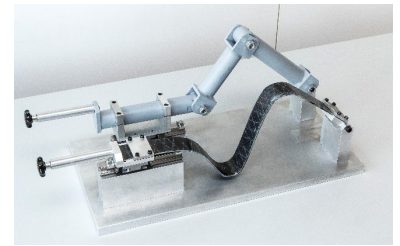


FIG. 1.8: Steel crank with three integrated elastomer elements at the joints (left) and compliant fibre-reinforced composite spring (right). (Lehmann et al. 2015)

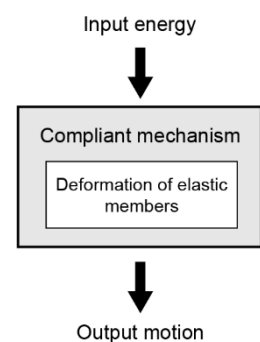


FIG. 1.9: Definition of a compliant mechanism.



FIG. 1.10: Tape-spring hinge for deployable space structures fully deployed, partially folded. It is made from ultrathin two-ply plain-weave laminate of carbon-fiber reinforced plastic. Adapted from (Mallikarachchi and Pellegrino 2011).

to temperature variations. This is due to thermal expansion of the material and also due to the temperature dependent material properties, which modifies the compliance values (Lobontiu 2003). Further, the stored elastic energy can be of advantage in some applications but also carries disadvantages. To hold a specific position, energy needs to be introduced into the system constantly or special devices need to be installed. Depending on the size of the system, the stored energy might also pose a security risk. In addition, special requirements are imposed on the material used in compliant mechanisms. It usually needs to withstand large deformation and large number of load cycles. Therefore, the fatigue properties of the material used, need to be known. The fatigue life must exceed the expected life of the compliant mechanism. Other effects, such as stress relaxation of the material, need to be considered as well during the design (Howell et al. 2013).

As mentioned above, compliant mechanisms consist of fewer parts taking over several functions. Therefore, these systems can be more difficult to design. Additionally, the deflections of compliant mechanisms are usually well into the non-linear range and the simplified linear equations cannot be applied anymore. This makes the design of compliant mechanisms even more complex. Thus, in the past the much easier concept of rigid parts connected by hinges was usually favored (Howell et al. 2013; Lobontiu 2003). However, the increasing computational capabilities and the availability of new elastic materials expanded the use of compliant systems in the past few decades. Improving hardware and software of modern computers allows it to solve non-linear problems more easily and faster, enabling the sophisticated design process. The evolution of plastics allowed the use of so-called flexure or living hinges in everyday objects as shampoo bottles or grippers. Further, advances in material science, including stronger and reliable materials like high-performing thermoplastic polymers and fiber reinforced plastics (FRPs), as well as new and improved manufacturing technologies might further promote the wide-spread use of compliant mechanisms. Even today the applications of compliant system range from high-end, high-precision devices to ultra-low-cost packaging and in scale from nanometers to large-scale machines (Howell et al. 2013). Some examples for compliant mechanisms are shown in FIG. 1.11.

To summarize, compliant mechanisms can undergo substantial reversible deformability. They are a promising alternative to conventionally designed mechanical systems but pose a greater challenge to design, also due to fatigue. Their design is a trade-off between weight efficiency, functionality, and manufacturing costs. Further, compliant mechanisms inherently bear the conflict to combine large deformability and sufficient stiffness, to dead weight and external loads. These inherently opposing features need to be balanced and might be overcome by implementing a variable stiffness concept (Kuder et al. 2013).

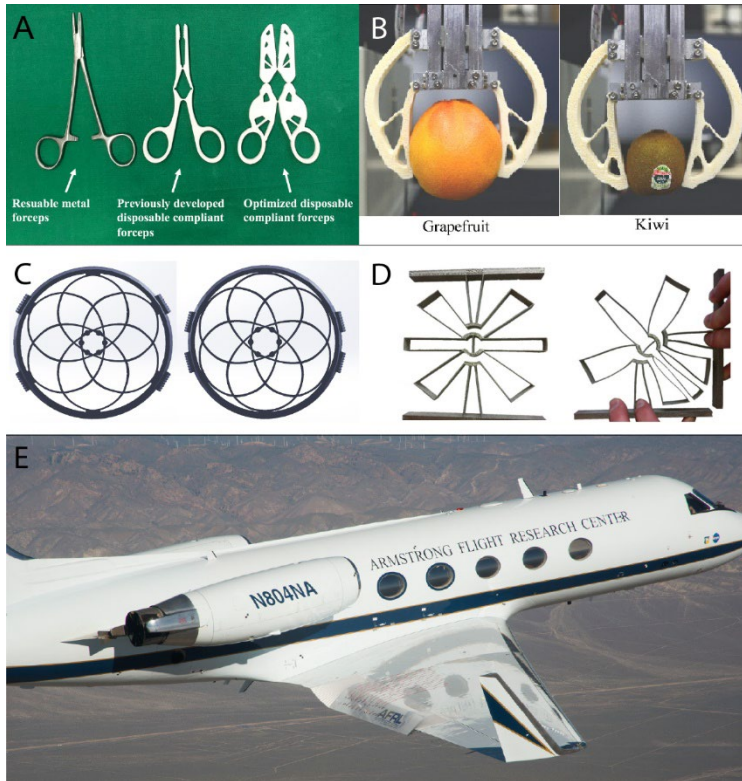


FIG. 1.11: Examples for compliant mechanisms:

(A) Monolithic plastic forceps. (Sun et al. 2020) /© 2020, IEEE

(B) Compliant gripper grasping vulnerable objects. (Liu et al. 2018) /© 2018, IEEE

(C) Compliant two-ring iris circle opening and closing mechanism. Left: closed; right: open. (Photos (left & right) by Pascal Berger / CC BY-SA 4.0)

(D) A compliant titanium hinge capable of $\pm 90^\circ$ of motion for space applications. (Merriam et al. 2014)

(E) The experimental Adaptive Compliant Trailing Edge flap on NASA's modified G-III Aerodynamic Research Test Bed aircraft. (Photo by NASA/Carla Thomas)

1.2.3.2 Material choice for compliant mechanisms

The design and performance of compliant structures depends to a great extent on the properties of the material used. Based on the functional principle of compliant mechanisms, the materials have to be chosen to enable the envisaged flexibility rather than maximizing the stiffness (Howell et al. 2013). As the minimal realizable bending radius is proportional to the ratio of bending stiffness and bending strength, materials possessing a high strength combined a low bending stiffness are especially suitable for the realization of compliant structures. Due to their high strength to stiffness ratio, these materials can undergo larger deformation before plastic damage or failure occurs. FIG. 1.12 depicts the strength to stiffness ratio for a series of common construction materials. The highest ratios can be found in the class of polymers. Accordingly, this group is especially suited for compliant and elastic kinetic mechanisms. Many everyday examples, as living hinges in shampoo bottles or other types of packaging, are made from plastics like polypropylene. However, the low absolute Young's modulus of polymers limits the use to small-scale applications with low external loads to be carried (Schleicher 2015). For the envisaged large-scale application, materials with a higher Young's modulus are needed.

Next to the Young's modulus and strength, further parameters are of importance, such as a low density and a stable long-term behavior. This is particularly important for large-scale applications

and kinetic structures, where the restoring of the original shape happens solely by the elastic energy stored in the material. This behavior takes place only as long as no permanent creep occurs. As stated by Lienhard, the combination of all these necessary criteria is solely met by fibre-reinforced polymers (FRPs) and bamboo (Lienhard 2014). This makes them the material of choice for the realization of kinetic compliant structures.

FRPs combine the properties and benefits of their constituents, namely the polymer matrix and the reinforcing fibres. Common matrix materials are thermoset or thermoplastic materials such as for example epoxy. The reinforcing fibres can consist of a broad range of materials. Widely distributed are glass-, carbon-, ceramic, or natural fibers. Whereby, glass fibres are the most used reinforcement for FRPs. They are widely available, comparably cheap and combine a high strength (2400 N/mm²; E-glass) with a comparably low Young's modulus (73000 N/mm²; E-glass). This makes them suitable for bending active and kinetic structures. However, they possess a rather high density (2.54 g/cm³). This limits the scale of bending active structures made from GFRP due to the high self-weight. Carbon fibres exhibit a considerably lower density (1,8 g/cm³) in combination with a higher strength (3430 N/mm²; HM-fibres) as well as higher

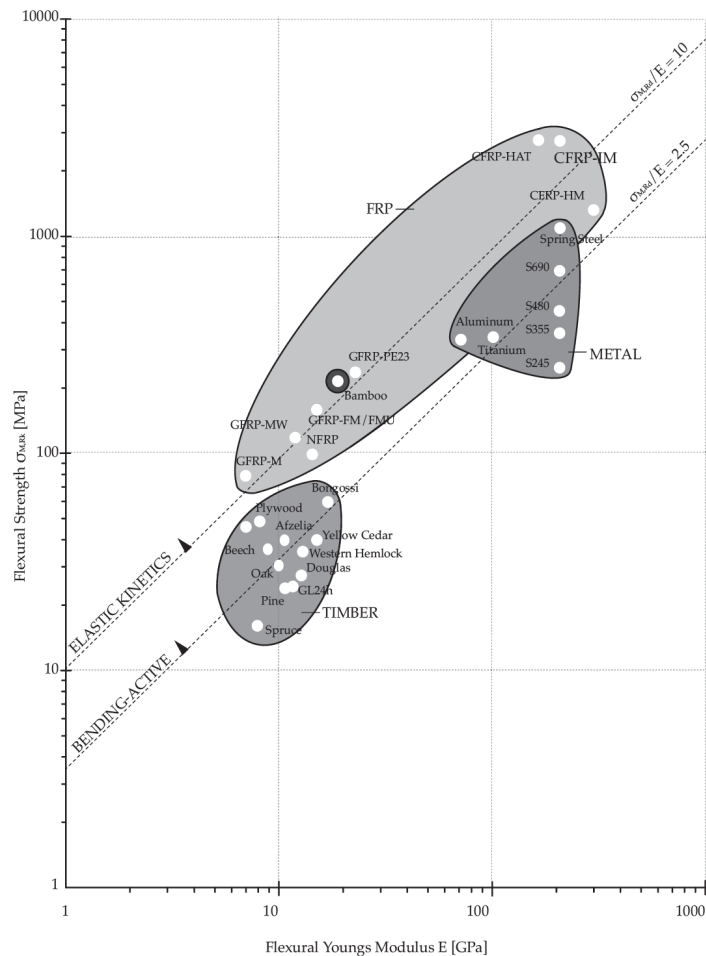


FIG. 1.12: Strength to stiffness ratio of common construction materials.
 FRP - fibre-reinforced polymer
 GFRP - glass fibre-reinforced polymer
 NFRP - natural fibre-reinforced polymer
 $\sigma_{M,Rd}$ - permissible bending stress
 (Lienhard et al. 2013).

Young's modulus (392000 N/mm²; HM-fibers). Their high strength-to-weight ratio outperforms that of steel and aluminum. However, their use is often limited by the high cost (Schürmann 2007). The superior fatigue and flexural properties of FRPs allow them to withstand large elastic deformations as well as cyclic loading. To design a reliable compliant mechanism, precise knowledge on the material's fatigue properties is needed. Fatigue describes the yielding or fracture at stresses lower than the ultimate strength of the material due to cyclic loading. The repetitive application and removal of loads causes the growth of initial micro cracks with each loading cycle. When they reach a critical size, they cause complete rapid fracture. 'S-N curves' provide data for the number of cycles (N) a system can withstand at which stress level (S) (Schijve 2003). FIG. 1.13 shows typical S-N curves for aluminum, steel and FRPs. Two more important aspects make FRPs especially suitable for the realization of compliant mechanisms. Firstly, the composition of their constituents and the controllability over their inner structure such as fibre lay-up, fibre orientation or fibre content allows a high differentiation of the local mechanical properties. This makes it possible to tailor the material set-up of FRPs to specific demands. Secondly, additional elements as sensors or specific actuators can be integrated into the layered built-up of the material itself.

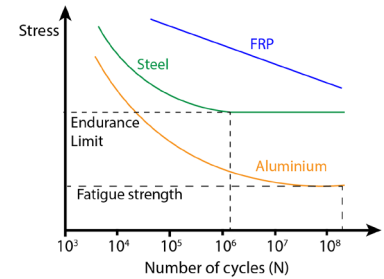


FIG. 1.13: S-N curves for aluminum, steel and FRPs.

1.2.3.3 Compliant mechanisms in architecture

The use of compliant mechanisms in architecture is a topic of ongoing research. Application fields are the same as those of conventional kinetic systems and range from spatial, over visual to energetic applications. Often several demands are fulfilled at the same time. Spatial applications include variable and movable walls used to divide space according to user demands. Visual applications focus on the aesthetics and stage the motion within compliant kinetic systems. An example is the BMW Gina, a car with a compliant envelope perfectly fitting onto its body (Schumacher et al. 2010). Another main field of application is the area of energetic applications. It is based on the regulation of the climate within buildings influenced by solar radiation and ventilation. Here, compliant mechanisms show their potential and enable mechanisms that would otherwise not be possible. Consequently, this investigation focuses on compliant mechanism used for façade shading.

1.2.3.3.1 Bio-inspired compliant façade shading

The design of compliant mechanisms itself can already be considered as biologically inspired (Howell et al. 2013). As this design principle is widespread in the plant kingdom, plants can further serve as models for specific kinetic principles. This is the case in the subsequent examples. Efficient adaptive façades, controlling the energy exchange between the building and its

surrounding, are of special importance in reducing the building's energy consumption. Therefore, robust, and reliable shading mechanisms requiring little maintenance that can be applied externally and to non-planar surfaces, are vital. Fulfilling these demands, a series of plant-inspired compliant shading devices were developed at the ITKE in cooperation with biologist of the Plant Biomechanics Group Freiburg (PBG) at the Albert-Ludwigs-Universität Freiburg. Subsequently, also animal-inspired systems were developed in cooperation with the Institute of Evolution and Ecology (EvE) at the University of Tübingen. These advanced and deployable architectural systems are described in more detail in the following section. They are all hinge-free. This means they operate without technical hinges, which increases their robustness and decreases maintenance.

Flectofin[®]

The Flectofin[®] represents the first of a series of compliant shading devices (Lienhard et al. 2011). The kinematics of this hinge-less shading device is inspired by the valvular pollination mechanism of the Bird-Of-Paradise flower (*Strelitzia reginae*), in a bottom-up approach. For sexual reproduction, the plant relies on birds to transfer pollen from one flower to the other. The valvular pollination mechanisms consist of a protruding perch with two petals attached to it. The weight of a bird landing on the flower to reach for the nectar causes the perch to bend downwards. Consequently, the petals flap sideways and expose the pollen that now can attach to the bird's feet. As soon as the bird leaves the flower, the perch closes again due to the elastic energy stored in the system. The described mechanism is based on the effect of lateral-torsional buckling and can be rebuilt by a thin shell element attached orthogonally to a beam. Usually perceived by engineers as a failure mode, this phenomenon is used by the *Strelitzia reginae* as a hinge-less, reversible deformation mechanisms with multiple deflected equilibrium positions. Therefore, this kinematic principle offers itself as an adaptive façade shading system, the Flectofin[®] (see FIG. 1.14). The Flectofin[®] is composed of a beam with attached fins. Both are made from glass-fibre reinforced composite (GFRP). As explained above, this material combines the necessary high strength and low bending stiffness. The opening motion is triggered by the bending of the beam.

Flectofold

To address some remaining issues of the Flectofin[®] that arise from the distributed compliance of this system, the compliant façade shading device Flectofold was developed. The rather homogeneous and stiff material set-up of the Flectofin[®] causes stress concentrations and high required actuation forces. A solution to overcome this problem is the use of concentrated compliance with distinct hinge zones. These enable deformation with reduced stresses and actuation energy.

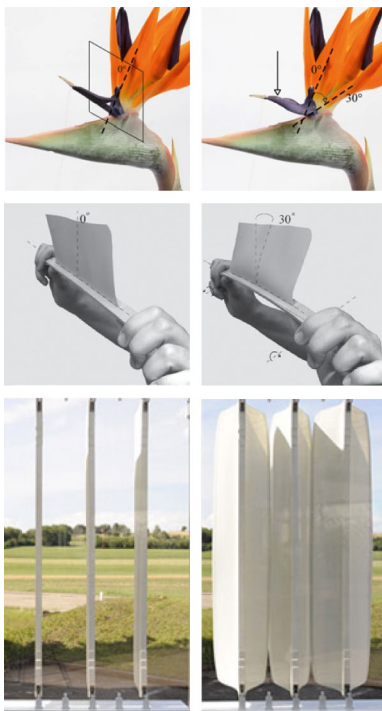


FIG. 1.14: Top: Elastic deformation of *Strelitzia reginae* upon applying a load indicated by the arrow. Adapted from (Lienhard et al. 2011).

Middle: Simple physical model of the abstracted deformation principle. Adapted from (Lienhard et al. 2011).

Bottom: Flectofin[®] demonstrator made from GFRP. Adapted from a photograph by Boris Miklautsch / Architectural photography workshop at the University of Stuttgart.

The design of the Flectofold was inspired by the snap-trap of the carnivorous aquatic waterwheel plant (*Aldrovanda vesiculosa*) (see FIG. 1.15). The plant possesses traps to catch miniscule aquatic prey. These traps are 4-7 mm in size and consist of a pair of lobes connected by a midrib. Each lobe shows a thin and flexible marginal region and a stiffer central region. The supposedly purely hydraulically driven motion is triggered by a so-called motor zone located in the central region. A rapid decrease in turgor pressure, triggered by sensory hairy structures inside the trap, causes a bending of the midrib. The comparably small motion is amplified by the folding mechanism and leads to the complete closing of the trap within ~10–100 ms (Poppinga et al. 2019; Poppinga and Joyeux 2011; Schleicher 2015; Westermeier et al. 2018).

The motion amplifying folding pattern can be transferred to a technical system. The kinematics of the abstracted curved-line folding principle is depicted in FIG. 1.16. The plane defined by the fold line functions as a mirror plane during folding. Consequently, the curvature of both adjacent surfaces (midrib and flap) equals. Through this principle, a small deformation of one surface leads to an amplified folding motion of the attached surfaces. Within a shading device, the manipulation of the midrib curvature can be used to control the degree of folding (Körner et al. 2018; Schleicher et al. 2015). The radius of the curved folding line determines the degree of motion amplification and the actuation force required. A smaller radius requires a strong bending of the midrib, and subsequently, a large displacement of the midrib support points is necessary. A larger radius decreases the deflection needed, but at the cost of an increased actuation energy. Flectofold prototypes were materialized using GFRP in combination with an elastomer foil and a covering PVC film (FIG. 1.17). To minimize bending stresses, a strategic graded transition area between the hinge zone and the stiffer midrib, as well as the positioning of the elastomer layer within the hinge-zone were considered. The hinge zone needs to be flexible enough to undergo repeated extensive bending, while also needing to be stiff enough to provide stability against self-weight and external loads. Further, the unfolding of the element through the stored elastic energy needs to be ensured (Körner et al. 2018).

Flexafold

Another example for a compliant façade shading element is the Flexafold. Unlike the previous plant-inspired mechanisms, it is inspired by the folding of insect wings. These also are equipped with a joint-free kinematic. Insect wings consist of cuticle. Like plant cell walls, the cuticle is a fiber-composite structure. Foldable insect wings are differentiated into rigid plates (sclerites) and pliable regions (membrane). FIG. 1.18 shows the biological role model *Graphosoma lineatum italicum* with one

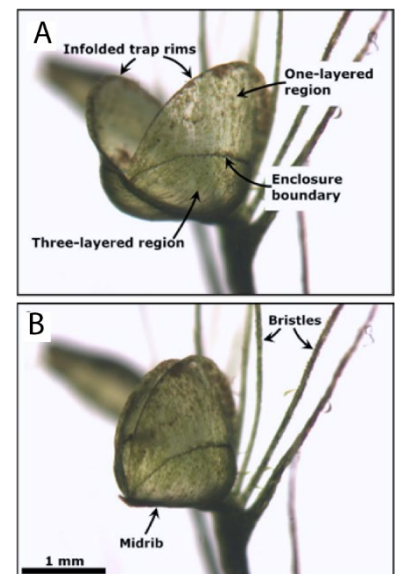


FIG. 1.15: Snap-trap of the waterwheel plant *Aldrovanda vesiculosa* in (A) open and (B) closed conditions. Adapted from (Poppinga et al. 2019).

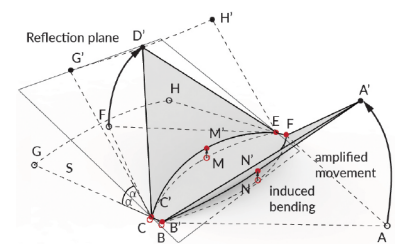


FIG. 1.16: Abstracted kinematic principle of curved-line folding approximated with the method of reflection. Adapted from (Körner et al. 2018).

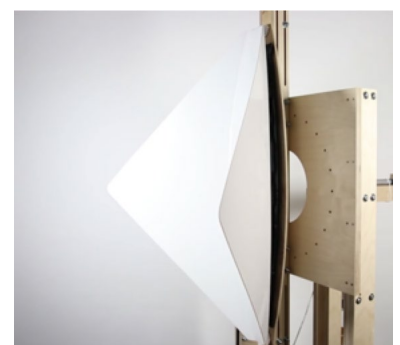


FIG. 1.17: Physical prototype of a Flectofold manufactured from GFRP with an elastomer layer and a covering PVC film. Midrib length in open position: 850 mm. (Photo by ITKE/Saman Saffarian)



FIG. 1.18: The biological role model for the Flexafold, the minstrel bug *Graphosoma lineatum italicum*. Forewing (FW) and hind wing (HW) partially extended on the left and completely folded on the right. Head-body length: 13 mm. (Schieber et al. 2017)

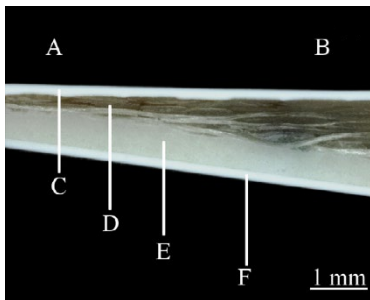


FIG. 1.19: Micro-section image of the graded transition between stiff (thick) and flexible (thin) regions of the Flexafold. A: Hinge zone. B: Rigid component area. C/F: PVC foil. D: Gradually stacked prepregs. E: Elastomer foil. Adapted from (Schieber et al. 2017).

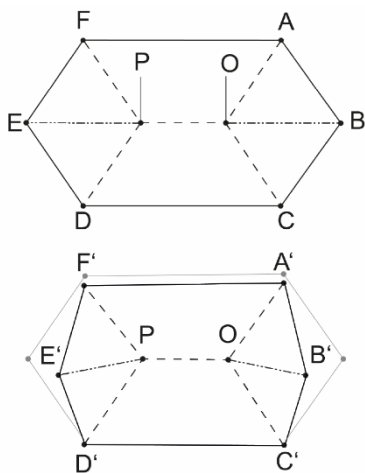


FIG. 1.20: Abstracted kinematic principle of the Flexafold. Adapted from (Mader et al. 2020a).

folded and one unfolded wing. The folding takes place along defined pliable regions, the folding zones. Several construction principles in the structure and material composition support the function of the folding zones. These were distinguished as an adaptation to specific demands required in order to withstand repeated folding and unfolding (Schieber et al. 2017).

Some of these structural principles were transferred to the distinct hinge zones connecting rigid plates to realize a compliant folding mechanism. Like the cuticle of the insect wing, the technical composite consists of continuous layers of material. The examination of the insect wings revealed a decreased thickness in the hinge zone, as well as a higher relative content of resilin-enriched mesocuticle. As resilin is a rubber-like polymer with a high elasticity, it is believed to avoid material failure within this region. Next to the decreased thickness and different material composition, a third important aspect is the graded transition between the stiffer and more flexible wing sections (see FIG. 1.19) (Schieber et al. 2017). These three structural principles are transferred to a technical hinge zone, with a continuous layer of elastomer representing the resilin-enriched mesocuticle and a GFRP the high sclerotization of the stiff exocuticle (Born et al. 2017). To further reduce the bending stresses, the GFRP prepreg layers pass through the hinge zone with a fibre orientation of $\pm 45^\circ$. The material set-up is similar to the Flectofold described above. However, the Flexafold differs from the Flectofold by having straight instead of curved fold lines. This allows an easier and faster design and production.

The folding pattern of the Flexafold is based on the flexagon. Next to the zigzag pattern, it is one of the two fundamental folding principles found in insect wings. The simplest flexagon model is composed of four flat panels connected by four creases with a single degree of rotational freedom (Haas and Wootton 1996). For the flexagon folding principle, three creases fold in the same direction while the fourth folds in the opposite direction (i.e., three convex mountain folds and one concave valley fold or vice versa). The global geometry of the system is defined by the four angles between the fold lines around the central point. A model can be folded flat only if all angles sum up to 360° . For a complete folding, the non-adjacent angles must sum up to 180° . Analog to the curved-line folding, a motion amplification takes place and by choosing the angles, the folding behavior can be influenced. The folding pattern of the Flexafold is shown in FIG. 1.20.

1.3 ACTUATION

Motion requires actuation. As machines, actuators face the same challenges and shortcomings as other kinetic systems. Conventional actuators follow the design paradigm of rigid body

dynamics. Consequently, conventional actuators address mainly the motion needs of conventional kinetic mechanisms. These are translation and rotation as input for Simple Machines. Schumacher defines an actuator as a driving machine that converts energy into mechanical work (Schumacher et al. 2010). Within this chapter, the focus lies on the current state of actuators in architecture and their use for actuating compliant shading devices. A more extensive review on different actuator types with their specific advantages and shortcomings is given in chapter 2.1.

Small to medium-scaled kinetic mechanisms in architecture, such as windows or doors, can partially be actuated by human labor. Automated systems and larger-scale structures entail actuators. For architectural applications, these usually require a high positioning force and a long positioning distance. Furthermore, small actuation speeds are sufficient. Rapid motions are normally not required and might even pose a safety issue.

Today, mainly electric motors or electric pumps in combination pneumatic or hydraulic systems are in use. Gearboxes and transmissions can be used to transfer the forces from the drive unit to the work machine. Thereby they adjust power, direction of force and, if necessary, also type of motion, transferring translation into rotation and vice versa. Electric motors come in form of linear or rotation motors. The maximum thrust of electric linear motors is in the low double-digit kN range. However, rotation motors are cheaper and more common. Their rotary motion can be transferred into linear motion employing a timing belt or racks. In combination, these mechanisms are used to open doors and windows or to control blinds. Electric motors are available in a broad range of sizes, from millimeters to heavy-duty engines. On the other hand, fluid-driven actuators are characterized by their large power output. However, this comes at the cost of a lower energy efficiency. A further advantage of fluid-driven systems is that the main part of the actuator, the electric pump and possible pressure tanks, can be placed decentralized. The pressure medium can be transported over wide distances. Pneumatic tubing can span up to 1,000 m, and hydraulic tubing up to 100 m. Especially, hydraulic systems can provide high actuation forces of up to 3,000 kN, created by pressures of up to 600 bar. Pneumatic systems operate with pressures of up to 6 bar and generate forces up to 30 kN. They offer the advantage of not requiring a closed circuit. Both types of fluidic actuators can be built as translation motors in the form of cylinders or as rotation motors. The specific advantages of the rather complex fluidic rotation motors, such as overload protection and dust resistance, are usually not relevant to the building sector. Therefore, electric rotation motors are preferred. Next to pneumatic or hydraulic cylinders, special designs such as artificial muscles that generate tension forces as well as lifting



FIG. 1.21: Flectofin® demonstrator actuated by electric motors. (Photo by ITKE)



FIG. 1.22: Hydraulic system actuating the up to 14 m high bendable lamellas of the kinetic façade of the Ocean One pavilion at the Expo 2012. (Photo by ITKE)

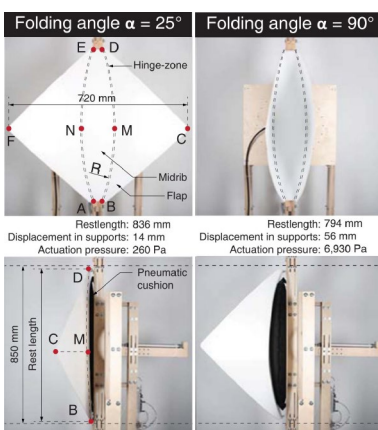


FIG. 1.23: Motion sequence of the Flectofold. The prototype is actuated by a pneumatic pouch placed behind the midrib and a stiff substructure. Adapted from (Körner et al. 2018).

bags exist. These indicate the emergence of novel approaches also in the design of actuators (Schumacher et al. 2010).

So far, physically realized compliant shading devices are actuated by the conventional actuators described above. For all compliant systems considered here, bending is the underlying deformation mechanism that allows the spatial adjustment of the shading device. The bending is introduced by different means. The Flectofin® demonstrator is actuated by electric motors applying a compression force to the midrib, which results in the bending (see FIG. 1.21). Similarly, the large-scale façade of the EXPO Pavilion in Seoul is bent by hydraulic cylinders (see FIG. 1.22). The application of the external compressive force creates high stress concentration and requires additional reinforcement of the midrib. Further, the overly complex mechanical systems, which need maintenance and lubrication regularly, contradict the advantages gained from the use of a compliant construction principle. A first step towards reducing mechanical complexity also within the actuation system and supports is made with the Flectofold prototypes. As FIG. 1.23 shows the midrib of the Flectofold is bent by a pneumatic pouch placed between the Flectofold and a stiff substructure (Körner et al. 2018).

1.4 BIOMIMETICS

Following the development of the bio-inspired compliant kinetic mechanisms, it is only natural to look to nature for integrated design principles to actuate these systems as well. Therefore, this thesis follows a biomimetic approach to develop bio-inspired integrated actuation principles for these mechanisms. The central idea of biomimetics is the transfer of biological principles to technology. In an innovative process, knowledge gained from analyzing living systems, is used to find solutions to technical problems. The disciplines of biology and technology are combined to solve technical problems by abstracting, transferring and applying knowledge about biological models. The word biomimetics tries to describe the above explained developmental process by merging the words “biology” and “mimesis”. Although the latter of the two words is the Greek term for imitation, this shall not induce that biomimetics is the mere mimicking of nature. To better capture the innovative potential of the abstraction and transfer process, alternatively, more encompassing adjectives as “biologically inspired” or “bio-inspired” are endorsed. In languages as French and German, new terms such as “Bionique” or “Bionik” are created by combining the words biology and technology (ISO 18458: 2015-05; VDI 6220 Blatt 1: 2012-12).

The underlying idea of biomimetics is that during the 3.8 billion years of evolution, through mutation, recombination, and

selection, optimized biological structures evolved to adapt to constantly changing environments. These structures must fulfil a variety of tasks. Many of those are similar to challenges technological developments face. Since the same underlying physical laws and constants apply to both domains, biology and technology, solutions and principles can be transferred by an abstraction process. As to date more than 2.5 million different species are known, there is a virtually inexhaustible source of ideas and inspirations available (Knippers et al. 2016; Schleicher 2015; VDI 6220 Blatt 1: 2012-12). However, it needs to be kept in mind that because of the multifunctionality of biological systems, biological solutions are very rarely optimal. As usually multiple functions must be fulfilled at the same time, the optimization of one character of function results in a deterioration of one or several others. Thus, biological systems can best be described by a pareto-optimum (Knippers et al. 2016).

The approach of looking into nature for inspiration for technical design is almost as old as mankind. However, during the area of industrialization, biology was greatly overlooked as source of inspiration. Since the 1990s a new area of biomimetics did arise, mainly due to rapid advances in the fields of computer science, nanotechnology, mechatronics, and biotechnology. Digital technologies allow the direct exchange of information and data between different fields of sciences. This broadens the transdisciplinarity of biomimetic research and the application of engineering methodologies to biological research. Technologies as computational imaging, simulation, and digital fabrication, enable the investigation of local differentiation at various scales as well as the analysis of the form-structure-function relationship. Furthermore, these advances also enable the manufacturing of more complex structures (Knippers et al. 2016; VDI 6220 Blatt 1: 2012-12). Biological and technical constructions often look amazingly similar at first glance; however, a closer look reveals some fundamental differences. As already mentioned, biological structures are usually multifunctional and need to fulfill different, often contradictory, functions. At the same time, they must provide a high level of reliability and adaptivity. To achieve this, these structures usually are very failure tolerant and possess the ability to self-organize (VDI 6220 Blatt 1: 2012-12). This becomes even more impressing when considering that only a limited number of molecular building blocks are available to living organisms. The properties of biological structures also arise from the complex hierarchical structure, often spanning five to seven levels and up to twelve orders of magnitude. This results in heterogeneous, anisotropic and highly differentiated properties, often tailored exactly to the specific local demands (Knippers and Speck 2012). Therefore, it becomes merely impossible to distinguish between material and structure in many biological structures. In this regard, biological structures differ clearly from the technical approach. Here, material and structure are designed and

optimized independently (Knippers et al. 2016). However, the paradigm shift away from using as many equal building parts as possible has already begun. Computer-aided design and manufacturing processes enable the automatized production of individualized parts (Knippers and Speck 2012).

Based on the increased media attention biomimetics received over the past decades, one might expect that it already is a well-established scientific discipline with a defined research methodology. Nevertheless, biomimetics still is a comparably young field of science (Schleicher 2015). In 2012, the Association of German Engineers (VDI) provided a framework for biomimetic applications with the guideline 6220 (VDI 6220 Blatt 1: 2012-12) and in 2015 an ISO standard was released (ISO 18458: 2015-05). The development of new ideas is fundamental to the application-oriented biomimetic research. Based on this idea, a biological model is analyzed in detail and in a next step the underlying functional principle is abstracted. Suitable experiments or model-based analyses of the technical objectives are designed and conducted. The gained results are the basis for possible explanations which are formulated in the abstraction phase. In the development phase an invention in the form of either a new product or a new process is designed, tested, and evaluated. As the specific course of action differs between the scientific disciplines, no generally applicable methodology is specified. However, it is stated that a product can only be labeled as biomimetic when all three phases have been conducted. A biological role model needs to be available, which has been abstracted and transferred to a technical application that is at minimum in the state of a prototype. Only after the successful introduction of the biomimetic invention it becomes an innovation. FIG. 1.24 depicts this ideal linear biomimetic process. Experience showed that these steps cannot always be followed linearly and successively. It is rather the case that many steps happen in parallel or are carried out recursively. For example, initial ideas for the technical process or product will usually be generated already during analysis or the abstraction phase, or even at the beginning of the biomimetic process with the development of new ideas. The starting point for the development of new ideas can come from biology or the engineering sciences. Therefore, two biomimetic development processes, namely the biology push (bottom-up process) and a technology pull (top-down process), are differentiated. In the first one the basis for the biomimetic development process is knowledge from the field of biology gained from basic research. A technology pull process is triggered by an existing technical product or process and the will to improve it. Biomimetics is an interdisciplinary process relying on the close cooperation among all disciplines along all steps of the process. A process sequences in biomimetic research that will the basis for the following investigations is given by Speck & Speck (Speck and Speck 2008). Moreover, biomimetics is not solely about the

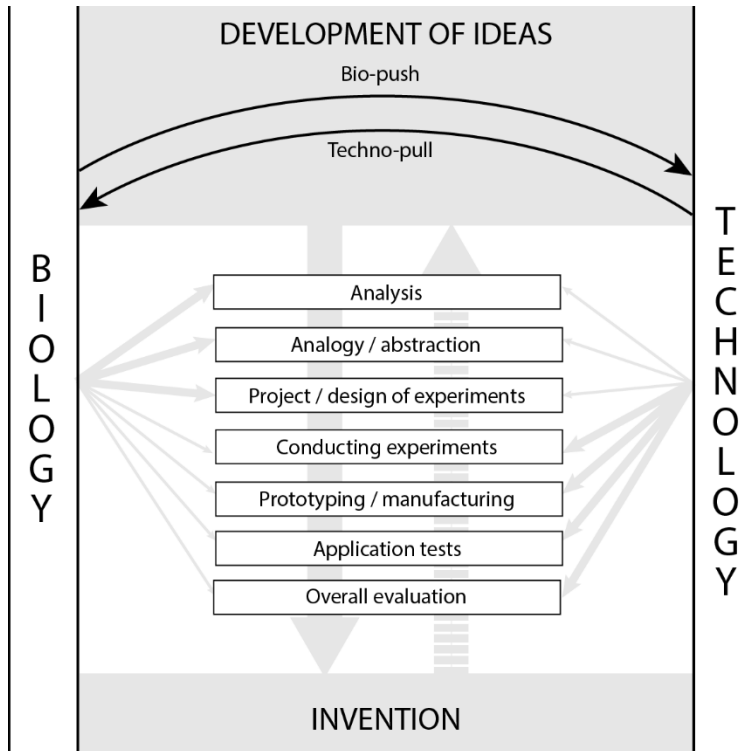


FIG. 1.24: Ideal, simplified biomimetic development process. Based on (VDI 6220 Blatt 1: 2012-12).

transfer of biological insights to technology. Further methods of engineering are applied to the biological models and this way the understanding of these is deepened (Speck and Speck 2008; VDI 6220 Blatt 1: 2012-12).

1.5 RESEARCH HYPOTHESIS AND AIM

Background

The previous chapters described the background and starting point for this investigation. It is situated in the realm of bio-inspired compliant kinetic mechanisms made from FRP that are used as architectural shading devices. The bio-inspired compliant construction principle allows them to be applied also to doubly curved façade geometries and shows a reduced mechanical complexity. This makes them robust and reduces the proneness to failure as well as maintenance intensity. These properties are a great advantage over conventionally designed shading devices.

Problem statement

The bio-inspired compliant kinetic systems, with all their described advantages, however, are still actuated by conventional actuators. They are actuated externally by applying compressive forces with conventional actuators such as electric motors or hydraulic systems. These face the same problems as conventional kinetic systems. Namely, a high number of parts causing a high mechanical complexity, as well as stress

concentrations where the forces are introduced into the system. Structure and actuator are separate parts of the construction requiring delicate connections. For many applications conventional actuation systems are difficult to apply and entail a high weight as well as space requirements.

Another problem inherent to compliant mechanism is that they must meet contradicting demands in terms of their stiffness. On the one hand, they need to be flexible enough to allow the deformation necessary for the desired motion, on the other hand, they need to be stiff enough to withstand the external loads. The stiffness also directly influences the actuation force and energy needed to trigger the motion. Therefore, it would be of great advantage to adapt the stiffness according to the current requirements. A low stiffness state that facilitates spatial adjustment and a state of increased stiffness that allows the system to withstand shorter periods of increased external loads while maintaining the full system functionality. Up-to-date compliant shading devices need to retract to safety positions at high external loads, which limits their functionality.

Research question

The underlying aim of this thesis is to extend bio-inspired compliant construction principles to the actuation for benefits such as reduced weight, mechanical complexity, failure susceptibility and maintenance. Since nature has already served as a model for 2-dimensional compliant mechanisms, this promises to be a promising approach for actuator technology as well. Nature is full of examples for joint-free kinematics. Their actuation mechanisms are to be examined more closely in terms of their function and their potential for transfer to technical systems. Consequently, this research aims to investigate whether the actuation principles of biological compliant systems can contribute to the development of an actuation mechanism for technical compliant systems. Within a biomimetic process, biological role models will be investigated, and their functional principles abstracted to develop a joint-free actuator with continuous kinematics that can be integrated into 2-dimensional compliant systems. This integrated approach might also possess advantages over conventional systems, such as lower actuation forces, more distributed force introduction and the need for less mechanical supports. Another aspect to be investigated in this context is whether also mechanisms for achieving variable stiffness in biology can be used to develop an actuator that also has an adaptive stiffness. This is for temporary support or softening depending on the current need.

From this research questions arises following hypothesis: *The functional principles of biological role models for an integrated, compliant actuation can be transferred to technical joint-free actuators with continuous kinematics for the actuation of 2-*

dimensional compliant systems. With the derived actuation principles also a variable stiffness concept can be developed.

The term continuous kinematics describes a deformation that can be controlled continuously and where any state between the minimum and maximum deformation can be achieved by actuation. Further, the term “compliant actuator” is used here to describe a joint-free mechanism.

General framework

This thesis is based on the preliminary work of Mohammad-Reza Matini, Julian Lienhard and Simon Schleicher on bio-inspired kinetic systems for architectural applications. Their work is summarized in their dissertations with the titles “Elastic structures in architecture on the basis of bionic principles”, “Bending-active structures”, and “Bio-inspired compliant mechanisms for architectural design” respectively (Lienhard 2014; Matini 2007; Schleicher 2015).

Great parts of this research were conducted within the Collaborative Research Center SFB-TRR 141: Biological Design and Integrative Structures – Analysis, Simulation and Implementation in Architecture sponsored by the DFG and the project BIAG sponsored by the Baden-Württemberg foundation. Within the SFB-TRR 141 the project A03 dealt with the topic “Inspired by plants and animals: actively actuated rod-shaped structures exhibiting adaptive stiffness and joint-free continuous kinematics”. The project was conducted as close collaboration between biologist (Plant Biomechanics Group Freiburg (PBG), Albert-Ludwigs-Universität Freiburg and Institute of Evolution and Ecology (EvE), University of Tübingen) and engineers (Institute of Applied Mechanics (CE), Institute of Building Structures and Structural Design, University of Stuttgart). Further, the developments were carried out in close cooperation with the project A04 “Kinematics of planar, curved and corrugated plant surfaces as concept generators for deployable systems in architecture”. Parts of the following work were conducted within the interdisciplinary biomimetic research project BIAG (Bio-inspired adaptive facade shading systems). These developments were conducted together with biologist of the EvE and material experts of the German Institutes for Textile and Fiber Research (DITF), Denkendorf as well as Institute for Textile Technology, Fiber Based Materials and Textile Machinery (ITFT), University of Stuttgart.

Thesis objective and scope

According to the research questions, the objective of this thesis is to develop new joint-free, bio-inspired actuators with continuous kinematics that can adapt their stiffness. These actuators are developed in a biomimetic development process. The aspiration of the following is to lay out the complete biomimetic process from the search of the biological role models

to the fabrication of first prototypes. Within this process, the aim is also to gain new insight on the working mechanisms of the investigated biological role model. The actuator prototypes developed in this workflow are intended as a proof of concept to demonstrate the general technical applicability of the developed actuator concepts to exemplary cases. Determining the exact boundaries and physical limits of the system is not part of this investigation.

Further, the actuation mechanism in the biological role models as well as the technical development need to be active. This means the actuation can be actively manipulated by the user and is not an autonomous passive reaction to changes in the environmental conditions. For the adaptive stiffness concept, the focus is on short-term and reversible stiffness variations not considering long-term stiffness changes that are related to growth or changes in the material composition.

Methodology & structure of the thesis

The structure and methodology of this thesis is displayed in FIG. 1.25. After the general introduction that provides an overview on actuation mechanisms as well as adaptive stiffness concepts in biology and engineering the thesis is divided into two parts representing two case studies. The two case studies follow the top-down biomimetic development process and differ in the heritage of their biological role model. Case study I is oriented towards the plant kingdom, case study II towards the animal kingdom.

Both approaches follow the aim of developing a joint-free biomimetic integrated actuation concept. However, the starting point for the investigations are different. In the case of the plant-inspired development the search for a biological role model was not limited by a pre-defined technical working principle or the actuator. The fascination for the compliant, integrated actuation of plants combined with their observable stiffness change was the starting point. For the animal-inspired part a predefined idea of how to realize a joint-free pneumatic actuation existed. The starting point was the approach of integrating pneumatic pouches into the layout of a GFRP. However initial test showed a delamination of the adjacent layers. Finding a solution to this technical question was the underlying question for the second, top-down biomimetic development process.

The biomimetic development process for both case studies follow the steps of a typical top-down biomimetic development process. The first step is the search for a biological role model with a joint-free integrated actuation with continuous kinematics. The biological model will be analyzed to understand the functional principle. In the abstraction phase the functional principle will be transferred to a technical solution. The technical feasibility is then checked, and prototypes are built to achieve an improved product. By applying the tools of engineering (like

finite-element-simulation) to biology new insights into the working principles of the role models will be gained as well.

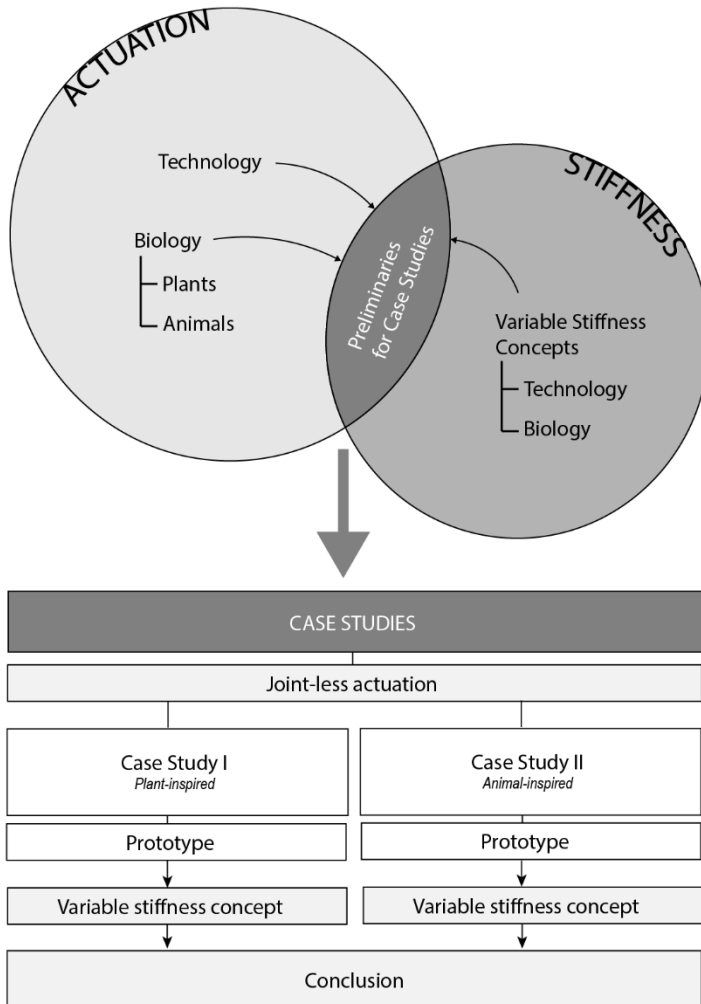


FIG. 1.25: Structure of this thesis.

2 BACKGROUND

2.1 ACTUATION IN ENGINEERING

2.1.1 Introduction to actuators

An actuator is defined as a functional element connecting the information processing part of an electronic control system with a technical or non-technical process. Actuators control the flow of energy, mass, or volume within a system. To do so, an actuator requires a control. The functional structure of actuators is built by “energy controllers” and “energy converters” (see FIG. 2.1). These are the two elementary functional components. The energy converter is the central part of the actuator. The input and output of an energy converter are energies. These energies can be of the same kind, as is the case for current transformers or torque converters, or of different kinds, as is the case in electromagnetic or piezoelectric transducers. In literature and the scientific community, the term actuator often refers to only the energy converter, leaving out the controllability by a low-power electrical system. An energy controller provides the energy of an auxiliary power supply which is controlled by the input variable. Typical examples for energy controllers are transistors or valves. The auxiliary power actuators can draw from chemical, electrical and mechanical sources (Janocha 2004b).

In simpler terms an actuator forms the active part of a system. It provides the necessary driving force and motion for natural as well as man-made systems. The term system includes the power source and the device converting the power into a form appropriate for the actuator. I.e., electrically driven actuators usually draw their energy directly from a national electricity grid, while hydraulic or pneumatic actuators require additional devices that provide the compressed fluid. The specific requirements for an actuator, such as force, displacement, stiffness, size, mass, operating frequency, power, efficiency and resolution, arise from the specifics of the countless applications. Other requirements that are important as well but more difficult to quantify are costs, durability, maintenance, as well as environmental aspects (Huber et al. 1997; Zupan et al. 2002). Typical applications of actuators span from large-scale, high-force applications to small control devices in the range of microns. Some common application fields are aerospace (e.g. the movement of flight control, landing gear or air brakes), automotive (e.g. braking, active suspension or airbag deployment) and industrial equipment (e.g. automation machinery, presses or lifting tools), as well as electrical goods (e.g. automatic switches, thermostats, disc reading heads and camera auto-focus) (Huber et al. 1997).

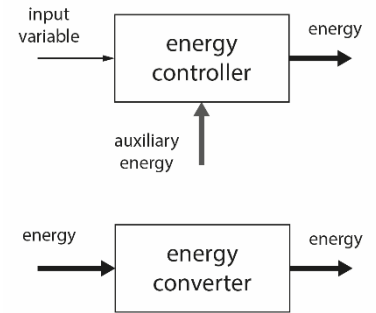


FIG. 2.1: Definition of an energy controller and energy converter. Based on (Janocha 2004b).

Depending on their functional principle and how widespread their use, actuators can be subdivided into following three classes: electromagnetic, fluidic and unconventional actuators. The later one includes smart materials, such as shape memory materials as well as piezoelectric or magnetostrictive actuators. Electromagnetic and fluidic actuators are the standard actuators found in the vast majority of applications. All other actuators are referred to as “unconventional actuators”. In recent years different types of unconventional actuators gained increasing significance. This is mainly due to their increasing number and broad range of applications (Janocha 2004b). In the following subchapters a short summary of function, implementation, as well as specific advantages and disadvantages is given for different classes of actuators.

2.1.2 Conventional actuation systems

2.1.2.1 Electromagnetic

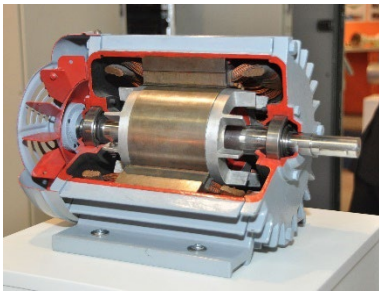


FIG. 2.2: Cutaway view showing the components of an induction motor. The electromagnetic forces make the rotor rotate. (Photo by S.J. de Waard / CC BY-SA 3.0)

Electromagnetic actuators transform electrical into mechanical energy (and vice versa) (Stölting 2004). Commonly used are three different types of electromagnetic machines, namely solenoids, moving coil transducers and electric motors (Huber et al. 1997). They all make use of the Lorentz force that results from the interaction between a magnetic field and the current running through wires wound into an electromagnetic coil. A multitude of electric motors (see FIG. 2.2) is available on the market. Sizes and forces that can be created range from miniature devices as electric clockworks and high-precision positioning devices for handling tasks in laboratories, over rotors, fans, household and machine tools, to large-scale applications such as pumps or electric motors for cars. The great variety of applications is based on the numerous construction principles. Depending on the source of power, there are DC (direct current) and AC (alternating current) motors. Further they might use permanent or electric magnets, and may be brushed or brushless. All this has an influence on price and durability (Stölting 2004).

Next to electric motors, so-called limited motion drives are based on electromagnetic principles of force generation. They create only a short linear or rotational movement that can be unique or oscillating (Stölting 2004). One example are solenoids that consist of a fixed magnetic element, a coil and a moveable highly permeable rod. Upon energization the rod is moved by the magnetic field (Huber et al. 1997; Stölting 2004).

Gearboxes can be used to transfer the forces from the drive unit to the work machine thereby adjusting power, direction of force and, if necessary, also type of motion by transferring translation into rotation and vice versa (Schumacher et al. 2010).

2.1.2.2 Fluidic actuation

Fluid-power actuators transfer the power of a fluid into a specific mechanical output. This is usually a longitudinal or rotatory motion with a specific stroke, speed & force or angle of rotation, rotatory speed & torque respectively (Backé and Klein 2004; Janocha 2004a). Fluidic actuators are very common and applied in nearly all fields of industry. Fluidic actuation is part of our daily life, as there is almost no product that is produced without its help (Watter 2015). The fundamental principle utilized in fluidic actuation is that a fluid with a static pressure P exerts a force F on a surface A .

$$P = \frac{F}{A} \quad (1)$$

Fluids can be gases or liquids. The term includes all substances with a shear modulus of zero. Depending on the pressure medium used, fluidic actuators subdivide into hydraulics and pneumatics. Compared to other types of actuation hydraulics is characterized by a high energy density. Here fluids are used as pressure medium. Hydraulic systems usually operate at high pressures of up to 420 bar. Pneumatics, use gases as pressure medium and usually operate in the pressure range of 6 to 10 bar. It is distinguished by an efficient and inexpensive construction (Backé and Klein 2004; Huber et al. 1997; Janocha 2004a). To generate a rotatory or translatory motion, a variety of hydraulic or pneumatic motors and cylinders exist. The functional principle of a fluid-driven cylinder is shown in FIG. 2.3.

To control the output motion, pressure valves are required to direct the pressure flow and regulate the pressure level. Proportional valves are electrically controlled and allow the connection to an electronic control system. Also, a pressure source that provides the pressurized fluid is part of the system (Backé and Klein 2004). These are usually displacement machines as pumps and compressors (Watter 2015). Especially the possibility to transfer the fluid-power energy to a motion generating consumer by using pipes or tubes, offers a great advantage over mechanical mechanisms of energy transmission. These are limited in reach by geometrically given energy paths. A comparison of transmission distances and pressure levels between pneumatics and hydraulics is given in Table 1.

Table 1: Comparison of pneumatics and hydraulics key parameters. (Data from (Watter 2015)).

	Pneumatics	Hydraulics
Energy source	Compressor	Pump
Pressure	≈ 6 bar	≈ 30 - 400 bar
Transmission range	≈ 1000 m	≈ 100 m

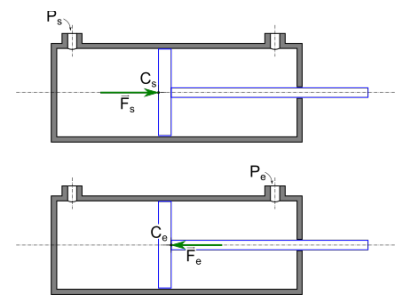


FIG. 2.3: Top: Pneumatic cylinder that converts the energy stored in the compressed fluid into a linear motion. (Photo by Giaquini)

Bottom: Simplified cross-section of a double acting cylinder. The piston slides outwards or inwards when fluids are pumped into the respective parts of the sealed cylinder. The force generated is proportional to the pressure P of the fluid. (Image by Cdag / CC BY-SA 3.0)

A further outstanding characteristic of fluidic actuators that deserves special emphasis is the low energy weight and the low space requirements of the energy converters. However, for fluidic actuators special attention must be paid to the maintenance of the pressure fluid, as filtration or draining of ingressed water. Also, leakages must be avoided. These waste energy and might also cause undesirable noises (Backé and Klein 2004). Although similar functional principles are used, there are some specific, inherent advantages and disadvantages associated with the use of a fluid or a gas-like pressure medium.

2.1.2.2.1 Hydraulics

Hydraulics utilize liquids as pressure medium. Mostly synthetic or petroleum-based oils are used. They are often combined with other additives to guarantee not only the force transmission but also lubrication, heat dissipation and corrosion protection. In some special cases, e.g. in connection with food production, water may be used as pressure medium as well.



FIG. 2.4: Hydraulic cylinder on excavator. (Photo by SKas / CC BY-SA 4.0)

As fluids are considered incompressible, they offer the advantage of being able to transfer high forces. Due to the high energy density of hydraulic actuators, they can generate high forces and torques at small dimensions and masses. This results in other advantages such as fast starting and stopping speeds, easy change of motion direction and continuous velocity control. The energy density is approximately 10 times higher than that of electric motors. Therefore, hydraulics is used where high forces are required. This might for example be heavy equipment for construction or elevators (see FIG. 2.4). However, also some disadvantages are associated with the use of hydraulic oils as pressure medium. They have to be filtered and due to the high viscosity and resultant frictional losses in the piping or tubing, the transmission distance of hydraulic systems is low. In combination with possible leakage losses this reduces the efficiency in comparison to mechanical drives. Also, the acquisition costs of hydraulic components are high as they require a high precision. This is also relevant for control as for the control relevant properties such as viscosity, density and compressibility of hydraulic fluids vary with temperature and pressure. Further, as most hydraulic oils are harmful to the environment, special environmental regulations exist for their use (Watter 2015).

2.1.2.2.2 Pneumatics

Pneumatics uses air as pressure medium. Air consists of nitrogen (79 vol.-%), hydrogen (21 vol.-%) and less than one percent noble gasses. One major difference to the aforementioned hydraulic system is that the pressure medium in pneumatic systems is compressible. This means the density is not constant:

$$\rho = \frac{m}{V} \neq \text{const.} \quad (2)$$

$$P \cdot V = m \cdot R \cdot T \quad (3)$$

Through the compression, energy is stored within compressed air. From that arises danger at the sudden expansion of compressed air to the volume at ambient pressure. Therefore, the pressure of pneumatic systems is usually limited to 6 to 10 bar. The expansion also results in exhaust noises at leaks or pressure outlets. The compressibility of air also makes the system compliant to varying external load (Watter 2015).

On the other hand, the compressibility also makes it possible to store compressed air and allows the use of a centralized system. Due to its low viscosity, the compressed air can be transported over long distances with comparable small frictional losses. This is an advantage over hydraulic systems as well as mechanical ones (Backé and Klein 2004; Watter 2015). Also, except of the energy losses, no special care must be taken of leaking pipes (Watter 2015).

2.1.3 Unconventional actuators

A great variety of actuators is listed under the label unconventional actuators. This term summarizes all actuators not being of electromagnetic or fluidic nature. In the following a selection of actuators which are already applied in industry is introduced.

2.1.3.1 Shape memory materials

2.1.3.1.1 Shape memory alloys (SMAs)

Operation principle: The shape memory effect of certain metal alloys was first discovered in the 1950th. It is based on the reversible transformation from the martensite to the austenite phase at the according temperatures. A transformation cycle is displayed in FIG. 2.5. Four different temperatures are of special relevance to the process. T_{As} and T_{Af} mark the start and finishing of the transformation from the austenite to the martensite phase during heating, while T_{Ms} and T_{Mf} indicate the corresponding temperatures for the cooling down process. A hysteresis of 10 to 50 °C in temperature is inherent to the overall process. Depending on the alloy used, its composition and its microstructural constitution, the temperature can be set in the range of -200 °C to +200 °C. The change in crystal structure associated with the change between the martensite and the austenite phase can cause an intended shape change. The corresponding crystal structures are shown in FIG. 2.6. For the shape memory effect, it is distinguished between the one-way memory effect and the two-way memory effect. The first one

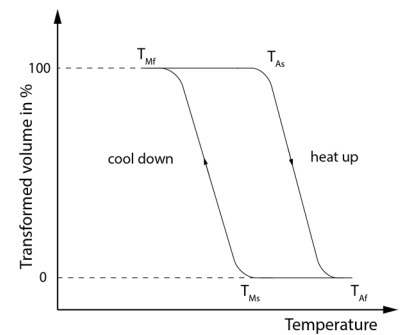


FIG. 2.5: Reversible transformation cycle of a SMA. Based on (Janocha 2004c).

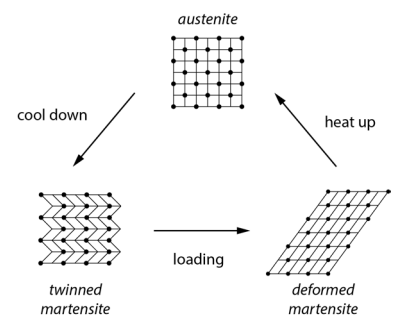


FIG. 2.6: Crystalline structure in the transformation cycle of a SMA.

describes the restoring of an apparent plastic deformation induced in the martensite state by heating the SMA above T_{Af} . Only the hot austenite shape is remembered. To induce a two-way memory effect the SMA is trained during a thermo-mechanical treatment to “remember” the austenite as well as martensite state. Upon heating and cooling it is switched between two distinct shapes (Janocha 2004c).

Technical implementation: Various materials show a shape memory effect. Best suited for most commercial application are SMAs based on nickel and titanium, also known as Nitinol®. Especially the strong memory effect, the low risk of overheating as well as the good long-term stability and corrosion resistance make NiTi-alloys interesting. Besides that, a high electrical resistivity makes them easier to activate electrically. SMAs are available in the form of taut wires, coil springs and torsion or bending elements, as well as custom formed elements (see FIG. 2.7). The heating needed to activate the SMA can happen by radiation, conduction or convection as well as direct inductive or resistive heating. The later one is mostly used as it allows a fast and homogenous response. The frequency of actuation depends directly on the time necessary for heating up and cooling down. Usually, heating can happen within milliseconds. Cooling down is the limiting factor, as it can only happen by circulation of the surrounding medium. As cooling down is faster and easier for smaller masses, SMAs are especially attractive for micro devices. A possibility to increase actuation frequencies is the use of antagonistic structures resetting the systems to its original state. Nowadays SMAs are used in series in a broad range of applications, from automobile and aerospace industry, over electronics and medical technology to precision engineering. Often SMAs are used in control, safety, or lock mechanisms. Also, devices for the prevention of overheating are common as well as miniature drives. After the successful implementation of SMAs in the field of micromechanical systems one of the expected developmental trends is the application in large-scale structures. Especially the temperature resistance over 100 °C and the embedding of woven, knitted or braided SMA fibres into fibre reinforced composites for actuation or sensory purposes are a major field of ongoing research (Janocha 2004c).



FIG. 2.7: Nitinol Memory Alloy paperclip in deformed state (left) and with restored shape due to heating (right). (Photos (left & right) by Petermaerki / CC BY-SA 3.0)

Advantages and disadvantages: A major advantage of SMAs is their high energy density. This means they can produce high forces at a low self-weight. Further, due to the formability of the material they can perform a great diversity of motions such as elongation, contraction, torsion and bending. The mechanism itself is simple. This reduces the mechanical complexity of the actuator system, and allows a clean, silent, and spark-free operation. The deformation is controllable stepwise by the temperature in intervals. However, a major drawback is the stability of the memory effect over time. It depends strongly on the quality of the alloy. Further the material is expensive, and the development of an actuator requires a high degree of expertise.

As the SMA needs heating to be actively controlled the energy efficiency is low. The heating and cooling process also restricts the bandwidth of operation (Janocha 2004c).

2.1.3.1.2 Shape memory polymers (SMPs)

Operation principle: Similar to SMAs the shape memory effect of SMPs arises from a transition within the molecular structure. On the molecular level a SMP possesses two distinct domains referred to as an elastic and a transition segment. Upon external stimulation the transition segment undergoes substantial stiffness variations. The activation stimulus in most cases is thermal, but transition can also be electric, magnetic, mechanical or light. In case of thermally triggered SMPs the transition temperature is of fundamental importance. During the programming of the SMP the polymer is heated above this temperature. In the resulting soft polymer state the transition domains become compliant and allow the easy deformation of the material into the desired state. During the deformation process the elastic domain follows the strain path. Cooling down the material under the applied stress causes the transition domain to harden again. Thereby it maintains the deformed shape and prevents the elastic recovery of the elastic domain. If the system is heated above the transition temperature once again, the consequent softening of the transition domain allows the release of the elastic energy stored within the deformed state and the shape changes to the initial state again (Kuder et al. 2013).

Advantages and disadvantages: Compared to SMAs the advantages of SMPs are based on their lower density as well as larger reversible strains possible. Their thermo-mechanical characteristics are easier to adapt to particular needs and alternative stimulants are possible. Further materials, manufacturing and processing costs are lower for SMPs. At the same time, they offer a higher fabrication flexibility. On the other hand, realizable actuation forces are much lower and the limited fatigue life typically allows only around 10^4 cycles to failure. Further the transformations taking place around the transition temperature are accompanied by substantially altered mechanical properties of the polymer (Kuder et al. 2013).

2.1.3.2 Piezoelectric actuators

Operation principle: The piezoelectric effect describes the feature of an electric polarization due to an elastic shift of ions in the crystal lattice by an external mechanical force. This effect is shown in FIG. 2.8. The phenomenon was first discovered in 1880 and is the basis for piezoelectric sensors. The reverse effect, the so-called reciprocal or inverse piezoelectric effect, describes a change in dimension of a crystal due to an applied electric voltage and the consequent changes in the crystal lattice (see FIG. 2.9). It is utilized within actuators (Janocha 2004c).

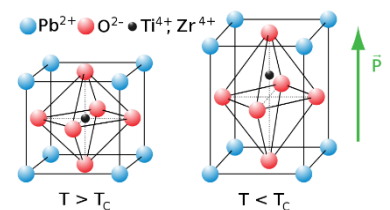


FIG. 2.8: Electric polarization due to an elastic shift in crystal lattice of perovskite-type lead zirconate titanate (PZT) unit cell. Left: unit cell in the symmetric cubic state. Right: Tetragonally distorted unit cell. (Image by Pinin / CC0)

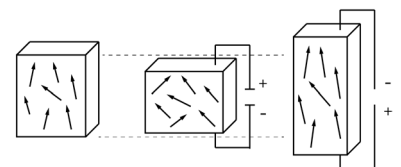


FIG. 2.9: Direct piezoelectric effect. Mechanical stress generates an electric charge due to the shifting of positive or negative charge centers. The inverse piezoelectric effect causes a dimensional change due to an applied voltage.

Technical implementation: Piezoelectric properties can be found in different materials. They can be grouped into natural crystals such as quartz or tourmaline, and polymers, like polyvinyl fluoride, or polycrystalline ceramics. In actuators mainly sintered ceramics are used. The piezoelectric effect arises from a polarization process, where a strong electrical DC field is applied to arrange the regions of crystallites with a uniform dipole orientation. This polarization remains to a large extent also when the DC field is switched off. Especially PZT (lead-zirconium-titanite) is used. Since the 1980s so-called multilayer ceramics gained importance. These achieve the same elongations as ordinary piezoelectric ceramics but at significantly lower driving voltages. Piezoelectric ceramic elements are available on the market as plates or discs in length of 0.3 to several millimeters. Most of them utilize the piezoelectric effect to create a longitudinal elongation. Also bending elements, where a piece of piezoelectric ceramic is attached to a piece of metal (unimorph) or two opposing ceramic strips (bimorph), are used. In addition, due to the relatively small strokes achieved by piezoelectric material, several mechanisms to amplify the motion exist (Janocha 2004c).

Advantages and disadvantages: Piezoelectric actuators can exert high forces and possess a high stiffness. Furthermore, they exhibit a high electromechanical efficiency and require very short response times in the range of milliseconds. Another interesting aspect is that they show a negligibly low power consumption in a static operation mode. The characteristic values of the piezoelectric ceramic change with temperature and age and the piezoelectric effect can be lost by high temperatures, large electrical fields or mechanical shock. Another fact limiting the application of piezoelectric actuators is the fact that the strokes created by these types of actuators are very small (Janocha 2004c).

2.1.3.3 Magnetostrictive actuators

Operation principle: When a magnetic field is applied to a magnetostrictive material it changes its shape, as magnetic domains reorient. The volume, however, remains constant. This phenomenon is called the Joule effect and is the most important part of magnetostriction (Janocha 2004c).

Technical implementation: Magnetostrictive effects can be induced in alloys containing iron, nickel or cobalt. Here it can produce actuation strains in the range of 10-30 $\mu\text{m}/\text{m}$. Higher strains can be generated by so-called giant magnetostrictive materials. They are based on rare-earth iron alloys and create strains of up to 2000 $\mu\text{m}/\text{m}$. Terfenol-D[®], from terbium and iron (ferrum), is the most common magnetostrictor. It is known for its high energy density which is many times higher than that of piezoelectric materials. Giant magnetostrictive materials are usually produced as rods, with a length of up to 300 mm and a

diameter of 70 μm , or plate elements. By sputtering, also thin magnetostrictive layers can be produced which can achieve actuation strains in the range of 500-1000 $\mu\text{m}/\text{m}$ (Janocha 2004c).

Advantages and disadvantages: Many of the performance characteristics are similar to the ones of piezoelectric actuators. Accordingly, they show the same advantages as the high actuation forces and modulus as well as high electromechanical efficiency and very short response times. The power density is high and exceeds that of piezoelectric actuators by a factor of 10. Further, no stacking is required, and magnetostrictive actuators are applicable over a wide range of temperatures and are not destroyed if the Curie temperature is exceeded. The disadvantages are also similar to the ones of piezoelectric actuators. The characteristic values depend on the temperature and the material itself is brittle and difficult to machine. Up to now magnetostrictive actuators are expensive and only few suppliers are on the market. For their use a sophisticated magnetic circuit is necessary (Janocha 2004c).

2.1.4 Comparison of different actuators

The previous chapters showed a selection of the great variety of actuators. To describe and compare them, performance characteristics can be used. Some well-defined performance characteristics are listed in Table 2. They are normalized attributes which are roughly characteristic to a whole class of actuators. This brings to light the fundamental differences between the actuator classes and therefore allows a general comparison.

To be able to better compare the performance characteristics of the different actuators, Huber et al. displayed them in actuator property charts (Huber et al. 1997). Similar to the material property charts introduced by Ashby for the systematic selection of materials in engineering design, the relationships between the different classes of actuators become evident by the graphical plotting (Ashby 2013). This also makes a quantitative comparison possible.

Table 2: Performance characteristics of actuators. Adapted from (Huber et al. 1997)

performance characteristic	description	
σ	actuation stress	Applied force per unit cross-sectional area
ϵ	actuation strain	Nominal strain produced (length $l =$ initial length $L \cdot (1 + \epsilon)$)
ρ	actuator density	Ratio of actuator mass and initial volume
E	actuator modulus	Ratio of small increment σ and corresponding increment in ϵ
η	efficiency	Ratio of mechanical work output and energy input
ϵ_{min}	Strain resolution	Smallest increment of ϵ

In FIG. 2.10 the actuation stress versus the actuation strain is plotted comparing actuators of equal size. The graph also displays that even within one class of actuators, parameters as deflection, force, or operation frequency, can span over wide value ranges. Actuators able to provide high displacements per unit length, are positioned on the right side of the plot. Actuators that are placed towards the top of the plot generate high forces relative to their cross-section. As the information is presented on logarithmic scales points on a straight line with a slope of -1 represent constant volumetric stroke work and therefore indicate potential competing systems. The lines with the positive slope are those with a similar actuator modulus.

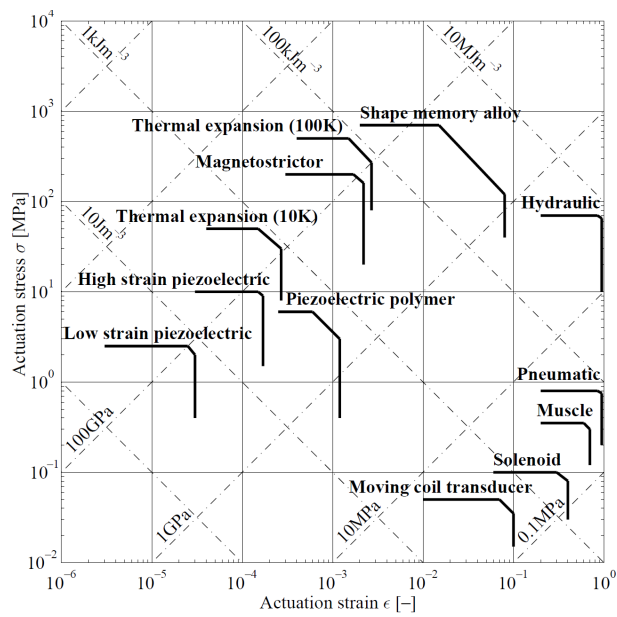


FIG. 2.10: Comparison of actuation stress σ and actuation strain ϵ of different actuators. The lines mark the upper performance limits. (Huber et al. 1997)

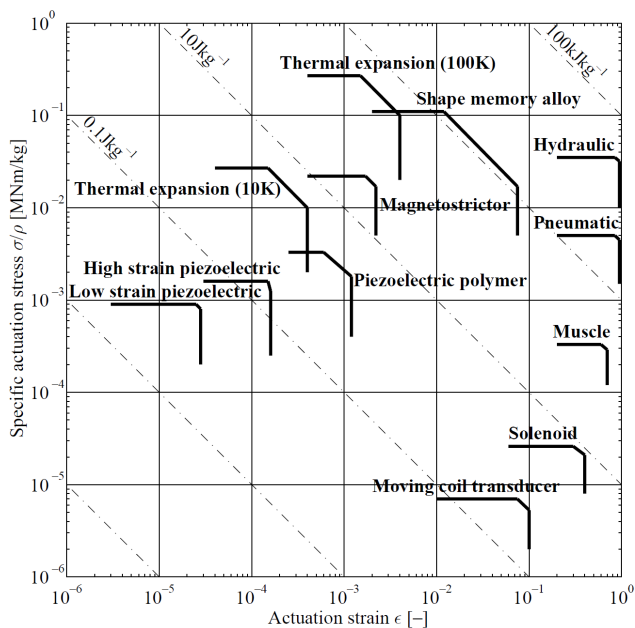


FIG. 2.11: Comparison of the specific actuation stress σ/ρ and actuation strain ϵ of various actuators. The lines mark the upper performance limits. (Huber et al. 1997)

In FIG. 2.11 actuators are compared with respect to their mass. The specific properties become relevant for application scenarios in which weight is a critical factor. For this comparison only the masses of the actuators themselves without the necessary peripheral devices, like power supplies such as a compressor, were used.

Also other important characteristics that are not displayed in the graph but need to be considered when choosing an actuator are the resolution (step size) and, especially when it comes to cyclic loading, the frequency, the power and the efficiency (Huber et al. 1997).

2.1.5 Conclusions

For the actuation of large-scale compliant kinetic systems, high strokes at high forces are necessary. To follow lightweight construction principle also a low mass is desired. As can be seen from FIG. 2.11 this set of specifics is fulfilled very well by fluidic actuators such as hydraulics or pneumatics. Also, SMAs and thermal expansion seem valid candidates.

The integration of unconventional actuators as SMAs, piezoelectric devices or utilizing thermal expansion for actuation are fields of ongoing research. However, piezoelectric actuation, although being very precise, can produce only small strains. The active material with integrated piezoelectric fibres is capable to control of structural vibration, aeroelastic response and acoustic transmission (Bent et al. 1995; Brunner et al. 2005; Hagood and Bent 1993). Thus, it may be used for vibration suppression, and noise control (Nelson 2002). The integration of SMAs into a fibre composite is capable of achieving large structural changes also in large scales. However, the activation temperature of the used material is with 30-60 °C too low for a façade application conditions (Briggs and Castaneda 2002; Hübler et al. 2013). Further the concepts include no active means for cooling of the actuators. Therefore, a control of the shape recovery is not possible and depends on the cooling rate and environmental conditions (Hübler et al. 2013). Similar holds true for other thermally induced actuation concepts. This is a major drawback as the controllability and short response times are of major importance for the user satisfaction. The cooling of large-scale thermally actuated systems might cause an issue in that regard. Moreover, the activation temperature of these system needs to be significantly higher than the temperature expected on a façade under full solar radiation. These would be temperatures well above 80 °C and cause significant thermal stress on the polymeric matrix material of the FRP. In addition to hold a position, the temperature in the composite would need to be maintained. It needs to be ensured that this does not reduce the lifetime of thy systems significantly. Further the design of SMAs systems is challenging and requires a lot of experience also for small variations in the application. Also, preliminary test of

utilizing thermal expansion within a GFRP to cause a bending showed only poor success.

Fluidic actuation offers the advantage that a central pressure source, that is easy to access and therefore maintain, can supply numerous individual actuators. With its long transmission range, this holds true especially for pneumatics. For a potential application in façade shading further the uncritical consequences of small leakages is a point for pneumatics over hydraulics. By a pneumatic system great forces, strokes and actuation frequencies can be realized in an inexpensive way. Further, the above-mentioned description and comparison was made considering conventional fluidic actuators as pistons or motors. In recent years new approaches towards utilizing pressurized artificial muscles (PAMs) or textile pneumatic actuators (see FIG. 2.12) have been investigated (Binz 2016; Finckh et al. 2019; Takosoglu 2020; Zhang and Philen 2012). These systems show a significantly reduced weight. Moreover, the design freedom is increased and at the same time the costs are reduced. Especially textile actuators are interesting for the integration of the actuation into a material set-up, which is a goal of this investigation. A comparison between these, fluidic muscles and a conventional pneumatic cylinder is given in Table 3.

For these reasons, this investigation focuses on pneumatic actuation, which introduces no heating into the element, reacts instantly and is inexpensive while generating high forces and displacements.

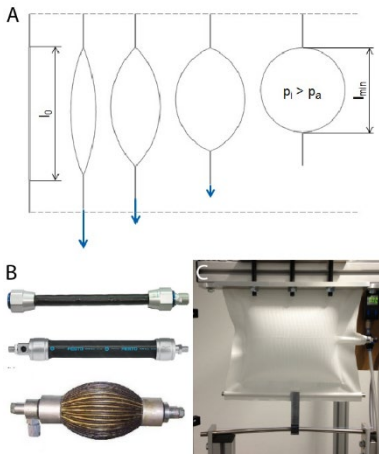


FIG. 2.12: (A) Functional principle of pressurized artificial muscles (PAMs) and textile actuators. An increase in internal pressure p_i maximizes the volume and thus reduces the length l of the actuator ©DITF. (B) shows some examples for PAMs (Takosoglu 2020) / (CC BY 4.0) and (C) an textile pneumatic actuator ©DITF.

Table 3: Comparison of properties of a conventional pneumatic cylinder with those of a fluidic muscle and textile pneumatic actuator.

	Conventional pneumatic cylinder	Fluidic muscle	Textile pneumatic actuator
Specifications	Festo (AND-80-70)	Festo (DMSP-40-28N)	DITF (200*200 mm)
Max. stroke	700 mm	Approx. 700 mm	Approx. 700 mm
Self-weight	1853 g (high weight)	748 g (medium weight)	54 g (low weight)
Tensile force produced at 1 bar	~500 N	~1 kN	~ 1,8 kN
Tensile force produced at 0.1 bar	self-retention	~ 100 N	~500 N
Fabrication	complex and expensive	complex	simple and inexpensive
Other properties	not integrable; large dimensions; only linear motion	not integrable; only linear motion	integrable; various deformations possible; easily customizable

2.2 ACTUATION IN BIOLOGY

2.2.1 Definition

The definition of an actuator in the previous chapter also holds true for biological systems. Hannaford and Winters defined actuation as the process of converting different types of energy into a mechanical form. Any device conducting this conversation is named an actuator. The second essential property is the controllability by an input modulating the process (Hannaford and Winters 1990). By this definition, an actuator is related to a motion. Therefore, the search for actuation principles is tied to motions occurring in biological systems. The function and generation of an intended movement differ for flora and fauna. Plants are sessile and bound to one place, nevertheless movement occurs as a response to environmental influences such as solar radiation or is utilized for fertilization. In the animal kingdom, movement is often linked to motility or locomotion, allowing the organism to change its location. Plants and animals have developed numerous highly specialized mechanisms to foster these movements, making them more rapid, energy efficient or robust. The following two sub-chapters are meant to give a general overview of the basic principles of movement and actuation mechanisms found in plants and animals.

2.2.2 Actuation in plant movements

2.2.2.1 Overview plant movements

Plants are usually considered sessile. Although or especially because they are commonly bound to one location, they utilize motion to adapt to changing environmental conditions. Motions can be reversible and repeatable, or related to growth and therefore be irreversible. Nultsch refers to a motion as plant movements if there is an observable change in location or position of a whole organism or parts of it happening in a relatively small period of time. He differs between autonomous (endogenous) and induced movements as a reaction to a stimulus (Nultsch 2001). Others define plant movements more narrow as the reaction of a plant or parts of its body to a perceived stimulus with a specific autonomous motion (Li and Wang 2016). Plants developed a great variety of sophisticated motion principles that are tightly adjusted to their environment. In speed plant movements range from rapid motions, such as the closing of traps (e.g. the Venus flytrap (*Dionaea muscipula*)) or the explosive dispersal of seeds with a speed of approx. 10 m/s, over the leaf folding of the touch sensitive plant *Mimosa pudica* (FIG. 2.13), the reorientation of leaves or flowers with the sun, to growth related motions with a speed of approx. 1 mm/h. The speed of plant movements ranges over seven orders of



FIG. 2.13: *Mimosa pudica* folding its leaves after mechanical disturbance. (Photo by Science and Plants for Schools / CC BY-NC-SA 2.0)



FIG. 2.14: Example for Phototropism. Lentil sprouts growing towards the light. (Photo by Russell Neches / CC BY 2.0)

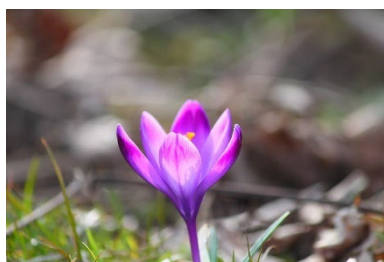


FIG. 2.15: Thermally triggered opening of Saffron (*Crocus sativus*) as an example for a nastic plant movement. (Photo retrieved from pxfuel)

magnitude. A good overview on different plant movements and actuation types is given by Li & Wang as well as by Schleicher (Li and Wang 2016; Schleicher 2015). The following partially summarizes their reviews.

Classification of plant movements: Depending on the local range and reversibility of the motion, plant movements can be subdivided into taxes, tropisms and nastic movements. A taxis is defined as a plant not being bound to one location but being able to perform free local movements. This motility allows the organism to orient itself towards or away from the perceived stimulus. Examples for non-sessile plant organisms, capable of changing location, are algae colonies possessing flagella that enable the locomotion. Also, the propagation of seeds, fruits or spores by wind, water, or animals, is considered as taxes. Tropism is termed the ability of a sessile plant to move parts of its body in response to a stimulus by irreversible growth movements. The stimuli can be manifold. The orientation of plant organs towards the sun or light is named Heliotropism or Phototropism (see FIG. 2.14). The response of a climbing plant to friction when growing up a wall or winding around a supporting structure is referred to as Thigmotropism. The probably most interesting class of plant movements on the search for novel actuation principles are nastic movements. These are reversible and repeatable motions in response to a stimulus. In contrast to tropisms, they are non-directional but pre-determined by the plant's anatomy. Usually, nastic movements are triggered by changes in turgor pressure and can be attributed to highly specialized and smartly located motor cells. Their structural adjustments drive and control the motion. The motion can be triggered by endogenous signals, originating from within the organism, or exogenous signals from the surrounding environment. The diurnal unfolding and folding of leaves and petals are famous examples of nastic movements (Nyctinasty). The response to light as a trigger for movement is called Photonasty while the opposite is called Skotonasty. Nastic movements can also be triggered by other stimuli such as temperature (Thermonasty). An example is shown in FIG. 2.15.

2.2.2.2 Actuation mechanisms

All plant movements are based on the interplay of water and the cell wall material to create motion (Forterre 2013). This can be in the form of changes in the inner cell pressure, or due to hygroscopic shrinking and swelling. Further, Li & Wang determined physiological features that are crucial for specific motion mechanism (Li and Wang 2016).

Hygroscopic shrinking and swelling: Cell walls are composed of hydrophilic material. Upon exposure to dry atmosphere, it will shrink as water evaporates. This effect is reversible. So, as soon as the moisture of the ambient environment increases again, the

absorption of water leads to swelling and thus increase in volume. This humidity-driven actuation mechanism can cause shape changes in a purely passive way, without the consumption of biochemical energy. Hygroscopic shrinking and swelling can be of surprising magnitude and is responsible for a series of plant motions in living, as well as dead sclerenchyma tissues. A prominent example is the seed capsule opening of the ice plant *D. nakurense* (see FIG. 2.16). It is initiated by a hygroscopic swelling process (Harrington et al. 2011). The cells in the keel tissue possess an elongated hexagonal shape. Upon swelling this leads to a unidirectional elongation of the tissue along only one axis. Another interesting feature enabled by hygroscopic swelling are the opening of pine cones or chiral seed pods, as well as the self-burring of wild wheat awn. Here locally differentiated fibre orientations in the cell wall are associated with locally differentiated swelling behaviors. In combination these lead to bending and twisting motions of entire plant parts (Li and Wang 2016).

Turgor pressure: Plants are cellular structures. The internal cell pressure created by osmosis is called turgor. This phenomenon is vital for plant motion, growth and also the stiffness of thin-walled plant tissue (see FIG. 2.17). Variations in turgor are known to be the hydraulic motor for most plant movements since the 19th and early 20th century (Forterre 2013). The internal hydrostatic cell pressure in living plant cells is generated by an osmotic gradient between the cytoplasm and the surrounding environment (Li and Wang 2016). The gradients in water potential results in an exchange of water between the cell and its environment. The water potential Ψ stands for the chemical potential of water per unit volume. Water will flow until an equilibrium is reached and the water potential of the cell cytoplasm is the same as outside the cell. The water potential of the cell vacuole and the turgor pressure P can be related to each other by $\Psi = P - \pi$, with $\pi = cRT$ (where c is the molar concentration of the solute and RT can be approximated by 2436 J/mol) (Forterre 2013). The semi-permeable cell membrane allows the diffusion of water in both directions and at the same time controls the transport of ions and molecules by specialized pumps. So-called plant motor cells can therefore actively change their internal water potential and vary their turgor. For fully hydrated cells, turgor pressures of 0.4 to 0.8 MPa are common. But the turgor varies significantly between different cell types and can reach values of up to 5 MPa in the guard cells of stomata (Forterre 2013; Li and Wang 2016). The turgor also plays a major role in the growth process. Growth is usually referred to cell proliferation, meaning an increase in the number of cells by cell division. This is an irreversible process that leads to the formation of additional material. Growth can however also refer to cell expansion. This is an enlargement in cell volume and potentially reversible (Schleicher 2015). This makes a clear distinction between plant movements and growth difficult. One

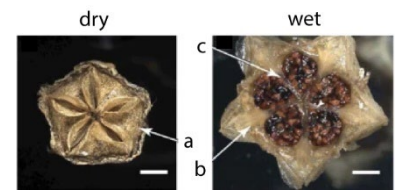


FIG. 2.16: Ice plant (*D. nakurense*) seed capsule in dry, closed condition (left) and hydrated, open state (right). When sufficiently hydrated the capsules open and thus disperse seeds when the conditions are the most favorable for growth. a: Protective valve; b: Hygroscopic keel; c: Septum. (Harrington et al. 2011)

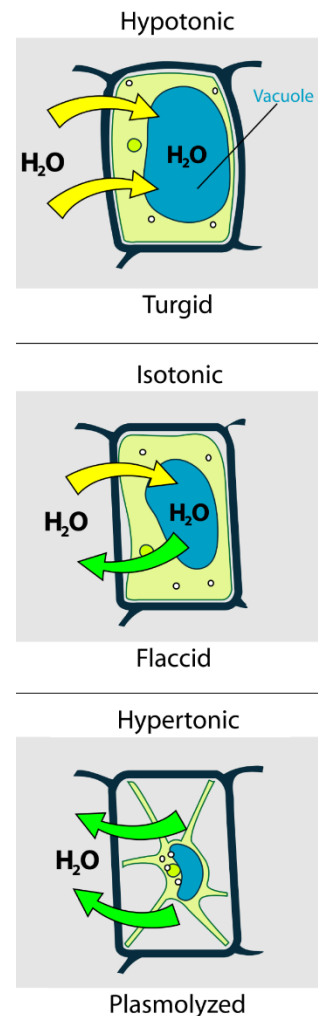


FIG. 2.17: Different states of plant cell turgor pressure. (Based on an image by LadyofHats / CC0)

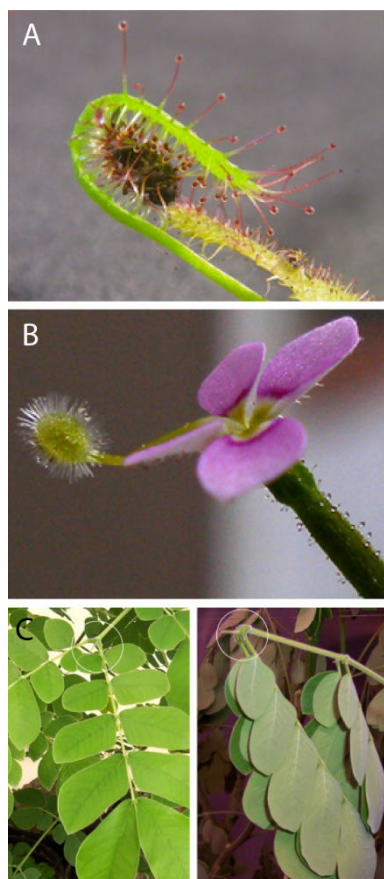


FIG. 2.18: Examples for turgor-based movements in plants. (A) *Drosera capensis* tentacles catching prey. (B) *Stylidium debile* flower. The protruded column is used to attack insects within milliseconds. (C) Folding of *Samanea* leaf. Same leaf at noon (left) and evening (right). Photos: (A&B) (Sinibaldi et al. 2014), (C) (Moran 2007).

possible way of classification is the mechanical response of the cell wall to turgor induced stresses. Below a critical turgor, the cell wall stretches elastically but above the yield pressure it behaves viscoelastic, starts to flow and deforms plastically. This process takes place in cell division. Mature cells that stopped growing lose the irreversible extensibility of their cell wall and small changes in turgor result in reversible, small changes in cell volume (Forterre 2013).

Water-driven motions in plants are a result of the tripartite interaction of the gradients in water potential (I) that induce water flow and consequently results in the turgor pressure (II) that in turn acts in the cell wall and causes its deformation (III) (Forterre 2013). The small, microscopic shape changes due to osmosis in individual cells can accumulate to macroscopic deformation on the tissue level and move entire parts of plants (Li and Wang 2016). The turgor driven structural adjustments on the cellular level are the primary actuation mechanism for many reversible plant movements. Well-known examples are the opening and closing of stomata or the circadian, light-induced movements of leaves and flowers (Forterre 2013; Li and Wang 2016). Some examples are also shown in FIG. 2.18. Interestingly, not only the turgor pressure but also the cohesion of water can cause plant movement. This is the case in the fern sporangium *Polypodium glycyrrhiza* (Forterre 2013; Schleicher 2015).

Physiological features: Besides the osmosis-based turgor pressure or hygroscopic swelling effect, there are physiological features responsible for directing the actuation to a targeted motion or amplifying the actuation motion. A summary is given in FIG. 2.19). One physiological feature is the closed-walled *cellular structure* of plants. This not only provides better specific stiffness and strength but also entails the possibility to achieve complex deformations by differentiated pressurization. Bending for example is created by the uneven extension of the abaxial (lower) adaxial (upper) side. A resulting downwards bending of a petal or leaf is called epinastic movement, while for an upwards bending one speaks of hyponastic movement. The bending of the pulvinus of the touch sensitive plant (*Mimosa pudica*), the opening of flowers or sleeping movements of leaves are examples using this principle. In addition, anisotropic shapes of individual cells can set the directions of deformation (Li and Wang 2016; Schleicher 2015). As mentioned above the *cell walls* play a major part. They are a fibre-reinforced composite made from stiff cellulose fibres cross-linked by other polysaccharides like hemicellulose or pectin. The fibre alignment can vary and cause anisotropic material properties that transform the changes in pressure or hygroscopic swelling into sophisticated, directed motions. This effect can be observed on the individual cell level as e.g. in the opening and closing of guard cells, where the intrinsic fibre orientation within the cell wall supports the bending motion. However, the effect also exists on the tissue level, where the differential cell wall fibre orientation of many

cells leads to an anisotropic motion of the tissue. Examples are the hygroscopic bending or twisting of pine cones, awns and seed as mentioned above (Li and Wang 2016).

The speed of osmotic driven plant motions is limited by the physical ability of water to diffuse through the cell membrane or the hydrophilic cell wall. To overcome this limitation, plants make use of *elastic instabilities*, such as snap-through. These mechanisms can significantly amplify the velocity and magnitude of a motion. Elastic instabilities are usually considered failure modes. They are characterized by sudden elastic deformation of a structural element as a mean to reduce high tensile or compressive stresses by transitioning into a new less strained geometric state. The probably most studied elastic instability is the bi-stable trap closing of the Venus fly-trap (*Dionaea muscipula*). The snap-through mechanism features some attractive characteristics as it enables the reversible rapid closing of the trap by a comparatively small osmosis intruded trigger. Further the bi-stability allows the remaining at either state without requiring continuous pressure supply. Other examples are rapid fracture induced explosions speeding pollen and seeds over wide distances (Li and Wang 2016).

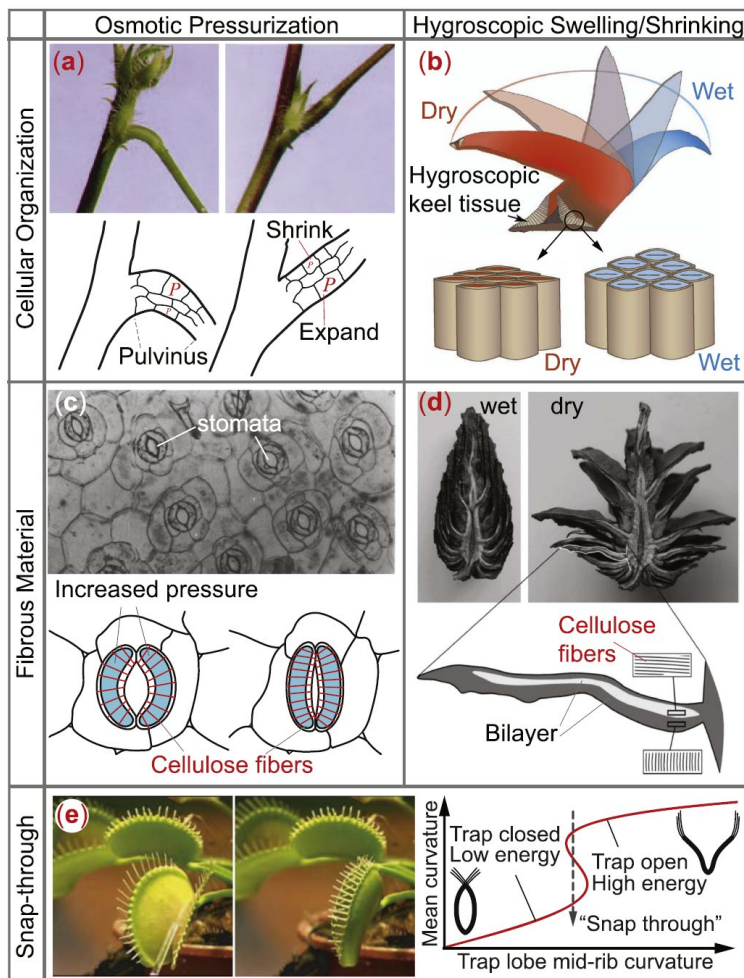


FIG. 2.19: Overview of actuation mechanisms and physiological features promoting plant movement with examples. (a) Bending of *Mimosa pudica* pulvinus. (b) Opening of the ice plant seed capsule. (c) Bending of stomata guard cells. (d) Opening of a pine cone. (e) Closing of *Dionaea muscipula* leaf trap. (Li and Wang 2016)

2.2.3 Actuation in animal movement

Despite the various examples of plant movements in the previous chapter, movement and motility is widely considered a typical property of the animal kingdom. Even the few sessile animals move at least parts of their body to catch prey and feed. Most animals, however, are capable of locomotion. That describes the ability to move from one location to another. Locomotion is considered essential for animal life as it is necessary for finding food, escaping dangers or finding mates. Based on the functional principle, it can be distinguished between three types of animal movement. These are (1) the beating of cilia and flagella driven by the interaction of kinesins and dyneins, (2) the cell crawling of amoeba and (3) the contraction of muscles. Hereby (2) and (3) are based on actin and myosin interaction, while (1) is based on kinesin and dynein interaction (Betz et al. 2016; Campbell et al. 2016). In the following the function of the motion generating interaction between the different protein chains will be described in more detail.

Kinesin and dynein interaction: Cilia and flagella are protuberances of some eukaryotic cells. They are composed of an arrangement of microtubules that create a beating movement. Unicellular eukaryotes or small metazoans use this beating for locomotion in water. The cilia on the surface of epithelial cells can collectively promote liquids over the tissue surface. Cilia usually have a diameter of $0.25\ \mu\text{m}$ and a length of $2\text{--}20\ \mu\text{m}$. Possessing a similar diameter but a length of $100\text{--}200\ \mu\text{m}$, Flagella are significantly longer. Besides their length cilia and flagella differ in their propulsion motion (see FIG. 2.20). While flagella carry out a conical rotary motion that creates an impulse in the direction of the longitudinal axis, the motion of cilia resembles the stroke of a paddle. They perform a fast (40–60 beats per second) forward- and backward movement that propels the cell forward in a direction perpendicular to the cilia axis. To reduce the flow resistance the cilium bends during the backwards stroke and stays close to the cell wall. Usually, a dense population of cilia is found on a cell surface, while flagella occur individually or in small groups. Still, in both, cilia and flagella, the motion is created in the same way. A set of doubled microtubules is surrounded by a group of nine other doubled microtubules, so they form a tube in the so called “9+2”-arrangement (see FIG. 2.21). The motion is generated by large motor proteins, so-called dyneins, placed on the microtubules. They possess two feet that are connected to the microtubules by proteins. Using ATP as a source of energy, the dynein feed “walk” along the microtubules. This ATP-powered “walking” mechanisms is like the actin and myosin interaction which will be explained in more detail below. As only at one side of the interconnected microtubules-complex is active at the same time, the organelle bends to one side (Campbell et al. 2016).

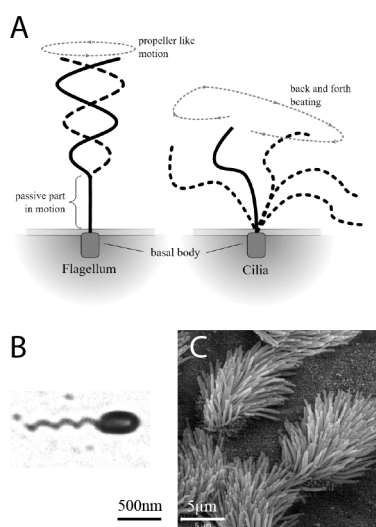


FIG. 2.20: Comparison of flagella and cilia. Top (A): Motion principle. Bottom: example organisms. (B) shows a flagellated bacterium and (C) image of lung trachea epithelium covered with ciliated and non-ciliated cells. (Image A by Kohidai, L., Urutseg / CC BY 3.0; image B by Jonathan Ferooz, Jean-Jacques Letesson / CC BY-SA 2.0; image C by CNX OpenStax / CC BY 4.0)

Actin and myosin interaction: Cell crawling and the interaction of muscles both work through the interaction of actin and myosin. Amoeboid cell crawling occurs in unicellular Amoeba and some human white blood cells. It enables the cell to crawl over a surface by the forming foot-like dynamic surface extensions of the gel-like ectoplasm called pseudopodia. By the alternating extension and retraction of these pseudopodia the cell moves forward (see FIG. 2.22) (Betz et al. 2016; Campbell et al. 2016). The functional principle of the actin-myosin interaction is the same as for the muscle contraction described below.

Muscles are based on approx. 7 nm thick microfilaments built from the globular protein actin. Further, the motor protein myosin and some regulatory components are involved in the functional structure of muscle. A muscle transforms chemical energy into mechanical energy in the form of a muscle contraction. This contraction is caused by microfilament movement. The skeletal muscle is made from muscle fibres which themselves consists of myofibrils. These are formed by so-called thin filaments and thick filaments. Thin filaments consist of two strands actin and two strands tropomyosin, wound around each other. Thick filaments are large myosin molecules. Thin and thick filaments are arranged in functional units called sarcomere. A sarcomere represents a basic contractile unit. The inner structure of a sarcomere is shown in FIG. 2.23. The actin-containing thin filaments are connected to the so-called Z discs. The free ends of the thin filaments are directed to the center of the sarcomere. The thick myosin filaments on the other hand start at the center of the sarcomere and are directed towards the Z-discs. However, in the relaxed state they do not reach them. In this "starting" position thin and thick filaments overlap each other only partially. According to the sliding filament theory the contraction of a muscle is caused by the gliding of the two filaments along each other so that their overlap region increases, and the sarcomere length shortens.

The sliding or gliding motion along each other is enabled by the motion of the myosin heads. The working principle is shown in FIG. 2.24. Every myosin molecule possesses a head that extends from the long thin tail. Around 300 of these heads can be found on one thick filament. The myosin heads can bind ATP and hydrolyze it to ADP and an inorganic phosphate. This hydrolysis releases energy and moves the myosin head into an energetic higher, cocked configuration. Further it enables the myosin to form a cross bridge to the actin filament. Once the myosin binds to the actin, the inorganic phosphate is released. The myosin undergoes a conformational change to the lower energy state. Thereby it performs a power strike that pulls the thin filament inwards, towards the center of the sarcomere. Afterwards, the myosin releases the ADP. As soon as a new ATP binds to the myosin, the cross bridge to the actin is loosened and a new cycle begins. This process takes place about five times per second for each myosin head and lets the muscle

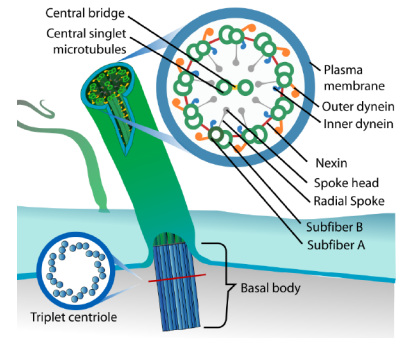


FIG. 2.21: Ultrastructure of a eukaryotic flagellum or cilium, showing the "9+2"-arrangement of the microtubule doublets and dyneins. They create a bending motion by "walking" along the microtubule using ATP as a source of energy. (Image by LadyofHats / CC0)

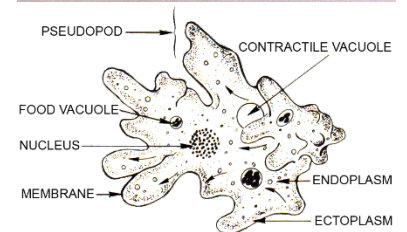
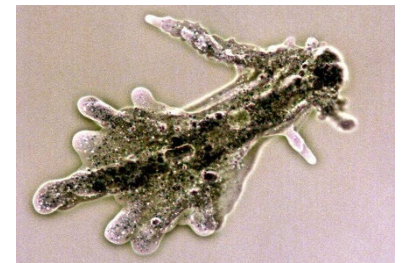


FIG. 2.22: Microscopic picture of Amoeba proteus with clearly visible pseudopodia (top) and line art drawing of a prototypical amoeba. (Upper image by Cymothoa exigua / CC BY-SA 3.0; lower image by Pearson Scott Foresman / CC0)

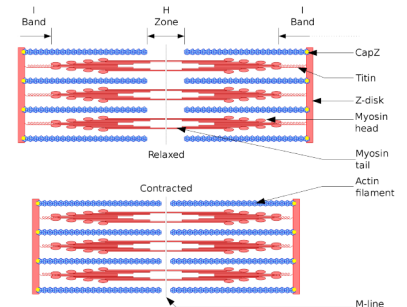


FIG. 2.23: Structure of a sarcomere. The graph illustrates the muscle contraction based on the sliding filament theory. (Richfield 2014)

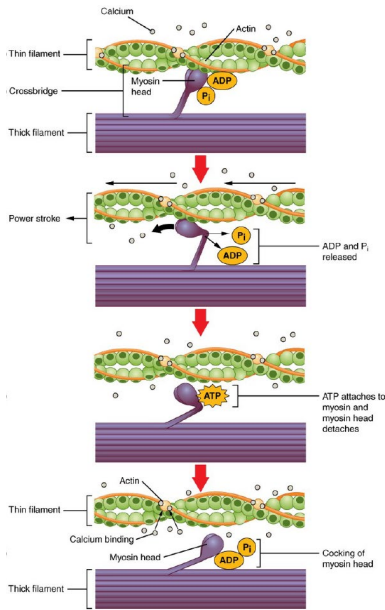


FIG. 2.24: Actin and myosin interaction cycle. It is the basis for muscle contraction. (Image by OpenStax / CC BY 4.0)

contract. The extension of a muscle takes place passively by the contraction of an antagonistic muscle. For a muscle to cause another than a purely shorting motion the interaction with a skeleton is needed (Campbell et al. 2016).

Skeletons: To make an animal, or parts of it, move, muscles require the interaction with a skeletal system. During evolution different kinds of skeletons have evolved.

An *exoskeleton* is a hard shell surrounding the body outside. It is typical for many molluscs and arthropods (see FIG. 2.25). The exoskeleton of arthropods is made from cuticle, a composite built by chitin fibrils embedded in a protein matrix. In regions the cuticle is required to be stiff to protect the animal, it is hardened by organic compounds. In regions that require flexibility, the proteins are less interlinked and thinner to allow movement as necessary e.g. in joint regions. The cuticle moreover possesses ledges and noses for the muscles to attached to. (Campbell et al. 2016)

An *endoskeleton* is the notation of stiff structural elements embedded in the animals' soft tissue. The skeleton itself can have many forms. Porifera (sponges) possess needle-like structures from inorganic material. The endoskeleton of Echinodermata consists of sclerites, hard magnesium carbonate and calcium carbonate crystal plates, located underneath the skin. Chordates (including vertebrates and thus also mammals) are specified by an endoskeleton made from cartilage, bones or a combination of the two (see FIG. 2.25) (Campbell et al. 2016).

The third and phylogenetically the oldest type of skeleton is a *hydrostatic skeleton*. Here a fluid-filled cavity is surrounded and held under pressure by a tension resisting fibre-reinforced skin or wall. Movements and shape changes are created by the muscles transmitting pressure to different parts of the body (Betz et al. 2016). As the contained fluid is technically incompressible, hydrostats possess a constant volume. Thus, an increase in pressure due to muscular contraction transmits equally throughout the entire cavity. This mechanically supports the body of the animal, creates motion, and may also vary its stiffness. Worms utilize the hydrostatic skeleton for locomotion in various ways. Nematoda (roundworms) possess a longitudinal, unstructured body cavity enclosed by longitudinal muscles. By the alternating contraction of the dorsal and ventral muscles an undulating movement is generated that creates propulsion. In Annelida, the coelom is segmented into many smaller compartments by septa and the coelomic fluid functions as the hydrostatic skeleton. The segmentation allows varying internal pressure of each segment individually and thus to isolate movement. This makes it possible to produce a peristaltic movement, where waves of shortening and extension travel along the body. Propulsive forces are generated by the elongation of some segments using the circular muscles, while



FIG. 2.25: Examples for an exoskeleton (external) and endoskeleton (internal). The upper image shows the cast-off skin (exoskeleton) of an Egyptian grasshopper (*Anacridium aegyptium*), the lower image the endoskeleton of a Swordfish (*Xiphias gladius*). (Upper photo by JackMonik / CC BY-SA 4.0; lower photo by Postdlf / CC BY-SA 3.0)

at the same time the friction with the substrate is increased by the thickening of other segments through the contraction of the longitudinal muscles (Betz et al. 2016; Campbell et al. 2016). Other interesting joint-free mechanisms are the effective protrusion of body parts as the mouthparts of insects or the proboscis of some coelomate worms (Betz et al. 2016). For example, freshwater polyps such as Hydra can elongate their cylindrical body by filling their digestive cavity with water and sealing it. Through the contraction of the body wall (perisome) and the resulting reduction in diameter, the digestive cavity will elongate as the containing water stays constant in volume (Campbell et al. 2016). Other animals that are characterized by a more or less cylindrical body (e.g. sea anemones or “worms”), elongate and shorten due to the fibre-orientation in their body wall. Inextensible fibres such as collagen fibres, stiffen and strengthen the body wall. They helically wrap around the body in a fibre-crossed arrangement. While fibre orientations of less than 55° cause a shortening and thickening of the cylinder upon pressurization, fibre angles above that value cause an elongation and reduction in diameter (see FIG. 2.26).

Muscular hydrostats do not possess a fluid filled cavity. In contrast to hydrostatic skeletons, they are built solely from muscle tissue. Muscle tissue, consisting mainly out of incompressible water, is constant in volume. Therefore, muscles can antagonize each other also without additional fluid cavities or rigid skeletons. Usually, they form cylinders with muscle fibres running in various directions which enables them to a wide range of motions and stiffness variation (Betz et al. 2016). Muscular hydrostats are often organs of animals with a specific function where the lack of a skeleton offer an advantage. Some examples are the arms and tentacles of squids, the human tongue and the trunk of an elephant (see FIG. 2.27). Muscular hydrostats allow a higher flexibility as skeleton from bone but offer only a limited support and strength. Therefore, they are also limited in size.

Pressure-based actuation - Some animals utilize pressurization to directly create a movement. The creation of the pressure itself is also based on muscular contractions explained above. Arachnids and some insects utilize their hemolymph to antagonize or support muscles. They use a hydraulic mechanism to straighten their legs during locomotion. Each leg possesses two pivot joints. A contraction of muscles attached to the exoskeleton retracts the subsequent segment. However, as muscles can only contract, these two leg joints cannot be extended by muscular action. The extension happens by an increase in hemolymph pressure inside the leg. The legs are connected to the central body of the spider (prosoma) and the open blood circulation system. Increasing hemolymph pressure inflates a bellow-like membrane situated below (ventral side) the pivot joints (see FIG. 2.28) (Landkammer et al. 2016). An increase in hemolymph pressure may also be involved in the wing

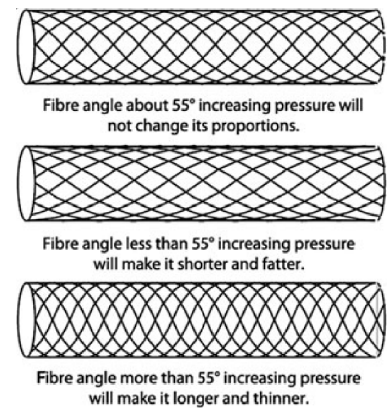


FIG. 2.26: Cylinders with different fibre angles and the consequent shape change upon pressurization. Adapted from (Betz et al. 2016).

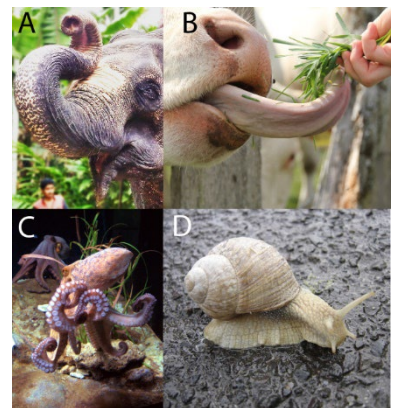


FIG. 2.27: Examples for muscular hydrostats: (A) Elephant trunk; (B) cow tongue; (C) octopus arms; (D) snail. (Image A by Deepanoffl / CC BY-SA 4.0; image B by PixelBandit / Pixabay License; image C by Anneli Salo / CC BY-SA 3.0; image D by Inkub0 / CC BY-SA 3.0)

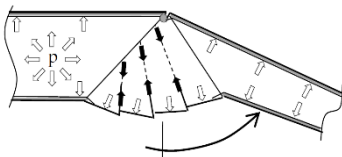


FIG. 2.28: Functional design of a spiders' tibia-metatarsus joint. An increase in hemolymph pressure inflates the bellow-like membrane and causes an extension of the leg. Adapted from (Landkammer et al. 2016).

unfolding of the hindwings in the beetle *Dorcus titanus platymelus* (Sun et al. 2014). The unfolding of the two main cross-folding joints corresponds to the two main peaks in the hydraulics pressure in the wing veins. This strongly suggests that the unfolding process is at least partially supported by an increase in hemolymph (see also chapter 3.2.1.2). As the two examples show, the actuation by pressure allows the creation of motion where the placement of muscles is difficult due to limited space as e.g. in joints. By the force transfer via a pressure medium a more compact design is possible.

2.2.4 Conclusions

Plants are characterized by their cellular structure. The actuation is pressure-driven and causes geometrical changes within the individual cells. Therefore, the typical distinction between structure and actuation that is present in many animal movements and technical structures is overcome. Especially turgor-driven plant motions can therefore be a valuable source of inspiration for integrated actuation approaches. Although also swelling and shrinking can be responsible for plant motion, the following investigation will focus on turgor-driven mechanisms because of the active character of the actuation. Also, motion amplification mechanisms as elastic instabilities are not within the focus of this investigation, as they promise less applicability in large-scale applications due to the high energies being released. The search for biological role models will be in the realm of pressure-driven shape change of cells that causes a specific reversible plant movement. The turgor-driven actuation mechanisms of plants differ greatly from the motion principles of animals that are tied to an endo- or exoskeleton. Muscles, as contractile units, create a desired movement by the interplay with each other and with a stiff and rigid supporting skeleton with joints. However, in the animal kingdom also fluid-based actuation principles for motions evolved and can provide a promising route for biomimetic design. On the fundamental level the pressure variations needed for these pressure-driven mechanisms are also created by a contractile unit such as a muscle. However, the pressure medium can transfer the induced energy to parts within the body where no muscles are (and potentially cannot be) placed. Therefore, the effects triggered by the pressure variation and the features used to enable or support its function shall be the focus in the following.

The fluid pressure-based actuation principles, present in the actuation of plants as well as in some animals, are more distributed, energy efficient, and completely integrative. This is of special relevance for this investigation. They are also very related to the fluidic actuators in engineering and therefore combine the same advantages of this actuator type as a high force, stroke, and power to density ratio, with those of the joint-free compliant mechanisms, namely a reduced number of parts

and the absence of moving joints. Pressure further exhibits a great influence on the stiffness of a system and may therefore be used to alter it. This is the second focus of this investigation and the subject of the following major chapter.

2.3 BIO-INSPIRED ACTUATION

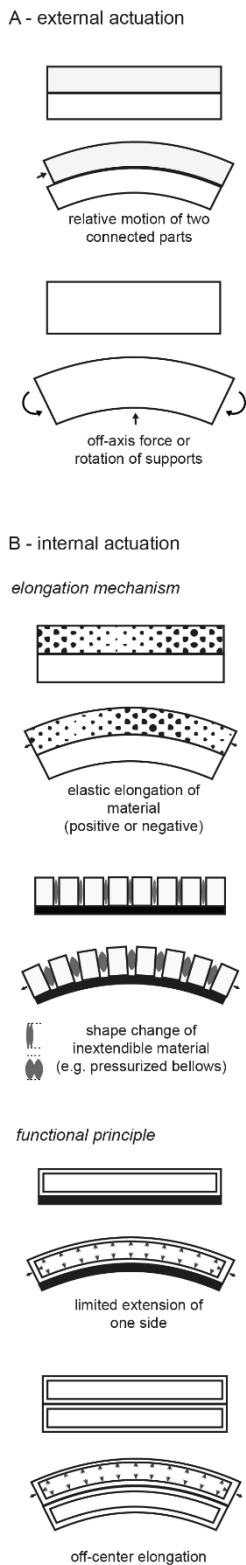


FIG. 2.29: Different designs and actuation principles of compliant bending actuators.

Due to the interesting properties of biological actuation mechanisms a series of bio-inspired actuation systems have been developed. They span widely different size scales and functional principles. The transferred mechanisms range from a passive actuation based on hygroscopic swelling over active, low-power osmosis-based actuators (Sinibaldi et al. 2014), to larger pressure-driven actuators such as artificial muscles (Daerden 1999), composites with embedded pressure elements (Philen et al. 2006a; Philen et al. 2007) or cellular structures (Gramüller et al. 2014; Pagitz et al. 2014). An overview on plant-inspired actuators based on different principles is given by Poppinga et al. (Poppinga et al. 2018) as well as by Li & Wang (Li and Wang 2016). Kim et al. (Kim et al. 2013) give an overview on animal-inspired soft robotics actuation.

Here a special focus lies on active actuation for the creation of a bending motion, as this is the underlying motion principle of the developed bio-inspired compliant mechanisms. The basic mechanism of bending is the extension of one side with respect to the other. This can be triggered in various ways. FIG. 2.29 summarizes the different actuation and construction principles of bio-inspired bending actuators found in literature. Through external actuation off-axis forces or the rotation of supports can cause the bending of an element. Next to that, external forces can engender the relative motion of two connected parts. A bending actuator can therefore be built from two separate parts, connected e.g. with a spring-groove connection. If the two parts are fixed together at one end, a motion of the two parts relative to each other can create the same effect as the elongation or shortening of one side. This principle is also found in biology and has been described for the ovipositors of parasitic wasps or the feeding apparatus of assassin bugs (Betz et al. 2016). Apart from external forces the motion (extension or shortening) can be triggered by other influences that cause effects intrinsic to the material. An example hereof are different thermal expansion coefficients of two materials (bilayers), or SMA's and piezoelectric materials that create an elongation or shortening in a defined area of the actuator. In this case, the bending is based solely on the elastic extension of the material. Hygroscopic swelling also falls into this category. Inspired by this are hygromorphic actuators bending due to sorption or desorption (Mazzolai et al. 2017). Also, swelling-driven honeycomb actuators inspired by the ice plant seed capsule (Guiducci et al. 2016) were developed. Another concept is to cause a differentiated elongation by pressure changes of fluid chambers filled e.g. with air or water. The functional principle of fluidic actuators can be based on the use of extensible materials, which elongate because of the fluid pressure, or they work with

inextensible material as pressurized pouches. Bellows built from a strong inextensible material undergo a shape change and elongation. As Yao et al. state, a surface curvature can be achieved either by the shortening of a pressure-pouch with low elasticity or the elongation of air cavities in a material with high elasticity (see FIG. 2.30) (Yao et al. 2013). For the second case, the specific bending motion can be created by different construction principles. The asymmetric limitation of the elongation by the addition of stiffer material creates a bending towards the respective direction. The placement of several local extension limiting layers or fibres in combination can create complex 3-dimensional bending motions. Several examples for pressure driven soft robotics based on this principle are given by Polygerinos et al. (Polygerinos et al. 2017). A review from Landkammer et al. shows how bio-inspired spider legs are realized though both concepts. Some concepts function with bellow-like structures, while for others the motion is based on material extension (Landkammer et al. 2016). Another possibility to create a bending motion is an asymmetric initiation of the elongating forces. When they are applied with an offset to the centroid of the cross-section, a bending motion is generated. By the arrangement of multiple off-center elongates in the cross-section of an actuator, complex motions can be generated. Next to pressurization, variable length tendons can be used to apply the force causing the bending motion. These mostly are implemented in the form of tension cables or SMA actuators (Rus and Tolley 2015). Kim et al. give a comprehensive overview on bio-inspired soft robotics based on this principle (Kim et al. 2013). Typical role models are the caterpillar or the arms of an octopus (see FIG. 2.31). The aim is to endow robots with the capabilities that enable them to adapt and interact with unpredictable environments. These robots, that resemble biological trunks or tentacles and can fulfill complex bending motions, are also referred to as continuous backbone robot manipulators (Walker 2013).

However, the number of bio-inspired large-scale active actuation systems suitable for architectural applications is small (Poppinga et al. 2018).

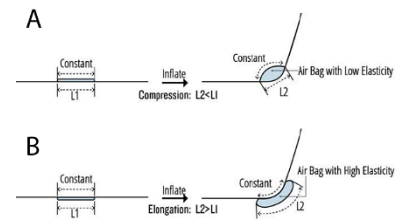


FIG. 2.30: Different means of creating bending by pressurization of a pouch with (A) a low elasticity or (B) of a pouch with high elasticity. Adapted from (Yao et al. 2013) (CC BY-NC-SA 4.0).

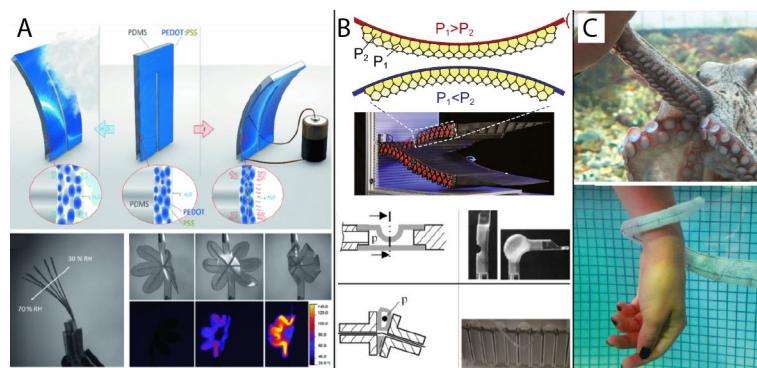


FIG. 2.31: (A) Hygromorphic actuator, based on the sorption of humidity. Adapted from (Mazzolai et al. 2017). (B) Upper: Plant inspired pressure actuated cellular structure. Adapted from (Li and Wang 2016). Lower: Two different bio-inspired actuators inspired by the spider leg principle. Adapted from (Landkammer et al. 2016). (C) Biological role model and technical implementation of an octopus-like robot actuated by SMA. Adapted from (Kim et al. 2013).

2.4 VARIABLE STIFFNESS

2.4.1 Definition of stiffness

The stiffness of an object describes the relation between the load applied to a structure and the resulting deformation (Baumgart 2000). In other words, the stiffness refers to the amount of force needed to cause a certain deformation. In its basic form stiffness is the applied load divided by the resulting deformation. The term rigidity describes the property of a structure that does not deform under an applied load (high stiffness), while the opposite is referred to as flexibility (low stiffness). The load applied to a structure can have different forms such as forces or moments. Further, the stiffness varies with the position and direction of the load applied (Baumgart 2000). Therefore, different definitions of stiffness exist: The stiffness k of a structure is defined as a constant property, assuming a uniaxial loading as pure tension or compression (see FIG. 2.32), and an entirely linear elastic material behavior. It results from the relation between the force F and the displacement ΔL . This results in the unit N/m.

$$k = \frac{F}{\Delta L} \quad (4)$$

For a beam under pure tension it can also be written as $k = EA$, where A is the cross-sectional area and E the Young's modulus of the material (Baumgart 2000; Spura 2019). The flexural rigidity of a beam subjected to pure bending is not only dependent on the cross-sectional area but the geometry as well (see FIG. 2.33). The second moment of area J needs to be considered. The bending stiffness k_b is defined as $k_b = EJ$. This results from the relation

$$M = Ejk \quad (5)$$

where M is the bending moment and k the curvature, which is the reciprocal of radius of curvature ($\frac{1}{r}$). Accordingly, the torsional stiffness depends on the shear modulus and torsional moment of inertia. Considering more complicated geometries or systems, the separation according to load types is usually not possible, as these are often interrelated. A tensile force may e.g. cause a twisting as well (as is the case for a helix structure).

As the stiffness usually varies for the different loading directions, several coefficients of stiffness are to be distinguished if needed. These may also take into account a material axes orientation relative to the load configuration. The different coefficients are part of the material stiffness matrix C . Following Hooke's law, for a three-dimensional state in the linear tensor equation the linear stress vector s and linear strain vector ε need to be considered ($s = C \cdot \varepsilon$). A three-dimensional stress state

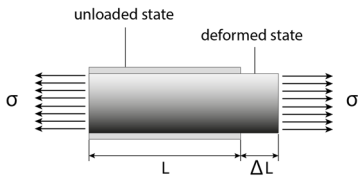


FIG. 2.32: In axial direction the stiffness is defined by a linear relationship between the normal stress acting on the cross-sectional area and the strain measures ($\varepsilon = \Delta L/L$) in that direction. Based on (Baumgart 2000).

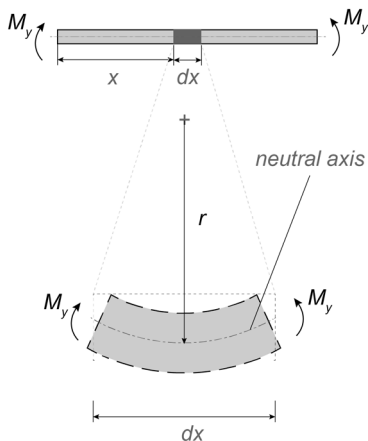


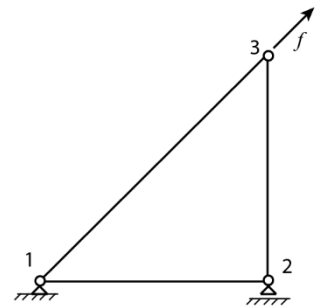
FIG. 2.33: A beam that is loaded by a pure bending moment M_y . As a result, the beam deforms with a radius R of the neutral axis, that does not change in length when under bending. For the definition of the bending stiffness the reciprocal value of r is used as the deformation parameter. Based on (Baumgart 2000).

consists of three normal stress components acting perpendicular to three different planes and three shear stress components acting in three different planes. So, in total there are six independent components of stress present in the stress vector s . In complete analogy a strain vector exists that describes the local deformation. The three direct strain components represent the relative elongation in the directions of the three axes of the coordinate system and the three shear strain components represent the change of the angles between two edges of a considered particle. As each stress component can cause any of the strain component in total 36 (six times six) different stiffness coefficients exist (see FIG. 2.34). These are the components of the material stiffness matrix C . The material behavior determines the number of independent stiffness coefficients present in the material stiffness matrix. In the case of orthotropic material behaviour, the stiffness matrix contains six independent coefficients, while in the case of isotropic material behaviour there are only two (Baumgart 2000).

$$\begin{bmatrix} \sigma_1 \\ \sigma_2 \\ \sigma_3 \\ \sigma_4 \\ \sigma_5 \\ \sigma_6 \end{bmatrix} = \begin{bmatrix} C_{11} & C_{12} & C_{13} & C_{14} & C_{15} & C_{16} \\ C_{21} & C_{22} & C_{23} & C_{24} & C_{25} & C_{26} \\ C_{31} & C_{32} & C_{33} & C_{34} & C_{35} & C_{36} \\ C_{41} & C_{42} & C_{43} & C_{44} & C_{45} & C_{46} \\ C_{51} & C_{52} & C_{53} & C_{54} & C_{55} & C_{56} \\ C_{61} & C_{62} & C_{63} & C_{64} & C_{65} & C_{66} \end{bmatrix} \begin{bmatrix} \varepsilon_1 \\ \varepsilon_2 \\ \varepsilon_3 \\ \varepsilon_4 \\ \varepsilon_5 \\ \varepsilon_6 \end{bmatrix}$$

FIG. 2.34: Material stiffness matrix C . It describes the stiffness of a material particle with the relation $s = C \cdot \varepsilon$, with as the linear stress vector and ε as the linear strain vector. (Baumgart 2000)

Similar, for a system consisting of different elements, the relation between the force applied, and the resultant deformation can be described by the force vector f , global stiffness matrix K and the displacement vector u . An exemplary system is shown in FIG. 2.35 with the relation $f = K \cdot u$. An explicit expression of the stiffness matrix, however, cannot be given. Still the initial definition of stiffness as the relation between "load" and "deformation" is the same, here in the form of "load" is "stiffness" times "deformation".



$$\begin{bmatrix} f_{x1} \\ f_{y1} \\ f_{x2} \\ f_{y2} \\ f_{x3} \\ f_{y3} \end{bmatrix} = \begin{bmatrix} k_{11} & k_{12} & k_{13} & k_{14} & k_{15} & k_{16} \\ k_{21} & k_{22} & k_{23} & k_{24} & k_{25} & k_{26} \\ k_{31} & k_{32} & k_{33} & k_{34} & k_{35} & k_{36} \\ k_{41} & k_{42} & k_{43} & k_{44} & k_{45} & k_{46} \\ k_{51} & k_{52} & k_{53} & k_{54} & k_{55} & k_{56} \\ k_{61} & k_{62} & k_{63} & k_{64} & k_{65} & k_{66} \end{bmatrix} \begin{bmatrix} u_{x1} \\ u_{y1} \\ u_{x2} \\ u_{y2} \\ u_{x3} \\ u_{y3} \end{bmatrix}$$

FIG. 2.35: To describe the stiffness of a system first it is deconstructed into its elements. These are analyzed individually, and in a next step converted into an element stiffness matrix in the coordinate system for the entire structure and merged into a global stiffness matrix K . The system behaviour can be described by the equation $f = K \cdot u$.

Still, for technical as well as biological systems there are few key parameters that can be utilized to create a system with adaptive stiffness properties. Directly involved in the calculation of the stiffness k of a beam are the material property and the geometry (second moment of area). Further the boundary conditions (supports) and non-linear effects can be used to control the response of a system to an external load. All aspects will be considered more closely in the following chapters. In contrast to the previous chapter on actuation, this chapter will consider the fundamental underlying principle first and subsequently elucidate examples found in engineering and biology in the same subchapter. First, however, a short overview on the aim of variable stiffness concepts is given.

2.4.2 Variable stiffness concepts

The ability to actively vary the stiffness of a system would offer a solution to various current challenges in lightweight construction. Variable stiffness bears the potential to revolutionize design principles and is considered a key property to maximize efficiency in lightweight design. It would allow the adaption of a system to various changing requirements. There are various application scenarios where the variable stiffness of a system offers great benefits (Kornbluh et al. 2004; Kuder et al. 2013). One area of current research are noise, vibration and shock absorbing applications. Here the damping is maximized, and resonance modes can be avoided by a shift in stiffness of the system. Further application scenarios are adaptive prosthetics, orthotics, and robotics. In robotics not only the safe human machine interaction is the focus of current research but also the adaption to different grasping and locomotion tasks can be realized (Schubert and Floreano 2013). Morphing structures and skins are dealing with the inherent contradiction of an adapting, compliant system to be stiff enough to carry external loads and at the same time allow for elastic deformation and low actuation forces. Variable stiffness would be a way to unite these opposing features (Kornbluh et al. 2004). Especially in the aerospace and automotive industry concepts of morphing applications are envisioned. These systems would require to be rigid in one state, become compliant during a shape change, and get rigid again in a new configuration. For this, field changes in stiffness by a factor of 100 are necessary. Besides airplane wings that adapt their shape for a better performance during different flight conditions, wind turbines, deployable buildings, personalized seats or prosthetics and transformable robots are future prospects for morphing structures (Kornbluh et al. 2004; Kuder et al. 2013). Another interesting aspect of a variable, adaptive stiffness is to avoid failure at high loads. In civil engineering variable stiffness materials (based on SMAs) are applied to reduce damage induced by wind or earthquakes (Janke et al. 2005). This approach is of special interest for this investigation as well. The concept is to stiffen a structure for the case of seldomly occurring high load peaks and allow the system to be less stiff while performing under "normal" operation conditions. This might allow for lower actuation energies and greater deformation ranges.

Ways to change the stiffness of a system are numerous but follow some basic categories that can be defined as follows. Kuder et al. grouped the variable stiffness notions from the perspective of morphing applications into four areas: material engineering, active mechanical design, semi-active techniques and utilization of the elastic structural behavior (Kuder et al. 2013). An exhausting summary of variably stiffness materials and concepts is given by Kornbluh et al. and by Kuder et al. with a special focus on morphing applications (Kornbluh et al. 2004;

Kuder et al. 2013). Table 4 gives a summary of the experimentally achieved stiffness changes for different stiffness variation concepts. The following subchapters will describe the different options to influence the stiffness in more detail.

Table 4: Stiffness variability of selected variable stiffness materials and concepts. Adapted from (Kuder et al. 2013).

Material	Stiffness variability	Conditions
<i>Shape memory alloys</i> 55-NiTiNOL	$E_{hot}/E_{cold} \approx 4$	82-38°C
<i>Shape memory polymers</i> Polyurethane of polyester polyole series Polystyrene-based CTD-DP-5.1 bulk thermoset resin	$E_{cold}/E_{hot} \approx 100$ $G_{cold}/G_{hot} \approx 326-517$ $E_{cold}/E_{hot} \approx 100$	Below and above $T_g = 55^\circ\text{C}$ At T_{room} and $T = -95^\circ\text{C}$ 20-80°C
<i>Elastic memory composite</i> Reinforcement: Carbon fibre (T300) Resin: Styrene-based Veriflex® S, VF62	$E_{cold}/E_{hot} \approx 79$	23-90°C
<i>Shape memory composite topology concepts</i> Constant-variable stiffness layer laminate Reinforcement: 1095-steel hexagonal plates Resin: Polyurethane-based Diaplex 5510	$E_{cold}/E_{hot} \approx 15-77$	35-75°C
<i>Fluidic flexible matrix composites</i> Tube: $\pm 35^\circ$ carbon fibre, silicone matrix Working fluid: water F ² MC sheet Four carbon fibre/silicone matrix tubes Sheet resin: Silicone	$E_{closed}/E_{open} \approx 25$ $E_{closed}/E_{open} \approx 22$	Open/closed valve Open/closed valve

2.4.3 Material properties

The stiffness of a system is linearly proportional to the Young's modulus of the material it is made from. Consequently, to influence the inherent material property is one way to control the stiffness of a system. The physical properties of materials are dependent on different environmental parameters such as temperature or humidity. Some materials show a drastic change in Young's modulus with these parameters. This effect can be utilized in a variable stiffness concept. The most important ones will be explained briefly below.

The mechanical properties of all materials depend on the temperature. In general materials are more brittle in cold conditions and become ductile with increasing temperature. While this effect is almost negligible for metals and ceramics at normal operation conditions, the effect on polymers is significant. This is true for all polymers and amorphous materials, regardless if of natural source or man-made (Saavedra Flores et al. 2013). FIG. 2.36 shows the change in modulus of a polymer from a relatively stiff state below glass transition temperature, to a rubbery state. This drop in modulus occurs between the glass transition temperature and the melting point of the material, as the intermolecular connection between the polymer chains loosen (Balani et al. 2014). Due to this strong effect, polymers are usually operated only within an operational temperature range where the Young's modulus is almost constant. Temperatures higher or lower than this range result in a sudden increase or decrease in stiffness. This holds true for technical as well as biological materials. For example, for byssal

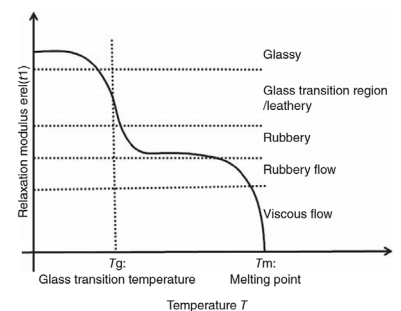


FIG. 2.36: Variation of the relaxation modulus and material behavior of a polymer with increasing temperature. (Balani et al. 2014)

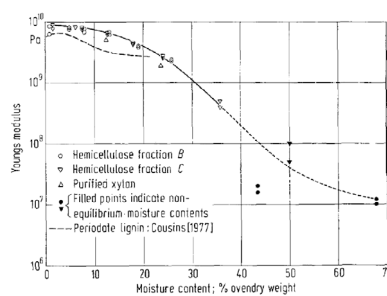


FIG. 2.37: Variation of hemicellulose Young's modulus with increasing moisture content. (Cousins 1978)

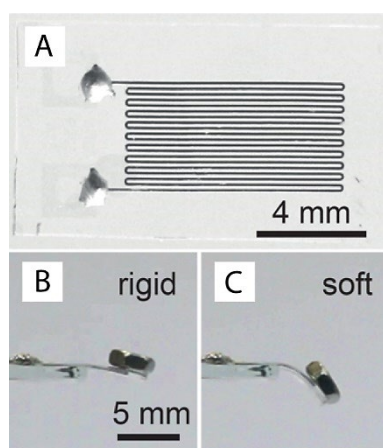


FIG. 2.38: (A) Variable stiffness device with low-melting-point alloy (LMPA) embedded in poly(dimethylsiloxane) (PDMS). (B) and (C) illustrate the softening effect associated with the melting of the LMPA. (Schubert and Floreano 2013)

threads of mussels, the Young's modulus increases by almost one order of magnitude at temperatures below the operational range (Saavedra Flores et al. 2013). This effect of glass transition is starting to get used in variable stiffness applications. For example, Chenal et al. investigated a variable stiffness fabric for wearable devices that is produced by coating a SMA wire with a thin film of SMP. The SMA can directly be used as a heating element. Is the polymer heated above its glass transition temperature, the stiffness of the fabric decreases within 15 seconds by one order of magnitude (Chenal et al. 2014).

Especially for natural materials also the humidity has a strong influence on the mechanical properties. Dry material is stiffer and more brittle. The ductility increases with moisture content but the Young's modulus decreases. Hemicellulose is a well-known material showing a high dependency of the Young's modulus on the moisture. The variation between a nearly dry and a moist state spans over three orders of magnitude (2 GPa dry compared to 0.02 GPa moist) (Saavedra Flores et al. 2013). Similar values are given by Cousins as shown in FIG. 2.37 (Cousins 1978).

However, the most drastic change in stiffness can be seen between the different states of aggregation. When the melting temperature is reached, a material changes from a solid to a liquid state and cannot withstand shear forces anymore. Upon further heating the material eventually evaporates to a gas. Schubert et al. developed a variable stiffness material utilizing the phase change of a low-melting-point-alloy (LMPA) (see FIG. 2.38). A microstructure filled with the LMPA is embedded into a soft polymer (poly(dimethylsiloxane)) (PDMS). Upon heating the rigid LMPA melts and thereby softens the entire structure. By direct Joule-heating a change in stiffness from 40 MPa to 1.5 MPa in less than one second was measured (Schubert and Floreano 2013). Further, examples of variable stiffness materials in biology and engineering, as well as for bio-inspired concepts are given below.

2.4.3.1 Examples in engineering

Materials commonly used in engineering usually are considered to show fixed mechanical properties that cannot be changed. However, there are some materials that upon an external stimulus undergo changes in their molecular or microscopic structure, which affects the mechanical properties. These materials are called *intrinsically adaptive* as the effective Young's modulus of the material changes. The most prominent examples are SMAs and SMPs, as well as ionic gels (Kornbluh et al. 2004).

SMAs and SMPs

Besides the previously described memory effect, these materials show a remarkable change in Young's modulus upon their activation temperature. Whilst SMAs attain greater attention in the field of actuation, SMPs are more promising for

the realization of adaptive stiffness (Kuder et al. 2013). SMPs, which are mostly based on polyurethanes or liquid crystal elastomers, can show strain of up to 200%. This makes them especially suitable for morphing applications. The transition temperature range can be tailored to the application. The changes in Young's modulus within this transition range can be in three orders of magnitude. However, the exact control of properties within the temperature range proves challenging. Compared to SMAs, the material and processing costs are much lower and polymers possess a significantly lower density. On the other hand, the Young's modulus is low at elevated temperatures and due to the low thermal conductivity additional heating elements are required. As for all thermally controlled materials, the response speed of SMPs is dependent on the time it takes to heat up and cool down the elements, which might be challenging for larger-scale applications. This is accompanied by a poor energy efficiency as heating is required to maintain a state. Also, the long-term durability and reliability is still unclear (Kornbluh et al. 2004; Kuder et al. 2013). The comparably low mechanical properties of the SMPs can be improved by fibre reinforcement. These SMP composites (SMPCs), also named elastic memory composites, are intended to combine a sufficient stiffness and large deformation for morphing applications, such as deployable space structures (Kuder et al. 2013). FIG. 2.39 shows the temperature dependent storage modulus of a SMP and SMPC. Both show a strong drop at elevated temperatures (Lan et al. 2009). An additional advantage of SMPs over SMAs is the potential to use other triggers than thermal stimulation.

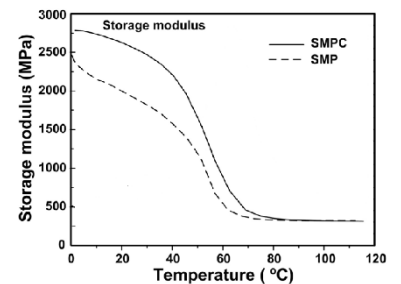


FIG. 2.39: Variation of the storage modulus with increasing temperature of a shape memory polymer (SMP) and a shape memory polymer composite (SMPC). Adapted from (Lan et al. 2009).

In SMAs the variable stiffness effect is much more moderate. They usually display a change in Young's modulus associated with to the phase change from martensite to austenite by a factor of 2 to 3. SMAs show the same drawbacks as SMPs, as difficult control, limited response time and energetic inefficiency. At least in the case of SMAs heating can happen by directly applying electric current to the material (Kornbluh et al. 2004). SMAs also possess a limited fatigue life of about 10^4 cycles and in the case of embedded structures debonding problems due to heat occur (Kuder et al. 2013).

Ionic gels

In ionic gels the uptake or release of fluid is influenced by the concentration of ions within the gel. For some electricity can be used to control the ionic concentration. The subsequent change in water content is accompanied by a change in mechanical properties. Moisturized gels will thereby be more flexible while drier will be stiffer. Their application is hindered by that fact that gels are slow in reaction and influenced by the ambient temperature. Further, they are often not environmentally stable over longer time periods (Kornbluh et al. 2004).

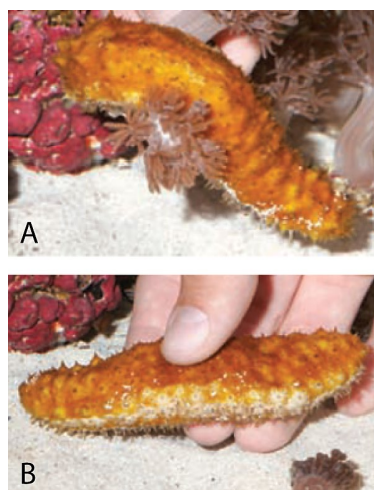


FIG. 2.40: Sea cucumber in relaxed state (A) and stiffened state (B). The stiffness variation is created by a modulation of interactions on the molecular level. Adapted from (Capadona et al. 2008).

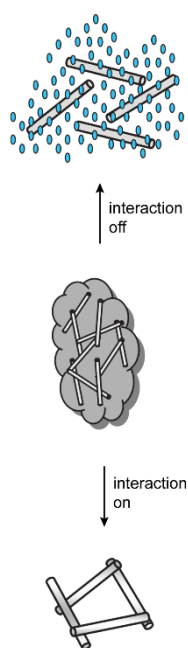


FIG. 2.41: Schematic representation of stiffness-changing nanocomposite. Strong hydrogen bonds ("on") between nanofibers maximize stress transfer and overall Young's modulus. The modulus decreases if interactions are prohibited ("off") by a chemical regulator that allows for competitive hydrogen bonding. Adapted from (Capadona et al. 2008).

2.4.3.2 Examples in biology

As emphasized above, especially in biological polymers, the stiffness and strength depend to a great extent on outer factors as moisture and temperature. The already mentioned hemicellulose is a prominent example, but also the byssal threads in mussels show a change in Young's modulus over one order of magnitude with a change in temperature around the glass transition temperature. For spider silk Plaza et al. reported a drop in Young's modulus from 10 GPa at the lowest moisture content to 0.03 GPa at the highest moisture content. The change in Young's modulus is associated with a transition from the glassy to the rubbery state, where the transition depends on both factors, temperature and humidity (Plaza et al. 2006).

Actively controlled, rapid and reversible stiffness changes, as often envisioned in technical applications, occur seldomly on the pure level of material. The probably most prominent example of a rapid and reversible stiffness change in biology is the inner dermis of sea cucumbers (see FIG. 2.40). Their connective tissue consists of a rubbery low modulus matrix made from fibrillin microfibrils that contain a network of stiff collagen fibres with a high aspect ratio. This nanocomposite structure is a chemo-responsive material. Its stiffness is altered by soluble macromolecules secreted by special, neuronally controlled effector cells. These macromolecules modulate the interactions between the collagen fibrils that form a network through transient connections. If there are many connections between the collagen fibrils a strong network is formed which stiffens the tissue. However, if the formation of connections between the fibrils is blocked and consequently the stress transfer between the adjacent collagen fibrils is reduced, the Young's modulus of the tissue decreases significantly. For the dermis of *Cucumaria frondosa* a drop in modulus by a factor of 10 (from 50 to 5 MPa) is reported (Capadona et al. 2008). For other sea cucumbers an even higher stiffness variation by more than a factor of 20 is mentioned (Kornbluh et al. 2004).

2.4.3.3 Examples for bio-inspired concept

Although still not fully understood, this behavior of the sea cucumber dermis and other echinoderms, has inspired researcher to develop composites showing similar stimuli-responsive stiffness changes. Mendez et al. introduced rigid cotton cellulose nanowhiskers into a rubbery polyurethane matrix. The resulting composites showed a water-responsive shape memory effect and a change in Young's modulus from 1 GPa to 144 MPa when moisturized (Mendez et al. 2011). Further Capadona et al. developed a similar polymer nanocomposite mimicking the architecture of the leathery sea cucumber skin. The chemo-responsive composite made from a rubbery polymer matrix and rigid cellulose nanofibers is capable of a reversible reduction in Young's modulus by a factor of 40.

As represented in FIG. 2.41, a chemical regulator influences the formation of nanofibre interactions similar to the mechanism suggested being responsible for the stiffness change in the sea cucumber dermis (Capadona et al. 2008; Saavedra Flores et al. 2013).

2.4.4 Second moment of area

Besides the properties of the material used, the cross-sectional shape of the structure in respect to the load applied plays a major role for its stiffness. This geometric effect is represented by the second moment of area (also area moment of inertia or second area moment) for bending and torsion respectively. As the height of a system usually goes into the calculation by the power of three, the stiffness of a system can be increased most effectively by increasing the structural depth. The picture in FIG. 2.42 clearly illustrates the influence of the cross-sectional geometry on the bending stiffness of a system. FIG. 2.43 shows the remarkable effect of cross-section morphing on the second moment of area for three different cross-sections with the same overall area.

2.4.4.1 Examples engineering

There are many means to change the effective height of a cross-section. Some approaches rotate an element with a rectangular cross-section that has a stronger and a weaker axis (Ghorbani-Tanha et al. 2011). Others try to bond several thinner layers together by a reversible connection (see FIG. 2.44). For a simple rectangular cross-section with the width b and the thickness h , the theoretical change in stiffness through ideal bonding can be calculated with the help of following formulas:

$$J_{not\ bonded} = \frac{n \cdot b \cdot h^3}{12} \quad (6)$$

$$J_{bonded} = \frac{b \cdot (n \cdot h)^3}{12} \quad (7)$$

Accordingly, the second moment of area increases through ideal bonding by the factor of n^2 , where n is the number of layers (Ham et al. 2009). One approach is the transmission of the shear forces through friction. The necessary normal forces are created by applying a vacuum. Kawamura et al. followed this approach to create wearable robots with variable mechanical impedance. Further, the utilization of electrical bonding is possible. Bergamini et al. used an electrical field to bond two thin additional CFRP plates to an GFRP I-beam to increase its stiffness (see FIG. 2.45). The system has the purpose to suppress vibrations caused by resonance (Bergamini et al. 2007). Other approaches use variable material properties to influence the transfer of shear forces. Some multi-layered controllable



FIG. 2.42: A single, flat paper strip (left), and a single, channel-folded paper strip (right) demonstrate the influence of the cross-section on the bending stiffness of a system.

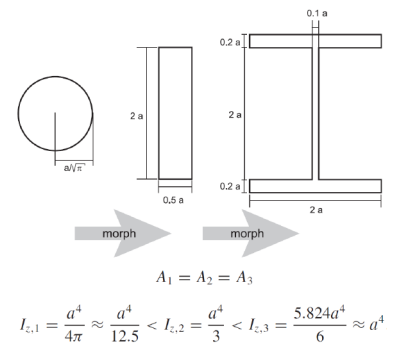


FIG. 2.43: Effect of cross-section geometry morphing on the second moment of area of a beam. Adapted from (Bergamini et al. 2007).

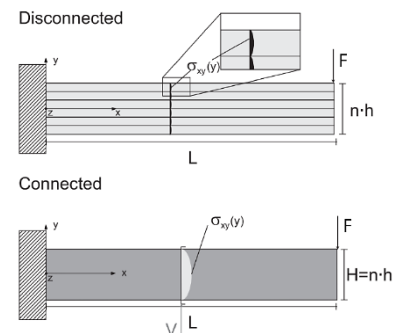


FIG. 2.44: Layered beam consisting of n disconnected parallel beams. No shear forces are transferred between the surfaces (top). Solid beam with the same cross-sectional area. A comparison of the second moment of area is given by formula (6) and (7). Adapted from (Bergamini et al. 2007).

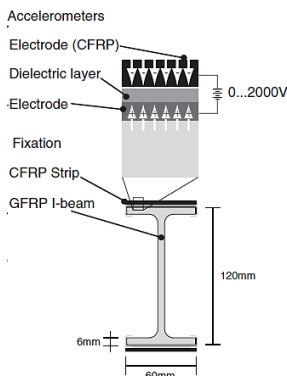


FIG. 2.45: Test set-up of a GFRP I-beam with two CFRP strips that can be bonded to it through an electrical field to vary the overall stiffness of the beam. (Bergamini et al. 2007)

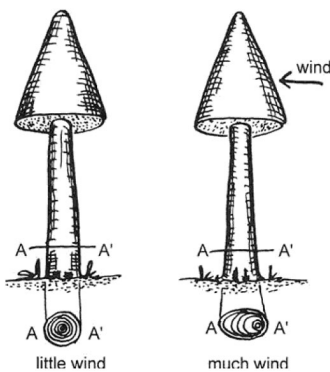


FIG. 2.46: Cross-section adaption of tree trunk. Ovalization in the direction of the strongest wind takes place. (Mattheck 1998)

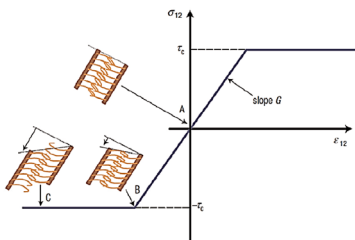


FIG. 2.47: Velcro-like sacrificial bonds between two cellulose fibres at the molecular level in the wood cell-wall and the corresponding shear stress σ_{12} and shear strain ϵ_{12} relation. (Saavedra Flores et al. 2013)

stiffness beams for morphing applications use polymers as bonding layers. The shear modulus of these polymers, and thus their capacity to transfer shear forces, is reduced by heating the material above the glass transition temperature. Consequently, the overall stiffness of the system decreases by up to 95% (Murray and Gandhi 2010). Besides that, smart materials are used to increase and decrease the bond between layers. Henke et al. use a shape change that is induced by electroactive polymers to increase the friction between layers by interlocking structures (Henke et al. 2012).

However, there are still some shortcomings to these concepts. The bonding applied is not ideal and thus the transmittable shear forces are limited. Depending on the binding method, measured stiffness changes are therefore far below the theoretical values. The bonding forces created by a vacuum or an electrical field are limited. Moreover, as the connection relies on friction, the precise control proves difficult. The heating of the elements for the softening of polymers on the other hand requires much energy and, depending on the size, also time (Ham et al. 2009; Kuder et al. 2013).

2.4.4.2 Examples biology

The increase in stiffness by the adaption of the cross-sectional shape is used in nature as well. In trees and bones the cross-sectional shape is adapted to occurring loads by adaptive growth. Over time a tree that experiences wind mainly from one direction will form an oval cross-section in the direction of the strongest wind (FIG. 2.46) (Mattheck 1998). This is a long-term adaption. As an immediate and reversible adaption, natural materials, especially biological polymers, vary their stiffness by so-called sacrificial bonds. These are molecular cross-links connecting polymer chains to each other. Upon a high load, these connections break leading to a reduction in stiffness. They form again once the stress is removed, fully recovering the mechanical properties. These sacrificial bonds are reported for bones, nacre and also wood (FIG. 2.47). This effect is compared to a velcro-like mechanism connecting the cellulose fibres. This enables a plastic response through a stick-slip mechanism found at the molecular scale (Saavedra Flores et al. 2013). Although this mechanism probably can be considered rather a mechanism to avoid failure than a mean to actively control the stiffness.

2.4.4.3 Examples bio-inspired concept

A prominent bio-inspired approach to a variable stiffness composite is inspired by biological materials as nacre, dentin, and bone. These natural materials are composed of hard mineral platelets connected by a soft and ductile protein matrix. This combination leads to tough composites. They combine a high stiffness (that arises from the ceramic platelets) with a high strain to failure. The high strain values are possible through a rigid body translation of platelets embedded in the soft matrix.

The elasticity of the surrounding polymer allows them to move with respect to one another. In the technical transfer the stiff platelet (made from spring steel) linkage is further actively controllable by a SMP matrix (McKnight et al. 2010; McKnight and Henry 2005). These composites are developed for morphing structures requiring a variable stiffness and large reversible strains. Tests showed a stiffness drop from the range of 7.7 – 12.3 GPa in the stiff state to a Young’s modulus of 0.12 – 0.79 GPa when heated above the glass transition temperature of the SMP. This corresponds to a Young’s modulus ratio of 15 to 77 (McKnight and Henry 2005). As can be seen in FIG. 2.48, the softening of the polymer matrix allows the different layers to move independently in the bio-inspired material built-up.

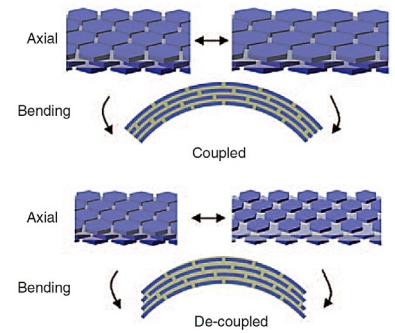


FIG. 2.48: Bio-inspired variable stiffness material consisting of segmented, overlapping platelets from stiff, reinforcing material combined with a variable stiffness SMP matrix. (McKnight et al. 2010)

2.4.5 Boundary conditions

The above-described parameters are directly involved in calculating the stiffness k of a beam. Next to that the boundary conditions of a system have a distinct influence on the response of a system to external loads. As becomes apparent from FIG. 2.49, the support conditions and the free length of the structure clearly influence the resultant deflection of an external load. The free length of a cantilever beam and the distance between the supports in a simply supported beam go into the calculation of the deflection by the power of three. The change in support conditions from simply supported to fixed supports for a beam with a center load reduces the maximum deflection by a factor of 4. Thus, next to the Young’s modulus and second moment of area, the boundary conditions are an effective means to influence a system’s behavior. Here also the pressure within a vessel shall be considered a boundary condition. The internal pressure of thin-walled vessels directly influences the system’s response to external loads. The effect the pressure has on the apparent stiffness of a system is manifold and may act on different levels. I.e. the higher the internal pressure of a vessel, the more energy is needed to change its volume; thus the stiffness is increased (Nilsson et al. 1958; Vos et al. 2011). Further, the magnitude of the pressure influences the amount of pre-stress present in the surrounding walls, making them more resistant to external loads and increasing the apparent Young’s modulus of pressurized structures (Karam and Gibson 1994; Niklas 1989).

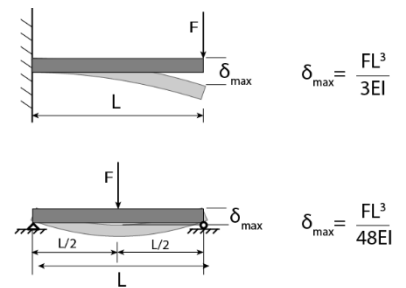


FIG. 2.49: Maximum deflection formulas for a cantilever and a simply supported beam.

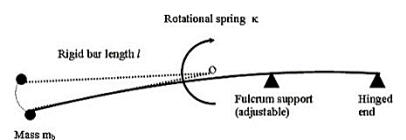


FIG. 2.50: Diving boards with an adjustable fulcrum. The variation of the supports changes the deflection behavior of the board’s free end. (Upper photo by) Ben Freeman / CC BY-NC 2.0; lower image by (Cheng and Hubbard 2008))

2.4.5.1.1 Examples engineering

Additional supports or the variation of the distance between supports are an easy and effective means to influence the stiffness. Illustrative examples are diving boards with an adjustable fulcrum (see FIG. 2.50). The further the fulcrum is shifted towards the loose end of the board, the stiffer its behavior (Cheng and Hubbard 2008). Often additional supports



FIG. 2.51: Vibrissae of mammals. These compliant sensory hairs possess a so-called blood sinus (a blood-filled cavity), which is assumed to be able to change the stiffness of the whole system dependent on the blood pressure. (Zarate et al. 2019) / © 2019, IEEE

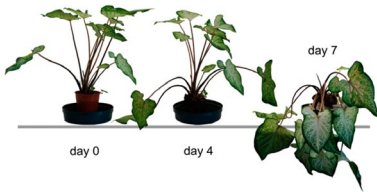


FIG. 2.52: Decreasing stiffness with reduced turgor becomes apparent in a wilting experiment carried out with *Caladium bicolor*. Habitus of well-watered plants (day 0) compared to habitus of plants without watering for 4 and 7 d, respectively. (Caliaro et al. 2013)

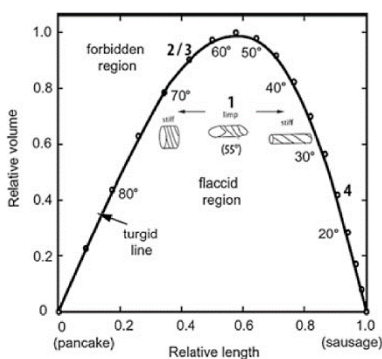


FIG. 2.53: Relative volume and relative length relation as a function of the fibre angle of helically wound cylinders. Natural hydrostats: (1) low-pressure worms, (2) high-pressure worms, (3) tube feet of echinoderms, (4) mantle of squids. (Betz et al. 2016)

which are hit and therefore active only after a critical deflection happens within the system are present.

Vos et al. developed a pressure-adaptive honeycomb structure where each cell is pressurized with an individual pouch. This structure can alter the stiffness through the internal cell pressure. They further developed an analytical model to determine the pressure induced modulus. The equivalent material stiffness E_{eq} of the pressurized honeycomb structure is determined by the sum of the Young's modulus of the honeycomb material E_m and the pressure-induced modulus E_p (Vos et al. 2011).

2.4.5.1.2 Examples biology

A change in support conditions or internal pressure is also used by biological systems to adjust the stiffness. One example are the vibrissae of mammals. These are compliant sensory hairs. Their follicle is surrounded by a so-called blood sinus, which is a blood-filled cavity (see FIG. 2.51). The blood pressure varies the blood volume within the blood sinus, which is suggested to control the stiffness of the overall sensory system. This stiffness adjusting system is suggested to prevent damage due to overloading (Carl 2008). This approach also inspired the development of a variable stiffness tactile sensor (Carl 2008; Zarate et al. 2019).

The inner pressure also influences the apparent stiffness of other biological structures. The apparent Young's modulus of thin-walled plant tissues also is dependent on the inner cell pressure (turgor). The higher the turgor the higher the stiffness of the tissue. On the other hand, a loss of turgor reduces the stiffness of tissues and entire plant organs. A strong variation in apparent Young's modulus of the tissue with the turgor has been investigated especially for potato parenchyma (Finney and Hall, JR. 1967; Niklas 1989; Nilsson et al. 1958). Finney et al. measured an initial Young's modulus of 3.72 MPa increasing to approximately 5 MPa upon a pressure increase from 0.1 to 0.6 MPa (Finney and Hall, JR. 1967). The turgor dependent stiffness also shows clearly in the petioles of *Caladium bicolor* (see FIG. 2.52) (Caliaro et al. 2013).

Also, animals use internal pressure to adjust their stiffness. Worm-like invertebrates and other organisms under hydrostatic pressure are a prominent example. They represent pressurized helically fibre-reinforced cylinders. The fibre angles determine the consequent shape change (see FIG. 2.53). Cylinders with a fibre angle of approx. 55° do not change in shape upon increasing pressure. Fibre angles lower or higher however will cause the cylinder to become shorter and fatter or longer and thinner, respectively. Natural hydrostats can additionally use their muscles to control the shape change, thereby actively reducing the volume and increasing the internal pressure. In their relaxed

state “low-pressure” worms (1) as limp worms and flatworms are situated underneath the curve in the flaccid region. This means their volume is not at a maximum. By contracting the longitudinal muscles, these worms become shorter, thicker, and more circular in shape (pancake). They also become stiffer than their internal pressure increases. By contracting their circumferential muscles, the worms becoming longer, thinner and stiffer as well (sausage). “High-pressure” roundworms (2), such as Nematoda, and tube feet of echinoderms (3) are situated on the turgid line in the graph. They possess longitudinal muscles only. Upon contraction of these the worms shorten, reduce in volume and therefore stiffen (Betz et al. 2016). So, muscle contraction against the internal fluid controls the internal pressure and stiffness. FIG. 2.54 shows an anesthetized caterpillar with no muscle tension (Lin et al. 2011).



FIG. 2.54: Anesthetization of the caterpillar suppresses muscle tone and causes the loss of inner pressure and thus stiffness. Adapted from (Lin et al. 2011). © The Company of Biologists

2.4.5.1.3 Examples bio-inspired concept

During locomotion humans and animals adjust the stiffness of their limbs continuously in reaction to internal needs and external influences. In the field of robotics researchers developed a mechanism for the modification of a C-shaped leg by means of a sliding mechanism. The change in support position by the slider varies the proportions of the covered part of the leg that is rigid and the exposed compliant part (see FIG. 2.55). The higher the proportion covered by the slider the higher the stiffness of the leg (Galloway et al. 2013).

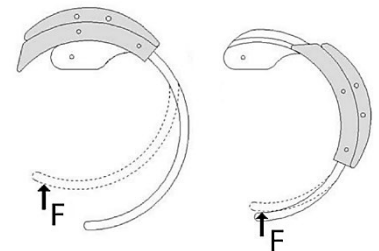


FIG. 2.55: A structure-controlled stiffness mechanism consisting of a slider changing the support (point of deflection) of a robotic C-leg. Adapted from (Galloway et al. 2013).

Inspired by the fibrillar network in plant cell walls Philen et al. developed a variable stiffness adaptive structure consisting of fibre-reinforced fluid-filled flexible matrix composite (FMC) tubes embedded in a flexible matrix. Similar to worm-like invertebrates (see above) or artificial muscles actuators, the fibre angle within these tubes controls the response to pressurization and thus induce a shape change. Further, significant stiffness changes of the tubes can be achieved by the pressurization and valve control. The system is easily deformable at open valves and becomes stiff when the valve is closed. This is due to the incompressibility of the contained fluid (Philen et al. 2006a). Modulus ratios of more than 20 were measured between the two states (Philen et al. 2007). Based on the described concept Chen et al. developed a morphing skin with embedded pneumatic muscles. This composite is capable of stiffness changes over more than two orders of magnitude upon pressurization (see FIG. 2.56) (Chen et al. 2011).

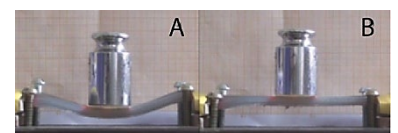


FIG. 2.56: Deformation of a morphing skin with embedded pneumatic muscles under an external load at (a) an internal pressure of 0 MPa, and (b) a pressure of 0.4 MPa. Adapted from (Chen et al. 2011).

2.4.6 Non-linear effects

Non-linear effects influence the stiffness of a system as well. Non-linearities can occur due to three different effects. These are non-linear material behavior, non-linear boundary conditions and geometric non-linearity (Bischoff 2015; Lienhard 2014).

Some of the just described parameters influencing the deformation behaviour of a system can induce a non-linear system behaviour. To quantify the influence of these effects requires a non-linear analysis of the system.

2.4.6.1 Non-linear material behavior

Many materials show a non-linear relation between stress and strain before failure. The non-linearity can have different underlying mechanisms. It may arise from material damage occurring already at low stresses, or from rearrangements in the microstructure of the material. Metals and some polymers for example show a strong non-linear stress-strain relation associated with plastic deformation (see FIG. 2.57). Microfailures and plastic deformation are irreversible. Other materials as e.g. elastomers show a non-linear elastic behavior. This means the non-linear behavior it is not tied to damage or plastic deformation. This reversibility of deformation is important when aiming to utilize the change in Young's modulus with an applied stress or strain level for a variable stiffness concept. Especially interesting are materials that show an increase in Young's modulus with elevated strain. With a strain-dependent Young's modulus the application of a controlled pre-stress or pre-strain allows to "start" from a different point on the stress-strain curve. Thus, the response of a material to external load can be varied.

FIG. 2.57: Stress-strain curves of traditional building material and typical polymers. Only GRPF and CFRP show a completely linear elastic behavior. Based on (Knippers et al. 2011).

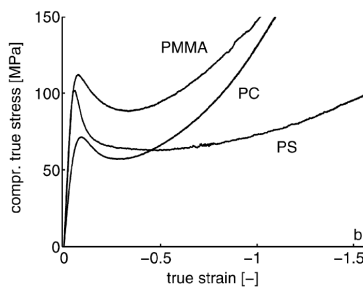
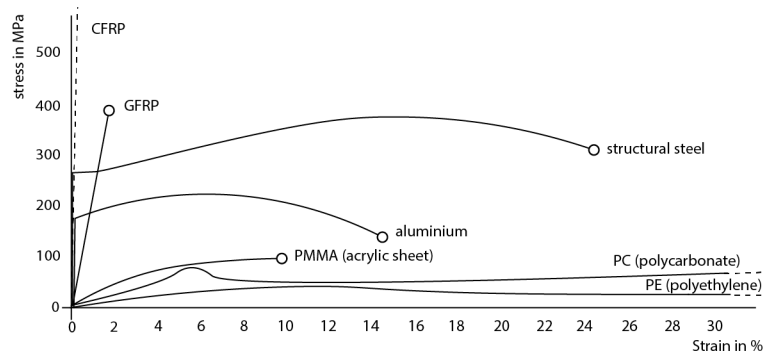


FIG. 2.58: Compression behavior of PMMA (polymethylmethacrylate), PS (Polystyrene) and PC (Polycarbonate). (van Melick et al. 2003)

2.4.6.1.1 Examples engineering

As mentioned above many construction materials such as metals or polymers show a non-linear stress-strain relation. However, a strain stiffening is usually preceded by a strain-softening. Van Melick et al. examined the strain hardening in glassy polymers as PMMA (polymethylmethacrylate), PS (Polystyrene) and PC (Polycarbonate) (van Melick et al. 2003). The hardening effect occurs in tension as well as in compression. For the mentioned examples, it is prominent, especially in compression (see FIG. 2.58). As can be seen from the graph, the initial modulus is still higher than that achieved by the strain hardening. Further, strain hardening only takes place after yielding.

Elastomers are known for their elastic strongly non-linear behavior and strain hardening (see FIG. 2.59). They are further characterized by a low Young's modulus (a few MPa) and high strains (up to 300% without rupture). At high strain, several elastomers exhibit crystallization. This is the parallel alignment of the polymeric chains, now forming a regular crystalline structure. In such a configuration several chains carry the load at the same time. This increases the strength and stiffness compared to non-crystallizing elastomers, where the chains fail one at a time (Baumgart 2000). Due to their low Young's modulus however they are not useful as construction material (Knippers et al. 2012).

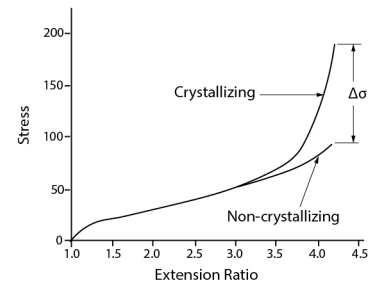


FIG. 2.59: Typical extension behavior of elastomers with and without strain induced crystallization. Based on (Bauman 2008).

2.4.6.1.2 Examples biology

While most synthetic gels and rubbers show a linear elastic material behavior or a decrease in stiffness with increasing strain, in many structural biopolymer-networks a significant stiffening with strain is present (Storm et al. 2005). Remarkably the strain-stiffening takes place without prior softening and the behavior is elastic (see FIG. 2.60). Examples are fibrin gels (which are responsible for blood clotting), actin filaments (which are present in cellular cytoskeletons), or collagen. It is suggested that the strain stiffening behavior prevents damage by avoiding exposure to large deformations. The exact underlying principles of the elastic non-linearity are a topic of ongoing research. Nevertheless, the biological materials are a role model to the development of artificial biomaterials showing a similar behavior. The strain stiffening behavior results from the self-assembled polymer network composed of macromolecules interconnected with weak, non-covalent bonds (Erk et al. 2010). Such an arrangement in an open cross-linked mesh invariably stiffens when stretched. No specific architecture or combination of the multiple elements with different intrinsic stiffness is required (Storm et al. 2005). A similar material with a stress-strain-behavior highly adapted to specific needs is spider silk. FIG. 2.61 shows the non-linear stress-strain behavior of silk threads. It includes softening at a yield point and significant strain stiffening at large strains. The behavior is also suggested to contribute to the robustness of spider webs by an increased resistance to structural defects (Cranford et al. 2012).

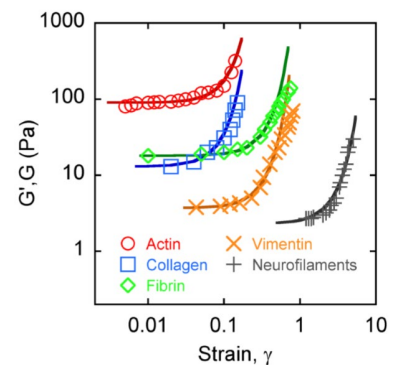


FIG. 2.60: Strain stiffening of different biopolymer networks. Dynamic shear storage moduli measured at different strain amplitudes. G' : shear storage modulus; G : shear modulus (at zero frequency). (Erk et al. 2010) / © 2010, American Chemical Society

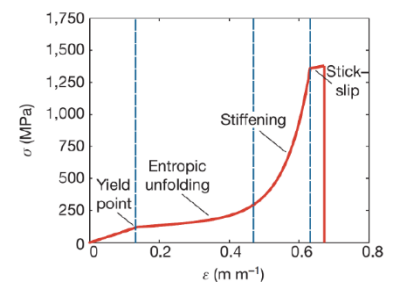


FIG. 2.61: Stress-strain curve of drag line spider silk. The typical behavior is (1) stiff initial response governed by homogeneous stretching, followed by (2) entropic unfolding of semi-amorphous protein domains, then stiffening (3) takes place as molecules align and finally (4) stick-slip deformation before failure. (Cranford et al. 2012)

2.4.6.1.3 Examples bio-inspired concepts

The development of strain-stiffening materials as described above is ongoing research. Apart from that, Park & Cho developed a bio-inspired variable stiffness mechanism based on the non-linear compression behavior of common elastomers. The set-up of the stiffness adaptive structure is inspired by the endoskeleton. FIG. 2.62 shows the spine with its alternating stiff (bone) and compliant (cartilage) segments. This construction principle is transferred to a technical system equipped with a

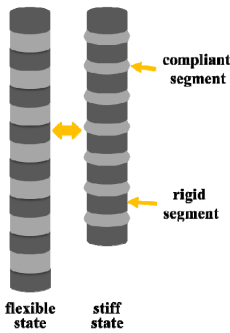
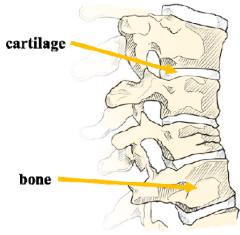


FIG. 2.62: Variable stiffness concept inspired by the vertebral column of mammals. The stiff state is achieved by compression of the compliant segments. Adapted from (Park and Cho 2013).

tendon inside the alternating stiff and compliant segments. Upon shortening of the tendon, the compliant segments are compressed. These compliant segments are made from an elastomer that shows non-linear strain stiffening. Thus, the stiffness of the overall structure is increased by compression (pre-stressing) of the compliant elements. The bio-inspired structure is used within a robotic fish to increase the thrust produced by a fin through stiffness variation within the flapping cycle (Park and Cho 2013).

2.4.6.2 Geometric non-linearity

In non-linear systems, a non-linear relationship of external forces and deflection exists. This means, in contrast to linear system behavior, the system equations cannot be written as a linear combination of system variables. The equilibrium equation of a deformed state cannot be formed as a multiplication of the force vector f and the unknown displacement vector u with the same factor n . This is possible only for linear systems with a constant stiffness matrix K :

$$\underline{f} \cdot n = \underline{K} \cdot \underline{u} \cdot n \quad (8)$$

In the case of a non-linear system behavior, the stiffness matrix $K(u)$ is no longer constant but is dependent on the actual deflections. Consequently, an n times larger force vector results in an m times larger deflection (with $n \neq m$):

$$\underline{f} \cdot n = \underline{K}(\underline{u}) \cdot \underline{u} \cdot m \quad (9)$$

Geometric non-linearities arise from large deflections of a structure which are considered in the static equilibrium that is formed on the deformed system. This results in changes of the stiffness matrix. The stresses present in the deformed state of the structure influence the response of the system to further external loading. In geometric non-linear analysis the stiffness matrix is referred to as tangent stiffness matrix K_T . It composes of the elastic stiffness matrix K_e (which is constant, and the stiffness used in linear calculations), the initial displacement stiffness matrix K_u , (that takes into account deformed geometry of the system), and the geometric stiffness matrix K_g :

$$\underline{K}_T = \left(\underline{K}_e + \underline{K}_u + \underline{K}_g \right) \quad (10)$$

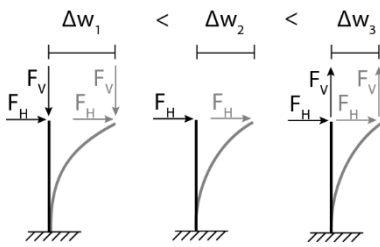


FIG. 2.63: Influence of a tensile or compressive force F_v in the stiffness and resulting horizontal deformation Δw of a clamped mast subjected to a horizontal force F_H . Based on (Lienhard 2014).

K_g , also referred to as initial stress-stiffness, quantifies the contribution of changing stiffness due to inner forces during deformation. It is to a great extent determined by normal forces occurring within the structure. The example shown in FIG. 2.63 illustrates the phenomenon of *geometric stiffness*. Assuming a mast with clamped support loaded at the tip with a horizontal load. A tensile normal force decreases the horizontal deformation and thus stiffens the system, while a compressive normal force decreases the stiffness as it increases the

horizontal deformation. The stiffening effect of the tensile force arises from its straightening influence that reduces the eccentricity (Bischoff 2015; Lienhard 2014)

This stiffening effect of tension normal forces or stresses on the geometric stiffness matrix is referred to as stress- or more precisely tension-stiffening. It becomes apparent only in systems with a low elastic stiffness like especially slender structures with a low bending stiffness compared to the axial one. For such systems like cables, thin beams, and shells, as well as bending-active structures this effect may lead to an improvement of the structural performance. Therefore, these slender systems are pre-tensioned (linear elements such as cables) or pre-stressed (planar elements, such as slabs and membranes) to increase the stiffness of a structure. The forces are usually introduced prior to external and dead loads, to create internal stresses that counteract these. Staying within the linear-elastic range of the material properties, pre-tension and pre-stress are only relevant for forces applied in the perpendicular direction and generally do not increase the load bearing capacity of a system (Lienhard 2014).

The effect of geometric non-linearities influences the stiffness of a system without changing the material properties or second moment of area. Also, non-linear material properties with strain stiffening are not required for the effect of an increased geometric stiffness by pre-tension. An extensive explanation of the influence of residual stresses in the bending of cantilever beams is given by Shi et al. (Shi et al. 2012). A variation of pre-tension or pre-stress could potentially be utilized to vary the stiffness of a system during its usage.

Non-linear behavior and an associated variation in stiffness can also arise from non-linear boundary conditions. This may include geometric boundary conditions as for example a support sliding up a non-linear slope but may also arise from static boundary conditions where the magnitude and direction of loads depend on the deflections within the system. This is the case for pressure loads that always act perpendicular to the surface (Bischoff 2015).

2.4.6.2.1 Examples engineering

Well-known examples in engineering are pre-tensioned cable nets or pre-stressed membranes. Cables are usually tensioned against external supports. Membranes can be tensioned against stiff or cable edges, as well as pneumatically through differential air pressure. Another illustrative example to grasp the increase in geometrical stiffness are the strings of a guitar. Associated with an increase in stiffness due to a pre-stress, is an increase in Eigenfrequency. The Eigenfrequency of a string corresponds to the note it produces. So, the higher the tension inside the

string the higher the note. Thus, the pre-tension is used to control the response of the system (Lienhard 2014).

2.4.6.2.2 Examples biology

A similar example are the vocal folds. These are a band of muscle, in humans also referred to as vocal cords. To produce a sound the vocal folds are tensed. This brings together the vocal folds to reduce or close the glottis. This term refers to the opening between the vocal folds. Through the airflow that is initiated by the contraction of the lungs, the vocal folds are excited into a self-sustained vibration. The tighter the chords are stretched the higher-pitched is the sound (Campbell et al. 2016; Zhang 2016). Another example using pre-stress to increase the stiffness of a system are pressurized plant tissues. Especially parenchyma, where the cell walls are thin. The turgor pressure sets the cell wall under pre-stress. Next to others effect taking place at the same time, this pre-stress is responsible for an increase in the stiffness (Karam and Gibson 1994; Nilsson et al. 1958).

2.4.6.2.3 Examples bio-inspired concept

Inspired by the antagonistic set-up of muscles around a joint and the non-linear force-stiffness response of muscles, different researchers developed a variable stiffness actuation concept for a human-friendly robot technology. One example is shown in FIG. 2.64. The different approaches utilize the geometrically non-linear response of springs (Petit et al. 2010) or artificial muscles (Annunziata and Schneider 2012; Daerden 1999) to vary the stiffness of a pivot joint. An antagonistic set-up allows the application of a pre-stress, changing the response of a system to external loads.

2.4.7 Conclusions

The means to achieve a stiffness variation within a system are manifold and range from changing material conditions, over the second moment of area, boundary conditions to non-linearities, such as material or geometric non-linearities. This applies equally to biological and technical systems. A clear distinction between the different effects taking place is often difficult as several of them may occur combined. This study targets a composite material technology that is environmentally tolerant and can efficiently change stiffness. The aim of the adaptive stiffness concept is to overcome the inherent conflict between the requirements of movement and the capacity to carry external loads, by a system that can temporarily and fast vary its stiffness. Large changes in stiffness by a factor of 100, as is a typical requirement for morphing applications, will not be necessary here. Nevertheless, many of the systems described above need to be excluded as they are too sensitive to changes in the

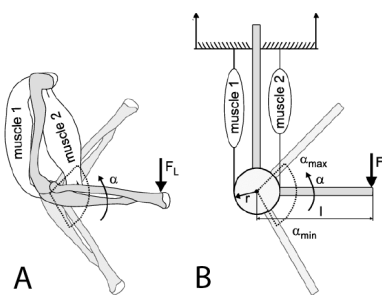


FIG. 2.64: (A) Simplified depiction of the human arm. The elbow joint is moved by two antagonistic muscles. Co-contraction of these increases the joint stiffness. (B) Technical interpretation of the antagonistic joint set-up of the biological role model. Adapted from (Annunziata and Schneider 2012).

environmental conditions. Façade structures exposed to solar radiation in summer can heat up to 80 °C. For a temperature-based concept, the activation temperature needs to be clearly above the temperature occurring in normal operation conditions. On the other hand, the activation temperature should not be too high in order not to require unnecessarily vast amounts of energy, and to be achievable fast. Further, the used materials and systems need to be able to bear all other occurring environmental influences (humidity, UV radiation, ...) for years. Thus, rain and humidity changes that occur naturally should not passively activate the device and humidity-based approaches are excluded here. Other materials or principles are not suitable as they are simply not stiff enough for an application in large-scale shading devices. Materials and system that meet the above-mentioned criteria furthermore must work reliable and predictable. In that regard the approaches changing the cross-sectional area by jamming or electrical bonding are not considered further at this point. Materials that seem most suitable to meet the above-mentioned criteria are SMAs and SMPs. However, they have some other distinct disadvantages. SMAs are considered energetic inefficient. SMPs show a strong drop in stiffness with heating, are difficult to control and expensive. Both require constant heating to maintain an actuated property. Thus, they offer themselves for a concept where the system is inherently stiff and is softened to allow the deformation SMPs would require softening and therefore heating for every activation of the compliant device. However, this approach is rather suitable for morphing applications that undergo large shape changes but less frequently. Further, as in large-scale applications some time is needed to heat up and, especially, to cool down again, the system might not be able to respond quick enough to the user demands.

Another objective of the investigation is to reduce the mechanical complexity of kinetic systems. Therefore, solutions that are multifunctional and can enable both functionalities, actuation and an adaptive stiffness at the same time, are preferred. Next to SMAs, especially pressure-based approaches seem promising. The cellular structure of plants is a perfect example in this regard. Also, the antagonistic set-up of muscles or suitable technical actuators shows a possible approach to combine actuation and stiffness adaption. Following this, a pressure-based fluidic actuation and stiffening principle is designed, where additional stiffening takes place only once required for rare and time-limited exceptionally high loads.

Considering all the mentioned restrictions and demands, varying the stiffness of a system with a controlled applied pressure seems a promising concept. Also, varying the pre-tension in an antagonistic arrangement of actuators like muscles offers a potential solution for systems combining motion generation and adaptive stiffness properties. Depending on the chosen actuators this approach also has the potential of meeting the

other requirements. Both have the potential to work reliable under the given environmental conditions and for a large amount of load cycles. Pressurization (fluidic and hydraulic) allows instant activation, vastly independent of environmental influences such as heat or humidity. In an integrated approach large changes in stiffness will most likely not be achieved, but smaller changes to adapt to extraordinarily high loads occurring seldomly might be realized.

3 CASE STUDIES

This chapter describes the biomimetic development process for two case studies (see FIG. 3.1). Both deal with the development of a joint-free biomimetic actuator with an incorporated variable stiffness concept. The driving vision behind this development is the application in 2-dimensional compliant mechanisms. The development of the compliant actuator ends with a demonstrator applied to such 2-dimensional compliant device, while for the adaptive stiffness the aim is to develop first functional prototypes independent of the application scenario.

The case studies follow the process steps of a top-down biomimetic development. Inspired by the distributed actuation of plants, whose pressurized cellular tissues also show a turgor dependent stiffness, a pressurized cellular actuator is developed. The second case study is inspired by the animal kingdom. The ultrastructure of pressurized wing veins in flying beetles provides a solution for the material built-up of FRPs with an integrated pneumatic actuation. The antagonistic muscle-set-up gives inspiration for the incorporation of an adaptive stiffness.

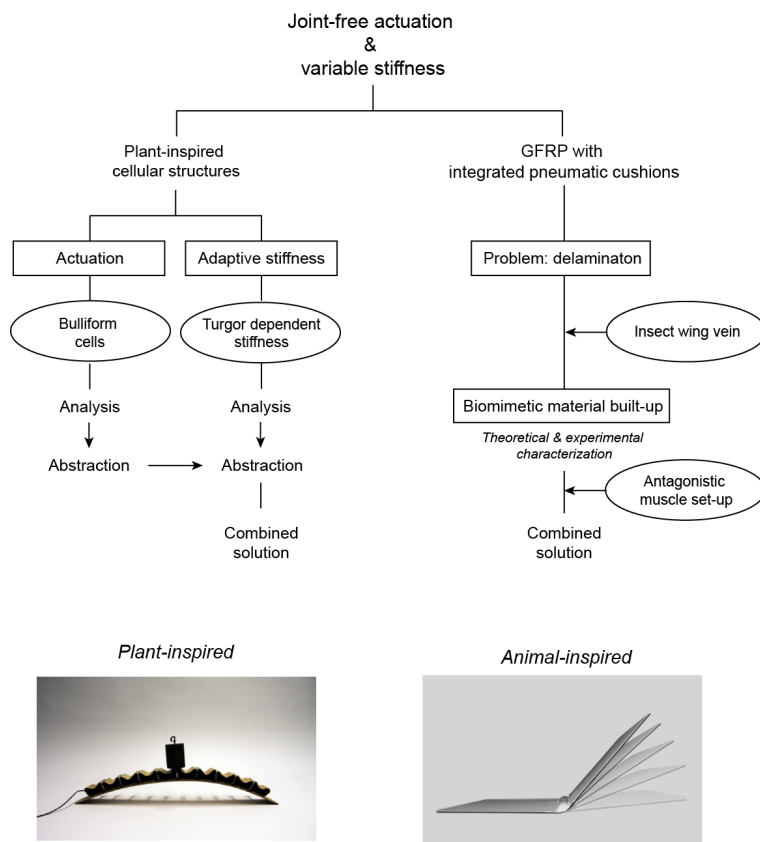
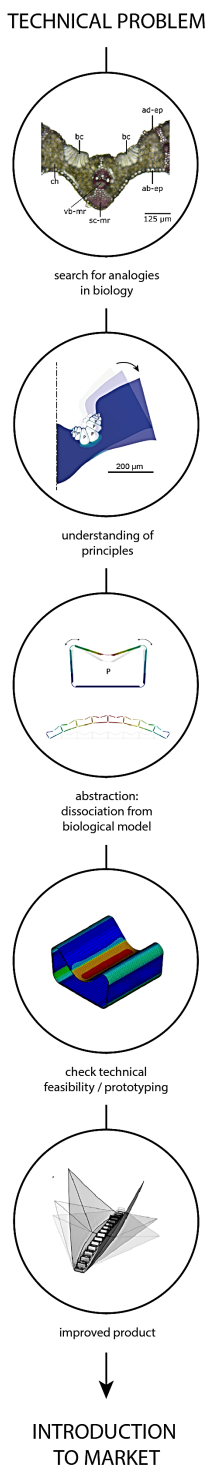


FIG. 3.1: Plant-inspired and animal-inspired top-down development process of a joint-free actuator and an integrated adaptive stiffness concept.



3.1 CASE STUDY I: PLANT-INSPIRED ACTUATION AND ADAPTIVE STIFFNESS

The starting point for this biomimetic process is the ability of plants to fulfill motions without any distinct external actuators and the turgor-dependent stiffness some plant tissues exhibit. The aim is to transfer these properties to a technical compliant kinetic system. Both properties fundamentally rely on the turgor within plant cells. Therefore, a closer explanation of turgor is given here as an introduction. Plant cells are filled with water. Due to osmosis this water flows between neighboring cells and exerts a pressure on the cell wall. The flow of water is induced by different solute concentrations. The cell membrane is a semi-permeable membrane. This means it is permeable for water but not for solutes. Water will pass from the less concentrated solution to the higher concentrated solution to equilibrate the two concentrations. This process continues until the concentration of the two solutes are equal or further water flow is restrained by some potential. This potential might result from gravity, or the elastic potential of the cell wall being stretched upon the water inflow. The water influx presses the protoplast membrane against the cell wall and increases the cell pressure. The pressure at which osmosis stops is called turgor (Nultsch 2001). The turgor is commonly quantified as relative pressure in excess to the atmospheric pressure. In other words, the hydrostatic pressure that is named turgor results from an osmotic gradient that living plant cells generate and maintain between the cytoplasm and the ambient surrounding.

The following chapter will describe the development process of a plant-inspired actuator and the addition of an adaptive stiffness concept. Aiming to solve the technical challenge in a joint-free actuation and adaptive stiffness concept, the steps of a top-down biomimetic development process are followed (see FIG. 3.2). This investigation was carried out in close collaboration with the Plant Biomechanics Group Freiburg (PBG) at the Albert-Ludwigs-Universität Freiburg that conducted the screening process and the physical investigations of the biological model.

FIG. 3.2: Steps of the top-down biomimetic development process in plant-inspired case study I. Based on (Speck and Speck 2008).

3.1.1 Plant-inspired cellular actuation

The principles found in plant movements can be a valuable source of inspiration for new approaches to create kinetic systems in engineering. Their incapability of changing location makes it especially vital for plants to be able to adapt to changes in their habitat. They do so by short-term responses or long-time adaptations (Lambers et al. 2008). Therefore, although considered static, plants exhibit a great variety of means to react to external stimuli by movements (Li and Wang 2016). As discussed in chapter 2.2.2 reversible plant movements are based on osmotic pressurization (turgor) or hygroscopic swelling and shrinking. Plant movements vary over many orders of magnitudes and are limited in speed by the poroelastic timescale of water diffusion through soft plant tissue. Some species utilize mechanical instabilities, such as snap-buckling or explosive fracture, to speed up the motion (Anderson 2004; Dumais and Forterre 2012; Skotheim and Mahadevan 2005). Due to the intended large-scale application and the prerequisite of a completely controllable movement in the technical application, this investigation excludes the mechanisms of swelling or elastic instabilities. Therefore, the focus lies on the turgor-driven nastic plant movements. Nastic plant movements are based on changes in turgor pressure that cause changes in the volume of the plant cells, resulting in macroscopic motion. In most cases, the motion originates from highly specialized and smartly located motor tissue. The turgor puts the plant cell wall under tension and deforms it as the turgor changes. The cell geometry and cell wall material properties are designed to fit a given set of target shapes and stiffness requirements. The specialized plant motor cells can actively change their turgor by transporting ions and molecules across their cell membrane, changing the internal osmotic potential (Li and Wang 2016). As plant tissues consist of numerous cells, small changes on the cell level accumulate to a macroscopic effect. The interesting actuation features unique to plants arise from the cellular structure of their tissues. It provides both movement as well as structural rigidity. Compared to the muscular motions of animals or most technical structures, the clear distinction between the structure and the actuator is overcome.

FIG. 3.3 summarizes these different design principles of mechanisms with a single rotational degree of freedom. The actuation of systems based on the plant-inspired principle offer the appealing advantages of being distributed, energy efficient and integrative. They combine the advantages of fluidic actuators, as a high force, high stroke, and good energy efficiency with the benefits of a compliant system. These are a reduced mechanical complexity due to a reduced number of parts and the avoidance of backlash, friction and wear (Li and Wang 2016; Pagitz et al. 2014). These properties make the cellular actuation principle of plants predestined to foster the development of adaptive engineered structures. This shows also

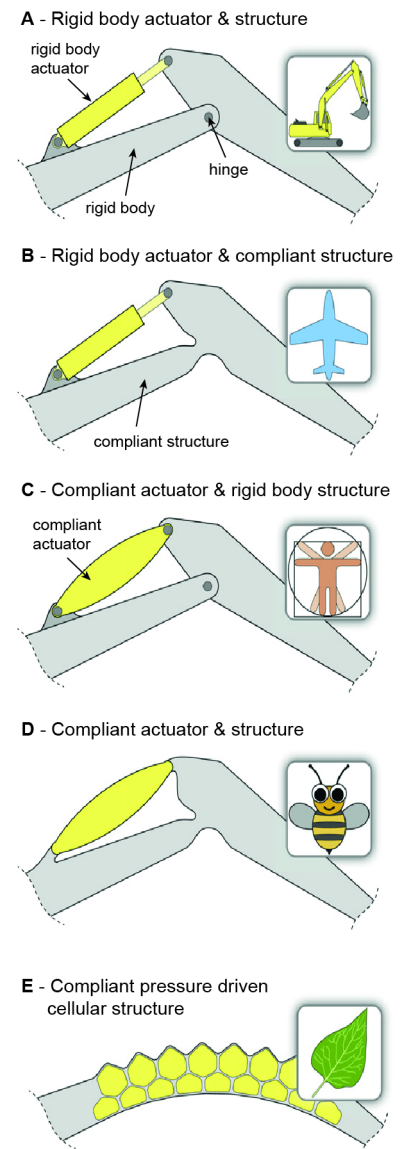


FIG. 3.3: Different design principles found in engineering and biology on the example of a mechanism with a single rotational degree of freedom. As the only principle the cellular approach does not distinguish clearly between structure and actuator. Adapted from (Pagitz et al. 2014).

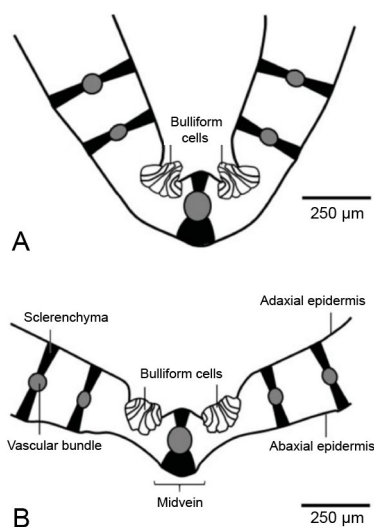


FIG. 3.4: Folding of grass leaf with a group of bulliform cells close to the midvein. (A) Folded and (B) open position. Adapted from (Mader et al. 2020b).

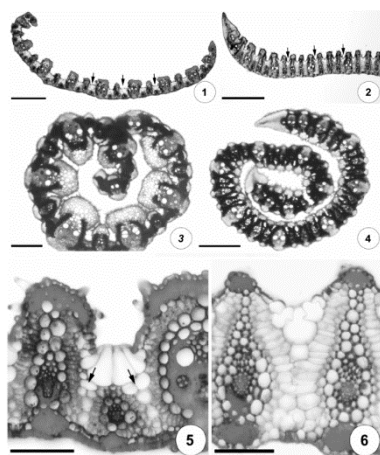


FIG. 3.5: Expanded and rolled leaf blade cross-section of *Loudetiopsis chrysothrix* (1&3) and *Tristachya leiostachya* (2&4). Arrows indicate groups of bulliform cells on the adaxial surface. Detailed image of bulliform cells from *Loudetiopsis chrysothrix* (5), which are accompanied by colorless cells (arrows) and *Tristachya leiostachya* (6). Scale bars = 250 µm (1), 208 µm (2), 400 µm (3, 4), 66 µm (5), 40 µm (6). Adapted from (Alvarez et al. 2008).

in an increasing number of publications in this field. These have been summarized thoroughly by Li & Wang in a review paper (Li et al. 2010; Li and Wang 2016). A series of so-called pressurized cellular systems have been developed so far (Gramüller et al. 2014; Pagitz et al. 2014; Vasista and Tong 2012). In the following, the development of a cellular actuator inspired by nastic plant movement is presented.

3.1.1.1 Search for analogies in biology

There are many examples of nastic plant movement, but not all of them have been investigated and understood in detail. An illustrative example of a reversible plant movement, still holding open questions, is the involution (opening and closing) of the leaf halves of grasses. Like the bio-inspired façade shading in the technical problem, this phenomenon allows plants to adapt to environmental influences.

As mentioned above, plants lack the ability to change their location in case of unfavorable environmental conditions, such as high solar radiation or drought. Nevertheless, or especially because of that, they developed means to adapt. A prominent example of these mechanisms is the rolling or folding of leaves, also referred to as leaf involution. By involution the leaf area exposed to the solar radiation is reduced significantly. In wheat, a complete rolling decreases the exposed leaf surface area by 41-48%, and by 61-65% in *Ctenanthe setosa*. Secondly, leaf rolling reduces the transpiration rates through the formation of a microclimate that allows for a higher humidity. In various xerophytic grasses the transpiration rate decreased through leaf involution by 46-83%. This might allow stomata to stay open so that photosynthesis and growth are still possible under drought conditions (Kadioglu and Terzi 2007). This makes the actuation mechanism that controls leaf involution or folding essential to many plants.

So-called bulliform cells are found in all monocotyledonous orders, except the Helobiae (Alvarez et al. 2008). Bulliform cells are enlarged, thin-walled epidermal cells on the adaxial side of the leaf (Li et al. 2010). They are arranged in groups, either located only close to the midvein or distributed over the entire surface of the leaf. In some species, these groups of cells are proposed to be responsible for a folding or a complete rolling of the leaf under drought (see FIG. 3.4 and FIG. 3.5). It is suggested that under drought stress the bulliform cells reduce their initial volume, thereby enabling the involution of the leaf. As soon as there is enough moisture again, the turgor in the bulliform cells increase and the leaf opens. However, the exact role of bulliform cells has not yet been investigated. Although, there is an increasing number of publications suggesting an involvement of the bulliform cells in the reversible, nastic involution motion (Alvarez et al. 2008; Li et al. 2010), a detailed description of the functional mechanism of the process is missing. In most

publications regarding bulliform cells only state that the turgor change enables or causes leaf movement. Some sources specify that under condition of turgor loss the bulliform cells constrict upon themselves or contract into themselves to assist leaf closure (Grigore and Toma 2011). It remains unclear whether the bulliform cells pull the leaves together or whether the loss of turgor causes a passive involution of the leaf due to pre-stresses present in the leaf. This is the starting point for this investigation.

To clarify the underlying principles, it is investigated whether a negative pre-stress is present in the tissue on the abaxial side of the leaf. This would mean that an increase in turgor actively opens the leaf against the internal pre-stresses and the leaf closes or folds passively as the volume in the bulliform cells decreases. Further, with the aid of a finite element analysis (FEA), it is investigated whether the bulliform cells can generate sufficient movement due to turgor changes that occur naturally in plants under drought stress. For these investigations the model species *Sesleria nitida* is chosen as it possesses a less complex bauplan compared to other grasses with bulliform cells. The bulliform cells occur only near the midrib, so that the examination can be limited to this region. A cross-sectional section of *S. nitida* is shown in FIG. 3.6 (A). The anatomy of the leaf represents the typical structure of a leaf lamina in the Poaceae family. The leaf possesses a symmetrical V-shaped appearance composed of a midrib and two straight lamina halves. Further, vascular bundles are present along the lamina halves at regular intervals, forming a parallel venation as typical for monocotyledons. In combination with the lignified sclerenchyma extending between the adaxial and the abaxial epidermis, they form spacers in the shape of I-beams. On each side of the midrib a group of nine so-called bulliform cells is located on the adaxial side of the leaf. A more detailed cross-section of *S. nitida* in the region of the midvein is shown in FIG. 3.6 (B). The thin-walled, fan-shaped bulliform cells are markedly wider and higher than the other epidermal cells and show a gradual transition in cell size from the edges to the center of the group (Mader et al. 2020b).

3.1.1.2 Understanding of the functional principle

To understand the functional principle behind the movement of *S. nitida* an experiment to reveal the pre-stress state present within the leaf was performed. In a subsequent step, a FEA based on the new insight and using the morphometric data of *S. nitida* is conducted.

Pre-stress analysis

To assess possible pre-stress states within the leaf, a manipulation experiment was conducted. With the help of a scalpel the bulliform cells were destroyed manually on one side of the leaf section. This was carried out as completely as possible, taking care not to damage the surrounding tissue. As

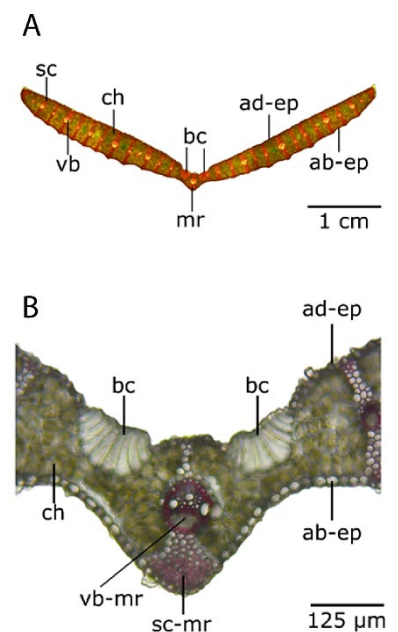


FIG. 3.6: (A) Cross-sectional of *S. nitida* leaf showing the typical V-outline with a midrib and two lamina halves. (B) Cross-section of *S. nitida* leaf in the region of the midvein with a typical group of bulliform cells. Adapted from (Mader et al. 2020b).

ab-ep: abaxial (lower) epidermis
 ad-ep: adaxial (upper) epidermis
 bc: bulliform cells
 ch: chlorenchyma
 mr: midrib
 sc: sclerenchyma
 vb: vascular bundles

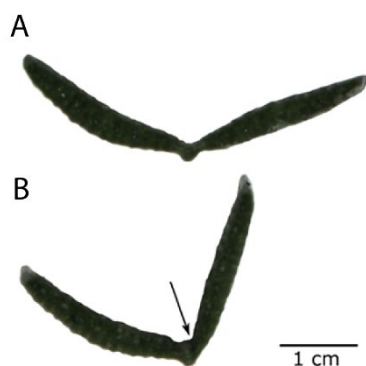


FIG. 3.7: Leaf segment of *S. nitida*. The bulliform cells are (A) undamaged while in (B) the bulliform cells situated on the right-hand side of the midvein were mechanically damaged to reveal the pre-stress within the leaf. The damage to the bulliform cells clearly causes an inward folding of the lamina half. Adapted from (Mader et al. 2020b).

FIG. 3.7 shows, mechanical destruction of the bulliform cells results in a clear folding of the respective leaf half. This suggests the presence of a pre-stress state within the tissues of the leaf. Thus, it is assumed that the turgor in the bulliform cells acts against this pre-stress to open the leaf. For *S. nitida* this further supports the hypothesis that upon drought stress and decreasing turgor pressure, the leaf closes due to pre-stress in the leaf. In addition to the manipulation experiment, a drying experiment was conducted. This experiment makes it possible to quantify the influence of the degree of turgescence of the bulliform cells on the opening angle. Opening angles of 10 samples (apical 50 mm of a leaf) were measured fresh and after being stored in dry air for 24 hours. The median opening angle of the fresh leaves was $90.63 \pm 10.91^\circ$ and of the wilting samples $36.30 \pm 20.21^\circ$. This is equivalent to an angular change of approx. 54° (Mader et al. 2020b).

Simulation of turgor-dependent motion of S. nitida

To further comprehend the role of bulliform cells in the leaf folding of *S. nitida*, a FE-simulation was conducted. The aim of this numerical experiment was to examine the capability of the bulliform cells to cause the leaf folding by using geometrical, material and pressure parameters as occurring in the natural system. The geometry derived from the light microscopy images (FIG. 3.5) was subsequently reconstructed with the help of computer-aided design software as described in (Mader et al. 2017). A 2-dimensional model of the leaf cross-section was remodeled. The microscopy image of the cross-sectional area was loaded into a computer-aided design software (Rhinoceros, version 5) and the outline of the leaf cross-section with the bulliform cells were re-drawn. Subsequently, the outlines were extruded to a 3-dimensional model suitable to be used in the FEA (ANSYS® Academic Research, Release 18.2). The process is depicted in FIG. 3.8. The cell walls of the bulliform cells were represented by 4-node structural shell elements (SHELL181). To simplify the numerical model, the surrounding tissues were modeled as one solid body (SOLID187, a higher order 3D, 10-node element). Due to the large deformations occurring, all simulation were non-linear. The material properties for the cell walls were taken from literature. The cell walls of the bulliform cells were assumed to have a Young's modulus of 5 MPa (Milani et al. 2011) and a Poisson's ratio of $\nu = 0.27$ (Konrad et al. 2013).

The Young's modulus for the surrounding tissue was derived according to the formula developed by Nilsson et al. to calculate the turgor-dependent stiffness of parenchyma tissue (Nilsson et al. 1958). To calculate the mechanical properties of the tissue, the cell wall diameter and cell wall thicknesses for the chlorenchyma of *S. nitida* was measured from FIG. 3.6 within a morphometric analysis. For the simulation, the behavior of both materials was assumed to be linear elastic. Table 5 summarizes the values used in the FE-simulation.

Table 5: Material properties and dimensions used for the FE-simulation of the turgor-dependent motion of *S. nitida*. (IQR: interquartile range; std: standard deviation)

	Surrounding tissue (chlorenchyma)	Cell walls (bulliform cells)	
Young's modulus E	E = 3.2 MPa calculated according to (Nilsson et al. 1958)	5 MPa (Milani et al. 2011)	
Poisson's ratio ν	ν = 0.27	ν = 0.27 (Konrad et al. 2013)	
Cell dimension	Cell wall thickness: Median = 2.32 IQR = 0.90	Intercellular cell wall	Exposed cell wall
	Cell diameter: Length: Median = 26.94 μm IQR = 12.52 μm Width: Median = 19.73 μm IQR = 4.81 μm Average: 23.33 μm	Measured: (mean ± std) 0.98 ± 0.15 μm (n = 10)	Measured: (mean ± std) 3.18 ± 0.45 μm (n = 10)
		Assigned: 1.0 μm	Assigned: 3.2 μm

FIG. 3.8 further depicts the process of geometry generation as starting point for the FE simulation. The microscopy image at the fully turgid state (FIG. 3.6) was taken as basis for the geometry generation. The pre-stresses within the leaf revealed by the manipulation experiment were taken into account. The closed state of the leaf was created by applying an external horizontal force of 50 μN to the lamina half. The resulting deformed state served as starting point for the following simulation. Prior to the subsequent simulation mimicking varying turgor, all stresses from the previous deformation due to the external horizontal load were set to zero. The creation of starting geometry results in an increasing cell ovalization through cell walls bending within the bulliform cells. The appearance of the bulliform cells resembles that of the cross-sectional images documented for other closed grass leaves (compare FIG. 3.4) and *Tristachya leiostachya* in FIG. 3.5 in particular. The sinuous thin wall outlines of the bulliform cells might enhance the volume change upon pressure fluctuations. Similar observations have been made by Matschi et al. (Matschi et al. 2020). They also have observed that the shape of dehydrated bulliform cells differs significantly from those in a fully turgid state. Their investigations showed that the cell size of all epidermal cells, including bulliform cells, reduces significantly through dehydration. The volume of bulliform cells decreases on average by 62%.

The change in opening angle created by the horizontal force applied is approximately 22°. This sums up to 44° for both leaf halves and corresponds roughly to the closing motion measured in the drying experiment.

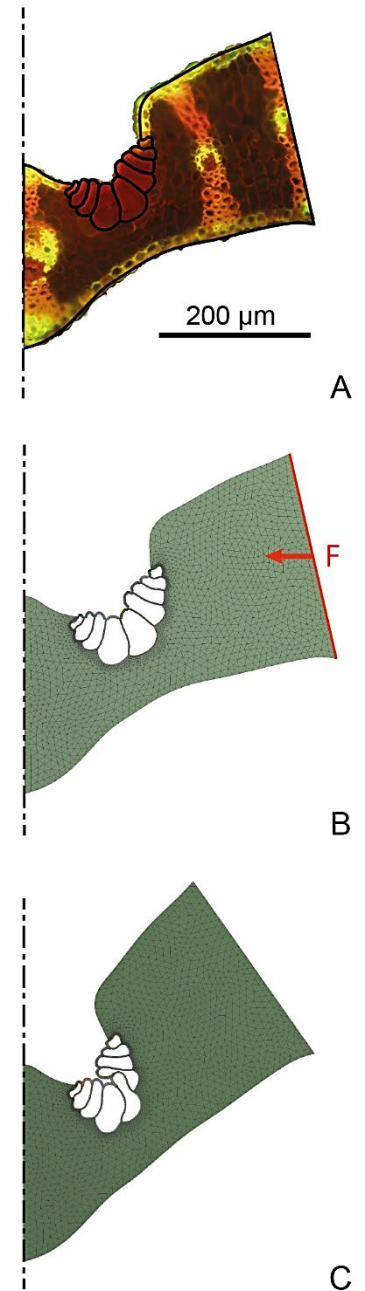


FIG. 3.8: Creation of the geometry for the FEA.

(A) The outline of the leaf cross-section and bulliform cells is transferred directly from the microscopic image.

(B) Auto-stresses in the leaf cause it to fold upon a reduction in the volume of the bulliform cells due to drought stress. To recreate this in the numerical model an external horizontal force is applied to the outer edge of the lamina geometry.

(C) Shows the resulting geometry. This closed position is the starting point for the following simulation.

Adapted from (Mader et al. 2020b).

Simulation of the motion with increasing turgor

To imitate increasing turgor, which should cause a leaf opening, a pressure was applied to the surface of the cell walls of the bulliform cells. The magnitude of the applied pressure is based on turgor variations measured for the parenchyma of *Caladium bicolor* petioles at the fully turgid state and under drought stress (Caliaro et al. 2013). There the turgor decreased from 0.45 ± 0.04 MPa at the fully turgid state to 0.38 ± 0.08 MPa under drought stress. Consequently, a pressure of 0.07 MPa was applied here to the bulliform cells to represent the increasing turgor after drought. The internal pressure applied causes a rotary motion of the lamina half. FIG. 3.9 shows a simulated, almost linear relationship between the turgor increase in and the angular change representing the rotary motion of the leaf lamina with respect to the calculated pivot point. The angular change is quantified with respect to the center of rotation and calculated from the displacement of the leaf blade ends by trigonometric functions. The calculation of the center of rotation was conducted for every time step individually, as with increasing pressure it shifts slightly. Considering the symmetry of the system, a change in opening angle of 52° is achieved for an increase in internal cell pressure (turgor) of 0.07 MPa. This is in good agreement with the mean difference in the opening angle of 54° for fresh and dried samples of *S. nitida* from the drying experiment.

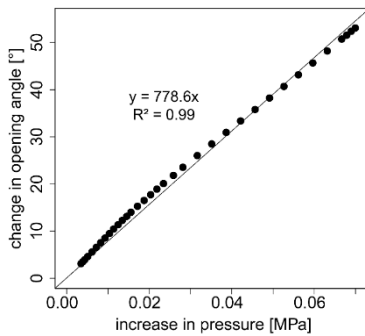


FIG. 3.9: Simulation results for the opening angle between the two leaf halves depend on the respective increase in turgor pressure inside the bulliform cells. The regression line and the coefficient of determination are presented. Adapted from (Mader et al. 2020b).

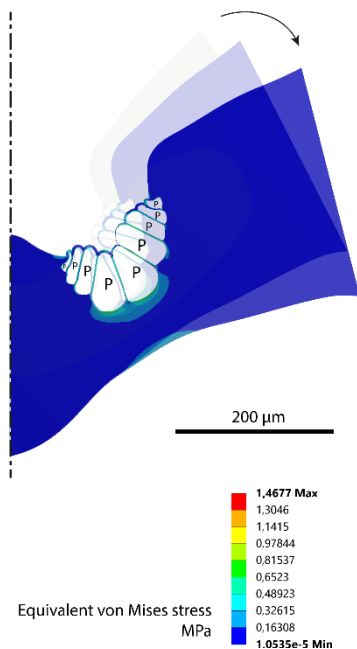


FIG. 3.10: Result of the FE simulation. An increase in pressure, solely in the bulliform cells, causes an increase in the opening angle of the leaf lamina by 26° on each leaf half. Adapted from (Mader et al. 2020b).

The opening motion of one lamina half is shown in FIG. 3.10. The maximum equivalent (von Mises) stress of the bulliform cells is 1.46 MPa. This represents the stress added to the cell wall by the pressure increase, because the turgor already present in the drought state is not represented in the FEA. The stress increase is in the same range as the calculated Hoop stress difference of 1.06 MPa. The Hoop stress ($\sigma_H = (P \cdot d) / (2 \cdot t)$) is 6.81 MPa for the turgid state and 5.75 MPa for the dehydrated state. For the calculation a mean internal diameter of $d = 29.67 \mu\text{m}$, a cell wall thickness of $t = 0.98 \mu\text{m}$ and a turgor pressure of $P_{\text{turg}} = 0.45$ MPa (for turgid cell) or $P_{\text{dehyd}} = 0.38$ MPa (dehydrated cell) was assumed. The maximum stress that occurs within the simulation and the calculated Hoop stresses are well below the tensile strength of the cell wall material. Gibson stated a tensile strength of 60 to 100 MPa for the cell wall of parenchyma and even higher values for wood cell walls (Gibson 2012).

However, also the 0.07 MPa turgor change measured in the parenchyma of *Caladium bicolor* petioles under drought, are just a rough approximation. It needs to be considered that the physiological prerequisites are fundamentally different for the two tissues. While for the parenchymatous tissue the governing task is the structural support also under drought conditions, the bulliform cells are presumably responsible for triggering the plant's response to drought stress. Therefore, it is likely that they

are more sensitive to fluctuations in water availability. Although it remains unclear if leaf involution is a distinct adaptation to reduce the impact of drought or rather a passive response to changes in the water potential of the cells (Kadioglu and Terzi 2007).

Other aspects that influence the angle change and are not considered here concern the surrounding tissue. It is likely that the mechanical properties of the surrounding tissues alter with water availability as well. Further, considering the surrounding tissue as a uniform material with linear elastic material properties calculated exclusively from the morphometric data of the parenchyma greatly simplifies the numerical model by neglecting the probably stiffer epidermis and veins. Also, the assumption that the cell wall material of the bulliform cells is linear elastic and quasi-isotropic reduces the inherent complexity and sophistication. Special features such as fiber orientation or regions of adjusted stiffness could be incorporated within the cell wall to enforce change in shape. The sinuous cell walls described above could be one example for this.

Nevertheless, the result of the FEA show clearly that the bulliform cells of *S. nitida* are physically and physiologically capable of causing a leaf opening and closing motion. Therefore, it seems reasonable to assume that the bulliform cells play a major role in the actuation mechanism for leaf folding.

3.1.1.3 Abstraction

The pressure-driven actuation seen in the bulliform cells of *S. nitida* relies on turgor-dependent changes in cell volume. Thus, it follows the same principle as other reversible plant movements. Plant cells are similar to hydraulic and pneumatic actuators in engineering and therefore especially suitable for a transfer to technical applications (Li and Wang 2016). The effort of maximizing the cell volume with increasing pressure can be transferred to technical pressurized cellular structures. FIG. 3.11 shows the abstraction process from the investigated V-shaped leaf segment of *S. nitida*, with group-wise arranged bulliform cells, to a technical cellular structure resembling the biological role model. With increasing internal cell pressure, the outer vertical cell walls tilt outwards due to maximization of cell volume. In a structure consisting in a 1-dimensional row of cells this sideways tilting of the vertical walls causes a bending motion.

For pressurized cellular actuators, it is crucial that the cell geometry is designed so that the volume changes initiate the desired motion upon pressurization. The technical cells are composed of rigid cell side walls connected by compliant hinges. This way the inner volume of the single cell can only be increased by varying the angle between neighbored cell side walls. As this work aims to create a bending motion, the following will focus on the development of a bending actuator. Bending is created by the differentiated expansion of the upper

and lower region of a beam. In a multi-layered cellular structure this can be achieved by a differentiated pressurization of the separate individual cell rows. In a single cell row set-up, bending can be triggered with an asymmetric geometry of the individual cells that causes a differentiated expansion upon pressurization.

Cell design

Pressure-driven adaptive cellular structures were first patented by Vos and Barrett in 2010 (Vos et al. 2011). Vasista et al. followed a similar approach and developed topology optimized cellular designs for morphing airplane wings (Vasista and Tong 2012). Lou & Tong built a compliant cellular structure able to fulfill linear motion (Luo and Tong 2013a, 2013b). Barrett & Barrett introduced plant-inspired biomimetic actuators for aircraft wings in 2014 (Barrett and Barrett 2014). Simultaneously, Pagitz et al. worked on pressure-actuated cellular structures (PACS) with pentagonal and hexagonal cell shapes (Pagitz et al. 2014; Pagitz and Kappel 2014). Based on these findings, Gramüller et al. designed and fabricated a first physical prototype of a single row cantilever consisting of 6 about 40 mm wide individual cells (Gramüller et al. 2014).

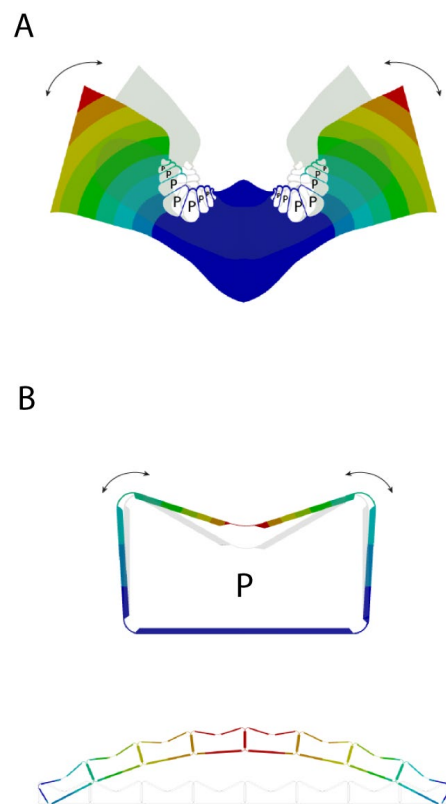


FIG. 3.11: Abstraction process from the turgor-dependent leaf involution of the biological role model *S. nitida* (A) to a technical cell (B). The vertical walls tilt outwards upon pressurization. Accumulated in a cell row this creates a bending motion. Adapted from (Mader et al. 2020b).

According to Gramüller the functional principle of a pressure actuated cellular structure is based on an increase in entropy ΔS due to the reduction of inner energy ΔU taking place by a maximization of volume V (Gramüller et al. 2014). It says that if the inner cell pressure is higher than the ambient pressure, the cell thrives to increase its volume. The behaviour is similar to a balloon (compare FIG. 3.12). Due to the compliant hinges the cell takes its original shape again as the pressure decreases. The equilibrium state is defined by the sum of the pressure induced moments and the moments induced by the hinge stiffness. A technical cellular structure offers the advantage that the cell's only function is to create the desired motion. Therefore, the cells can be designed to meet the requirements of each individual application scenario in the best possible way. The driving design parameter is the desired maximum sidewall actuation angle α and the maximum pressure P_{\max} that will be applied (FIG. 3.13). This determines the cell geometry, including the side wall thickness, the hinge geometry and thickness, as well as the material used (Gramüller et al. 2014). As some of these design variables are counteracting, it is possible to design cellular structures for a wide range of pressure and scales (Pagitz et al. 2014).

Compliant hinges

For the function of the system, it requires a fine balance between the flexibility and stiffness of the compliant cell hinges. They must be flexible enough to allow the reconfiguration, and at the same time must provide the necessary structural rigidity of the system, also in the not pressurized state. The maximum thickness of the compliant hinges is limited by the required angular distortion (α) that needs to be achieved at the maximum given pressure P_{\max} , as well as the strength of the material. In contrast to that, the straight cell walls are required to be stiff enough to not deform upon pressurization. The hinge geometry and stiffness, which defines the strength and reconfigurability of the structure, as well as the minimum cell side wall thickness, can be determined as described by Gramüller et al. for a pentagonal shaped single cell (Gramüller et al. 2014).

Material

Suitable materials for PACs range from metals, over elastomers and plastics to fiber reinforced plastics. For a given sidewall angle distortion, they can bear different maximum pressures. Predestined are materials that show a high yield strength to Young's modulus ratio. For increasing required sidewall angles, the optimal Young's modulus decreases exponentially, while bending energy and cell side thickness increase exponentially (Pagitz and Kappel 2014). Next to that a low density and the ease of fabrication and a stable long-term behavior are important, as the resetting of the original shape happens solely by the elastic energy stored within the material. According to Lienhard, the

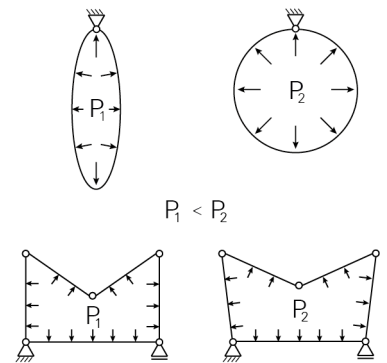


FIG. 3.12: A fluid-filled flexible membrane (above) and technical cell with rigid side wall and compliant hinges (below). The inner volume increases upon increase in the internal pressure from P_1 to P_2 .

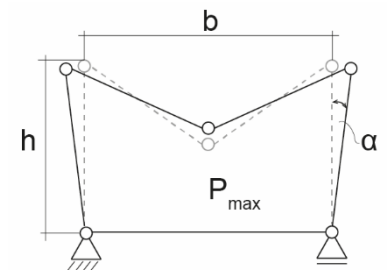


FIG. 3.13: Sidewall actuation angle α at the maximum internal pressure P_{\max} . h – cell height b – cell width

criteria necessary for compliant kinetic structures are best met by fiber reinforced plastics (FRPs) (Lienhard 2014). FRPs furthermore offer the advantage of an adjustable Young's modulus through fiber orientation. Therefore, fiber reinforced composites are used here to build the cellular actuator developed. Further, the material plays a crucial role for the scaling of pressurized cellular structures (Gramüller et al. 2014).

Scaling

The variation of certain counteracting design variables allows adaptive pressurized cellular structures to function over a wide range of scales (Gramüller et al. 2014). The size of the technical cells can range from centimeters to meters. Thus, the application scale is several orders of magnitude larger than that of plant cells, which typically measure a few tens of microns in diameter. For the scaling of pressurized cellular structures, the material and absolute pressures need to be adjusted. The inner cell pressure scales inversely proportional to the cell volume. For a given set of requirements, a cellular structure can be designed either consisting of few large cells made from a flexible material, or many smaller cells from a stiffer material.

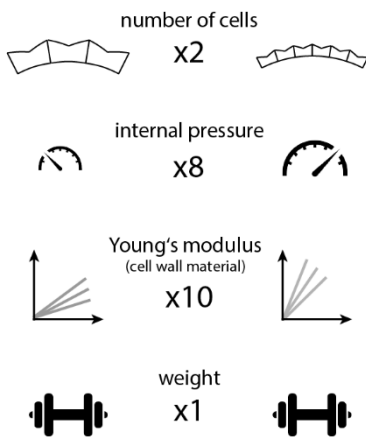


FIG. 3.14: Scaling of a pressure driven adaptive cellular structure. When for a given target shape the number of individual cells double (cell width halves), the cell volume quarters, the pressure to achieve the same stiffness increases by the eightfold, the optimal material for the structure shifts to one with a higher Young's modulus and yield strength, while the mass of the system stays almost constant, as the side wall thickness needs to be increased. Based on (Pagitz and Kappel 2014).

Assuming a given target shape and stiffness of an overall system spanning a fixed distance, a change in individual cell size affects the variables of the structure in the following way (see FIG. 3.14). As the number of cells doubles, the cell width and angular distortion α that is required to achieve the target shape half. To maintain the same stiffness of an individual cell, its pressure potential needs to be held constant. Therefore, the cell pressure needs to increase fourfold as the cell volume quarters. However, as the number of cells in the overall structure doubles, an eightfold increase in cell pressure is needed to achieve the same overall structural stiffness. Consequently, the forces within the cell side walls increase by the fourfold and the relative cell side wall thickness needs to increase. The overall weight of the structure is not affected considerably (Pagitz and Kappel 2014). These interrelations also explain the high internal cell pressure (turgor) of the small plant cells compared to the macroscopic technical application.

Pressure medium

Pressurized cellular structures can be driven by gasses as well as liquids. Disregarding technical challenges, gasses are suitable for larger cell volumes and small pressures, while the properties of incompressible fluids are advantageous for small volumes and high pressures. The compressibility of gas poses a potential safety risk in the event of an explosive expansion and is responsible for a lower energy efficiency. Therefore, the application of gasses is usually limited to about 10 bar. Fluids can operate at much higher pressures up to 700 bar, but at the cost of a much higher density and therefore weight (Pagitz and Kappel 2014). Due to the lower weight and the sufficiency of a lower

pressure range for the application considered here, air is used as a pressure medium in the following. Further Since air is widely available as a pressure medium via the atmosphere and can easily be provided by a compressor, the consequences of small leaks are less critical than with liquids.

3.1.1.4 Check technical feasibility & prototyping

To test the physical feasibility of the developed joint-free actuation concept, a prototype of the cellular actuator was manufactured. The dimensions were chosen according to those of a Flectofold prototype with a midrib span of 420 mm. The Flectofold geometry and dimension as well as the arising constraints for the technical cell are summarized in FIG. 3.15. The cell shape was derived from the following demands. The height of the cells is supposed to be small to offer a comparably inconspicuous actuation to the system. Therefore, the maximum height of the cells was limited to 20 mm, which is roughly $1/20^{\text{th}}$ of the midrib length. The cell width is defined by the number of cells and Flectofold midrib length. A cell width of 40 mm was given as a prerequisite which is equivalent to a 10-cell actuator. The maximum sidewall actuation angle of 4.7° was calculated to ensure a flap folding of 90° . The inverted pentagonal shape of the cell that resembles the outer appearance of a *S. nitida* leaf section, creates a higher momentum at the same internal pressure compared to a pentagonal cell shape. On the other hand, this design bears the risk of a snap through of the upper cell walls at higher pressures. This risk will be eliminated by the modification applied in the subsequent chapter. The side wall and hinge thickness are limited to the available thickness of the woven glass fiber epoxy prepreg. A numerical design process deriving the cell shape and the thicknesses of compliant hinges was conducted (ANSYS® Mechanical Products Release 17.2). The technical cells were represented by shell elements (SHELL181) and the contained fluid was represented by hydrostatic fluid elements (HSFLD242). The displacement of the hydrostatic fluid elements in the direction of the open sides was restrained substituting the pouches in the model. The material properties of the GFRP were assumed to be isotropic ($E = 15 \text{ GPa}$; $\nu = 0.3$). The final dimensions of the cells are displayed in FIG. 3.16. The required angular distortion is achieved, without exceeding the maximum strength of the material. The for the small-scale Flectofold prototype necessary angular deflection of 4.7° was achieved at a pressure of 0.2 bar. The maximum equivalent von Mises stress within the individual cell at that state is 80 MPa (see FIG. 3.17). This is well below the bending strength of the GFRP, also when considering the cyclic loading and reduced fatigue strength of GFRP. For the use in a cell row or the actuation of a compliant 2-dimensional device, higher pressures will be necessary to achieve the same actuation angles.

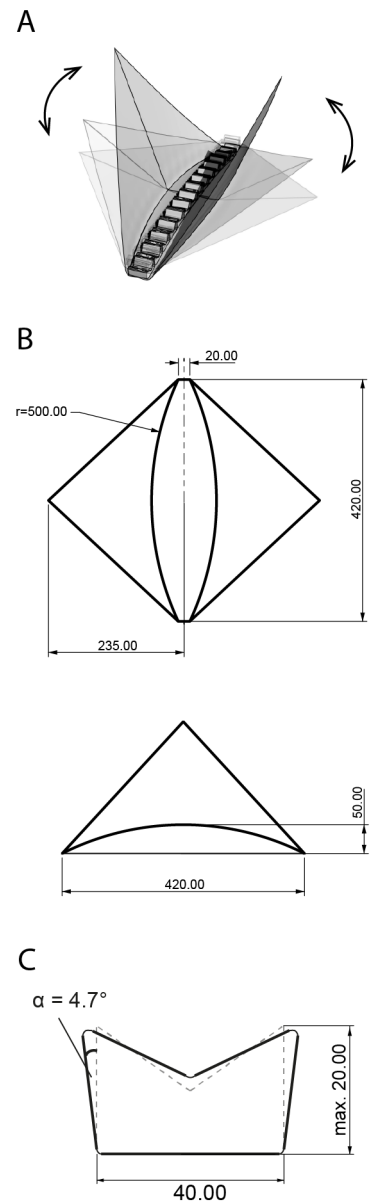


FIG. 3.15: Design restrictions for an individual cell arising from the actuating of a Flectofold prototype. (A) rendering of the final product appearance. (B) measures of the Flectofold in top view (upper sketch) and side view (lower sketch). The deflection of 50 mm needed in the midrib for a 90° folding of the flaps defines the max. actuation angle α . (C) shows the given cell dimensions. All measures in mm.

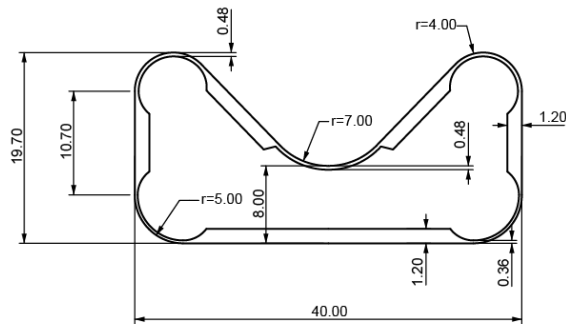


FIG. 3.16: Measures (in mm) of the individual cell within the cellular actuator prototype. Adapted from (Mader et al. 2020b).

FIG. 3.18 shows the entire pressure – sidewall actuation angle relation for the individual cell determined by the FEA. By the internal pressure the actuation angle can be controlled continuously.

The physical prototype was built with the help of a silicone mould representing the volume that can be pressurized. Layers of woven glass fibre epoxy prepreg sheets were stacked onto the mould in the according number of layers to achieve the defined cell wall and hinge thicknesses. The fibre orientation in the hinges was $0/90^\circ$. After stacking, the mould was placed into a vacuum bag. With the applied vacuum that pressed the prepreg sheets together, the epoxy was cured in an oven at 125° for 2 hours. Further details on the cell manufacturing are listed in appendix A1. The pressurization is realized by inserting airtight pouches made from TPU-coated nylon. This use of the rather inextensible fabric eliminated the need for endcaps that are required if a flexible pouch material like rubber is used.

FIG. 3.19 demonstrates the shape changing potential of a cellular actuator prototype. The cellular actuator prototype is not only capable of achieving the necessary curvature but also able to lift additional external loads. This is demonstrated by the lifting of a weight of 0.5 kg with an internal pressure of less than 4 bar (see FIG. 3.20). This shows the potential of merging the structure and the actuation and at the same time hints at the capability system to potentially function as an actuator to 2-dimensional compliant systems.

3.1.1.5 Improved product

Technical pressurized cellular structures inspired by the cellular design principle of plants are suggested to be easy to control, reliable and energy efficient, while exhibiting a good strength to self-weight ratio (Pagitz et al. 2014). This makes them a good candidate for adaptive structure and also promising actuators for 2-dimensional compliant mechanisms relying on bending or curved-line folding.

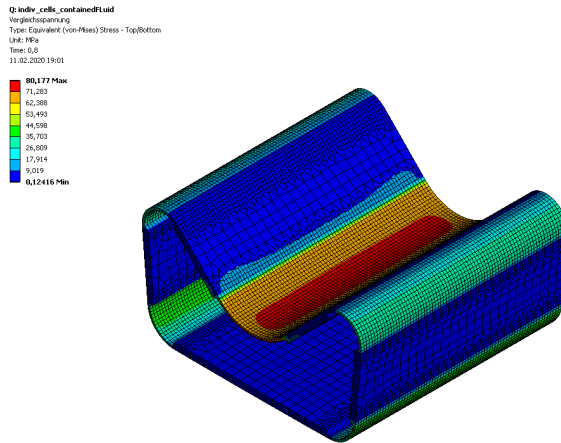


FIG. 3.17: Stresses that occur in the cell wall of an individual technical cell when an internal pressure of 0.2 bar is applied which is needed to achieve a sidewall actuation angle α of 4.7°. The cell width is 40 mm. Adapted from (Mader et al. 2020b).

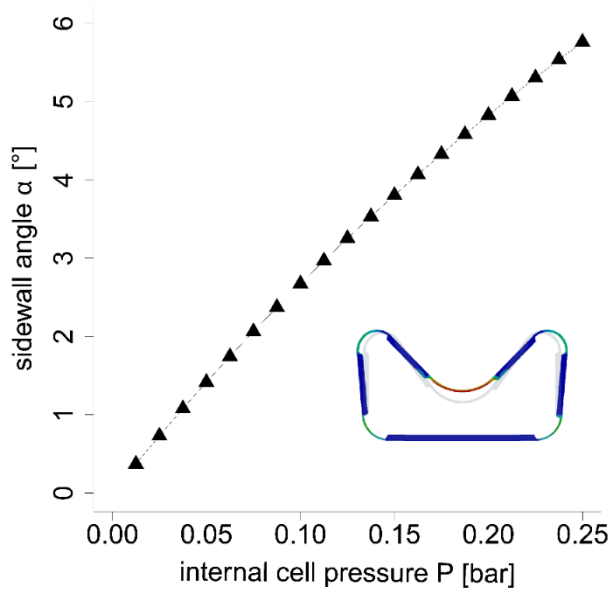


FIG. 3.18: Vertical sidewall angle α of the technical cell upon increasing internal cell pressure P . Adapted from (Mader et al. 2020b).

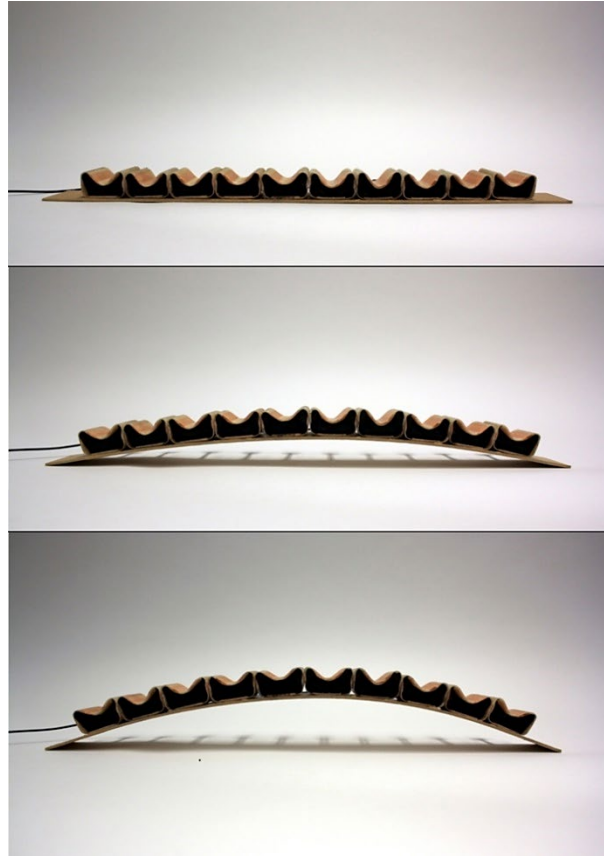


FIG. 3.19: Cellular bending actuator prototype consisting of a single cell row, mounted onto a 2 mm thick cardboard plate. The internal air pressure within the cells, and thus the bending, increases from top to bottom. The cell is 40 mm.

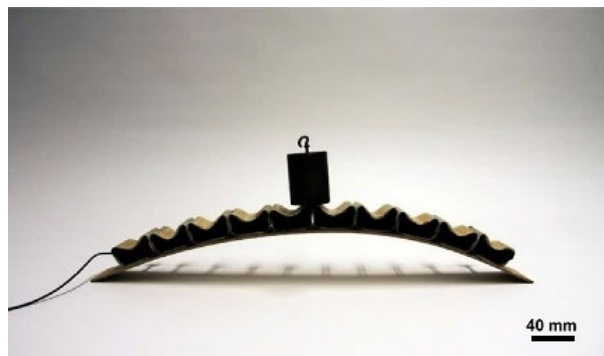


FIG. 3.20: Physical prototype of the cellular actuator, mounted onto a 2 mm thick cardboard plate. Already with internal cell pressures below 4 bar the actuator is capable of lifting a weight of 0.5 kg. Adapted from (Mader et al. 2020b).

The capability to function as a bending actuator for a compliant shading device is demonstrated by a physical demonstrator. The cellular bending actuator is attached to a Flectofold prototype with a 420 mm midrib span.

FIG. 3.21 shows the successful actuation of the structure with increasing inner cell pressure. The cellular actuator proved its capability to actuate a 2-dimensional compliant kinetic system. It can bend the Flectofold midrib and activate the curved-line folding pattern lifting the flaps. The bending is introduced uniformly over the entire midrib, no specific reinforcement or adaptation of the Flectofold is needed. In addition, the system is self-contained. It therefore does not require a substructure or bulky actuators in the vicinity, as is the case with electric motors or pneumatic pistons. In these first tests, a 90° folding angle of the flaps was not yet achieved. To improve the performance of the actuator a refinement of production process to increase the accuracy of the individual cells could improve the achieved results.

As the properties of the cellular actuator arises from the complex interplay of various also counteracting parameters such as wall thickness and hinge design, the maximum vertical sidewall angle, volume, material, as well as maximum pressure, the use also in larger-scale applications should be feasible as well. Beyond the connection of the developed cellular actuator to a 2-dimensional compliant mechanism shown here, the cellular design principle has further potential. With a more sophisticated pressurization concept and cell design, the actuation of more versatile motions as uniform and unidirectional bending is possible. Additionally, the pressurization of cellular structures bears the potential to also influence and control of a stiffness of a system. A further outlook is given in the subsequent chapter in the integration on the variable stiffness concept as well as in chapter 3.1.3.



FIG. 3.21: Physical prototype of the single cell row actuator actuating the 2-dimensional compliant shading device Flectofold. With increasing pressure from top to bottom the midrib of the compliant shading system Flectofold bends further and thus causes the folding of the flaps. Adapted from (Mader et al. 2020b).

3.1.2 Variable stiffness of cellular structures

The pressurized cellular structure of plants not only allows for actuation. Furthermore, the turgor has a distinct influence on the stiffness of thin-walled plant tissues. The following will explain the basic underlying mechanisms of turgor-based stiffness in plants and describe the abstraction and transfer to a technical demonstrator. The result is a compliant cellular actuator capable of varying its stiffness.

3.1.2.1 Search for analogies in biology

Especially for non-lignified tissues with large, thin-walled cells the stiffness of the tissue depends to a great extent on the turgor. The higher the turgor the higher the measured stiffness of the plant tissue. Typical objects of studies are the parenchyma of potatoes (Brusewitz et al. 1989; Finney and Hall, JR. 1967; Niklas 1989; Nilsson et al. 1958) or apples (Lin and Pitt 1986). Also, petioles of herbaceous plants, such as *Caladium bicolor*, have been the object of related investigations (Caliaro et al. 2013). These studies validate and quantify the influence of the turgor on the stiffness. A shortage of water leads to reduced turgor and therefore reduced stiffness. This shows in hanging leaves as for *Caladium bicolor* in a wilting experiment (see FIG. 3.22). As a result of extreme loss in water content, plasmolysis occurs. This means the cell protoplasm detaches from the cell wall, which causes wilting and subsequently mechanical failure (Lang et al. 2014).

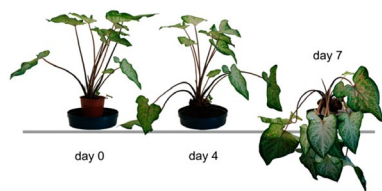


FIG. 3.22: Decreasing stiffness with reduced turgor becomes apparent in a wilting experiment carried out with *Caladium bicolor*. Habitus of well-watered plants (day 0) compared to habitus of plants without watering for 4 and 7 days, respectively. (Caliaro et al. 2013)

The stiffness of these plant tissue arises from the interplay of the turgor and the cell wall. Fully moisturized tissues of different plants show turgor pressures between 0.1 and 2 MPa (Karam and Gibson 1994). The cell walls that have to withstand these high turgor pressures are made from a composite material. The primary cell wall consists of a network of microfibrils that are connected to each other by hemicellulose tethers. It carries most of the tensile stresses introduced by the turgor (Pagitz and Kappel 2014). The Young's modulus of parenchyma cell walls is comparatively low and ranges from 0.1-4 GPa. The Young's modulus of lignified sclerenchyma cell walls is higher and reported to be in between 10 and 35 GPa (Karam and Gibson 1994). The low Young's modulus in combination with the small cell wall thickness explains the high sensitivity of parenchyma tissue to turgor variations. As mentioned above, the effect of turgor on the tissue's apparent Young's modulus has been investigated for different plants and tissues. Especially the pith parenchyma of potatoes has been the object of several studies as it shows a great sensitivity to turgor variations. Potato parenchyma is a suitable tissue for stiffness investigations as it possesses uniformly shaped, almost circular cells with thin cell walls. FIG. 3.23 shows the microscopic image of pith parenchyma from a potato tuber. Table 5 gives a summary of literature values of Young's moduli for parenchyma and the

associated stiffening constant with C^* . It represents the relation between the turgor and the tissue Young's modulus. To obtain the measured tissue Young's moduli at different turgor pressures is needed. The turgor of the tissue can be altered by immersion of the tissue samples into different concentrations of mannitol solutions prior to testing. C^* is then calculated to fit formula (11) that describes the stiffness increase with turgor pressure, assuming a linear relation. It is based on a formula by Nilsson et al. (Nilsson et al. 1958).

$$E_i = E_{ft} + C^* \Delta P_{ft} \quad (11)$$

E_i is the initial Young's modulus (at the beginning of the stress-strain curve) and E_{ft} is the Young's modulus of the fresh tissue. ΔP_{ft} is the turgor pressure in excess to the fresh tissue state. Finney et al. measured an initial Young's modulus of 3.72 MPa increasing by approx. 5 MPa upon a pressure increase from 0.1 to 0.6 MPa (Finney and Hall, JR. 1967). Lin & Pitt presented very similar data (Lin and Pitt 1986). Brusewitz et al. report a comparable Young's modulus for fresh tissue of 3.7 MPa rising to 3.9 MPa after soaking in 0.1 M mannitol solution (Brusewitz et al. 1989). Also, Niklas studied the influence of turgor pressure on potato parenchyma with physical experiments (Niklas 1988). Based on his data a stiffening factor C^* of 17.8 for a turgor increase of 1 MPa can be calculated.

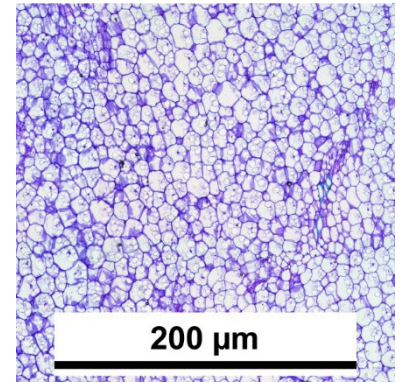


FIG. 3.23: Pith parenchyma from a potato tuber of the species "Annabelle". Photo: PBG Freiburg

Table 6: Re-interpreted literature data on the turgor dependent tissue Young's modulus of pith parenchyma from potato tubers. C^* is the turgor dependent stiffening constant and E_{ft} as the Young's modulus of the fresh tissue.

E_{ft} (MPa)	C^*	source
2.5	3.6	(Nilsson et al. 1958)
3.7	10	(Finney and Hall, JR. 1967)
≈2.2	17.8	(Niklas 1988)
3.6	10.4	(Lin and Pitt 1986)
3.7	≈5	(Brusewitz et al. 1989)

3.1.2.2 Understanding of principles

The internal cell pressure does not alter the intrinsic elastic properties of the cell walls (considering linear-elastic material properties). However, the apparent Young's modulus that is measured on the tissue level is affected. The turgor pressure influences the stiffness of plant tissues through different concomitant phenomena that take place at different levels: On the cell level the individual cells are stiffened by an increased turgor. On the tissue level the mobility of cells in a highly pressurized tissue is reduced, as the cells are pressed against each other. Quantifying the later effect is complex and therefore often neglected. Most studies focus on the stiffening of individual cell units. Nilsson et al. were among the first to derive a formula linking the apparent Young's modulus of parenchyma

to the turgor pressure of the individual cells (Nilsson et al. 1958). They considered the tissue to be composed of individual spherical cells and treated the cell wall as a membrane. In their model they derive the stiffness of the tissue from the potential of the enclosed fluid and the compression or tension inside the cell walls. That is calculated following an elastic surface energy approach. For potato parenchyma Nilsson et al. found the turgor-dependent macroscopic tissue initial Young's modulus to be given by

$$E_i(P) = 3.6\Delta P + 2.5 \quad (12)$$

Niklas considered plant tissues as natural cellular solids. He defined two stiffening agents acting in plant tissues. In this model, the macroscopic properties arise from the cell wall infrastructure (geometric) and the turgor within each cell (physiological). The increase in apparent tissue Young's modulus with increasing turgor pressure is explained by the increasing axial tension within the cell walls. This tension reduces the magnitude of cell wall deformations under an applied external load. From that the following formula for the apparent tissue Young's modulus is derived. The dependence on the turgor pressure results from its influence on the radial and circumferential stresses (σ_{rad} and σ_{θ}) of a pressure vessel.

$$E_t = \frac{\sigma_{\theta} - \nu\sigma_{rad}}{\epsilon_{\theta}} \quad (13)$$

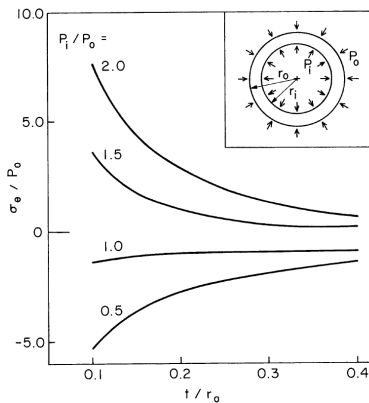


FIG. 3.24: Interrelation of the dimensionless ratios relating to the circumferential stress within the cell wall (σ_{θ}) and the thickness of cell wall (t). Turgor pressure is represented by P_i and outer pressure by P_o . As the ratio P_i/P_o increases, which is equivalent to higher turgor pressures, σ_{θ}/P_o increases, which is related to a higher Young's modulus of the tissue. This effect is stronger the thinner the cell wall in relation to the outer cell radius (t/r_o). (Niklas 1989)

Next to the turgor pressure the cell wall thickness governs the radial and circumferential wall stresses. FIG. 3.24 shows the complex interrelation between the dimensionless ratios σ_{θ}/P_o and t/r_o relating to the circumferential stresses σ_{θ} and the cell wall thickness t . r_o is the outer radius of the cell and P_i and P_o the inner and outer pressure, respectively. P_i/P_o represents the ratio between the inner cell pressure (turgor) and the ambient pressure on the outer cell wall. As P_i increases, the circumferential stresses in relation to the outer pressure (σ_{θ}/P_o) and hence the apparent tissue Young's modulus is expected to increase. A pressure lower than the outer one ($P_i/P_o < 1$) has a destabilizing effect on tissue stiffness. The graph further shows that the sensitivity to the inner pressure P_i depends on the cell wall thickness. It reduces with increasing cell wall thickness, as the flexural stiffness of the wall increases. In the graph σ_{θ}/P_o converges to a value of zero with increasing t/r_o , showing the reduced influence of the turgor pressure on the circumferential stresses with increasing cell wall thickness (Niklas 1989).

Pitt, on the other hand, proposed a model of a hexagonal structure incorporating compressive springs to represent the cell wall's elastic properties. Assuming an iso-volumic cell deformation he deduced an indubitable increase in internal pressure as soon as external loads are applied to the tissue. The

resultant upwards curvature of the stress-strain and pressure-strain curves depict the increasing stiffness of the system (Pitt 1982).

Instead of following an approach based on individual cells, other authors consider the plant tissue as pressurized closed-cell foams, filled with a fluid at turgor pressure. The approach of Karam & Gibson is based on a model for a gas filled closed-cell synthetic foam: The apparent Young's modulus is estimated by summing up the energy required for the bending of the cell edges, the stretching of the cell faces and the compression of the enclosed gas, following the ideal gas law. Karam & Gibson extended this approach taking into account the pre-tensioning effect of the internal pressure. The effect of turgor pressure on the stiffening of plant's parenchyma is modeled based on staggered closed cubic cells, with material concentration at the cell edges. They assume that the main deformation mechanism under an applied vertical stress is the bending of the horizontal cell walls. These are represented by beam elements loaded at their midspan (see FIG. 3.25 and FIG. 3.26). The internal pressurization causes axial tensile forces (pre-stress) in the cell walls and applies a restoring moment that counteracts the bending induced by external loads. This can be used to deduce the apparent modulus of the cellular structure. FIG. 3.27 shows the increase in apparent Young's modulus of the cellular material (E_a) in relation to the not pressurized state with increasing pressure to cell wall Young's modulus ratio, for different relative densities of the tissue. Further, this model shows that the higher the internal pressure and the thinner the cell walls (lower relative density), the stronger the effect of the pressurization on the stiffness of the tissue. From p_0/E ratios (turgor pressure / Young's modulus of the cell wall) of plant tissues found in literature, Karam & Gibson constituted an increase in apparent Young's modulus due to pressurization by a factor of two to five (Karam and Gibson 1994).

Summarizing, the increased stiffness of the plant parenchyma tissue arises from different causes, where the various models focus on different aspects. While some consider cell walls as membranes others see the main source of energy dissipation in the cell wall bending. All account for a higher stiffness with increasing internal cell pressure. The higher pressure introduces a higher tensile pre-stress within the cell walls, effecting the overall stiffness of the tissue positively. Further, the pre-tension induced into the slender cell walls increases their stiffness (geometric stiffness) and further counteracts compression or bending forces. Another aspect that has not been mentioned yet is that the pre-tension due to pressurization increases the individual cells' ability to resist bulking (Niklas 1989). This rises the macroscopic apparent Young's modulus of the overall structure. Next to the effects in the cell wall, the higher energy potential of the fluid increases the energy needed to change its volume and thus increases the apparent stiffness.

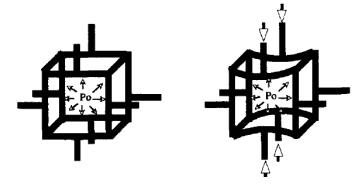


FIG. 3.25: Model of pressurized cubic cell undeformed (left) and deformed (b). Adapted from (Karam and Gibson 1994).

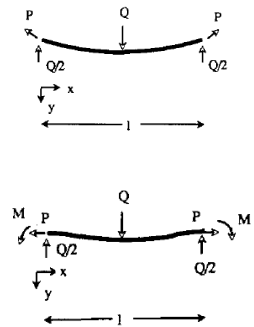
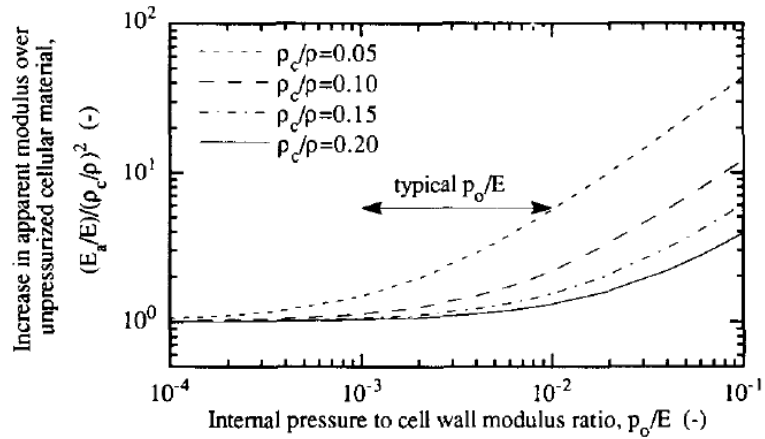


FIG. 3.26: Bending of the cell wall is assumed to be the major deformation mechanism in a vertically loaded cellular structure. With increasing turgor, the pre-tension within the cell walls counteracting the bending increases. This is equivalent to a beam element subjected to an axial tensile force P (induced by the turgor pressure) and loaded by a force Q . This can be used to deduce the apparent modulus of the cellular structure. The upper sketch shows a simply supported bending element and the lower one a fully restrained bending element. Adapted from (Karam and Gibson 1994).

FIG. 3.27: Increase in apparent Young's modulus over that of not pressurized cellular material (E_a) as a function of internal pressure (p_o) over the Young's modulus of the solid material, following the approach of a cell wall as a simply supported bending element. The relation is plotted for different relative densities of the cellular material ρ_c/ρ .
 ρ_c - density of the cellular material
 ρ - density of the solid material
 (Karam and Gibson 1994)



3.1.2.3 Abstraction; dissociation from biological model

Moving from the biological role model to a technical cellular structure, some aspects regarding the pressure medium need to be considered. Depending on the choice of pressure medium, different phenomena will dominate the stiffening effect through increasing internal pressures. In plants the fluid that fills the cells is incompressible in nature. This means the deformation caused by the application of an external force will be iso-volumic. The only possibility of reconfiguration is through cell wall stretching. As changes in cell volume due to elastic deformation of the cell wall are proposed to be negligible (Pagitz and Kappel 2014) an applied external load distorting a closed compartment away from the best pressure volume ratio, indubitably leads to an increase in internal cell pressure, which further increases the energy potential of the fluid. In the case of a compressible pressure medium, the volume of the cell can change as a result to external loads. Due to compressibility of the pressure medium a certain compliance will always be present in pneumatic systems. For both types of pressure medium, an increase in stiffness with increasing pressure, arising from the higher energy potential and the pre-stress in the slender cell wall, is given. Due to the above-mentioned advantages, air offers as a pressure medium in a technical application, such as a low-maintenance and lightweight design, and as low pressures will be sufficient, the focus in the further considerations remains on air as a pressure medium.

Vos et al. developed an analytical model for a pressurized cellular structure with perfectly hexagonal cells. Utilizing an energy approach relating the work needed to alter the volume of the pressurized compartment to the mechanical work imposed by an external force, they calculated the stress-strain behavior of a pressurized honeycomb foam. The individual cells were represented by rigid walls, connected with frictionless hinges in the corners. The stiffness of the structure therefore arises solely from the pressurized fluid filling the cells. The work needed to alter the volume of a cell is given by

$$W_{use} = \int_{V_i}^V P_i dV - P_a(V - V_i) \quad (14)$$

V_i = initial volume, P_i = inner cell pressure, P_a = ambient pressure

Assuming that the inner cell pressure is kept constant by a pressure regulator in the technical application, the formula above can be written as

$$W_{use} = (P_i - P_a)(V - V_i) \quad (15)$$

This expression shows that for the same volume change more work is required the higher the inner cell pressure. The overall increase in stiffness with the cell differential pressure ($\Delta P = P_i - P_a$) is linear. However, the relationship between stress and strain of a pressurized cellular structure is highly non-linear and stiffness increases with increasing (positive) deformation (see FIG. 3.28) (Vos et al. 2011).

These considerations show that the stiffness of a technical cellular structure can be controlled by the internal cell pressure, analogue to the turgor pressure in plants. This is possible independent from the pressure medium, and the principle can be transferred to the pressurized cellular actuator developed above. However, to add the feature of pressure-dependent variable stiffness some modifications to the geometry are necessary.

For the single cell row as presented in the previous chapter, a pressure change is associated with a change in configuration. For the pentagonal cell geometry that represents an anthropomorphic polygon, possessing a mouth (inward facing vertices), the pressure increase is limited also by the snap-through of the adjacent cell walls. However, the stiffening phase takes place at elevated pressures past the deformation phase. FIG. 3.29 shows the different phases for a pentagonal cell developed by Gramüller et al. (Gramüller et al. 2014). During the deformation phase at low pressures, the cell distorts out of its unstressed manufacturing shape. With increasing pressure, the sidewalls tilt outwards, increasing the angular hinge distortion (side wall tilting angle) $\Delta\alpha$. With increasing pressure, the maximum distortion value is approached asymptotically. When the angular distortion of the side walls reaches approx. 90% of the maximum distortion angle it is designed for, the transition phase begins. Here the stiffening of the cell begins, and only minor distortions occur. In the final stiffening phase further deformations of the cell are minimal, but a further rise in pressure increases the stiffness of the structure. So, for a single row cantilever, as considered so far, it can be stated that the higher the pressure the higher the stiffness. However, a substantial stiffening required to provide sufficient stiffening to

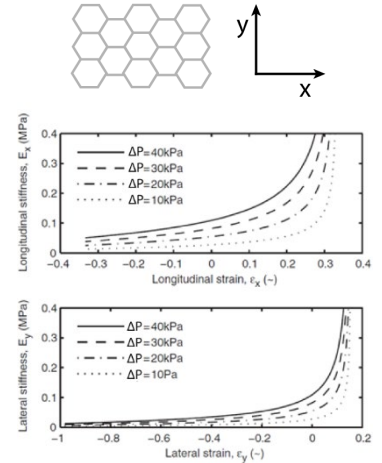


FIG. 3.28: Longitudinal (x-direction) and lateral (y-direction) stiffness of a pressurized, perfectly hexagonal honeycomb structure with increasing strain at different pressure levels. The graph depicts the non-linear relationship between stress and strain in the two principal directions. Further it shows the linear dependency of the stiffness on the cell differential pressure ΔP ($\Delta P = P_i - P_a$). Adapted from (Vos et al. 2011).

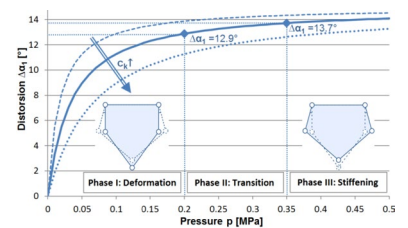


FIG. 3.29: Pressure-dependent angular distortion $\Delta\alpha$ of an exemplary single cell. With increasing pressure $\Delta\alpha$ approaches the maximum distortion angle of 15° it is designed for asymptotically. Additionally, curves with different geometry dependent hinge stiffness factors c_k are plotted. With increasing hinge stiffness, the curve flattens. In all cases sufficient stiffening through the internal pressure takes place after major distortion. Adapted from (Gramüller et al. 2014).

external loads, takes place only in the stiffening phase and is always associated with the state of maximum volume.

To overcome this limitation, a second, diamond-shaped cell row that counteracts the deformation of the given pentagonal cells upon pressurization, will be added (see FIG. 3.30 (A)). This step decouples the angular cell wall distortion from the pressure applied and allows higher internal cell pressures at any desired configuration. The resulting design resembles the cellular structures for shape morphing developed by Luo & Tong rather than the pentagonal and hexagonal (Luo and Tong 2013a; Pagitz et al. 2014). The decisive factor is the pressure difference between the upper and lower cell compartment. This enables to utilize the stiffening potential of a high internal cell pressure also at small or without angular distortions of the sidewall. Furthermore, the second cell row offers the potential to create bending in the opposing direction and thus broadens the possible range of target shapes and applications scenarios (see FIG. 3.30 (C)). This potential has been emphasized before (Gramüller et al. 2014; Pagitz et al. 2014; Pagitz and Kappel 2014). However, so far, no investigation that focuses in greater detail on the stiffening potential exists.

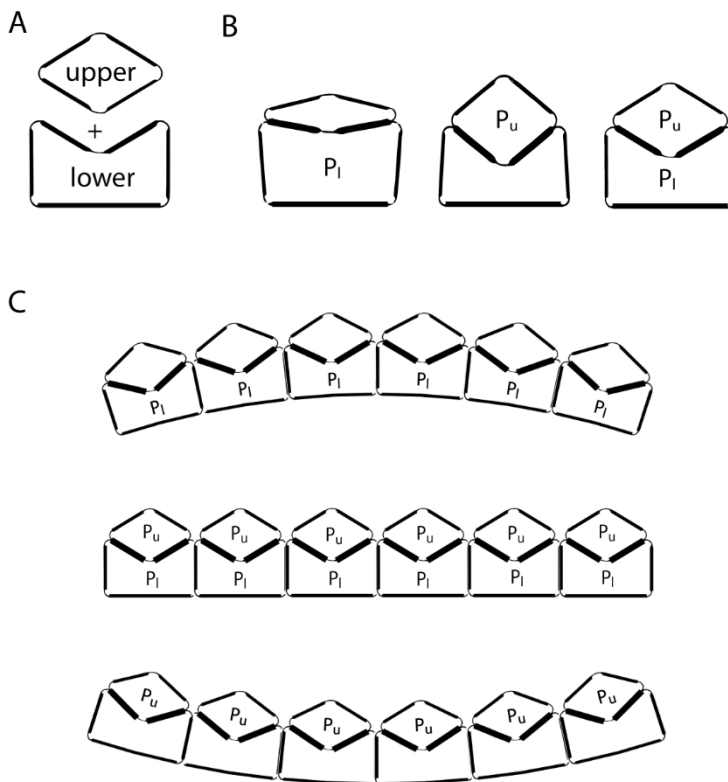


FIG. 3.30:

(A) To decouple pressure from deformation, an additional upper, counteracting, cell compartment is added to the pentagonal lower cell.

(B) Pressurization of the different cell compartments causes opposite geometrical deformations. Thus, a pressurization of both cell compartments with the equivalent pressure ratio allows elevated internal cell pressures also with no geometrical shape change.

P_l – lower cell pressure

P_u – upper cell pressure

(C) Assembled in a double-cell row the cellular actuator allows for positive as well as negative curvature and the stiffening potential of high internal pressures can be utilized in any configuration.

3.1.2.4 Check technical feasibility & prototyping

The purpose of this section is to elucidate the variable-stiffness potential of a cellular double-rowed actuator numerically and physically. This exploratory investigation took place independent of the application in a 2-dimensional compliant shading device. Still, the cell dimension and maximum angular distortion were chosen to potentially fit a large-scale Flectofold prototype. Details on exemplary Flectofold measures are given in (Körner et al. 2018). Accordingly, a cell width and depth of 80 mm was chosen for the adaptive stiffness prototype. With this size, the actuator would span a Flectofold-midrib of approx. 1 m with about 12 cells. The cell dimensions and cell wall thicknesses of the built prototype are shown in FIG. 3.31. The hinge geometry and thickness were designed for the necessary angular distortion for a midrib curvature achieving a 90° folding angle in the hinges of the flaps. For the FEA the same approach as in the previous chapter, using shell elements to represent the cell wall, was followed. The physical prototype made from GFRP was fabricated following the same manufacturing process as described above (see also appendix A1).

As a first step, the pressure ratio between the upper and lower cell row was determined. This ratio allows applying elevated internal cell pressures without causing an angular distortion at the hinges and therefore no bending distortion of the actuator. In a FE simulation the internal cell pressure of a single double-cell was incrementally increased on either the upper or the lower cell compartment. The resulting angular distortion of the initially vertical sidewall were measured and sidewall tilting angle α of the lower hinge was calculated. The results are displayed in FIG. 3.32. The graph shows the non-linear relation between internal cell pressure and angular distortion. While a pressurization of the upper cell compartment (P_u) causes an inward tilting of the sidewalls, pressurization of the lower compartment (P_l) results in a distortion in the opposite direction. Further, the graph shows that higher pressures are needed in the upper cell compartment to achieve the same absolute angular distortion as for pressurizing the lower cell compartment. Despite the non-linear relation, the mean pressure ratio between the two cell compartments was calculated, as in the experimental setup the precision of the pressure regulator (VPPE-3-1-1/8-6-010-E1, Festo Vertrieb GmbH & Co. KG, Esslingen, Germany) is limited. Further, pressure applied with this mean pressure ration ($p_l/p_u = 0.8$) to the upper and lower cell compartment respectively, showed only minimal sidewall angle distortions. The results are plotted in the graph as well. To achieve an optimal balance, the ratio might have to be adapted as a function of pressure. As the focus of this investigation is on the pressure-dependent variable stiffness, the mean ration of 0.8 is precise enough to set a straight starting configuration at different pressure levels.

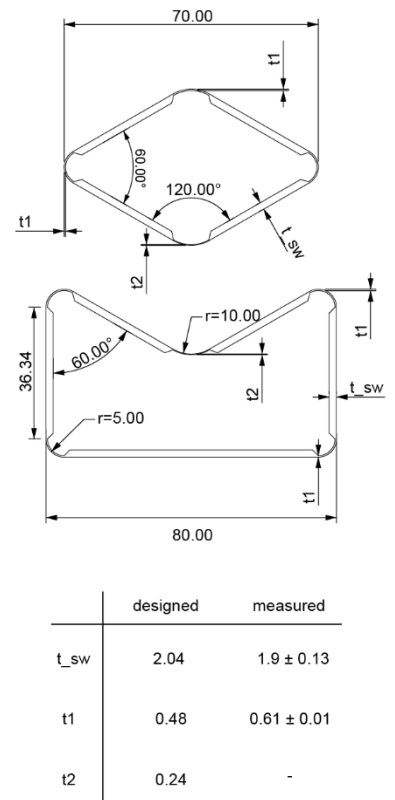
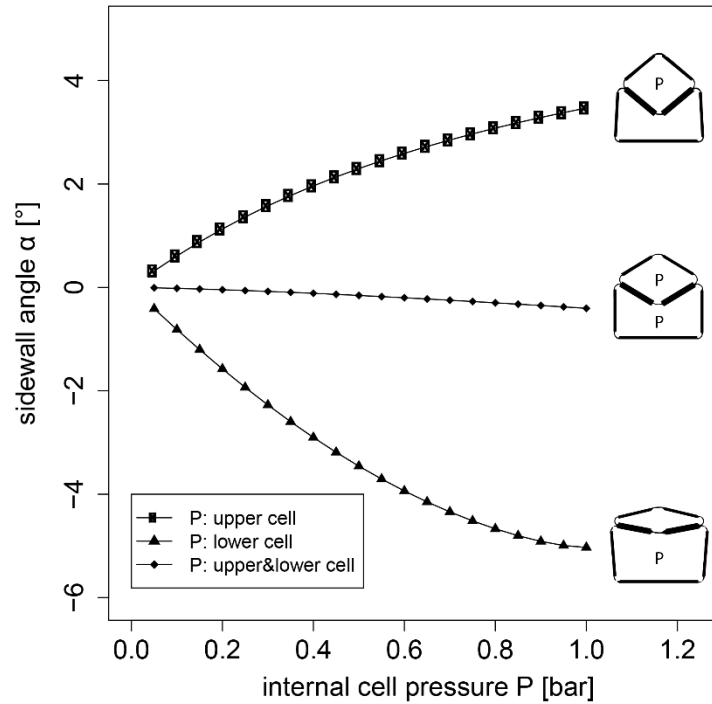


FIG. 3.31: Dimensions and cell wall thicknesses of the double-cell with an upper and lower cell compartment. All measures in mm.

FIG. 3.32: Pressure-angular distortion relation for a double-cell with two compartments. Pressurization of the upper compartment causes an inward tilting, pressurization of the lower compartment an outwards tilting of the sidewalls. Pressurization of both chambers with a specific pressure ratio enables elevated internal pressures with no angular distortion. The ratio between upper and lower compartment is 0.8. The abscissa shows the pressure of the upper cell compartment.



To quantify the stiffness variation, a bending test was conducted with different inner cell pressures in a physical experiment as well as in numerical simulations. In both approaches, the inner cell pressure was increased stepwise from 0 bar up to 1 bar for the upper and from 0 bar up to 0.8 bar and lower cell compartment. The physical test set-up is shown in FIG. 3.33. Analogue to the physical experiments, in the FEA the displacement of the supporting points is restrained in the vertical direction and a load of 50 N is applied in the center. Furthermore, a symmetry condition is applied to the central vertical cell wall to fix horizontal displacement. The pressure within the hydrostatic fluid elements inside the cells is kept constant, equivalent to the proportional pressure regulator controlling the pressure in the physical experiment. The orthotropic material properties of the GFRP are considered to represent the physical system as accurately as possible. The orthogonal material properties as well as further experimental details are given in appendix A2. Only one prototype of the cellular actuator was built, therefore no standard deviation is shown in the graphs. The reproducibility of the results for the single prototype was assured for a medium pressure level of 0.40 bar/0.32 bar. A load of 35 N is applied, and the displacement measured in three independent tests. The mean value is 15.46 ± 0.17 mm, thus the standard deviation of 1.12% proved to be negligible. FIG. 3.34 and FIG. 3.35 display the results of the physical bending tests and the FE simulations graphically.

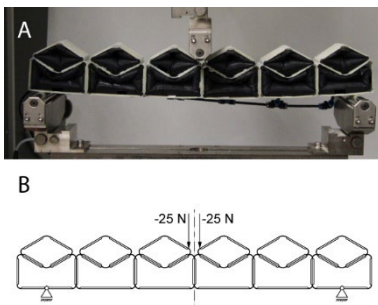


FIG. 3.33: Support conditions of the physical (A) and numerical (B) bending experiment to assess the pressure dependent stiffness of the double-row cellular actuator.

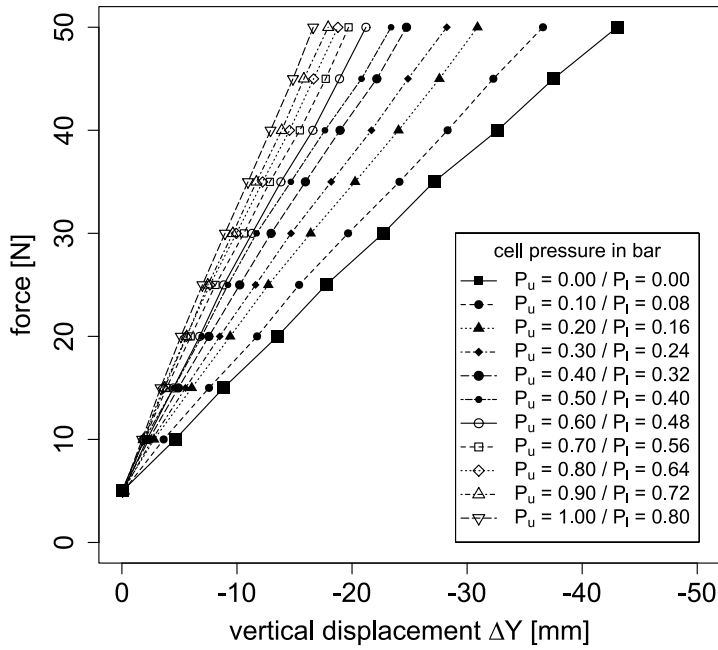


FIG. 3.34: Results of the physical bending tests with the double-cell actuator. Shown is the maximum displacement (ΔY) at different inner pressures in the upper (P_u) and lower (P_l) cell compartment.

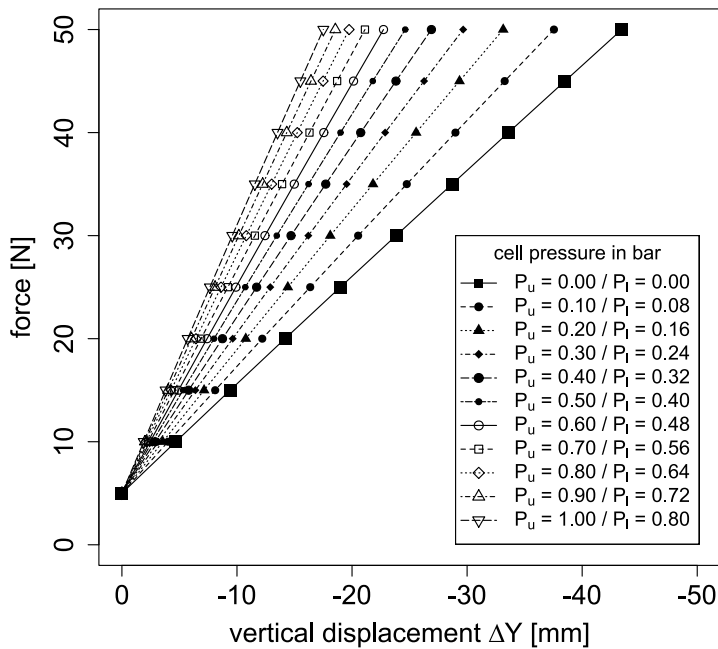


FIG. 3.35: Numerical results of the FE-simulations for the double-cell actuator. Shown is the maximum displacement (ΔY) at different inner pressures in the upper (P_u) and lower (P_l) cell compartment.

The obtained force-displacement curves of the physical experiment and the FEA are in good agreement. A direct comparison is shown in appendix A3. With increasing pressure levels, the induced deformation decreases clearly. This shows the increased stiffness of the structure due to the higher internal cell pressure. The vertical displacement at a force of 50 N reduces from approx. 43 mm without pressurization to approx. 17 mm when 1.0 and 0.8 bar are applied to the upper and lower cell compartment, respectively. So, the stiffness of the cellular actuator at an applied bending force of 50 N increases by a factor of 2.5 as result of a pressurization. The maximum vertical displacement ΔY is slightly lower for the physical experiment at all pressure levels. This may result from the manufacturing process leading to deviations in the hinge geometry (compare FIG. 3.31). Although the measured hinge thicknesses were used in the simulation, other derivations in the geometry may have occurred, or the assumed material properties need to be adjusted. Nevertheless, the trends and relative stiffness changes induced by the pressurization are nearly identical. Appendix A3 summarizes the measured values as well as the structure's increase in apparent bending modulus by the factor E^* at the different pressure levels for the physical demonstrator and the FE simulation in comparison. E^* is calculated by dividing the vertical displacement of the not pressurized state by the vertical displacement of specific pressure level. FIG. 3.36 shows the increase in stiffness with the different pressure levels concisely, and it becomes apparent that the stiffness (more specific E , as J remains constant) increases linear with pressure.

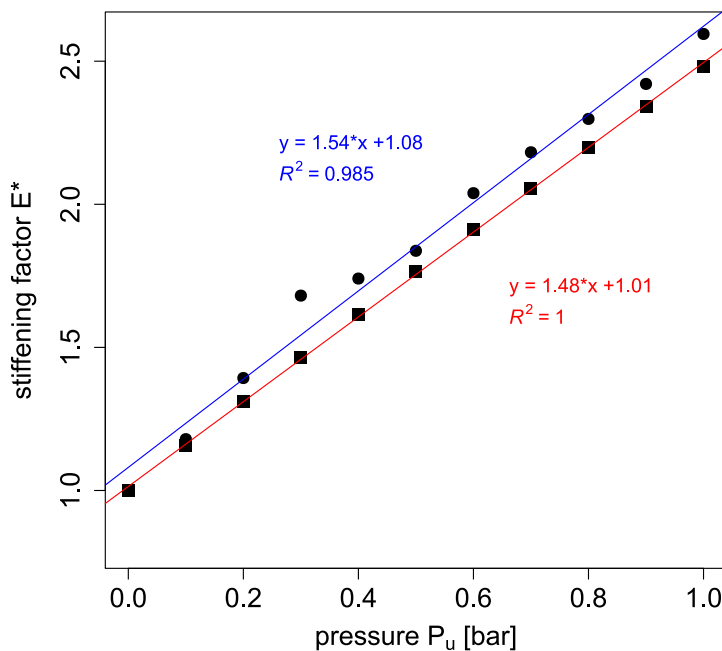


FIG. 3.36: Increase in apparent modulus of the variable-stiffness cellular actuator represented by stiffening factor E^* .
Simulation results: red & squares
Experimental results: blue & circles

Interestingly, the achieved increase in stiffness by a factor of 2.5 lies in the range of the stiffening factor of 2-5 calculated by Karam & Gibson for typical turgor pressure to cell wall Young's modulus ratios of plant tissues (Karam and Gibson 1994). However, many aspects differing the examples need to be considered, such a scale, different pressure mediums as well as geometry. The observed linear increase in stiffness with pressure is in line with the findings of e.g. Nilsson et al., Niklas and Vos et al. presented above (Niklas 1988; Nilsson et al. 1958; Vos et al. 2011). FIG. 3.26 shows graphically the linear increase in stiffness with pressure at a given strain level for the results of Vos et al. (Vos et al. 2011).

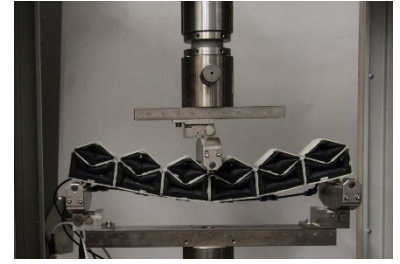


FIG. 3.37: Deformation of the variable-stiffness cellular actuator prototype under an applied vertical load.

FIG. 3.37 shows the deformation of the cellular structure during the bending test. The applied point load does not result in a perfectly uniform bending of the structure. Nevertheless, a similar pressure-driven stiffening behaviour is expected when a uniform surface load is applied. For the test set-up of the bending test, the lower cell compartments are counteracting the applied vertical load, as their volume is reduced by the bending. If an oppositely oriented vertical force was applied, the upper cell row would be the one counteracting the resulting reduction in volume.

The stiffness increase in this experiment is solely attributed to the higher energy potential of the compressed air and thus the linear increase in stiffness is to be expected. As the pressure is kept at a constant value during the experiment, the air does not get compressed during the volume change. Closing the valves in a system, trapping the pressure medium inside the cell, should lead to a stronger increase in stiffness. This is as additional energy is required to compress the pressure medium to allow for the volume reduction taking place during the bending of the cellular structure. In this case the stiffness depends also on the resulting deformation. For this closed valve approach that waives the active control of the pressure level during deformation, the air tightness of the system is elementary and a basic requirement for the control of deformation and stiffening. Even small leakages would result in a pressure loss and unpredictable system behaviour.

3.1.2.5 Improved product

The suggested variable-stiffness cellular actuator consisting of a double-cell row with two counteracting cell compartments allows the decoupling of internal pressure and deformation. Therefore, stiffness can be altered independent of the configuration. Further, the actuator can achieve a positive as well as a negative curvature. FIG. 3.38 shows the bending capability of the actuator and FIG. 3.39 demonstrates the stiffening potential by the internal pressurization. The pressurization of the cells clearly reduces the deformation caused by an applied external load. The experiments showed that stiffening effect is

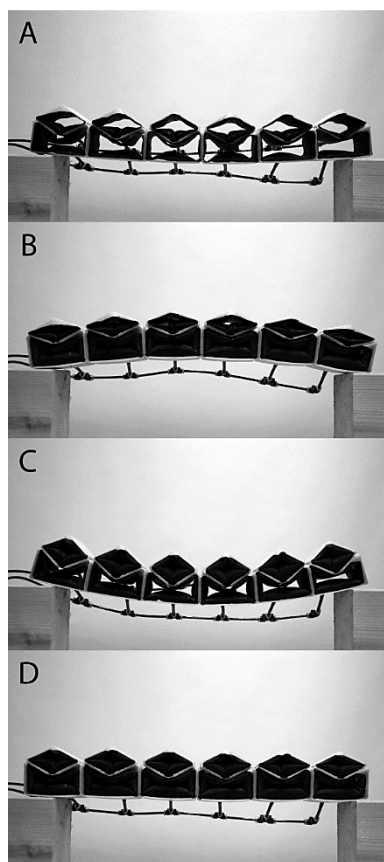


FIG. 3.38: Deformation range of the variable-stiffness cellular actuator. The configuration ranges from the not pressurized neutral state (A), to hogging bending caused by pressurization of the lower cell row (B) and sagging bending caused by pressurization of the upper cell row (C). Through the pressurization of the upper & lower cell row with the equivalent pressure ratio a neutral state can be achieved also by increased cell pressures (D). Cell width = 80 mm.

proportional to the inner cell pressure. With an inner cell pressure of 1 bar the stiffness of the variable stiffness cellular actuator increased by a factor of 2.5. The inner cell pressure is limited by the load bearing capacities of the containing pouches and cell walls. In general, pneumatic systems are limited to a pressure of 6 bar. As the pressure within this experiment are comparably low, there is further potential to increase the stiffening effect.

Pressurized cellular structures like this variable-stiffness actuator are lightweight, have strong shape changing capability and are energy efficient. However, pressurized cellular structures come with a high complexity. They consist of many small parts that in themselves are compliant. On the other hand, the additional cells for the variable stiffness approach also comes with the potential for sophisticated motion patterns. More advanced shape changes than a bending motion are possible by the double-row design. Within a two-dimensional cellular structure with a complete merging of structure and actuator with several cell layers would also allow for bidirectional reconfiguration from flat to double curved surfaces (Pagitz and Kappel 2014).

3.1.3 Further considerations & outlook

In to following a combined outlook on the development of the joint-free cellular actuator as well as the introduced variable stiffness concept is given.

Within the first part of this case study, it has been shown that a rod-shapes cellular actuator can be applied to a 2-dimensional Flectofold prototype and actuate it. Further studies could focus on more in-depth insights on the potential and the limitations of the system to be used in other shading devices. Here the specific requirements of the different applications are essential. Some first thoughts on that topic will be given in the conclusive comparison of the two case studies (compare chapter 4.1). Also, to what extent this stiffness variation achievable influences the stiffness of the compliant system it actuates, needs to be assessed in future investigations. In general, the forces and stiffness variation generated depend strongly on the pressure that can be applied to the cells. And this in turn depends on the actuation angle that needs to be achieved by the compliant hinges and the maximum pressure the pouch and cell can bear.

More detailed technical topics for the further development of the pressurized cellular structure are regard the used material. For higher pressures a different pouch system might have to be developed as e.g. proposed by Gramüller et al. with an elastomeric, flexible pouch and rigid end cap design at the cells' open ends (Gramüller et al. 2014). Further, when actuating 2-dimensional elements, adjustment for limiting the stronger cell deformations taking place within the two outermost cells should be considered in greater detail.

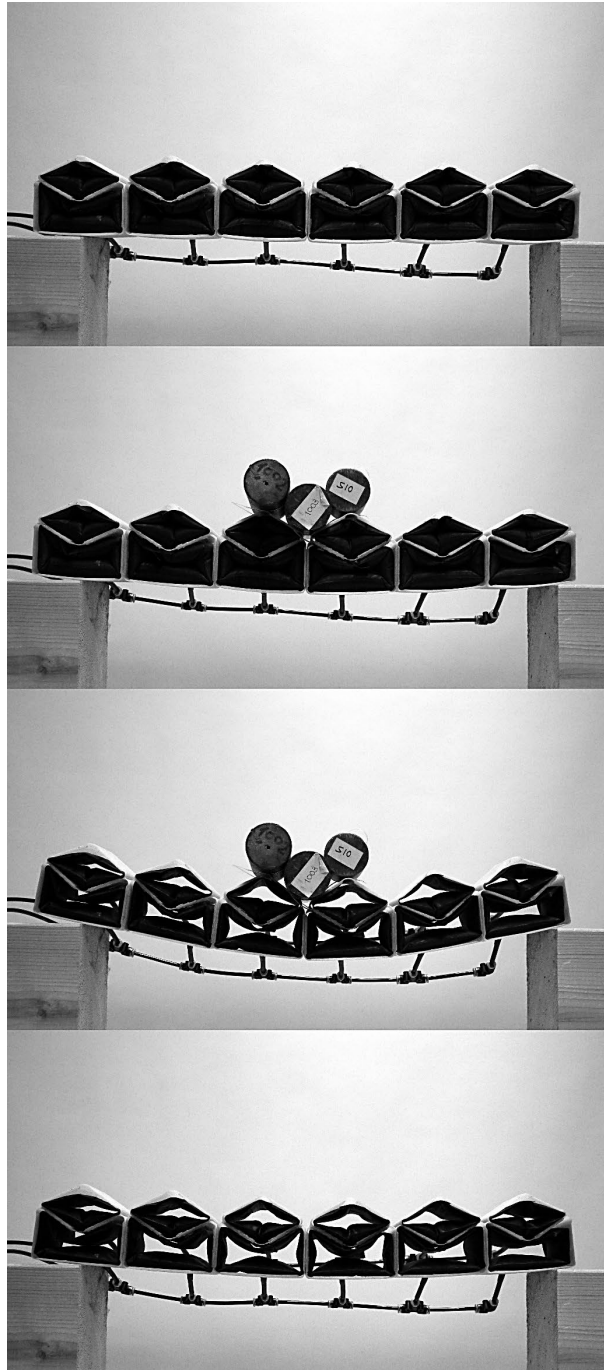


FIG. 3.39: Demonstration of the stiffening effect through the cell pressurization. The variable-stiffness cellular actuator was loaded with 25 N. Cell width = 80 mm.

Due to the necessary dimensions and tubing, a rod-shaped cellular actuator is a clearly visible structure when attached to a compliant shading device. This can be seen in FIG. 3.2. and might not meet the aesthetic demands. A smooth, uniform surface of the cellular structure could be potentially achieved by using flexible fillings e.g., from foam or elastomer. Also, the device could be attached from the opposing side. Nevertheless, the great advantage of the biological cellular role model is not met by this approach. In plant there is no distinction between structure and actuator. An approach closer to the biological role model of *Sesleria nitida* might be the miniaturization of the cells and a placement within the hinge zone to be actuated. The feasibility of this approach, especially when it comes to manufacturing, however, needs to be investigated. Another approach can be to extend the cellular actuator itself to a more 2-dimensional target shape. The cellular actuators materialized so far are conceptualized to generate 2-dimensional deformations on single-curved surfaces. However, also the generation of double-curved surfaces is possible as illustrated in FIG. 3.40 (Pagitz and Kappel 2014).

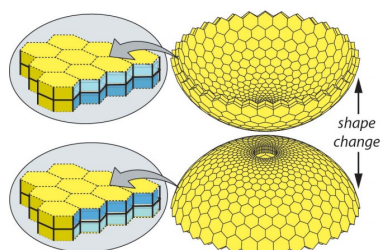


FIG. 3.40: 2-dimensional shape change achieved by a pressurized cellular structure (dark blue: high pressure; light blue: low pressure). Adapted from (Pagitz and Kappel 2014).

3.1.4 Conclusions

The investigation of the biological role model, the bulliform cells of *Sesleria nitida*, provided new insights into its underlying functional principles of leaf folding. Experiments showed the presence of a pre-stress state within the leaf that causes its folding upon turgor loss. The FEA based on the morphometric data determined for the model plant revealed that an opening of the leaf segment due to the turgor pressure within the bulliform cells is possible. A turgor variation in the magnitude as measured for plants under drought stress causes an opening and closing motion in the simulation that is well within the range of results from a drying experiment on *Sesleria nitida*.

In the biological role model, the volume change with varying turgor within the cells causes the observed plant motion. Based on these insights a cellular actuator was developed. This bio-inspired cellular actuator consists of individual pressurized GFRP cells with compliant hinges. With increasing inner cell pressure, the straight side walls of the cells tilt outwards. Arranged in a single cell row actuator the bending of the structure takes place upon pressure increase. A first prototype also proved capable of actuating a Flectofold demonstrator with a 420 mm midrib length.

In a subsequent step, this single-row cellular actuator was developed further. Besides the advantages when it comes to the creation of motion, the cellular approach allows a pressure-dependent variation of the system's stiffness. This approach is inspired by the turgor dependent stiffness of some plant tissues. For thin-walled tissues the apparent tissue modulus depends to a great extent on the inner cell pressure. It is increased by the

higher energy potential of the contained fluid and the increased cell wall pre-tension caused by higher turgor. This is accompanied by secondary effects such as an increased resistance of the individual cell walls to bending and buckling (for bending or compression loads respectively), as well as pre-stresses created on the tissue level.

This principle is transferred to the developed technical pressurized cellular structure. To be able to use the effect of higher internal pressures for stiffening at any actuator configuration, a second, counter-acting cell row is added. This allows the actuation in both bending directions. In the new double-cell row actuator, the deformation is controlled by the pressure ratio between the upper and lower cell compartment. Thus, bending and stiffness can be controlled independently. Physical as well a numerical investigation demonstrated the stiffening potential of the system. The numerical and physical results showed good agreement. In the above-mentioned experiments, the pressure was held at a constant value by a proportional pressure regulator and thus did not change with deformation. An internal cell pressure of 1 bar more than doubled the stiffness of the prototype.

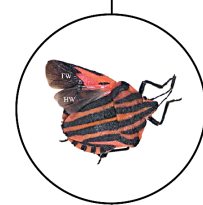
The advantages of pressurized cellular systems are a high force, high stroke, a good energy efficiency and a low self-weight. Further they are distributed and can offer an adaptive stiffness. As the deformation is pressure-based, the technical system can provide instant actuation with no or little time-delay. However, pressurized cellular systems come with the cost of an increased design and fabrication complexity. The complexity of actuation becomes insignificant when the potential it offers exceeds. Therefore, applications where the flexibility of a cellular design offers are fully exploited are preferable. As every cell contains an individual pouch, it can potentially be driven with an individual pressure. To keep the increasing complexity for the control and number of pressure regulators within limits, groups of cells can be formed. In return more complex motions are enabled. This suggests the application of cellular structures within larger(meter)-scale morphing applications.

3.2 CASE STUDY II: INTEGRATED PNEUMATIC ACTUATION AND ADAPTIVE STIFFNESS

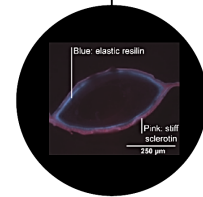
The example of the pressurized cellular structure demonstrates the widespread potential of pressurized composite structures. However, the cellular nature also inherently leads to a complex structure with a 3-dimensional fabrication process and a high number of individual pressure compartments possessing separate pouches. Therefore, a simplified approach where pneumatic pouches are integrated directly and completely into a fiber-reinforced composite laminate set-up is pursued within this case study. This allows a simple and fast, one-step production of 2-dimensional compliant kinetic systems with an integrated inconspicuous actuation.

However, for this approach of integrating pneumatic pouches into glass-fiber epoxy composites specific technical challenges are imposed. Initial tests showed a delamination between GFRP layers caused by the inflation of the pneumatic pouch. Thus, the brittleness of the stiff epoxy matrix that is needed for the load bearing capacity poses a problem. To overcome this issue, potential solutions are looked for in nature. A top-down (techno-pull) approach is pursued to solve this specific problem (see FIG. 3.41). This time, inspiration is sought within the realm of arthropods. The biological screening as well as the biological investigation took place in cooperation with the with EvE at the University of Tübingen. The materialization of the developed products happened with the support of the ITFT at the University of Stuttgart and the DITF. The development of an FRP with an integrated pneumatic pouch will be presented in the following. Within this chapter not only the process of bio-inspiration will be described but further the feasibility of integrated pneumatic pouches to actuate compliant kinetic systems will be explored. In line with the previous chapter, in a second step, the additional realization of an adjustable stiffness with the given approach is explored.

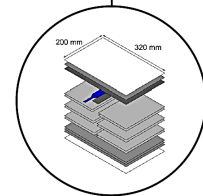
TECHNICAL PROBLEM



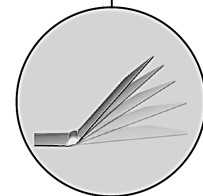
search for analogies
in biology



understanding of
principles



abstraction:
dissociation from
biological model



check technical
feasibility / prototyping



improved product

INTRODUCTION
TO MARKET

FIG. 3.41: Steps of the top-down biomimetic development process in animal-inspired case study II. Based on (Speck and Speck 2008).

3.2.1 Bio-inspired integrated pneumatic actuation

Due to their numerous advantages, there have been many approaches to integrate fluidic-driven actuators directly into the built-up of composite structures. Philen et al. embedded a network of pneumatic artificial muscles (PAMs) into an elastomeric matrix to create a composite capable of performing large structural shape and stiffness changes (Philen et al. 2006b). However, PAMs inherently have a cylindrical shape, making them bulky and hard to integrate into flat systems. Further, their fabrication process is comparatively complex. Therefore, Chillara et al. developed a morphing panel with channels for fluids molded directly into a fiber-reinforced elastomer composite. This results in a simple fabrication process. At the same time, it allows for a lower composite thickness, as the channels can have an arbitrary cross-section. The composite consists of a fluidic layer, a constraining layer, and a mechanically pre-stressed layer which induces an initial curvature. The composite decreases its curvature as the pressure channel lengthens in-plane due to pressurization (Chillara et al. 2016). Especially in the field of robotics, similar simple production approaches for a fluidic-driven actuation have been developed. So-called soft robotics possess pneumatic or hydraulic chambers that are directly integrated into a soft material, such as rubber. An increase in pressure within these chambers creates the desired motion. Similar to the just described approach, the actuation principle is based on the expansion of the soft material due to the forces created by the increasing internal pressure. To strategically control the motion the deformation is constrained in certain areas for example by added fiber-reinforcement. Contrary to that, pneumatic actuation principles can be based on the inextensibility of fluid filled pouches. In such a system maximizing the volume of the fluidic chamber results in an in-plane shortening of the pouch upon inflation. This can be utilized to attain a desired motion (Yao et al. 2013). Following this principle, Sun et al. worked on so-called pouch motors that can potentially be used to actuate self-assembling robots. These pouch-based actuators can easily be designed and produced 2-dimensionally in an automated manner (Sun et al. 2015). However, all the concepts described above are limited to a comparably small scale. A first step towards large-scale applications is the kinetic lightweight surface element developed by Schmid & Marinitsch. They glued a piece of woven pneumatic pouch onto a glass-fiber-metal composite panel. The curvature of the panel could then be varied by the pressurization of the pouch (Schmid and Marinitsch 2017).

In the following, a biomimetic approach to integrate pneumatic pouches into a load bearing FRP is described. As part of this process physical tests are carried out on specimens. Their angle-pressure relationship, reproducibility, and long-term behavior are characterized. To determine the predominant parameters and

physical boundaries of the system, an analytical model based on the energy approach, taking into account the bending stiffness of the surrounding composites layers, is laid out. Consequently, a parametric study with numerical calculations is carried out. Finally, prototypes of compliant shading devices with an integrated pneumatic actuation are fabricated and tested.

3.2.1.1 Technological problem statement

The aim of the following development is the complete integration of a pneumatic actuation into the laminate set-up of an FRP. This approach protects the pneumatic pouches from environmental influences, eases fabrication, and creates a slick, homogenous appearance. For the application to large-scale compliant shading devices, the material system must provide a certain stiffness to ensure the necessary structural performance, as well as the reverse motion by the stored elastic energy. Consequently, a glass-fiber-reinforced plastic (GFRP) consisting of thermoset (epoxy resin) and woven glass fibers was used. Within the concept of inextensible (stiff) material, motion is created by in-plane shortening as a result of pressurization. The principle is depicted in FIG. 3.42. With increasing internal pressure, a fluid-filled compartment thrives towards maximizing its volume. In the case of exactly the same bending stiffnesses around the fluid chamber, the formation of a circular cross-section with maximum volume causes a symmetric in-plane shortening of the composite plate. If the bending stiffness of the upper and lower layer surrounding the compartment differ, the more compliant side deflects to a greater extent. This causes a rotation of the attached plate ends in the respective direction. If the pouch is placed within the discrete hinge zone of concentrated compliance the resulting angular displacement actuates a folding motion. This is equivalent to the folding in the compliant hinge zones of the Flectofold and Flexafold. By placing a more widespread pouch with different chambers across the surface of a plate, a quasi-uniform bending of the plate can be created (FIG. 3.43). Such a bending motion is for example required for the bending of the Flectofold midrib.

However, first initial tests with a glass-fibre epoxy composite showed strong delamination between the individual plies when the pneumatic pouches were pressurized (see FIG. 3.44). This can presumably be attributed to the brittle nature of the epoxy matrix used. To overcome the problem of delamination a techno-pull (top-down) biomimetic process is pursued to find inspiration for a solution. The following investigation on the actuation will focus on the behaviour of a single distinct hinge zone. However, the underlying principle is identical for actuating a distinct hinge folding and creating uniform plate bending through integrated pneumatic actuation.

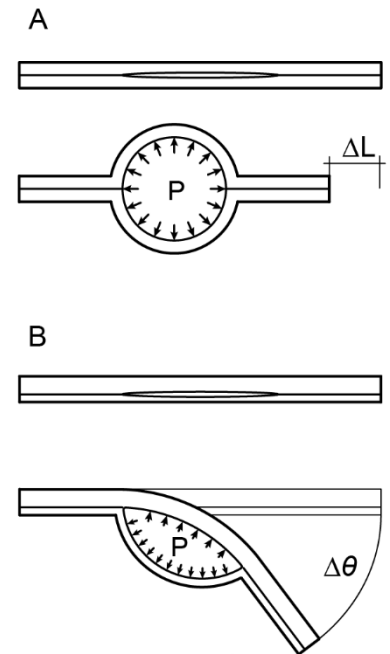


FIG. 3.42: Functional principle of integrated pneumatic pouch. Upon pressurization the fluidic chamber thrives towards maximizing its volume, thereby creating (A) a translational motion of the attached end plates in the case of an identical wall stiffnesses and (B) a rotary motion of the attached end plates in the case of differing wall stiffnesses. Adapted from (Mader et al. 2020a).

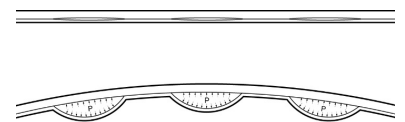


FIG. 3.43: Following the same principle quasi-uniform bending can be created in a plate with distributed compliance. Therefore, a pouch with several chambers or several individual pouches are required.

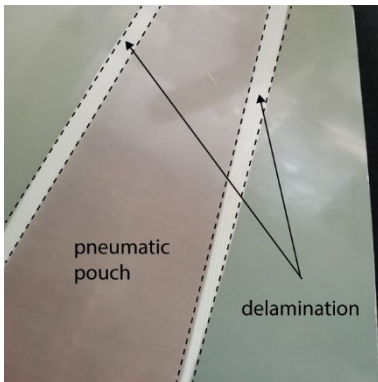


FIG. 3.44: Pure GFRP samples with inserted pneumatic pouch show delamination of the adjacent layers. Photo by Larissa Born / ITFT.

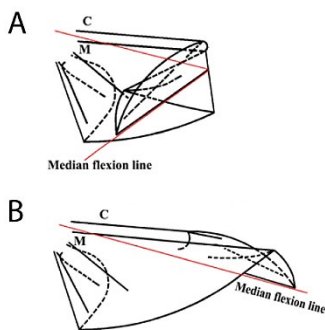


FIG. 3.45 The pressure-supported unfolding process of the hind wings of *Dorcus titanus platymelus*. (A) schematic representation of the folded wing and (B) of the completely unfolded wing.

C: Costa

M: Media posterior

Scale bar = approx. 5 mm

(C) Photograph of the hind wings in the process of unfolding. Adapted from (Sun et al. 2014).

3.2.1.2 Search for analogies in biology

The challenge to be addressed is to overcome delamination in pressurized FRPs with a brittle thermoset matrix (see FIG. 3.44). Therefore, inspiration is sought within the realm of stiff natural composites. Natural composites are e.g., the plant cell wall or the cuticle of insects. Interestingly, insects do not possess a vascular system with a closed blood circulatory system, but their body cavity is filled with hemolymph. The hemolymph pressure can be controlled by muscular activity. Several examples exist where a change in hemolymph pressure is utilized to create motion. A prominent example is the spider's leg. Cuticle is composed of chitin fibers within a chitin matrix. Therefore, fluidic actuation mechanisms in insects are searched for principles that reduce stress concentrations within the composite and enable a robust, reliable, and durable actuation.

Sun et al. investigated the hydraulic mechanism responsible for the unfolding process of the hindwings in the giant stag beetle (*Dorcus titanus platymelus*). As the large hindwings of certain insect orders such as Coleoptera are vulnerable to damage, they can be folded and stored underneath the stiff forewings. This usually includes longitudinal as well as transverse folding along folding lines present in the wing membrane. For most species wing extension of longitudinal folds presumably is driven by the contraction of muscles attached to the basalar or subalar sclerite of the wing base. The wing itself lacks any muscles. However, the wing veins are connected to the hemocoel. It is proposed that a hydraulic system based on temporarily increased hemolymph pressure might aid in straightening of the transverse folding at the costal margin (see FIG. 3.45). In retinal camera experiments Sun et al. found that the two cross folding joint expansions correspond to two detectable main pressure peaks in the hemolymph pressure. This data strongly suggests a partition of increased hemolymph pressure of the wing veins in the hindwing unfolding. It is likely that the hydraulic mechanism is utilized to overcome a spring mechanism in the cross-folding joint. For the beetle, the usage of a hemolymph pressure-based actuation offers different advantages. Small muscles in the abdomen are sufficient to control the pressure and generate a high-power output. Further, the hydraulic pressure medium allows an easy transfer of the energy over long distances. This reduces the required muscle mass. Additionally, as the muscles are located within the abdomen, this allows a greatly simplified wing design (Sun et al. 2014).

Thus, wing veins are subjected to internal pressurization due to the described hydraulic mechanism proven for *Dorcus titanus platymelus*, but also due to the connection to the hemocoel itself. As the wing veins are part of the wing membrane, a natural fiber composite, in the following their ultrastructure will be examined in more detail, searching for stress reducing mechanisms.

3.2.1.3 Understanding of principles

Although the functional principle of actuation in the technical application is not entirely the same as for the pressurized wing veins, the ultrastructure of the wing vein still represents an interesting inspiration as it is a pressurized composite structure. The investigations are carried out on the minstrel bug *Graphosoma lineatum italicum* (see FIG. 3.46). Transmission electron microscopy (TEM) revealed a sandwich structure of the wing membrane across the transverse section of the wing membrane. It consists of an exterior dorsal and an exterior ventral layer enclosing a central layer of proteinaceous material (Schieber et al. 2017).

The wing veins are part of the natural fiber composite of the wing membrane. FIG. 3.47 shows a detailed image of a semithin section through the leading vein of the hindwing of *Graphosoma lineatum italicum*. It is hollow and built from an outer sclerotized exocuticle layer and a soft resilin-bearing inner layer of endocuticle. The wide field fluorescence microscopy (WFM) shows clearly that the exocuticle exhibits a strong signal of sclerotin, making it stiff. The endocuticle, however, lacks sclerotin fluorescence, but shows strong fluorescence in the short wavelength range. This indicates an enhanced resilin content, which is a rubber-like protein. This resilin-bearing endocuticle present in the inner layer of the vein, may aid to the reduction of stresses and avoid delamination at increased internal pressures.

Resilin occurs where extra elasticity is needed, for example in mobile joints or folds. Its distribution pattern usual is coherent with the wing folding pattern (Haas et al. 2000). Further it can store elastic energy. Next to that, it plays a major role in the actuation as it is utilized in the leverage, storage, and release of elastic energy to promote motion. Although no proof exists that the wing unfolding process in *Graphosoma lineatum italicum* is promoted by an increase in hemolymph pressure the veins are still connected to the hemocoel. Wing veins of other beetles and insects of other orders possess a similar ultrastructure. For Dragonflies, resilin is present in the inner endocuticle as well, where it is supposed to increase energy storage and material flexibility, reducing the risk of wing damage (Appel et al. 2015). The resilin fulfills multiple functions. Through its high extensibility it avoids material failure during folding or flight.

3.2.1.4 Abstraction

For the abstraction of the construction principle of the biological role model, the stiff exocuticle is considered equivalent to stiff GFRP layers and the soft, extensible resilin within the endocuticle is represented by elastomer layers that are added around an integrated fluidic chamber. By encasing the pressurized cavity in an elastomeric layer, the delamination that would otherwise occur can potentially be avoided. The according



FIG. 3.46: *Graphosoma lineatum italicum* with a partially extended fore- and hindwing (FW and HW, respectively) on the left and folded on the right. Head-body length: 13 mm. The dotted line marks the leading vein of the hindwing. Adapted from (Schieber et al. 2017).

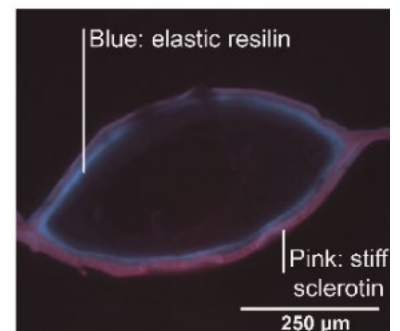


FIG. 3.47: Semithin section through the leading vein of the hindwing of *G. italicum*. The wide field fluorescence microscopy (WFM) image shows red (sclerotin) and blue (resilin) channels only. Adapted from (Schieber et al. 2017).

material set-up for the technical prototype is shown in FIG. 3.48. In a discrete hinge zone, a pneumatic pouch is placed within the laminate. As explained previously pressurization will cause a rotary motion due to the asymmetric laminate set-up (compare FIG. 3.42). The glass-fiber layer in the more compliant chamber wall is placed to avoid the elongation of the elastomer layer and in that way enforce rotation. The dimensions and thickness of the test samples are chosen according to the large-scale compliant shading demonstrators as the Flectofold and Flexafold. Both compliant systems possessed a span of approx. 1 m and 15-20 mm wide hinge zones.

A graphical summary of the inspiration, abstraction and testing process for the integrated pneumatic actuation is given in FIG. 3.49. The diagram also contains other aspects inspired by insect wings that aided in the development of the compliant composite hinge. Next to the elastomer surrounded fluidic chamber developed here, this includes the material composition in the less stiff hinge zone that is characterized by a higher elastomeric content at the compression zone, as well as a gradient transition in GFRP thickness between the compliant and stiff plate section.

3.2.1.5 Check technical feasibility/prototyping

To check the technical feasibility, prototypes are produced and the angle-pressure relationship, the reproducibility, as well as the long-term behavior of the system are characterized. Further, an analytical model based on the energy approach, considering the bending stiffness of the surrounding composite layers, is developed to determine the predominant parameters and physical boundaries of the system. Further, the system's feasibility to drive compliant shading devices is assessed.

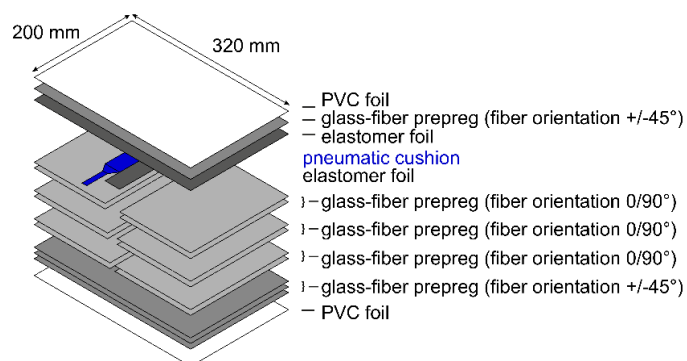


FIG. 3.48: Material set-up for an integrated pneumatic actuation where the pneumatic pouch in a compliant hinge zone is surrounded by elastomer, analogue to the resilin bearing endocuticle in wing veins. (Mader et al. 2020a)

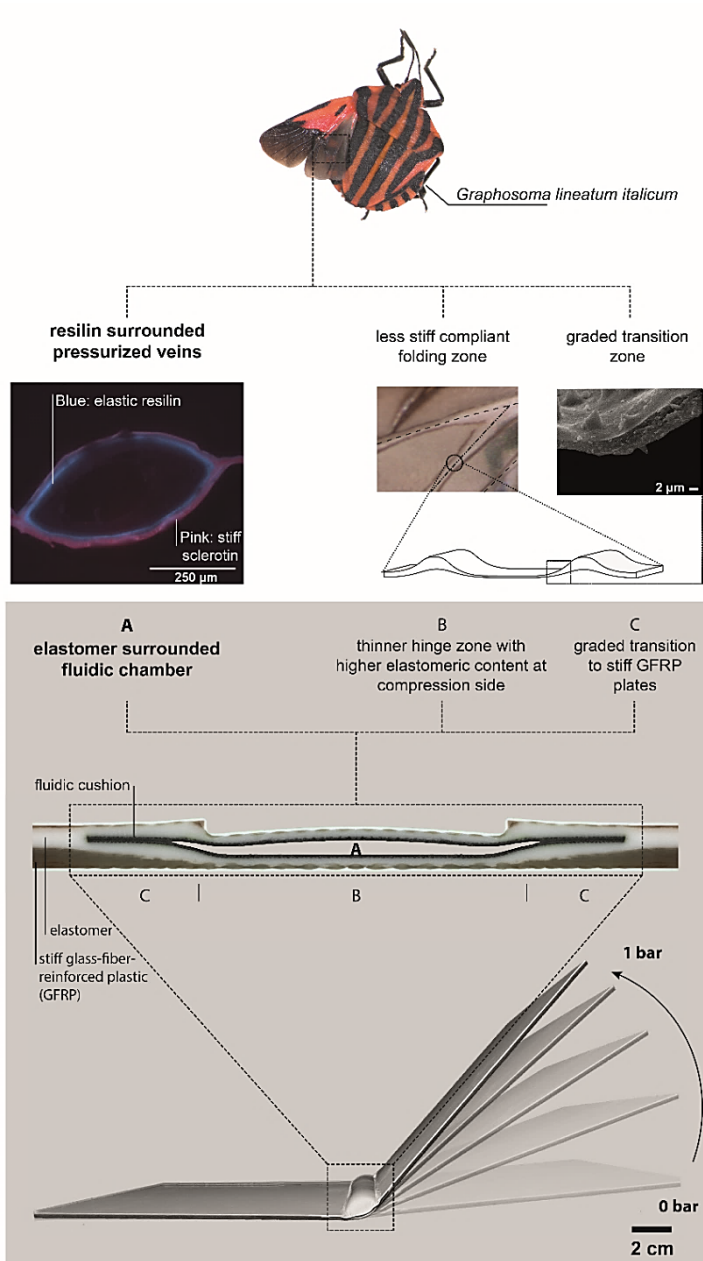


FIG. 3.49: Abstraction process from the biological role model to the technical abstraction of GFC components with integrated pneumatic actuation. For further details of features labeled (B) & (C) in the image, see Schieber et al. 2017; Born et al. 2017; Sun et al. 2015b).

3.2.1.5.1 Preceding T-peel tests

In a first step, the mechanical properties of the materials used are determined. T-peel tests were performed to quantify the interlaminar adhesion between the various materials used in the composite set-up and verify the positive effect of surrounding for the pressurized pneumatic pouch with elastomeric material. The experimental details are described in appendix B1 and B2. FIG. 3.50 shows the results of the tests and FIG. 3.51 micro-section images of the crack path. The samples for determining the peeling force between the glass fibre-epoxy prepreg layers (P-P) and between the elastomer and the glass fibre-epoxy prepreg layer (E-P) peeled off at the desired interfaces. The measured forces show that the peeling force between two brittle glass-fiber epoxy plies (P-P) is by far the lowest. Determining the interlaminar adhesion between the elastomer layers (E-E) proved difficult, as the crack path did not follow the epoxy layers interface. Instead, the samples peeled off at the interface between the glass fiber epoxy and elastomer layer (Mader et al. 2020a).

The measured values for these samples are therefore in the same range as for the E-P samples. Although no absolute value for peeling force can be given for the E-E samples from the specimen tested, it can still be concluded that the interlaminar adhesion between the elastomer layers is higher than the tensile strength of the elastomer. Further, both (tensile and interlaminar adhesion) must be higher than the interlaminar adhesion between the elastomer and the GFC layer (Mader et al. 2020a).

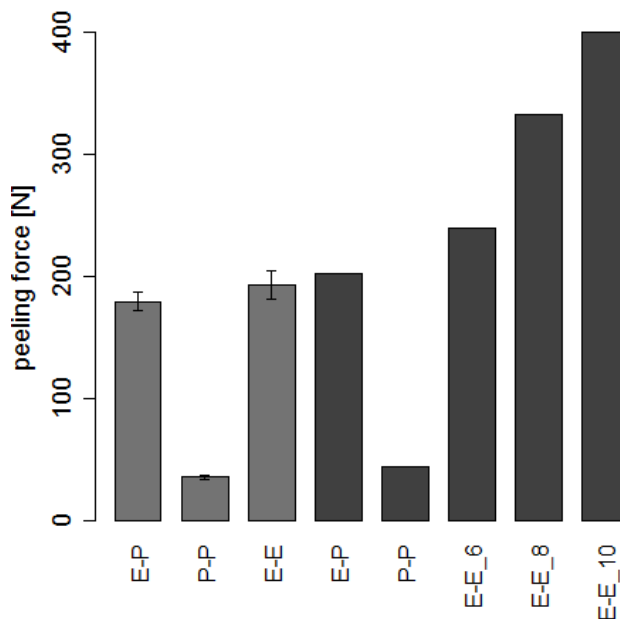


FIG. 3.50: Mean peeling force (light gray). E-P designates specimens characterizing the adhesion between elastomer and GFRP, P-P between two layers of GFRP, and E-E between two elastomer layers. Dark gray columns represent the maximum peeling force for the E-P and P-P samples. For the E-E samples with increasing overall thickness from E-E_6 to E-E_10, the tearing strength is shown as now peeling between the elastomer layers occurred. (Mader et al. 2020a)

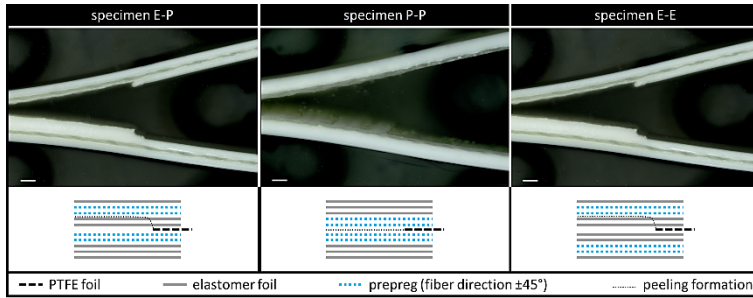


FIG. 3.51: Progression of the peeling for the different specimens E-P, P-P, and E-E. The micro-section images (scale bar = 1000 μm) and a schematic representation of the crack formation are shown. (Mader et al. 2020a)

The adhesion between the elastomer layer is this strong as the cross-linking between the molecules is completed only during the heat pressing, taking place during the sample production. The two elastomer layers cross-link chemically. Consequently, rather breakage than delamination occurs. These pre-tests confirm the stronger interlaminar adhesion between the elastomer layers. Thus, delamination is less likely with the bio-inspired built-up as shown in FIG. 3.48 and FIG. 3.49.

3.2.1.5.2 Angle-pressure relationship

In a next step, samples were produced to assess the relationship between rotary displacement and pressure. For further details on sample production and testing see appendix B1 and B3. The specimens were produced as shown in FIG. 3.48. They are 200 mm deep and 320 mm wide GFRP plates. In the centre they possess a 20 mm wide compliant hinge zone with a reduced thickness and a fiber orientation of $\pm 45^\circ$. Within this hinge zone, a 20 mm wide pneumatic pouch is embedded, placed between two layers of elastomer. The inflation of the pouch triggers a rotary motion of the adjacent stiff plate ends. The degree of rotation achieved depends on two major factors. The stiffness ratio (ratio of bending energies) of the upper and lower sidewalls surrounding the pouch and the overall compliance of the system to the pressure applied.

In the physical experiment, the pressure-angle relationship was measured for different test specimens. The experimental set-up was as shown in FIG. 3.52. The specimen is mounted vertically to avoid the influence of gravity. This also allows for an easier comparison to the mathematical model that does not take gravity into account. The pressure is increased stepwise from 0 to 2 bar in 11 steps, with a holding of 5 min time at each pressure level. During these 5 min at each pressure level, five measurements were taken in 1 min intervals. Due to the viscoelastic behaviour of the elastomer, the actuation angles vary slightly over time. Thus, the five measurements at each pressure level are averaged to define the actuation angle. Additionally, a pausing time 120 min was introduced after each actuation cycle to account for the viscoelastic material behavior. When actuating the specimen, the very first time, the pressure-angle curve changes clearly during the first load cycles. This presumably is a

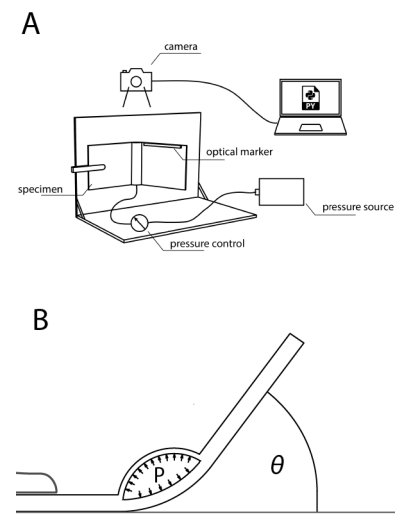


FIG. 3.52: Test set-up for measuring the angular displacement θ upon pressurization. A: (Mader et al. 2020a)

consequence of the pneumatic pouch material sticking to the elastomer what could not be avoided completely during production. To reduce the effect the pneumatic pouch was placed between two PTFE- foils with the same outline. The pressure-angle behavior stabilizes within the first five actuation cycles. Therefore, these cycles are not considered for assessing the angle-pressure relationship. The mean actuation angle of actuation cycle 6 to 15 are used instead. The small standard deviation around 5% shows that the further variation is low.

The graph in FIG. 3.53 shows the actuation angle θ as a function of pressure. The angle-pressure curve shows an asymptotic behavior. The actuation angle θ increases from 0° at 0 bar pressure to a maximum actuation angle θ between 43° and 47° (mean: $44.5^\circ \pm 2.4^\circ$) at 2 bar. The viscoelastic behavior of the elastomer shows in the curves, in form of a small residual actuation angle remaining also after a pausing time of 120 min at zero pressure. However, the residual actuation angle disappears completely after 24 hours. The viscoelasticity becomes apparent in the first loading cycles in particular. The residual actuation angle remaining after the pausing time increases for these and then stabilizes with increasing number of cycles.

The graphs display the result of every specimen individually, as the measured curves for angle-pressure behavior and maximum actuation angle differ for each of the three samples. Although all followed the same production procedure, this can be attributed to the variations of the thickness of the upper and lower sidewalls surrounding the pneumatic chamber (see Table 7). θ is highly sensitive to the bending stiffness ratio of the upper and lower hinge plate section. This is even more evident in the results of the finite element analysis (FEA). For the FEA (ANSYS Mechanical Products Release 17.2) the Young's modulus of the used material and the plate thicknesses were determined in preceding test. For further details see appendix B4. For each of three calculations, the geometry was adapted to the individual dimensions measured for the respective specimen. A non-linear 2-dimensional analysis was carried out using an 8-node structural solid (element number 183) and assuming linear-elastic material properties. The upper and lower plate sections were bonded together, except for the hinge region containing the pneumatic pouch. The mesh of the two plate sections each had three elements across its thickness. The pressure of the pouch was applied in the non-bonded region as a line pressure. The maximum displacement of the plate end was used to calculate the angular displacement by means of trigonometric functions. The commercial FE software allowed to conveniently obtain the behavior of the model over time (stepwise increase in the pressure), while at the same time providing results to verify the analytical model developed subsequently.

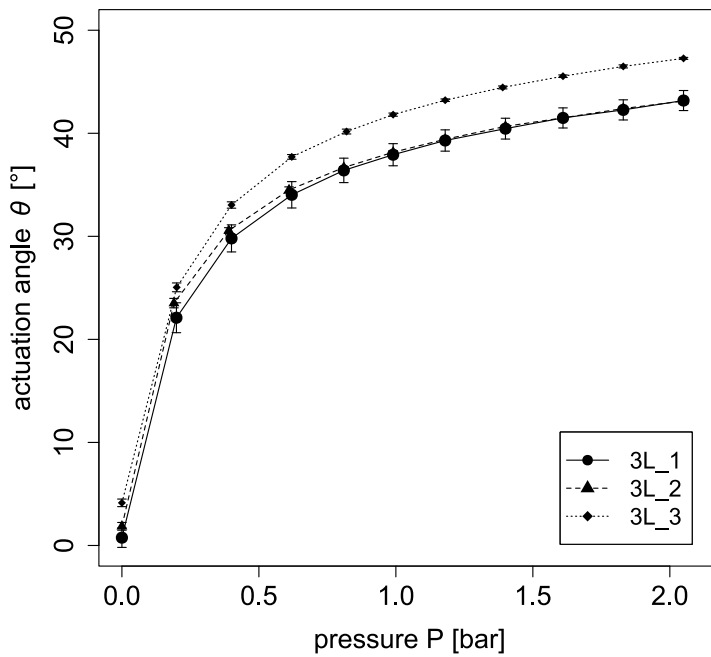


FIG. 3.53: Angle-pressure relationship for the three tested specimens. Shown are the mean values of cycles 5 to 15 with the according standard deviation. (Mader et al. 2020a)

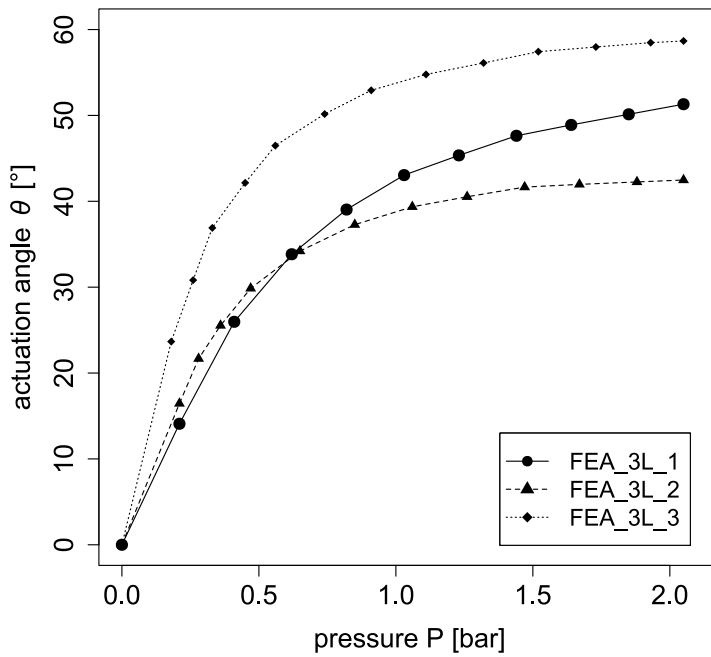


FIG. 3.54: Angle-pressure relationship results of the FEA. The simulation was conducted with the measured plate section thicknesses and experimentally determined Young's modulus of the physical specimen. (Mader et al. 2020a)

The results of the FE simulation are shown in FIG. 3.54. The maximum mean actuation angle measured in the physical tests is $44.5 \pm 2.4^\circ$. That of the simulation using the mean thicknesses of the three samples is 47.2° . Thus, the maximum mean actuation angles are in good agreement with each other. However, the courses of the curves vary clearly. The differences between the physical and numerical results also are apparent in FIG. 3.55. It depicts the direct comparison of the mean actuation angle of the three specimens, in direct comparison to the results of the FEA.

The observed deviations might arise from various causes. Simulations assume an ideal system. As the actuation angle is highly sensitive to various factors, small inaccuracies in manufacturing or in the placement of the pouch are likely to influence the results. The deviations in the thicknesses of the upper and lower plate sections measured for the different specimen will most likely also affect the Young's modulus of the specific plate sections, as the proportions of the material composition will vary in consequence. This is not considered in the simulations. The same holds true for non-linear or viscoelastic material behavior, which presumably effects the physical behavior of the system as well. Further, the fact that the pneumatic pouch possesses 5 mm wide seams on both sides is also not considered for the simulation. Here the pressure is applied directly to the composite over the full pouch length. The seams in the physical experiment could lead to a different inflation behavior, explaining the slightly lower maximum angular displacement and the deviations in the course of the angle-pressure curves. A good agreement between the physical test results and the outcome of the FE-simulations is important for the design of new compliant systems with an integrated pneumatic actuation. Also, the understanding of the influence the main parameters have on the system's behavior is of importance. Therefore, a parametric study was conducted with the help of a developed analytical model.

3.2.1.5.3 Parametric study

To predict the behavior of the system accurately, the bending stiffness of the upper and lower plate sections surrounding the pouch are included in the mechanical model. The deduction of the mechanical model is described in more detail in (Mader et al. 2020a). FIG. 3.56 summarizes the variables of the symmetric system considered. The developed model is based on the theorem of the minimum potential energy to derive the equilibrium position. In the case of the compliant elastic system considered here, which is loaded with a pressure vessel of volume V (representing the pneumatic pouch), the equilibrium position takes the form:

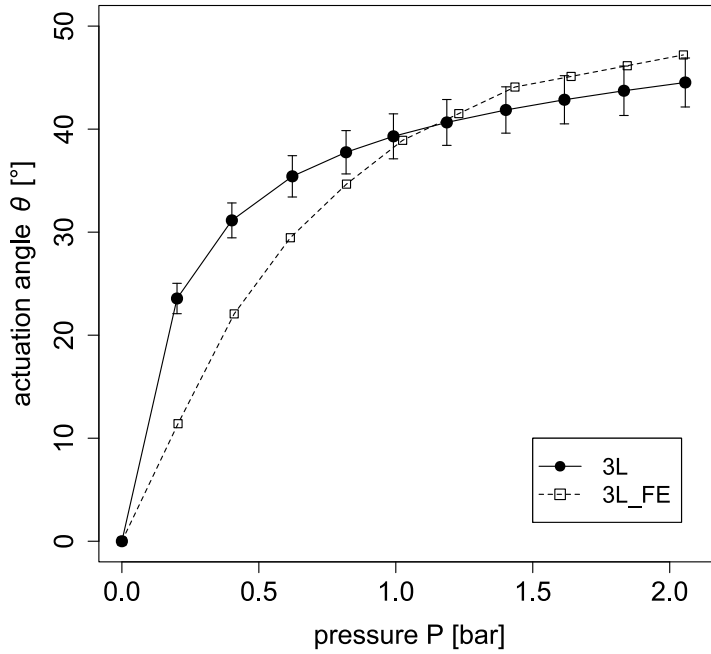


FIG. 3.55: Mean actuation angle at increasing pressure ($n=3$) and results of the FEA with the mean measured thicknesses of upper and lower plate sections. (Mader et al. 2020a)

Designation	3L_1	3L_2	3L_3
Upper plate section in μm (1 layer)	725 ± 12	682 ± 9	576 ± 124
Lower plate section in μm (3 layers)	981 ± 12	788 ± 21	810 ± 25
β	0.16	0.26	0.14
π	24	60	42
θ – prototype	43	43	47
θ – FE simulation	51	42	59
θ – own code	48	42	57

Table 7: Thickness of the hinge plate sections surrounding the pneumatic pouches and the resulting actuation angles θ . All measures of thickness in μm (mean \pm standard deviation) and of angles in $^\circ$. (Mader et al. 2020a)

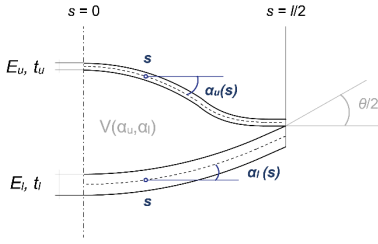


FIG. 3.56: Geometry used for theoretical analysis. (Mader et al. 2020a)

$$(\alpha_u, \alpha_l) = \underset{\alpha_u, \alpha_l, \text{constrained}}{\operatorname{argmin}} (W_{el}(\alpha_u, \alpha_l) - W_P(\alpha_u, \alpha_l)) \quad (16)$$

Where W_{el} is the elastic energy of bending the upper and lower plate section and W_P the work potential of pressure. The constraints over α_u and α_l refer to the above-defined symmetry conditions and the merging of the plate sections at the pouches end. Actuation angle θ is twice the angle at the plate ends of the symmetric system.

To obtain the overall angular displacement θ depending on the pressure P , formula (16) can be written as follows:

$$\theta(P) = 2 \underset{\alpha_u, \alpha_l, \text{constrained}}{\operatorname{argmin}} (W_{el}(\alpha_u, \alpha_l) - W_P(\alpha_u, \alpha_l)) |_{s=l/2} \quad (17)$$

The above equations do not explicitly show the two physical non-dimensional parameters β and π influencing the angle-pressure relationship. β represents the ratio of the bending energies of the upper and lower plate section, π stands for the compliance of the system to the pressure:

$$\beta = \frac{E_u t_u^3}{E_l t_l^3} \quad (18)$$

$$\pi = \frac{3Pw^3}{E_l t_l^3} \quad (19)$$

Where t is the thickness of the upper (t_u) and lower (t_l) plate section, respectively (see also FIG. 3.56). E are the respective Young's moduli and w the width of the pneumatic pouch.

As β and π are the only two physical parameters, the problem can formally be formulated as:

$$\theta(P) = f(\beta, \pi) \quad (20)$$

This shows that the actuation angle θ is a function of the ratio of the bending energies of the upper and lower plate sections and the overall compliance of the system with regard to the pressure. The influence of the parameters β and π on the actuation angle was examined in more detail using the analytical model developed above. It allows easy control of the inputs and outputs. At the same time, a developed 1-dimensional FE-model based on the analytical model, allows a faster calculation than with commercial 2-dimensional FEA used above. For the general overall assessment of the system behaviour the lower accuracy is still sufficient. A Python code (Python 3 with the libraries Numpy and Scipy, Python Software Foundation,

<https://www.python.org/>) was developed to approximate the solution and to plot the actuation angle θ as a function of β and π . The approximation of the equations requires a numerical approach. A Least Square optimization was used to approximate the solution. Each plate was subdivided into elements of the size $ds = l/N$, where N was the number of elements per plate (Mader et al. 2020a).

The actuation angle θ was calculated with β and π ranging from 0 to 0.4 and from 0 to 70, respectively. For the $\beta = 0.18$ and $\pi = 33$ given by the physical properties of the test specimen (see Table 7), the theoretical model described above predicts an actuation angle θ of 45.2. This demonstrates the proper accuracy of this approach.

In order to depict the system behaviour β and π are varied in a parametric study. FIG. 3.57 shows the obtained results graphically. Whenever $0 \leq \beta < 1$, the asymmetry of the bending energies between the upper and the lower plate section causes an angular displacement (actuation angle θ). The graph shows the distinct influence of β and the fundamental role of the ratio of bending energies in the physics of the system. For β -values larger than 0.2, the actuation angle is low and increases exponentially with decreasing β . To increase the maximum actuation angle θ , the stiffness ratio β needs to be reduced and π needs to be increased. This is achieved most effectively by increasing the stiffness difference of the upper and lower plate section by varying the thicknesses (to reduce β) or by increasing the width of the pneumatic pouch (to increase π). Especially the latter has a noticeable influence, as π is proportional to w by the power of three. This knowledge on the systems' behavior can be utilized in the developing process of compliant kinetic systems with integrated fluidic actuation.

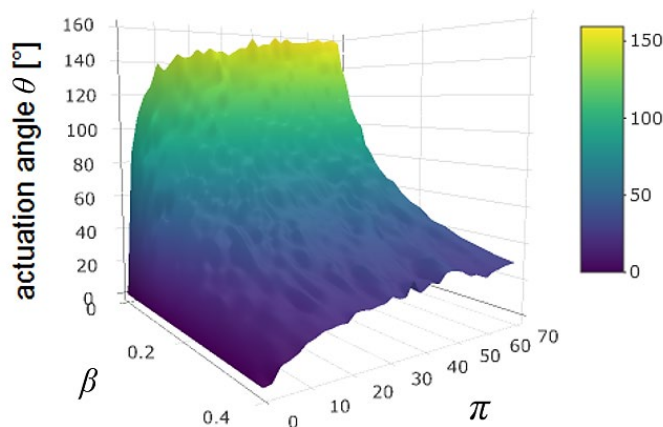


FIG. 3.57: 3D plot of the actuation angle θ , as a function of β and π . (Mader et al. 2020a)

3.2.1.5.4 Cyclic loading

One specimen was subjected to another 500 pressure cycles as a first assessment of the fatigue properties of the developed material system. FIG. 3.58 shows the mean and standard deviation for the prolonged cyclic loading of sample 3L_2. The number of steps and the holding time at one pressure level were adjusted to the increased number of cycles. Five steps with a holding time of 10 sec were used to attain an acceptable testing time. The pausing time between the cycles was set to 60 seconds. After the initial five cycles, only small changes in the angle-pressure behavior occurred. As above, this might be attributable to some viscoelastic effects of the elastomer material. The actuation angle at the same pressure level changes only slightly with increasing number of cycles and the differences become less significant with increasing number of cycles. I.e., the mean actuation angle of cycles 5 to 15 (cycle_005) is significantly different from the mean actuation angle of cycles 85 to 100 (cycle_100) for four of the six pressure levels (namely 0, 0.4, 1.62, and 2.06 bar). The mean actuation angles of cycle 385 to 400 and cycle 485 to 500 differ significantly only for the pressure level of 1.19 bar. Moreover, not all actuation angles of cycle_005 and cycle_500 differ significantly from each other. For more details on the statistical testing see appendix B5. This continuity in the pressure actuation angle relation makes fatigue damage within the sample unlikely as delamination or material damage in the FRP or elastomer due to the increased loading cycles should influence the actuation angles achieved at a certain pressure level.

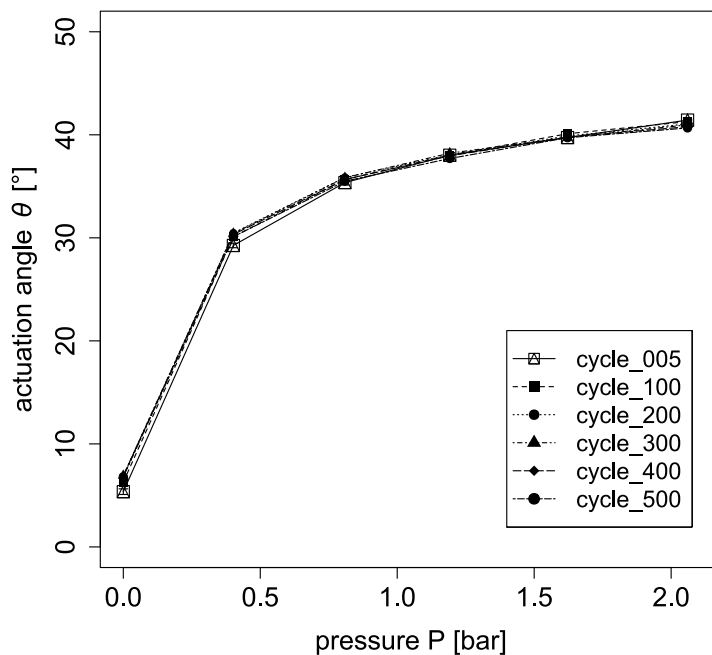


FIG. 3.58: Angle-pressure relationship for specimen 3L_2 after continuous loading for 500 cycles. Mean \pm standard deviation of 11 consequent load cycles. (Mader et al. 2020a)

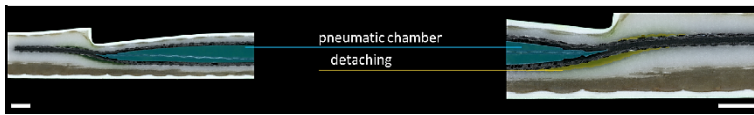


FIG. 3.59: Exemplary micro-section image of an actuation sample that underwent 1000 pressure cycles between 0 and 1 bar. The pneumatic pouch is marked blue, and detachment of the pouch from the elastomer is marked yellow. Scale bars: 1000 μm . (Mader et al. 2020a)

To further exclude that fatigue damage occurred, micro-section images of an actuation specimen that underwent 1,000 loading cycles to 1 bar were made. As visible in FIG. 3.59 the sample does not show any failure in the elastomer. The connection between the pneumatic pouch and the elastomer detached in the outer edge area. This is the area of greatest deformation during the actuation motion. Detaching took place on the upper as well as lower side of the pouch. However, this detachment does not affect the functionality of the pneumatic chamber. The chamber is still sealed airtight by the pouch material. Moreover, no delamination or cracks between the elastomeric layers were found. Thus, plastic damage of the material can be excluded.

The prolonged cyclic loading test shows additional influences of the viscoelastic material behavior. During the first 1-2 cycles, major changes in the angle-pressure behavior took place and again, a residual actuation angle remained after the pausing time with zero pressure applied. In addition, the results of this test varied from the previous test for the assessment of the angle-pressure relationship. The actuation angles achieved here were one to two degrees lower. This can be attributed to changes in the test set-up, such as less pressure steps and shorter intervals of constant pressure. The exact prediction of the angular deflection therefore will prove challenging as the achieved angle will depend on more influences than the applied pressure. These influences may be related to constant effects such orientation relative to gravity, but also may vary over time, such as wind, temperature, or the time-dependent viscoelastic material behaviour of the elastomer.

3.2.1.6 Improved product

The previous chapters showed that by integrating a pneumatic pouch into a laminate set-up of a glass-fiber-reinforced plastic, this pouch can be used to create an angular displacement reproducibly. The next step is the application of this mechanism to compliant kinetic systems. To demonstrate the potential to actuate 2-dimensional compliant mechanisms, prototypes of the shading devices Flectofold and Flexafold with an integrated pneumatic actuation are produced.

The integrated pneumatic actuation principle is first applied to a Flexafold prototype made from GFRP with a span of approx. 1 m. The folding pattern is based on the hindwing folding of beetle wings, which are also the source of inspiration for this material development. The Flexafold folding pattern is constructed of

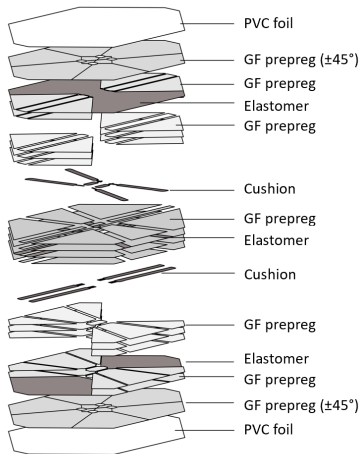


FIG. 3.60: Stacking of the Flexafold prototype with integrated pneumatic actuation. The span is approximately 1 m and hinge zone width 15-20 mm.

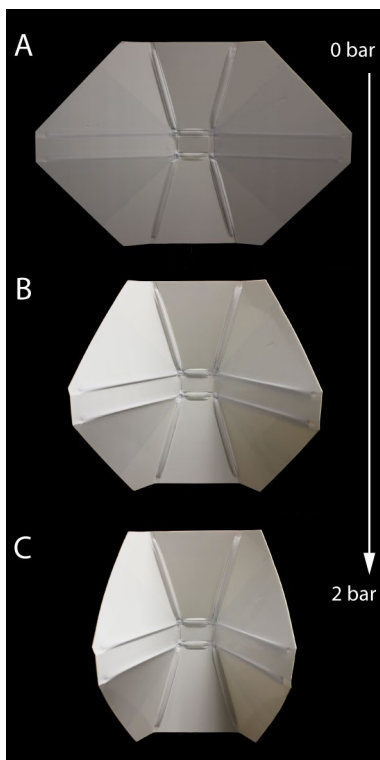


FIG. 3.61: Compliant kinetic shading systems driven by integrated pneumatic actuation. Flexafold at different pressure levels: 0 bar (A), 1 bar (B) and 2 bar (C). Scale bar = 20 cm. Adapted from (Mader et al. 2020a).

straight folding lines. As some of these folds are mountain folds and others are valley folds, the material built up and pouch placement needs to be adapted to the folding direction accordingly. This leads to the slightly more complex stacking sequence of the Flexafold shown in FIG. 3.60. Instead of a closed pneumatic pouch, a PTFE-foil inlay with a width of 30 mm was placed in the material built-up to create an air chamber. This approach makes it possible to avoid the pouch seams and thus also the effects that they potentially have on the predictability of the angular deflection. Also, higher actuation angles may be achieved with this approach. Further, material and a one production step are saved. However, this is at an increased risk of failure, as the redundancy of the pouch material is missing. The connection to the tubing still is realized by TPU-coated nylon fabric.

FIG. 3.61 shows the successful actuation of the Flexafold by the integrated pressure-based actuation system. Increasing pressure inside the air chambers within the compliant hinge folds the Flexafold from an opened, planar configuration to a closed one. However, the complete folding of the system was not achieved yet. An increase in the achievable angular displacement could be attained by different means. One option is the reduction of β (the stiffness ration of upper and lower adjacent layer) or the increase of π (the compliance of the system to the pressure). Another possibility is the placement of two individual pneumatic pouches staggered within one chamber. Another aspect to consider is that within this initial test all pouches were pressurized with the same pressure. In a more refined approach, the individual hinges could be controlled and pressurized individually, as their folding angles are different during the closing process. On the other hand, the different hinges can support each other during the folding process.

In contrast to the Flexafold, the Flectofold possesses curved folding lines. This requires the pneumatic actuation to not only fold the curved hinge-zones but also to bend the adjacent surfaces. Here, the possibility of several actuated hinge in the folding pattern to support each other or be folded passively is not given. As for the fabrication of the Flectofold prototype the hinge width was fixed and the availability of thicknesses of the different sheet materials was limited, the possible stiffness ratios of the upper and lower layer were restricted. Thus, as suggested above, here two pouches were placed on top of each other in the hinge zones to increase the maximum folding angle. This allowed the successful opening and closing of the compliant shading device as shown in FIG. 3.62.

FIG. 3.61 and FIG. 3.62 also shows one of the great advantages of the direct actuation of the folding lines. The system can start from a flat configuration and does not require a pre-fold as is the case for conventional actuation mechanisms. Another advantage of the integrated pneumatic actuation is the low weight, as only

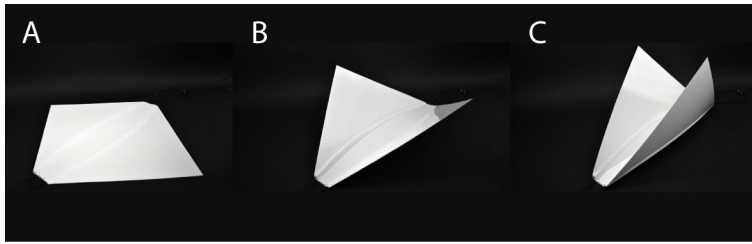


FIG. 3.62: Compliant kinetic shading systems driven by integrated pneumatic actuation. Flectofold at different pressure levels: 0 bar (A), 1 bar (B) and 2 bar (C). Adapted from (Mader et al. 2020a).

the pouches are added to the structure itself. Further, the integration of the actuation happens within the regular manufacturing step. The integrated actuation also enables a self-contained system, where no external supports are needed. The forces are introduced along the entire folding line. Thus, besides the placement of the elastomer, no additional structural reinforcement is needed where the force is introduced.

The curved-line folding could potentially be supported or even initiated by the bending of the midrib. This has been the actuation principle external applied loads utilized so far. For example, a pneumatic pouch is placed between the midrib and a supporting structure, or an in plane compressive force applied to the midrib. A quasi-uniform bending of a plate can also be achieved by a more extensive pouch placed in a plate with distributed compliance (no discrete hinge-zone).

First prototypes showed the feasibility of this approach. FIG. 3.63 and FIG. 3.64 demonstrate the high deformation potential as well as the potential of such systems to bear high external loads. For details on the pouch geometry and laminate built-up see appendix B8. The thickest samples contained 14 layers of 0/90° GF prepreg in the center region plus two additional $\pm 45^\circ$ GF prepreg layers. The large-scale Flectofold prototype for comparison, has a thickness of in total 9 - 11 GF prepreg layers. The actuation via the uniform bending of the midrib and/or flaps is sketched in FIG. 3.65.

The derived plate samples are also the starting point for the next step in the development. This is the integration of an adaptive stiffness feature by an antagonistic set-up.

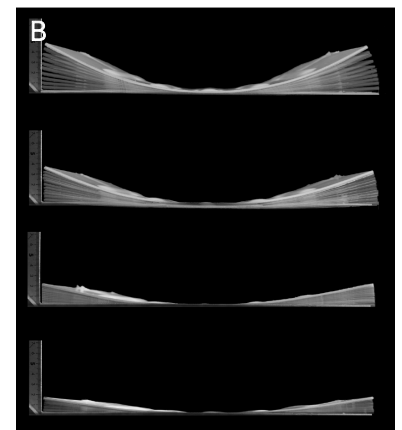
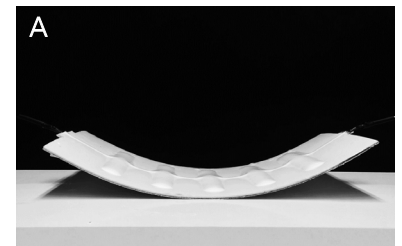


FIG. 3.63: (A) Bending of a plate without distinct zones of increased compliance by an integrated pneumatic pouch (plate length: 320 mm). (Mader et al. 2020a)

(B) Initial study on the influence of plate thickness on the bending by the integrated pneumatic actuation. Thickness increases from top to bottom (from 8 to 14 central 0/90° GF prepreg layers), while the pouch geometry remains unchanged. The maximum applied pressure is 3 bar. (Plate length: 320 mm). Adapted from (Fenton 2018).



FIG. 3.64: GFRP plate with integrated pneumatic actuation. The system can undergo large deformation upon pressurization as well as to bear high external loads. The applied weigh has a mass of 0.5 kg. The plate length is 320 mm.

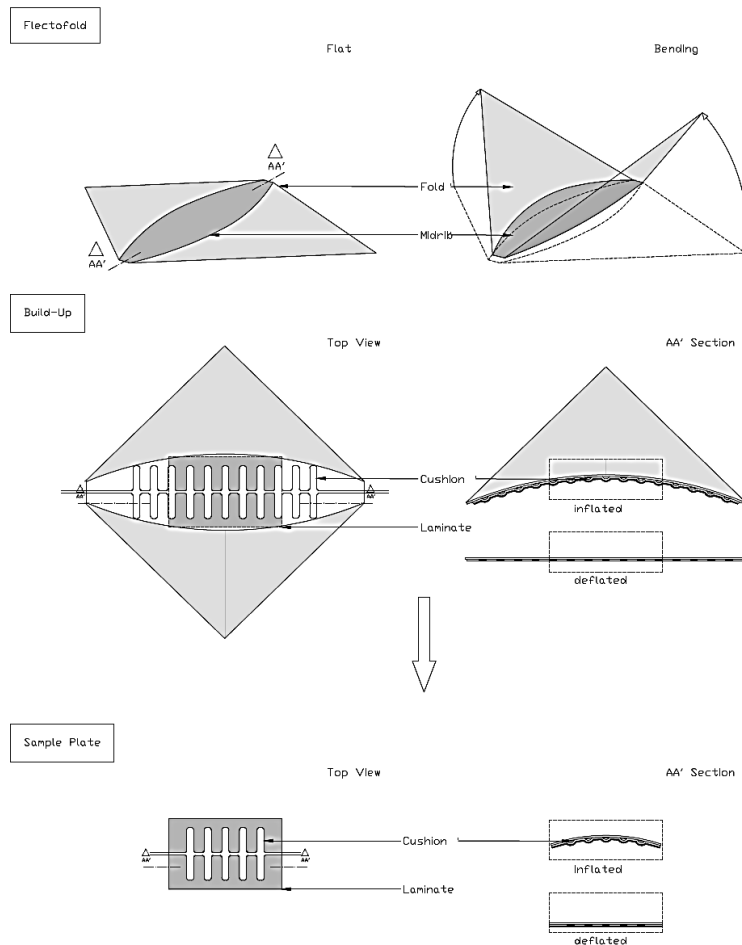


FIG. 3.65: Concept for actuating the Flectofold folding by a pneumatic pouch integrated into the midrib. Adapted from (Fenton 2018).

3.2.2 Variable stiffness through integrated pneumatic actuation

The previous chapter demonstrates that the integration of pneumatic pouches can actuate 2-dimensional compliant systems. In analogy to the previous case study, the consequent step, is the development of a pressure-controlled variable stiffness concept. In the following a top-down biomimetic process is pursued to find a solution to this challenge.

3.2.2.1 Search for analogies

Various methods to vary the stiffness of a system were described in the introduction (see chapter 2.4). Since the pneumatic actuators are already present in the composite to achieve spatial adaptation, the paradigm of reduced mechanical complexity suggests that they should also be used to control stiffness. A screening for role models that use the same actuators for both movement and control of stiffness in the animal kingdom led to the antagonistic construction of actuators, such as muscles. The independent control of joint angle (position) and stiffness is an essential feature for animal motion (Daerden 1999; Migliore et al. 2005).

Muscles, like the pneumatic pouches integrated into the composite, can act only one-directionally. Bidirectional motion can be achieved by the co-activation of opposing joint muscles. For the full functionality of the motion system, a modulation in joint stiffness is needed as well. To create a wide range of stable movements natural systems constantly have to adapt to unpredictable changes. Such unpredictable disturbance might occur in the requirements of the task at hand itself, or due to changing environmental conditions. Additionally, a certain stiffness is necessary to overcome gravitational destabilization and avoid the collapse of the skeletal system. At the same time the joints have to provide the compliance necessary to absorb mechanical shocks or perform delicate tasks (Daerden 1999). An illustrative example for these varying demands is human walking. During stance, the joints of a human leg are required to be stiff in order to support the body weight. During the swing phase, however, they need to be compliant to allow for the exchange of kinetic and potential energy and to decrease the destabilizing effect of a swing leg perturbation (Migliore et al. 2005). The exact means of stiffness modulation have not been revealed yet, and different theories on position and stiffness control through the nervous system exist. Regardless of the exact control mechanisms in animal locomotion, it is clear that stiffness modulation is crucial for vertebrate systems to move the way they do (Daerden 1999). In experiments voluntary muscle contraction of a muscle group was proven to increase joint stiffness (Riemann and Lephart 2002). This ability to enhance joint stiffness by increased muscle stiffness enables to resist sudden joint displacements more effectively.

The above-described requirements are very similar to those of the technical system to be developed. These include overcoming the counteracting demands of holding a stable position and withstanding changing external loads, while enhancing motion by an increased compliance. Further, similarities in the mechanical behaviour of the muscle and a pneumatic actuator exist. Pneumatic systems as well as animal joints both show an intrinsic compliance to external loads. For the pneumatic system this arises from the compressibility of the air. For the animal joint it arises from the musculotendinous system that is built from elastic elements. Thus, joints driven by them also possess an intrinsic compliance (Daerden 1999). For biological joints as well as similar technical set-ups an antagonistic actuator set-up is a means to increase stiffness through co-contraction. The underlying principle is analyzed below.

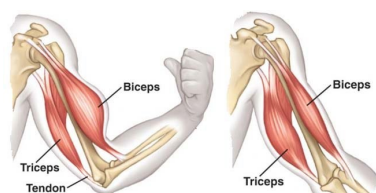


FIG. 3.66: Agonistic operation of the biceps and triceps. Contraction of the biceps flexes the arm, contraction of the triceps extends it. (Deaconescu and Deaconescu 2018)

3.2.2.2 Understanding of principles

Due to the antagonistic set-up of their muscles, animals can adjust position and stiffness independently by a superimposed motion of both actuators. A differential actuation of the two antagonistic muscles varies the joint angle. The co-contraction of the antagonistic muscles increases the stiffness of the joint by decreasing the passive compliance (Migliore et al. 2005). In other words, the position of a joint is controlled by the ratio of the muscular activation levels, the stiffness by the sum of these (Daerden 1999). The probably most well-known example for an antagonistic mechanism is the interaction of biceps and triceps in the human arm. As illustrated in FIG. 3.66, contraction of the biceps and relaxation of the triceps flexes the arm, while contraction of the triceps and relaxation of the biceps extends the arm (Deaconescu and Deaconescu 2018). This way, motion in both directions is possible, although muscles can only pull. Additionally, with this set-up a stiffening of the elbow can be achieved when both muscles contract. In contrast, when both muscles are relaxed, the elbow is very compliant and the arm hanging freely. Through the continuous control of both muscles, a wide range of positions and compliant behaviour is covered (Jafari 2014).

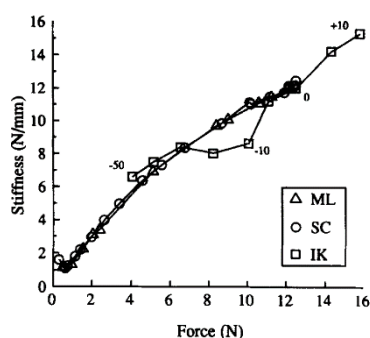


FIG. 3.67: Typical force-stiffness relation of the gastrocnemius medialis muscle-tendon complex of the rat

ML - Isometric contractions at different muscle lengths

SC - Isometric contractions with different stimulation current

IK - Isokinetic contractions with different velocities

Adapted from (Ettema and Huijing 1994)

Muscles are energy efficient, compliant actuators. An increase in muscle activation increases the number of parallel elastic elements in use. With increasing active elements the muscle stiffness and therefore joint stiffness rises (Migliore et al. 2005). FIG. 3.67 shows the measured increase in stiffness of the gastrocnemius medialis muscle-tendon complex of the rat with increasing contraction (Ettema and Huijing 1994). This effect holds true for isometric contraction, a contraction that is not associated with any change in muscle length, as well as for isokinetic contraction, where the muscle shortens with a consistent rate of speed. The behaviour of the muscle that

shows increase in stiffness with load, allows the adaption of the stiffness by a pre-stress introduced by the co-contraction of antagonists.

The above-described behavior of the muscle arises from its physiology and structural morphology. I.e., it is caused by the myosin heads moving along the actin filaments in the sarcomeres (see also chapter 2.2.3). To fully comprehend the principles underlying the variable stiffness of joints with an antagonistic muscle set-up, further details on the physiological properties of the muscle must be given. The force generated by muscle contraction (or more precisely by the shortening of the sarcomeres) is called muscle tension. Muscle tension is also created when the muscle is contracting against a load that does not move. In general, skeletal muscle contractions are distinguished between isotonic and isometric contractions. These types are also graphically represented in FIG. 3.68. Isotonic (constant tension) contractions are associated with a change in muscle length. Two modes are differentiated. A concentric contraction occurs when a muscle shortens to move load (e.g., when lifting a hand weight), while an eccentric contraction describes the controlled diminishing of muscle tension to lengthen the muscle (e.g., when lowering a hand weight). However, the muscle is also able to produce tension without creating a motion. One speaks of so-called isometric contractions. They occur when the force produced by the muscle is too low to overcome the applied load. This is for example the case if a load is too heavy to be moved or for maintaining a certain posture. In most cases, isotonic and isometric contractions work together to achieve a desired outcome (Betts et al. 2017). The nervous system controls all the described muscle activities. A so-called motor unit comprises the group of muscle fibres in a muscle that are innervated by one motor neuron. Usually, a muscle consists of many of these motor units, in a wide range of different sizes, to fulfill different tasks. Motor units may consist of a few muscle fibres, permitting extremely fine motion control as e.g., needed for moving the eyeballs or grasping delicate items. Or they may supply a large number of muscle fibres. Such large motor units are responsible for "gross" motions as the extension of the knee joint. The smaller motor units have lower-threshold motor neurons and therefore are more excitable. They are activated first and produce at relatively small degree of contractile strength (tension). The larger motor units are activated as more strength is needed. The more motor units are recruited the stronger the tension produced by the muscle. The tension produced, however, is not only influenced by the number of motor units activated, but also by the frequency of action potentials (nerve impulses). The so-called wave summation describes the effect that the twitch will be stronger if the previous twitch is still occurring as the second stimulus triggers the release of additional Ca^{++} ions. These activate further sarcomeres. Both parameters allow the control

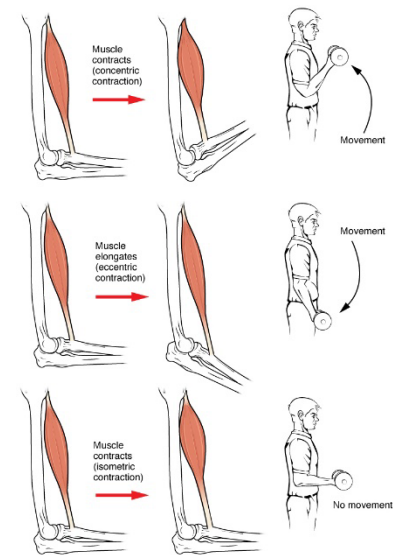


FIG. 3.68: Different types of muscle contraction. During isotonic (A&B) contraction the muscle length changes to move a load. During isometric contraction, the muscle length does not change as the load exceeds the tension the muscle generates. (Betts et al. 2017).

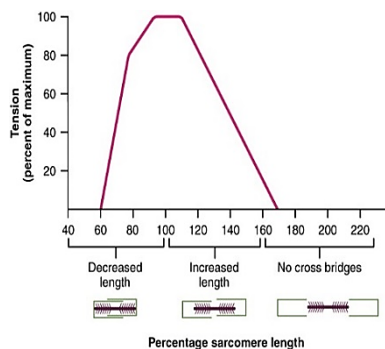


FIG. 3.69: Within the sarcomeres, in order for the myosin heads to attach to actin, the thin and thick filaments have to overlap already. This is necessary for forming cross-bridges to produce the muscle tension by pulling back the actin. Therefore, the length of the sarcomere effects the force generated upon contraction. The maximum tension is produced by a sarcomere between 80 and 120% of its resting length. (Betts et al. 2017)

of muscle tension in co-contraction (Betts et al. 2017). In an antagonistic set-up the tension of the antagonistic muscle opposes the tension produced. This co-contraction of muscles allows the individual muscle to activate more muscle strands in parallel, increasing the muscles stiffness. As the muscle stiffness itself is linearly dependent on the stress, co-contraction is a mean to increase the stiffness of the system.

Next to the level of muscle activation and the number of actin-myosin cross-bridges formed, the muscle stiffness arises from additional factors. These are muscle intrinsic as well as extrinsic. Further intrinsic factors determining the stiffness of single muscle fibres are the in FIG. 3.69 shown sarcomere length-tension relationship and the force-velocity relationship. The intrinsic component also encompasses the mechanical behaviour of the material forming the muscle tissue as well as the connecting non-contractile tissues, such as tendons and fascia. These molecules (mainly collagen) show properties of elasticity and viscosity. Therefore, the muscle stiffness also depends on the load-cycle history. Next to the contribution of the tendomuscular tissues, joint stiffness is a result of all constituents located within and over the joint. This includes tendons, ligaments, the joint capsule, and cartilage. In this regard co-contraction of the antagonistic muscles supposedly enhances joint stiffness also by increasing the compression between the articular surfaces. Further, intrinsically stiffened muscles are suggested to possess enhanced extrinsic factors of muscle stiffness. The increased activation level of stiffer muscles is believed to show more rapid reflex activity, as the transmission of loads to the sensory muscle spindles is eased and the electromechanical time delay is reduced. So, by the co-contraction of antagonistic muscles the initial resistance of a joint to displacement is increased by the elevated initial resistance within the muscle. Additionally, the reflexive response is improved (Riemann and Lephart 2002).

Summarizing, the stiffness control is realized by making use of the tension-dependent stiffness of the actuator (muscle) and non-linear material properties of the constituents comprising the joint. Both increase their stiffness through the pre-tension introduced by co-contraction.

3.2.2.3 Abstraction

In the abstraction process the antagonistic set-up of actuators for a stiffness control will first be considered for a mechanical joint system using conventional electric motors, before transferring it to a GFRP plate with integrated pneumatic actuation. As an intermediate step, specific aspects consideration for the use of external pressure-driven actuators, such as PAMs or compliant systems, will be explained.

Possible applications of a variable stiffness are broad, as well as the concepts to realize it. The antagonistic set-up of actuators has been implemented for grasping applications, tensegrity mechanisms (Azadi et al. 2009) and to increase the safety in human-robot interaction (Petit et al. 2010; Sardellitti et al. 2010). The current drawback of robotic systems to be solved by this approach, is the inability to independently control a joint angle and joint stiffness without complex electromechanical feedback loops, potentially reducing the system's stability (Migliore et al. 2005). The so-called variable stiffness actuation (VSA) concept reduces the risk associated with collisions between humans and robots as they enable the absorption of energy at an impact with a reduced stiffness, while also allowing precise joint positioning by an increase of the stiffness (Sardellitti et al. 2010).

The bio-inspired solution is to mimic the approach of an antagonistic actuator set-up to control position and stiffness independently as a function of co-contraction. For this principle, it is essential that the used actuators show a non-linear force-length relationship. Otherwise, the resulting joint stiffness is independent of co-contraction (Migliore et al. 2005). Unlike skeletal muscles, electric motors do not show the required non-linear behavior. Therefore, elastic elements with a non-linear torque-displacement characteristic are added to the joints as shown in FIG. 3.70. This so-called motor-spring unit enables to vary the stiffness of the systems by pre-tension and thus to adapt it to current demands. Moreover, the elastic elements can increase the efficiency of a system, as they can be used as energy storing mechanisms. FIG. 3.71 shows a series of stiffness-torque curves for a motor-spring unit with different pre-tensions. The lowest curve shows the behavior of a spring-motor unit at no pre-tension while the higher curves represent increasing pre-tension (Petit et al. 2010).

The stiffness induced by antagonistic forces present within a mechanism is also referred to as antagonistic stiffness. The pre-stresses an antagonistic arrangement of actuators can create is called antagonistic forces and is defined as the internal forces within the links of the mechanism, when the externally applied momentum is zero. To pose antagonistic forces, the mechanism needs to be kinematically singular or actuated redundantly. The antagonistic stiffness exists in parallel to the elastic stiffness of the mechanism. The total stiffness of a system is the sum of the two. For the antagonistic forces to influence the overall stiffness of a system significantly, the antagonistic stiffness is required to have the same magnitude as the elastic stiffness.

Next to the set-up with motor-spring units introduced in FIG. 3.70, actuators with an intrinsically non-linear behaviour exist. Especially pneumatic muscle actuators offer themselves for the application in antagonistic set-ups, as they inherently possess an increasing stiffness with applied pressure. This non-linear behaviour erases the need for extra components (Sardellitti et al.

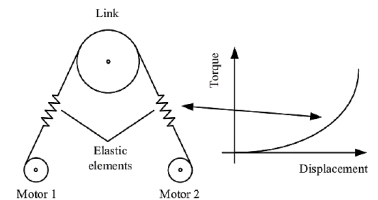


FIG. 3.70: Antagonistic set-up of two pulling actuators (A). The convexly increasing torque-displacement behaviour of the motor-spring unit enables a stiffness variation by pre-tension. Adapted from (Petit et al. 2010) / © 2010, IEEE.

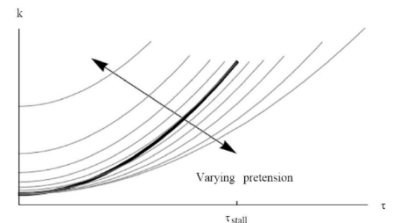
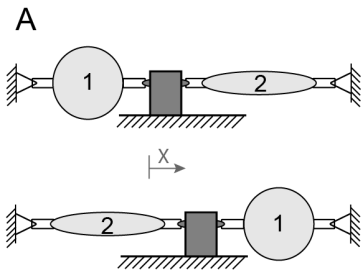


FIG. 3.71: Different stiffness-torque curves for increasing pre-tensioning of the non-linear actuators used in a variable joint stiffness concept. (Petit et al. 2010) / © 2010, IEEE

k – stiffness
 τ_{stall} – stall torque

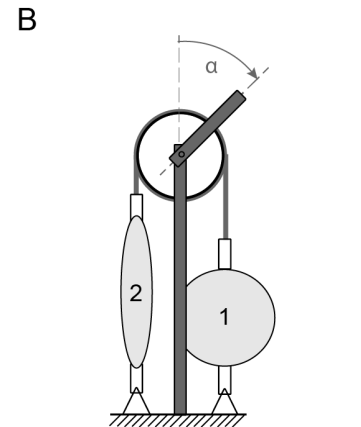
2010). In fact, pneumatic artificial muscles (PAMs) resemble skeletal muscles. Both are linear contractile engines that must be paired antagonistically to fulfill a bidirectional motion (see FIG. 3.72). Due to the non-linear actuation force-stiffness relation, pneumatic actuators can control a joint stiffness like skeletal muscles. The following describes the behaviour of PAMs in an antagonistic set-up in more detail.

Daerden (Daerden 1999) describes the force of two equally pressurized antagonistic PAMs in the set-up shown in FIG. 3.72 as follows:



$$F = F_1 - F_2 = -P_1 \frac{dV_1}{dl_1} + P_2 \frac{dV_2}{dl_2} = P_1 \frac{dV_1}{dx} + P_2 \frac{dV_2}{dx} \quad (21)$$

The stiffness can be formulated as:



$$K = -\frac{dF}{dx} = -\frac{dP_1}{dV_1} \left(\frac{dV_1}{dx} \right)^2 - \frac{dP_2}{dV_2} \left(\frac{dV_2}{dx} \right)^2 - P_1 \frac{d^2V_1}{dx^2} - P_2 \frac{d^2V_2}{dx^2} \quad (22)$$

This equation shows that stiffness and position can be controlled independently. The position is determined by the pressure ratio. By keeping this ratio fixed and increasing the pressure, the stiffness of the individual actuators, and thereby the overall system, increases. The stiffness of an individual PAM is defined by:

$$C^{-1} = K = \frac{dF}{dl} = -\frac{dP}{dV} \left(\frac{dV}{dl} \right)^2 - P \frac{d^2V}{dl^2} \quad (23)$$

From this dependency, it can be seen that the stiffness of the actuator is influenced by the pressure as well as its varying effective area. The second term shows that an increase in internal pressure p increases the stiffness linearly. The first term of equation (23) refers to gas compressibility. Here two cases need to be differentiated. In the first one considered, the pneumatic actuator is a closed system, meaning a change in actuator volume is associated with a change in pressure. Here the compressibility of the gas can be calculated assuming a perfect gas approximation and polytropic change of state.

$$\frac{dP}{dV} = -n \frac{P}{V} \quad (24)$$

Assuming the use of dry air, the exponent n ranges from 1.0 (isothermal changes of state) to 1.4 (isentropic changes).

If the joint is moved out of the equilibrium position by an applied external torque, in an antagonistic set-up, one of the two actuators will be stretched. Consequently, its volume will be reduced, and, in case of a closed system, the pressure rises. As

FIG. 3.72: Antagonistic set-up of PAMs. The antagonistic coupling can produce linear (A) or rotational (B) motion. Based on (Daerden 1999).

a result of the actuator elongation, and the pulling force will increase as well. The behavior of the other actuator will be opposite. Thus, a torque thriving to restore the equilibrium will act on the joint. Considering a system with constant pressure control, where pressure controlling regulators maintain isobaric conditions, the effects of compressibility are eliminated. The first term of equation (23) disappears and the actuators stiffness change is attributed solely to the variation in effective area. Thus, for an open system, the stiffness will not increase with increasing deformation (Daerden 1999). Still, for both pneumatic systems, the open and closed one, the stiffness is increased by a co-activation of the opposing actuators. The higher tension created by a higher internal pressure influences the stiffness of the system positively.

In general, antagonistic systems utilizing pneumatic actuators can be compared to the non-linear motor spring units described above. The stiffness, however, is not controlled by the behavior of the non-linear spring and the applied pre-tension, but by the internal pressure within the pneumatic actuator. FIG. 3.73 describes the difference between the two approaches graphically. In antagonistic systems, using non-linear springs in combination with electronic motors, the applicable pre-tension allows the system to start from a different point at the spring's non-linear force-elongation curve (see also FIG. 3.71). The intrinsic properties of the motor-unit are not changed. In a pneumatic system, the pressure level that is applied to the pneumatic actuator varies the intrinsic response of the system to an applied load. The antagonistic set-up is needed to decouple pressure from deformation and allow for higher pressures at smaller deformations.

The described effects also hold true for the integrated pneumatic pouches introduced in the previous chapter. In the developed integrated actuation for compliant mechanisms, the restoring the initial shape so far was fulfilled by the elastic energy stored in the GFRP. However, when installing a pressure-controlled stiffness, an antagonistic set-up of the actuators is required to decouple the actuation state from the pressure level applied. This decoupling enabled by an antagonistic set-up of the actuators is analogue to antagonistic muscles fulfilling an isometric contraction. Consequently, a pneumatic pouch will be integrated on both sides of the compliant GFRP plate. This principle is very similar to the previous chapter on cellular structures, although arising from a different biological role model.

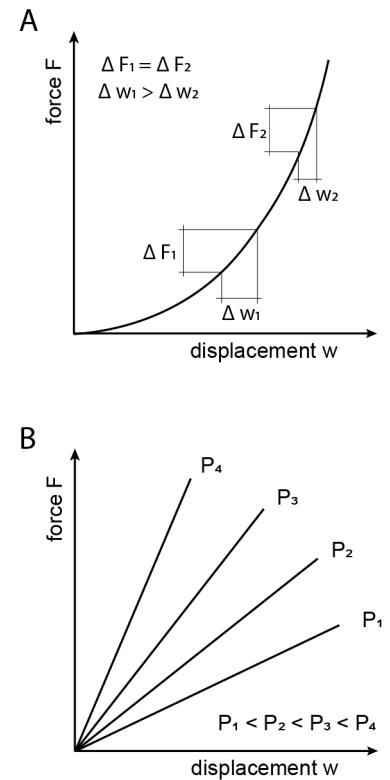


FIG. 3.73: (A) Non-linear force displacement behaviour of a spring used within a motor-spring unit to realize an adaptive stiffness within an antagonistic set-up. Stiffness increases with displacement. (B) Increasing stiffness with increasing internal pressure P of a pneumatic artificial muscle. By co-activation of two antagonistic actuators the internal pressure and thus stiffness can be altered.

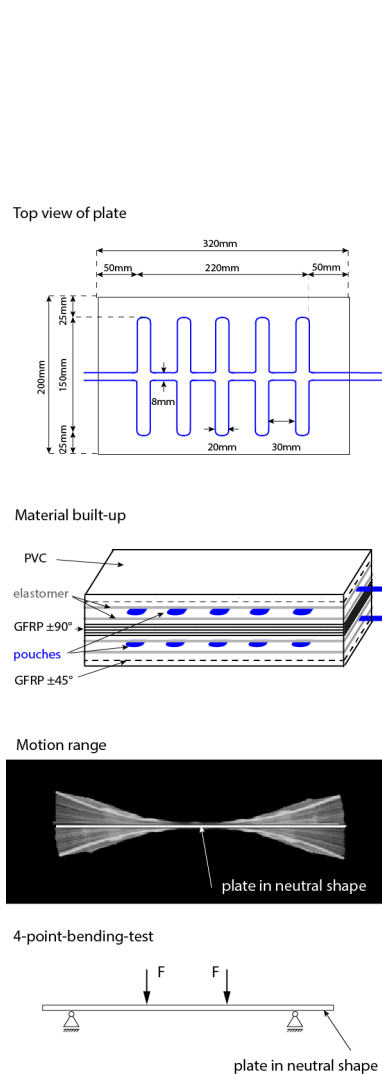


FIG. 3.74: The sample dimensions, the pouch placement within the laminate built-up and the motion range of a plate with antagonistic pneumatic actuators. Further, the setup for the bending test to determine the stiffening effect of the antagonistic actuator setup is shown.

3.2.2.4 Check technical feasibility & prototyping

As the volume of the integrated pneumatic pouches is comparably small and the stiffness of the GFRP plate high compared to a frictionless hinge, the influence of the internal pressure on the stiffness of the system is expected to be limited. To test the technical feasibility, physical prototypes of the GFRP plates with distributed compliance were manufactured. The sample dimensions, the antagonistic pouch placement and the laminate built-up with is shown in FIG. 3.74, together with the test setup for the bending test to determine the stiffening effect. The pouch orientation along the longitudinal axis is the one needed for the actuation of a compliant device through bending (compare FIG. 3.65). Thus, to keep the number of pouches at a minimum, this test assesses the stiffening potential of pouches potentially also used to realize the desired motion of the system, although higher stiffening values are likely to be achieved with a pouch orientation orthogonally to the longitudinal axis.

The tested setup allows the bending of the plate with positive and negative curvature. A pressurization with the same pressure level lets the plate remain in a planar configuration. The pressure ratio of the two antagonistic pouches allows the independent control of position and stiffness. To assess the stiffening potential, the apparent Young's moduli at different pressure levels were determined in a 4-point bending test. Four pressure levels, between zero and 1.8 bar were tested. The same pressure was applied to both pouches to achieve a planar starting position. The sample was tested at each pressure level within three independent rounds of pressurization. To remain in the linear elastic region of the sample, it was loaded with a maximum force of 50 N. The test speed was 20 mm/min the distance of the supports was 250 mm and of the load fins it was 83 mm. The apparent Young's modulus was determined between 0.05% and 0.1% elongation. Two different approaches were considered in the test. In the first one the pressure is held constant by the pressure regulator, referred to as open valve. In the second approach an additional valve is introduced to the set-up to seal the pouches. Consequently, in these closed valve tests the pressure varies as a result of deformation. The results of both approaches are plotted in direct comparison in FIG. 3.75. In both cases, the open and closed valve, the apparent Young's modulus of the pressurized composite plate increases with increasing pressure significantly. Also, the stronger effect with a closed valve becomes apparent. In the case of an open valve (isobaric; constant pressure) the apparent Young's modulus increases from 2.10 ± 0.03 GPa for the reference test at zero pressure to 2.93 ± 0.04 GPa at a pressure of 1.8 bar. With the closed valve test set-up, the value increases up to 3.49 ± 0.05 GPa. These results show that the apparent Young's modulus of a system can be increased significantly through pressurization. The stiffness increases by 40 and 66% respectively for a pressure increase of 1.8 bar. As explained

previously, at an increased internal pressure in the pouches the energy potential is higher. More energy is required to change its volume, thus the stiffness increases. With a closed valve, the air inside the (lower) pouch additionally needs to be compressed as the pouch is sealed air-tight. Consequently, the pressure increases further upon deformation and stiffening takes place to a greater extent. FIG. 3.76 and FIG. 3.77 show the individual stress-strain curves at each pressure level for the open and closed valve systems respectively. The graphs show the clear distinction between the stress-strain curves at the different pressure levels. Also, the stronger effect of a closed valve has on the stiffness of the system becomes apparent. All measured apparent Young's moduli differ significantly from each other, regardless if a constant pressure or a closed valve set-up (see appendix B9). The bump visible in some stress-strain curves might be attributed to the experimental set-up. To avoid an effect of bulging of the inflated pneumatic pouches in the measurements the plate was placed on distancers to make sure the plate is supported at areas of no pouch to avoid influences of the pressure inlet on the stiffness measurement.

Responsible for this stiffening is mainly the lower pouch, as this side is stretched during the deformation induced by the 4-point bending test. The stiffening effect of the single pouch is visible, although the volume of the pouch is small and the stiffness of the GFRP plate high, compared to a frictionless hinge. The second pouch that increases in volume during the bending, is still necessary as it enables to elevate the pouch pressure at any desired deformation.

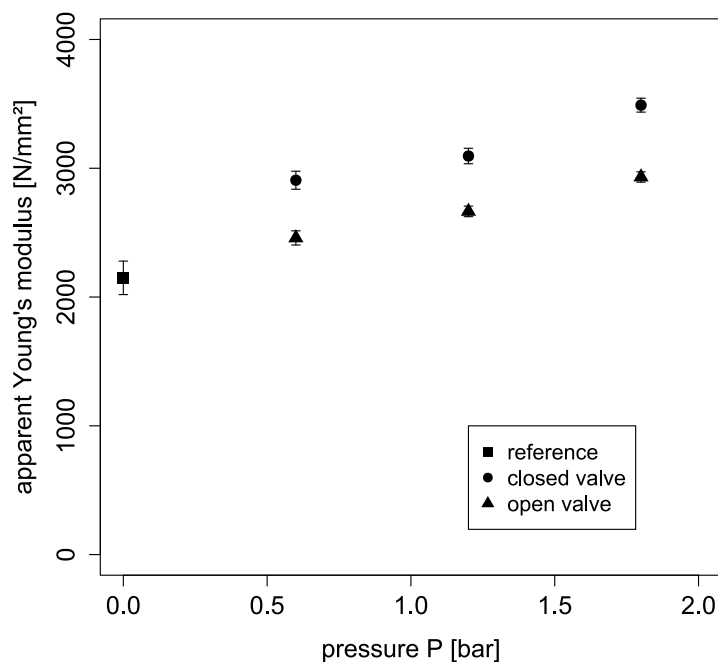


FIG. 3.75: Pressure-dependent apparent Young's modulus of a GFRP plate with integrated pneumatic actuation. The values were determined in a 4-point-bending test for a constantly regulated pressures (open valve) and an airtight sealed system (closed valve). The pressure refers to the starting pressure applied at before the start of the bending test.

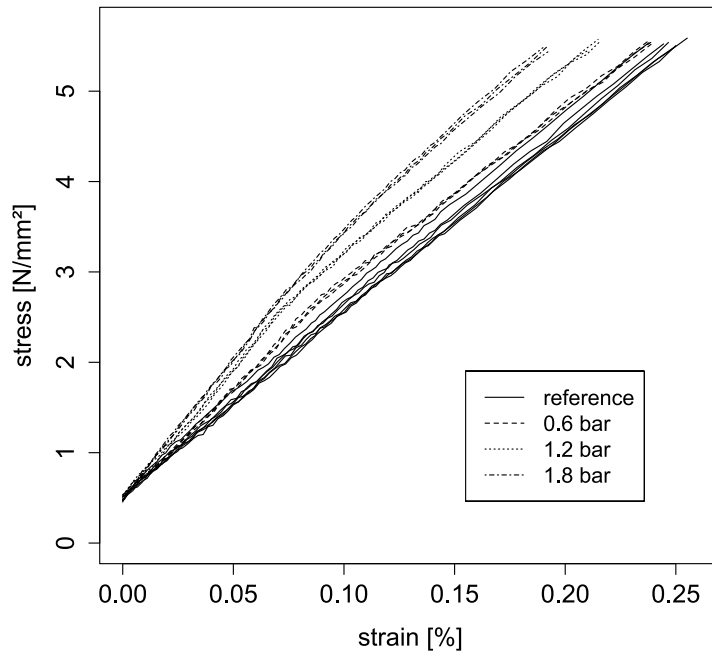


FIG. 3.76: Stress-strain curves of the 4-point-bending test with an open valve at different pressure levels.

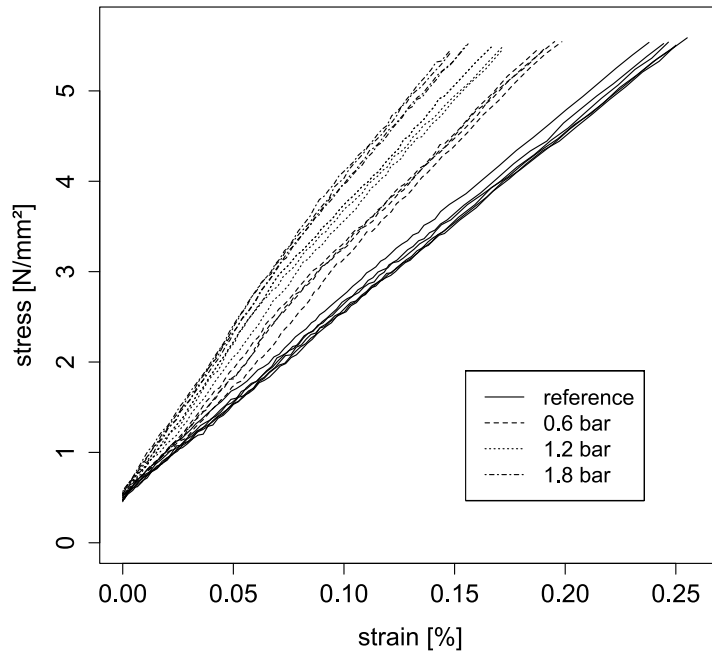


FIG. 3.77: Stress-strain curves of the 4-point-bending test with a closed valve at different starting pressure levels.

3.2.2.5 Improved product

The integration of pneumatic pouches in both opposing sides of a GFRP plate allows the independent control of position and absolute pressure level inside the pouches, influencing the stiffness of the system. The measured apparent Young's modulus of the GFRP plates with the integrated pneumatic actuation is 2.10 to 3.40 GPa. This is clearly lower than the Young's modulus of a quasi-isotropic pure GFRP plate that is around 15 GPa. These low material values can be attributed to the high elastomer content that arises from the integration of two pneumatic chambers requiring four layers of elastomer surrounding them. Due to the restriction of available elastomer foil thicknesses for this investigation these layers are comparably thick. Although some elastomer is also needed to ensure the functionality of the compliant hinge zone, the amount for the integration of the pneumatic actuation could potentially be reduced.

Nevertheless, compared to other variable stiffness composites the stiffening ratio is low, but the Young's modulus is high (see Table 8). For the adaptable pressurized sandwich components developed by Müller et al. the maximum bending force increased by 15% by the application of an internal pressure of 2 bar (Müller et al. 2015). For this material composition (woven glass fibre epoxy composite with an expanded polystyrene (EPS) core) similar to the here investigated samples, a stiffening factor is within the same range. The segmented steel reinforced SMP composite developed by McKnight et al. show a much higher stiffness ratio and apparent modulus values (McKnight et al. 2010). However, the response time of 1-2 minutes for heating and even longer for cooling, is slow.

Table 8: Comparison of (apparent Young's modulus (E) and stiffening ration of different variable stiffness composites.

Stiffness ratio	E	System
22	2.4-52.4 MPa (tensile)	Fluidic flexible matrix composites (F ² MC), (Philen et al. 2007).
27	1.5 - 40 MPa (bending)	Variable stiffness micro device with low-melting-point alloy (LMPA) embedded in poly(dimethylsiloxane) (PDMS), (Schubert and Floreano 2013).
1.15	- (bending)	Adaptable pressurized sandwich components, (Müller et al. 2015).
15-77	8-12 GPa (bending)	Shape memory polymer with segmented reinforcement (steel), (McKnight et al. 2010).
1.4-1.66	2.1- 3.4 GPa (bending)	GFRP with integrated pneumatic actuation and variable stiffness.

The stiffening approach with the antagonistic pneumatic pouches integrated into a GFRP plate offers the advantage of utilizing an already present actuation system. Thus, no additional actuation system for shape changes is required. Therefore, comparably little additional weight and thickness is added to the system. The actuation and stiffness adjusting system based on the integrated pneumatic pouches is very thin, especially when compared to the system with integrated pressurized flexible matrix composite (FMC) tubes. With thinner elastomer layers available, this can be reduced even further.

3.2.3 Further considerations & outlook

With the integrated pneumatic pouches and the bio-inspired material built-up, prototypes of 2-dimensional compliant kinetic systems could successfully be actuated. Nevertheless, further aspects should be investigated. A more intense testing of the fatigue behavior of the system will be necessary. The stable long-time time behaviour needs to be guaranteed as the pouches are integrated directly into the GFRP. Thus, they cannot be replaced in case of leakage. In the case of a failure, the entire element would need to be replaced. In the above-described investigations, the motion was generated by pneumatic pouches placed within the material built-up as well as by creating a pneumatic chamber directly in between the elastomer layers. Both approaches proved feasible and have different advantages and disadvantages. A chamber without pouch creates larger deformation as the seams of the pouch do not reduce the effective pouch width. At the other hand a pouch that is most likely more resistant to failure and can bear higher pressures. This adds safety and redundancy to the system. Which approach to follow can be decided depending on the priorities of the individual application.

Further, means to control the proposed motion needs to be considered. Where high precision in the motion is necessary, a feedback loop between a displacement sensor and the proportional pressure regulator might be a solution to overcome any unknown long-term behavior and variabilities of the system. These most likely will arise for example from the influence of the temperature on the FRP and the compressed air. In this regard also the installment of an additional vacuum systems might be needed to overcome the small remaining deformation from the viscoelastic material behaviour or in applications where the stored elastic energy in the system is not sufficient to press the remaining air out of the pneumatic pouches.

In terms of the used material system, the comparably thick elastomer layers add weight to the composite, increasing the dead load. For future developments, a way to decrease the weight of the planar flap areas that are not deformed during motion could be investigated. This is an option especially for the Flexafold with only straight-line folding. For the Flectofold it will

depend on where the pneumatic actuators are placed, but the elastomer could be reduced to these areas where it is needed for the functionality.

Further, in curved-line folding systems, several possible ways to actuate the system exist. The fold lines could be actuated as is the case for the prototypes. Potentially, the folding can also be triggered by a uniform bending of the midrib. Initial tests on using an externally mounted pneumatic pouch to bend the Flectofold midrib showed that, the pouch size needs to be adapted to follow the lens-shaped outline of the midrib. This way the surface area of the pouch segments in the centre is larger, and more force is generated where more force is needed to bend the midrib and lift the flaps (see FIG. 3.78). In an initial test to actuate a Flectofold with actuation of the midrib, the integrated pneumatic pouch was able to uniformly bend the complete structure but could not generate enough force to actuate the curved-line folding. However, parameters such as an adjusted pouch geometry, can be utilized to influence and optimize the pneumatic actuation for specific applications. First experiments shown in FIG. 3.79 demonstrate the influence of the pouch geometry on the induced deformation. The three integrated pouches possess the same area but a different number of fingers. The resulting deformation achieved by the same applied pressure levels, differs clearly. The larger finger induces a stronger, but less uniform bending to the plate. Also, the combination of several pneumatic actuators placed in different parts of the structure could have a supporting effect. On the other hand, the simultaneous actuation of several pneumatic pouches within one interrelated system might pose a challenge to the control, as different pressures might be needed in each of the pneumatic pouch. Those would need to be coordinated with the correct, potentially deformation dependent, pressure ratios. However, the combined approach would bring a redundancy to the actuation system.

In the variable stiffness experiments a significant increase in stiffness was achieved. An even stronger stiffening effect is expected from a placement of separate stiffening pouches perpendicular to the longitudinal axis and should therefore be tested as well. Depending on what pouches are used for the actuation, this approach may require a higher number of pouches placed and the material built-up. That may require additional layers of elastomer, making the composite heavier. Any pressure induced stiffness increase, however, will decrease for the intrinsically stiffer plates. Therefore, further investigation on the stiffening effect within thicker plates will be interesting. In the same regard examining the potential of pouch geometry on the stiffening is worth investigating. Also, the outline of the pouch could potentially be optimized to reduce stress concentrations. The applied pressure of less than 2 bar is comparably low for pneumatic systems and could be increased for a stronger stiffening effect. Therefore, an exact assessment

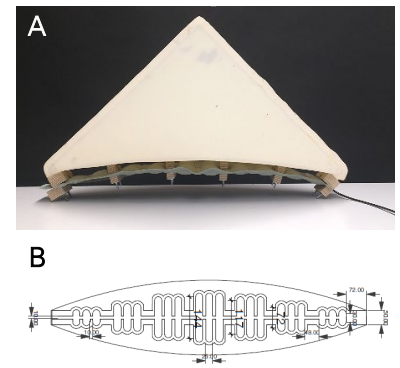


FIG. 3.78: (A) First prototype of a Flectofold actuated by an external pneumatic pouch attached to the lower side acting in tension. (B) Sketch of a pneumatic pouch showing the outlines of the chamber following the lens shaped midrib. In the centre higher forces are required therefore the chambers are larger there. Midrib length: 420 mm.

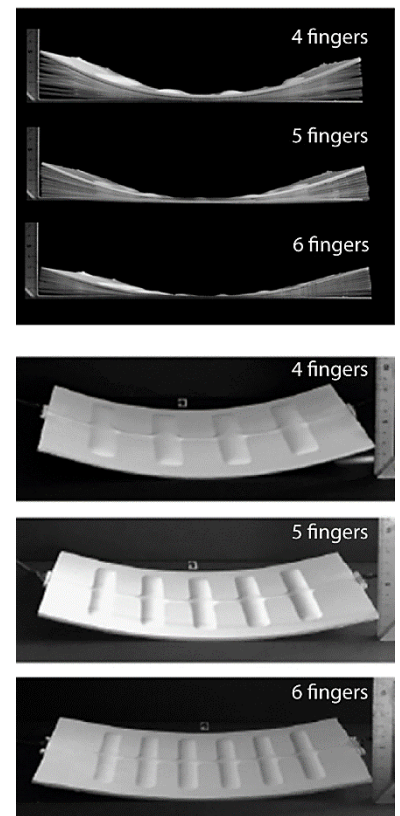


FIG. 3.79: Initial tests with different pouch geometries. At the same applied pressure and total pouch surface, a pouch with less, and therefore wider "fingers" causes a stronger curvature of the plate. The test samples contain 10 layers of 0/90° prepreg in the center (+ two ±45°) and the maximum pressure applied is 3 bar. Plate length = 320 mm. (Adapted from (Fenton 2018). For further details see appendix B10.

of the pressures the material systems can bear needs to be conducted.

A closed valve system achieves significantly higher stiffening values. However, in a closed system, unpredictably higher pressures could be induced by an external load, as the pressure increases with external deformation. Applying such a system, sufficient safety margins for the interlaminar adhesion need to be ensured. Independent of using an open or closed valve system, the maximum bearable pressure might be increased by new fabrication scenarios such as the 3D weaving technology, or the usage of other materials with a higher interlaminar adhesion. However, it needs to be kept in mind that larger pressurized volumes and higher pressures might pose a safety risk that arises from the rapid expansion of the compressed air upon a failure of the system. Next to the pouch geometry and maximum pressure that can be applied, the potential of using a liquid, such as water, as a pressure medium could be explored. Here a much higher stiffening potential exists due to the non-compressibility. However, this would come at the cost of increased weight as well as quality demands and maintenance effort (tightness of the system needs to be guaranteed to a greater extent than with pneumatics). Nevertheless, the stiffness increasing effect of the higher internal pressures has limitations and becomes apparent only as long as the elastic stiffness of the system is close to the antagonistic stiffness. Whether the antagonistic stiffening can contribute significantly to the system behaviour of a complaint shading device as the Flectofold will need to be the content of further investigations.

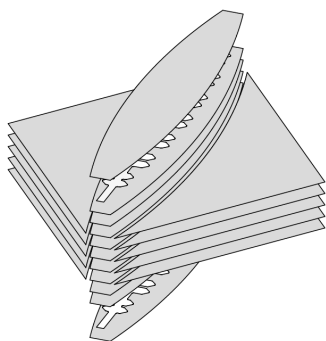


FIG. 3.80: Potential material built-up for a Flectofold with integrated actuation and adaptive stiffness. Two antagonistic pneumatic pouches placed in the midrib can bend this in concave and convex direction and by co-contraction potentially increase its stiffness.

In a Flectofold set-up as shown in FIG. 3.80 this potentially enables a short-term increase in stiffness to meet temporarily higher demands, as induced for example by extreme weather conditions. The placement of more extensive pouches in the area of distributed compliance to achieve a uniformly bending promises higher effective stiffness changes, due to the larger pressurized volume as compared to the actuation of a slender hinge. This means in the exemplary case of the Flectofold, pouches could be integrated into the midrib and folding of the wings could be induced by the bending of the midrib. To what extent the stiffening effect of the midrib created by the antagonistic pneumatic pouches is capable to positively affect the overall stiffness of the system, will need to be examined in more detail. A starting point could be the investigation on where the main source of deformation upon external load within the Flectofold is. If the main source of distortion is within the hinge zone and the curvature in surfaces is not changed the most effective way to increase the stiffness might be through a pouch integrated directly within the hinges. Even without an antagonistic set-up, the presence of the pouch should make the hinges more resistant to distortions. If the stiffening of the surfaces influences the overall stiffness of the positively, the

curved-line folding of the Flectofold offers the advantage that additional pouches might be placed within the flaps as well.

The specimen used in the variable stiffness experiments above contained seven layers of prepreg and an increase in stiffness by a factor of 1.4 to 1.66 was measured. The Flectofold midrib of the large-scale prototype contains nine layers of woven glass fibre prepreps (Körner et al. 2018). In general, for stiffer plates the proportion of pressure induced stiffening effect will reduce. The extent of the stiffening, however, also depends on the scaling, the size of the pouches and the pressure that can be applied without delamination.

To what extent the here achieved stiffness increase contributes to a higher improved performance and exceeds the cost introduced, such as increased fabrication and control complexity as well as weight due to the additional elastomer layers, needs to be investigated in a comprehensive analysis considering the reduced actuation energy required as well as extended deformation flexibility due to the reduced stiffness. Potentially, the usage of such an antagonistic adaptive stiffness system only pays off, when its full potential and additional functionalities such as a concave to convex curvature change are exploited. This may further broaden the range of possible applications.

3.2.4 Conclusions

In a biomimetic top-down approach, a material built-up to reduce delamination and enable an integrated pneumatic actuation for a GFRP plate was successfully developed. Inspired by the ultrastructure of the wing veins of the minstrel bug *Graphosoma lineatum italicum*, the pneumatic pouch (or chamber) for actuation was surrounded by elastomeric material, showing a stronger interlaminar adhesion. The technical feasibility was proven by different physical prototypes. The tested specimen with a pneumatic pouch integrated into a compliant hinge zone showed the expected angular distortion with increasing pressure. This angle-pressure relationship with a maximum actuation angle of 45° at 2 bar showed to be repeatable and fatigue resistant for at least 500 load cycles.

An integrated pneumatic actuation of two different 2-dimensional compliant shading devices with a span of approx. 1 m was successfully achieved by placing pneumatic pouches within the folding lines. The fully integrated approach allowed the inconspicuous actuation of the Flexafold and Flectofold with low additional weight and no additional space or support requirements (see FIG. 3.81). This enables a robust, slender, lightweight actuation. Further optimization to achieved higher folding angles might be necessary. The pneumatic pouch can be produced easily and in any arbitrary shape. This offers a large flexibility in pouch size and shape enabling simple and fast fabrication. FIG. 3.82 summarizes some potential pouch



FIG. 3.81: Flectofold with inconspicuous, integrated pneumatic actuation in the curved folding lines.

variations tailored to different applications and intended deformations.

Also, a quasi-uniform bending of a GFRP plate can be achieved. Next steps for a further development of the system is a more in-depth investigation of the curvatures that can be achieved with respect to the plate stiffness. With the current set-up, delamination takes place at pressures above 2 bar (see appendix B11). This sets a limit to the achieved deformation and stiffness variation. Therefore, means to increase this value are a possibility for further improvement. These include different material systems and manufacturing processes but also the outline and size of the pouch itself.

Additional pouches, placed in an antagonistic set-up, furthermore, offer the potential of a variable stiffness. This approach is inspired by the joint stiffening by antagonistic muscles. The opposing set-up allows the pneumatic actuators to operate at higher pressures, independent of the deformation. The increased pressure leads to an increased system stiffness. The antagonistic set-up of pouches for a quasi-uniform bending in a 7 GFRP layers thick plate showed a significant stiffening potential. The measured apparent Young's modulus increased by 40% at a constant internal pressure. For a closed system, the increase of 66% (from 2.1 to 3.4 GPa) is significantly higher. Future investigations will show whether the adaptive stiffness enabled by the antagonistic set-up of the pneumatic pouches can sufficiently increase the stiffness of the shading devices.

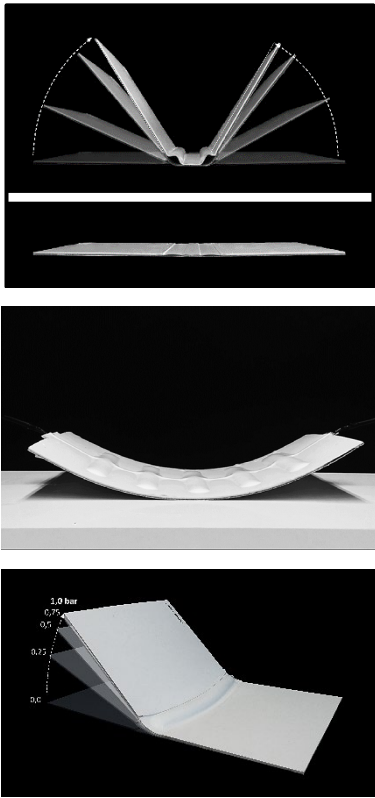


FIG. 3.82: Different forms of integrated pneumatic pouches. (Top) Straight line folding of compliant hinge. Placement of several pouches or folded pouches with a below-like behaviour increases the folding angle. (Middle) Quasi-uniform bending of a plate. (Bottom) Curved line folding where the pouch placed in the hinge also bends the adjacent surfaces indirectly.

4 CONCLUSIVE COMPARISON & FINAL CONSIDERATIONS

4.1 COMPARISON OF CASE STUDIES

The two case studies demonstrate the development of two different bio-inspired joint-free actuators with a variable stiffness potential. Based on different principles they possess specific strengths and weaknesses. However, they also show commonalities. These are foremost based on the pressure-driven function as well as the compliant design. The following subchapters highlight these common aspects as well as the specific advantages of each system within a summarizing conclusion.

4.1.1 Strengths and weaknesses

4.1.1.1 Commonalities of the systems

The most obvious advantages both developments have in common arise from the fluidic actuation. This allows a direct and fast reaction to a user request. In comparison to other variable stiffness concepts requiring heating and cooling, this is one of the major benefits. Both developed compliant actuators offer a continuous motion control thanks to pressure control. The resolution is only limited by the control of the pressure regulators. Furthermore, pneumatic actuation is characterized by the capability to create high forces at a good power to self-weight ratio. Additionally, both explored principles rely on an additional stiffening when required, and therefore do not need a softening for each reconfiguration under normal operation conditions. On the other hand, both actuators require constant pressure control to maintain a specific, actuated position.

The integrated design approach enables both systems to be self-contained and allows the actuation without external supports. Further, both actuators proved their capability to actuate 2-dimensional compliant façade shading devices. With the addition of a counteracting actuator set-up, additional functionalities arise. This is not only a stiffening by co-activation but also the broadening of the motion range. As the possibilities of the systems are not fully exploited yet, this is a field for future investigations and design studies. On the other hand, intrinsic limitations to the motion range of compliant systems exist. Continuous rotational motion, for example, are not possible by nature.

When air is used as a pressure medium a certain degree of compliance will always be present in the system. Further, the

dependency on other factors that might influence the system's behavior, such as the temperature or the viscoelasticity of the material, a control loop will have to be installed for an absolute and precise motion control. However, this degree of precision might not be necessary for the application scenario at hand. Still, depending on the number of elements, numerous individual pressure regulators and controls might be needed. However, conventional actuation mechanisms would also require the respective number of actuators as well as cabling. FIG. 4.1 shows the proportional pressure regulator panel of a large-scale demonstrator of a façade section with 36 Flectofolds, actuated by an external pneumatic pouch. Adding additional, antagonistic actuators in the integrated approach would double the number of pressure regulators needed. As discussed previously potentially more versatile motions could be generated by the actuators by placing several pouches and controlling them individually. However, it can be assumed that such a high motion variability is rather located in standalone elements that might be arranged in small groups. Thus, a lower number of controllable elements and therefore manageable number of valves might be needed. For applications requiring a high number of elements, the arrangement of several groups with pre-programmed motion patterns is possible to reduce complexity. The choreography of the created motions within compliant shading devices and the resulting effect on the viewer are part of ongoing research.



FIG. 4.1: Control panel of large-scale Flectofold demonstrator with 36 individual pneumatic actuators. (Photo by ITKE)

Due to the pressure-based actuation principle, both actuators can be divided in two functional elements: the energy providing elements (e.g. compressor or pressure regulator), and the energy converter, that modifies the received energy in order to obtain the desired pressure-driven deformation. Hence, a central supply of compressed air and control panels are needed but they can be placed within several hundred meters. On the application itself the actuator is slender, lightweight and in case of the integrated pneumatic pouches almost invisible. This is a major advantage, as for example pneumatic cylinders require at least twice their stroke as installation space.

4.1.1.2 Actuation

Specific conclusions of the actuation principle are given in the respective chapters within the case studies. Here they are provided in a summarizing direct comparison. Table 9 shows an overview on the most important aspects discussed. Further, a comparison to external actuation mechanisms that have been used so far to actuate the prototypes is given. However, selecting an actuation type additional, qualitative aspects not considered in this table, are of importance, such as for example the aesthetics.





	Pressurized cellular structure	Integrated pneumatic pouch	External pneumatic pouch	Electric motors
				
Stress concentrations	++	+	++	-
Motion range	++	+	-	-
Flectofin®	+	-	-	+
Flectofold	+	++	+	+
Flexafold	-	+	-	-
Mechanical complexity	-	+	+	--
Self-contained	+	+	-	-

Table 9: Qualitative comparison of the strengths and weaknesses of the two developed biomimetic actuation mechanisms and conventional actuation mechanisms used so far.

4.1.1.2.1 Comparison of forces and stresses

Due to the different scales and compliant prototypes actuated, only a qualitative comparison of the actuation energy as well as height and distribution of the stresses induced by the actuator is possible. For the pneumatic concepts developed no additional reinforcement is needed. Especially for the cellular actuator and the lens-shaped external pneumatic pouch, the bending is introduced uniformly over the entire length of the midrib. Due to the comparably higher pouch volumes, these systems should also be able to generate higher actuation forces. For the pneumatic pouches integrated into the laminate, high stresses are present around the fluid chamber, associated with the risk of delamination. The generated actuation forces are limited by the interlaminar adhesion of the composite.

First numerical studies on the stress distribution and needed forces have been conducted for conventional external actuators such as pneumatic pistons, or cables, but also the external pneumatic pouch (Körner et al. 2018). Similar studies would be needed for the assessment of the here developed cellular actuator and integrated pneumatic pouches. Further, aspects such as stiffness and weight that is added to the structure would need to be considered as well.

4.1.1.2.2 Comparison of the motion range

Depending on the radii and deformation range, the two bio-inspired actuators show some distinct differences. The range of motions that can be generated by the integrated pneumatic pouches is limited to single-curved bending. The cellular actuator itself could potentially also create a 2-dimensional structure that is capable of changing between double-curved states (Pagitz and Kappel 2014).

Both actuators proved capable to actuate 2-dimensional compliant devices. However, they are best-suited for the actuation of only certain compliant shading devices. The following gives some specific considerations on the actuation of the devices existing so far:

Flectofin®

The Flectofin® possesses no folding line or area of increased compliance to amplify the motion or reduce stresses. Thus, high actuation forces are required to induce the lateral-torsional buckling by a bending of the midrib. Due to the limited width of the midrib, the integration of pneumatic pouches that can generate high enough force seems little promising. Also, the placement of an external pouch between midrib and an external supporting structure is not likely to achieve the necessary actuation stroke within the given limits in dimension. More complex bellow-like structures would have to be developed. For the action of the Flectofold, a cellular structure is the more promising approach. Compared to an actuation by compressive force applied externally the forces will be distributed more evenly over the length of the midrib.

Flectofold

Both bio-inspired actuation principles proved their ability to actuate the Flectofold within functional demonstrators. By the integration of the pneumatic pouches within the curved folding line, additionally the pre-fold that is not required anymore. This eliminates the risk of functionality loss that would arise from a loss of the pre-fold. Potentially, the actuation by an integrated pouch bending the midrib and/or the flaps is possible as well.

The pressurized cellular actuator also proved capable to generate the required bending of the Flectofold midrib. However, as mentioned above, the actuation of the planar surface does not exploit the functionality of the system completely to justify the increased manufacturing complexity. An actuation of the folding lines is potentially possible but requires a miniaturization of the system. For the cellular actuator the complete merging of structure and actuator, as in the biological role model, should be envisaged.

Flexafold

As just mentioned, the actuation of distinct hinge zones with small measures is not feasible with the pressurized cellular actuator based on GFRP developed here. Further, as the Flexafold possesses only straight folding lines, indirect actuation by surface bending is not possible here. Straight-line folding is possible by the integrated pneumatic pouch, as demonstrated by the Flexafold prototype. Also, here no pre-fold is required. Further refinements are needed to increase the achieved folding angles. Still the actuation of folding lines can be considered one of the major strengths of the integrated pneumatic pouches.

Especially within the Flexafold also conventional actuation mechanisms reach their limits. Maintaining advantages as the self-contained system and no external supports or guiding structures for the motion, only an installed cable system could trigger the closing of the device.

4.1.1.2.3 Comparison on the mechanical complexity

The integrated pneumatic pouches or chambers can be designed, produced and integrated in a fast and simple way. The 2-dimensional fabrication process is of much lower complexity than the design and production of a pressurized cellular structure. Here, each cell and pouch need to be manufactured individually and joint in an additional process step. Moreover, for the actuation of a 2-dimensional surface, the mounting on this surface is necessary. On the other hand, the cellular approach offers the advantage that the individual cells and pouches are still accessible. Thus, they can be replaced or repaired if needed. This is not possible for the integrated pneumatic pouches within the laminate build-up of a composite. In case of a failure, the entire element needs to be replaced. In an entirely integrated approach like this, however, the pneumatic pouch is well protected from environmental influences.

Compared to conventional actuators, both bio-inspired actuation concepts possess a compliant construction principle. Due to the absence of friction and wear, no lubricants are needed at the component itself, reducing or even abolishing the maintenance of the elements. In comparison, the lens-shaped external pneumatic pouch is also easy to produce. However, the mechanical complexity of electric motors themselves is high. Additional constructional complexity and effort arises here from the mounting of the system with the hinges and joints that allow for rotation and translation. They require regular inspection and maintenance. The self-contained character of the biomimetic integrated actuators offers more freedom to the mounting detail. Further, the pressure supply can be placed centrally within the building, making access and maintenance easier than on the individual shading devices placed on the façade.

4.1.1.3 Variable stiffness

The concept of an adaptive stiffness promises remedy to the inherent conflict of compliant systems to be flexible enough to allow the envisioned deformation while at the same time being stiff enough to carry the self-weight and high external loads.

For both the developed biomimetic actuators the functionality of an adaptive stiffness can be added by a second counteracting actuator. This allows the decoupling of internal pressure and deformation. The increased internal pressure leads to an increased stiffness of the overall structure. Thus, the maximum stiffness depends greatly on the maximum internal pressure the cells or laminate with the integrated pneumatic pouches can

bear. With the maximum pressure given as limitations, the maximum stiffening potential is not given at all positions, as the pressure ratio between the counteracting actuators needs to be maintained to keep the desired deformation state.

For both actuation approaches the pressure dependent stiffness was demonstrated by the test specimen. The measured stiffening factor was clearly higher for the cellular structure (2.5 compared to 1.4-1.6). This can be attributed to the higher volume of the pressure pouches. Consequently, a higher pressure-dependent contribution to the overall stiffness exists for the cellular structure. Due to the high peeling stresses introduced by the integrated pneumatic pouches and the resulting limitations, the potential range of stiffening is potentially better for the pressurized cellular actuator.

4.2 REFLECTION OF RESEARCH HYPOTHESIS AND AIM

As stated in the research hypothesis, the two case studies demonstrated that the actuation principles of biological role models can contribute to the development of a joint-free actuation mechanism for technical compliant systems with continuous kinematics. As intended, the case studies laid out the entire biomimetic process from the search of the biological role models over the abstraction process to the fabrication of first technical prototypes. A pressurized cellular structure inspired by cellular built-up of plants in general, and bulliform cells of *Sesleria nitida* was developed. Further the ultrastructure of the pressurized wing vein of *Graphosoma lineatum italicum* provided inspiration for a laminate built-up that allows the integration of pressurized pouches for actuation into the laminate built-up of a fibre-reinforced composite without delamination. Within this process new insight into the functional principles of the investigated biological role model were gained. Within a FEA it was shown that the bulliform cells are capable to open to leaf folding against the present pre-stress with a variation in turgor naturally occurring. Microscopic investigation of the wing vein of *Graphosoma lineatum italicum* revealed the presence of extensible resilin around the pressurized chamber.

These principles were abstracted to develop a joint-free actuator that can be integrated into two-dimensional compliant systems and actively actuated. The developed actuation principles show the assumed advantages over conventional actuation mechanisms. The prototypes showed a reduced number of moving parts without friction or wear at the device itself. Also, the bio-inspired actuators are self-contained. This means they do not require external supports and allow for simplified mounting details. Further, no adaptation or reinforcement of the 2-dimensional compliant was needed due to the distributed

introduction of the actuation forces. Due to the integrated design, minimal additional space for the actuator is needed at the façade.

The physical prototypes also proved feasible to actuate an exemplary 2-dimensional compliant shading device. Thus, the final actuator prototypes of the biomimetic workflow are a successful proof of concept for the developed bio-inspired actuation concepts. Additionally, bio-inspired variable stiffness concepts based in an antagonistic actuator set-up were successfully developed within both case studies, and their functionality was demonstrated through physical specimen. Whether the developed variable stiffness concepts can temporarily stiffen the compliant systems they actuate, was not within the scope of this thesis and needs to be assessed in further investigations.

The development of the actuator and variable stiffness concept followed the top-down biomimetic process. Especially for the variable stiffness concept clear similarities between the abstracted functional principle showed. Due to the high abstraction level and the focus on fluidic actuation, this is not surprising as the same fundamental laws apply. Nevertheless, the technical implementations differ clearly. Within both case studies it became apparent that the biological role models are far more sophisticated when it comes to multifunctionality and complex construction on the different hierarchical levels. In the hierarchical built-up of biological materials, the different constituents are aligned down to the molecular level to serve their multifunctional purpose best. This bears great potential for further technical developments.

4.3 FUTURE DIRECTIONS

A specific outlook is already given for each case study. Therefore, only future directions for the topic of integrated complaint actuation shall be given here. To be used within architectural application for both developed concepts a more in-depth investigation of the used material system is needed to ensure the functionality over the entire service time, also when exposed to environmental influences such as UV radiation, humidity and temperature variations.

Developed biomimetic systems will only be successful if they fulfil the structural demands, such as expected loads or geometrical requirements, as well as more general demands such as low cost, high quality and reduced development time (Gramüller et al. 2014). Therefore, the next step could be to fully characterize the properties, limitations and physical boundaries of the developed actuation concepts and the design variables involved. These depend on many counteracting parameters, such as material, scale, and geometry, and can be adjusted to

specific demands. A design tool to support the design of compliant integrated actuation for compliant kinetic structures could be developed in the long term. For the application to 2-dimensional kinetic system, this becomes even more complex as additionally the interplay of actuation and folding pattern needs to be considered. The variables of the folding patterns can potentially be altered to support the actuation system actuation.

In addition, a further assessment of the adaptive stiffness concepts is needed, to see whether it is feasible to be deployed for the support against high external loads. Especially for the integrated pneumatic pouches some limitations in forces that can be generated are given by the peeling strength of the laminate. In this regard, it will also be of importance if the actuation system can be distributed or is restricted to a small region within the 2-dimensional compliant kinetic systems. In other words, if for the potential stiffening with the pneumatic actuators these can be applied to bending surfaces or if only the folding lines can be actuated, as is the case for straight line folding. It also should be analysed in more depth, which advantages and benefits arise from the variable stiffness concept compared to just building a stiffer overall system. These advantages might include a lower energy consumption during normal operation conditions and a higher deformation range capability. Such considerations might lead back to the basic question of whether a system should be inherently stiff and require softening for a shape change or it should be inherently compliant and require stiffening to bear temporarily higher loads. As mentioned in the beginning, both approaches have specific advantages and disadvantages. Which advantages predominate depends on the specific application.

Independent from the potential stiffness variation the antagonistic set-up of integrated actuators within the bending surfaces and/or the folding lines potentially enables the system to change from a concave to a convex configuration. Applications of this feature might be worth exploring. Regarding the pressurized cellular actuator, the potential that arises from merging of the structure and actuation could be explored. One aspect are shape variations of double curves surfaces. Here, application scenarios might be large-scale shape changing installations. The approach of the integrated pneumatic pouches already proved feasible for the integrated actuation of large-scale architectural installations. FIG. 4.2 shows the ITECH Research Demonstrator 2018-19, a large-scale compliant architecture. It is composed of two adaptive folding elements fabricated by industrial tape-laying technology from a composite of carbon fibers and a thermoset matrix. The kinetic behaviour of the two elements is achieved by the pneumatic actuation of distinct compliant hinge zones. The hinge zones can be actuated with comparatively low-pressure values of 0.8 bar in the horizontal and 0.4 bar in the vertical hinges. A continuous variation of actuation angles between 0° and approx. 80° is possible.



FIG. 4.2: ITECH research demonstrator 2018/19. (Photo by ICD/ITKE/ITFT)

The ITECH Research Demonstrator 2018-19 also is a good example for the intended contribution of the thesis towards the merging of structure and actuator in adaptive compliant kinetic systems and the new possibilities arising from nature's elegant and integrative design principles.

5 APPENDIX

A. CASE STUDY I

A1. Manufacturing process GFRP cells

To manufacture the GFRP cells with compliant hinges, a silicone mould representing the pressurizable volume was produced. Layers of woven glass fibre prepreg sheets (prepreg details: woven glass fibre fabric pre-impregnated with epoxy resin based on bisphenol A (40 wt%) Type ET222 (SAATI S.P.A.), multifilament: E glass (fineness 680d) weave: Twill 2/2, surface weight: 165 g/m²) were stacked onto it in a variable number of layers to achieve the defined wall thicknesses. The fibre orientation within the hinges was 0/90°. After the prepreg stacking, the mould was placed into a vacuum bag. The applied pressure pressed the prepreg sheets together while the epoxy was cured in an oven at 125° for 2 hours. The cells were pressurized by pouches made from heat-weldable airtight TPU-coated nylon (area density: 70 g/m²) placed inside the technical cells and connected by tubes.

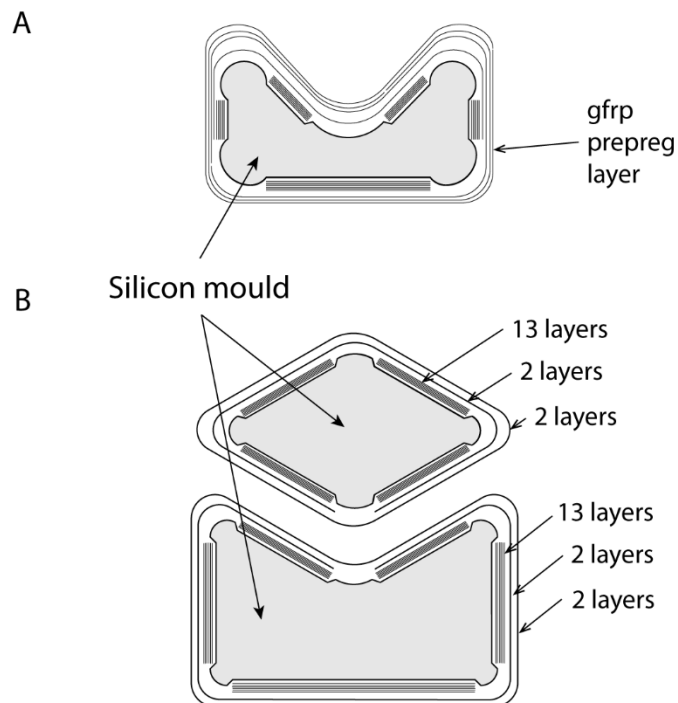


Figure A 1: Stacking sequence of the pressurized cellular structures. (A) The 40 mm wide for the actuation prototype and (B) the 80 mm wide cells for the variable stiffness prototype.

A2. Details on the variable stiffness cellular actuator FEA and physical testing

For greater precision orthotropic material properties were assumed for the GFRP (see Table A 1). Additionally, the thickness of the cell walls and hinges were adjusted to the values measured for the physical prototype (side walls: 1.9 mm, hinges: 0.61 mm). Further gravity was considered in this simulation.

Table A 1: Material properties assumed for the GFRP assumed for the FE simulation.

Density (g/cm ³)	1.8
Young's modulus X direction (MPa)	15,000
Young's modulus Y direction (MPa)	15,000
Young's modulus Z direction (MPa)	6,000
Poisson's ratio XY	0.05
Poisson's ratio YZ	0.3
Poisson's ratio XZ	0.3
Shear modulus XY (MPa)	5,000
Shear modulus YZ (MPa)	2,500
Shear modulus XZ (MPa)	2,500

In a numerical 3-point bending test, in accordance to the physical testing, the displacement of the supporting points (support distance: 400 mm) is restrained vertically and a load of 50 N is applied in the center. Further a symmetry constrained is applied to the centre vertical cell walls to restrict horizontal motion. The pressure inside the cells is kept at a constant level using the d command in the simulation and proportional pressure regulator valve (VPPE-3-1-1/8-6-010-E1, Festo Vertrieb GmbH & Co. KG, Esslingen, Germany) controlling the pressure in the physical experiment. The testing speed in the physical experiment was 10 mm/min and the experiments were conducted using a ZWICK universal testing machine 1455.

A3. Direct comparison FEA and physical test results

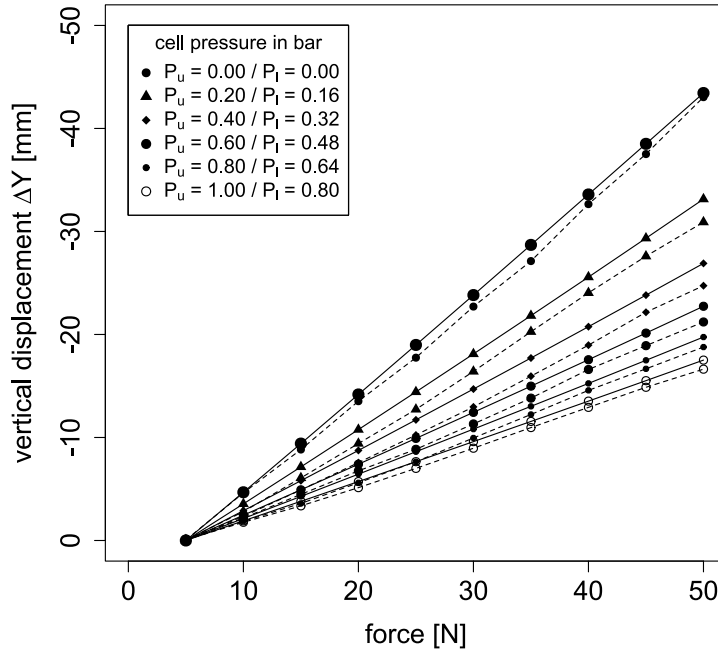


Figure A 2: Direct comparison of the results of the physical experiments and FE-simulations for the double-cell actuator. Shown is the maximum displacement (ΔY) at different inner pressures in the upper (P_u) and lower (P_l) cell compartment. — FEA - - - - experimental results.

Table A 2: Measured vertical displacement ΔY and the structure's increase apparent bending modulus by stiffening factor E^* for the physical experiments and the FE simulation at the different pressure levels.

P_u/P_l	ΔY		E^*	
	FEA	Physical	FEA	Physical
0.00/0.00	-43.4	-43.0	1	1
0.10/0.08	-37.5	-36.6	1.16	1.18
0.20/0.16	-33.1	-30.9	1.31	1.39
0.30/0.24	-29.7	-28.2	1.46	1.68
0.40/0.32	-26.9	-24.7	1.61	1.74
0.50/0.40	-24.6	-23.4	1.76	1.84
0.60/0.48	-22.7	-21.2	1.91	2.04
0.70/0.56	-21.1	-19.7	2.06	2.18
0.80/0.64	-19.7	-18.8	2.20	2.30
0.90/0.72	-18.5	-17.2	2.34	2.42
1.00/0.80	-17.5	-16.6	2.48	2.60

B. CASE STUDY II

B1. General sample information

Fiber-reinforced plastics components with an integrated actuation can be produced with a laminate set up known from previous general investigations of compliant FRPs. The laminate set-up consists mainly of glass-fiber-reinforced prepreg, elastomer foil, and PVC foil. The materials and their specifications are listed in Table B 1.

Table B 1: Materials utilized for the specimen production of fiber-reinforced plastics with integrated pneumatic actuation

designation	description	product details
glass fiber prepreg	woven glass fiber fabric pre-impregnated with epoxy resin based on bisphenol A (40 wt%) Type ET222 (SAATI S.P.A.)	multifilament: E glass (fineness 680d) weave: Twill 2/2 surface weight: 165 g/m ² thickness: 0.13 mm
elastomer foil	Kraibon Type HHZ9578/99 (Gummiwerk Kraiburg)	thickness: 0.50 mm elongation at break: 117%
PVC foil	soft PVC (polyvinyl chloride) coating foil, opaque (RAL 9016)	thickness: 0.18 mm
PTFE foil	glass fiber fabric coated with PTFE (polytetrafluoroethylene)	thickness: 0.13 mm
TPU-coated fabric	Ripstop-Nylon, 40den, TPU-coated (one-sided transparent thermoplastic polyurethane), heat weldable	Area density: 70 g m ⁻²

All specimens tested were manually stacked in the laminate sequence described in the following paragraphs for each test. The stacked laminates were pressed in a hot press under a vacuum of 150 mbar. The pressing parameters were: start/end temperature 60 °C; heating rate 6.67 °C/min; consolidation temperature 110 °C; consolidation time 40 min; cooling rate 5.45 °C/min; effective pressure 2.5 bar. A 20 x 1 mm metal inlay made of stainless steel was used to create the thinner hinge zone.

B2. Interlaminar adhesion (T-peel test)

The integration of expanding elements such as pneumatic chambers into fiber-reinforced plastics, which usually consist of multilayer structures, poses the challenge of interlaminar delamination. T-peel tests were performed according to (DIN EN ISO 11339:2010-06 2010-06) to determine the interlaminar adhesion between the various materials used. This test is generally used to examine the strength of an adhesive bond between flexible joined parts. The pressed individual layers of elastomer foil and woven glass-fiber prepreg in the composite can be considered as glued layers, so that the T-peel test can also be used to examine the interlaminar adhesion of the flexible specimens. The specimen size was 25 x 200 mm (width x length), whereby the evaluated test length was 150 mm as 50 mm were used for specimen clamping and not interconnected during pressing. To avoid adhesion in this area, an intermediate layer of PTFE foil (PTFE-coated glass fabric; thickness: 0.13 mm; nom. weight: 270 g m⁻²) was placed between the two middle layers before pressing. The test speed of the upper clamp was 10 m/min. The average peeling force was evaluated (n=10).

The adhesion between the GFRP (tested with a fiber direction of $\pm 45^\circ$, setting the tensile direction as the 0° axis) and the elastomer foil and between the two materials with themselves was tested. The samples were named:

E-P (elastomer3f/prepreg2f/PTFE foil/elastomer2f/prepreg2f/elastomer),

P-P (elastomer3f/prepreg2f/PTFE foil/ prepreg2f/elastomer3f) and

E-E (elastomer/prepreg2f/elastomer2f/PTFE foil/elastomer2f/prepreg2f/elastomer).

Micro-section images of T-peel test specimens were made to check the crack path and confirm the peel plane.

B3. Experimental details on determining the angle pressure relationship

Sample production:

The system is composed of several layers of glass-fiber prepreg with a fiber orientation of $\pm 45^\circ$ in a gradient hinge zone and an airtight pneumatic pouch surrounded by elastomeric layers. Actuation samples of the size of 200 mm x 320 mm with a 20 mm hinge zone and an embedded pneumatic pouch were produced. The pneumatic pouches, integrated into the FRP, were fabricated from airtight TPU-coated nylon fabric. Two pieces of the fabric were melted together by using an iron and pressure. A 20 x 160 mm rectangular piece of PTFE foil with rounded edges and a 7 mm wide extension was placed in between the two layers to create the air chamber and air inlet. After heat pressing, a tube (polyurethane, 4 mm outer diameter) was inserted into the pouch part and sealed airtight by using a shrinking tube and low viscosity superglue. Initial tests showed strong variations in angle-pressure relationship within the first loading cycles because of the stepwise detaching of the pouch fabric from the elastomer, followed by a stabilization in angle-pressure relationship. Therefore, the pouches were placed between two sheets of PTFE foil with the same dimensions to avoid an initial adhesion of the pouch fabric to the elastomer and to obtain reproducible angle-pressure relationship.

Angle measurements:

For assessing the angle-pressure relationship, one plate end of the samples was clamped onto a vertical board, whereas the other was allowed to rotate freely. A proportional pressure regulator valve (VPPE-3-1-1/8-6-010-E1, Festo Vertrieb GmbH & Co. KG, Esslingen, Germany) was used to apply pressure in a stepwise fashion from 0 to 2 bar. The angular displacement of the free plate end was measured in an automated manner by image processing. Green marks were attached to the edge of the rotating plate end. At set time steps, a picture was taken by using a webcam (Logitech C270 HD, hd 720p), and the slope was processed by a linear least-squares regression in Python 3 (Python Software Foundation, <https://www.python.org/>). Each sample was subjected to a total of 15 cycles, whereby the pressure was increased stepwise in 11 steps. Each pressure step had a holding time of 5 minutes during which five values were taken. The time of the pauses between the cycles was 120 minutes to diminish the influence of viscoelastic effects of the elastomer on the measured results and to allow the sample to relax as far as possible to an angle of zero once again.

B4. Sample properties used in the numerical approaches

To be able to compare the numerical results with the actually measured angular displacement of the physical specimen, the exact determination of the material properties, in particular the measurement of the bending modulus, in the hinge zone was necessary. In accordance with (DIN EN ISO 14125 2011-05), a three-point bending test was performed on two different test set-ups: specimen 3L (PVC/±45°3f/elastomer) and specimen 4L (PVC/±45°4f/elastomer). The results of these tests were used to calculate the Young's modulus of the material for all specimens that were considered in the numerical simulations. The radius of the supporting pins was 2 mm, and the radius of the pressure pin was 5 mm. The support and pressure pin were chosen conforming to the specimen thicknesses (specimen 3L = 0.99 mm; specimen 4L = 1.1 mm). The supporting distance was 20 mm, corresponding to the average specimen thickness of 1 mm, and the test speed was 0.7 mm/min.

From the 3-point bending test a Young's modulus of 770 ± 230 MPa and 920 ± 105 MPa for the 3-layer (PVC/glass fibre prepreg ±45°3f/elastomer) and 4-layer (PVC/glass fibre prepreg ±45°4f/elastomer) samples were calculated, respectively (n=10; calculation between 0.05 and 0.5% elongation). Using a polynomial fitting, a Young's modulus of 310 MPa for a 1 layer sample was approximated.

The thickness of the upper and lower hinge plate section was measured for all samples by using an endoscope (Xcsource TE71 3D Digital Microscope / Endoscope, 20-800x) and the image-processing program ImageJ (Rasband, W.S., ImageJ, U. S. National Institutes of Health, Bethesda, Maryland, USA, <https://imagej.nih.gov/ij/>, 1997-2018). For each thickness, 10 values were measured, and the mean values were calculated.

B5. Results of the statistical tests on the cyclic loading

All statistical tests were conducted by using R (R Development Core Team 2008). The Shapiro-Wilk-test was used as a test of normality followed by the F-test of the equality of two variances and, depending on the outcome of the Student's t-test or the Welch-test. For the exceptional cases of a not normally distributed result, a Mood-test followed by a Mann-Whitney-test is conducted. $\alpha = 0.05$ for all statistical tests. It needs to be considered that the sample size these calculations are based on are small ($n = 11$).

Table B 2: Results of the statistical test conducted for the cyclic loading of one specimen.

	0.00 bar	0.40 bar	0.83 bar	1.19 bar	1.62 bar	2.06 bar
Cycles: 400 & 500						
Equality of variances	p-value = 0.5276 (F-test)	p-value = 0.0359 (F-test)	p-value = 0.7767 (F-test)	p-value = 0.5527 (F-test)	p-value = 0.1829 (F-test)	p-value = 0.7139 (F-test)
	p-value = 0.1250 (t-test)	p-value = 0.1216 (Welch- test)	p-value = 0.1171 (t-test)	p-value = 0.0082 (t-test)	p-value = 0.4018 (t-test)	p-value = 0.0679 (t-test)
Cycles: 300 & 500						
Equality of variances	p-value = 0.6134	p-value = 0.00979	p-value = 0.6856	p-value = 0.09858	p-value = 0.4527	p-value = 0.5237
	p-value = 0.0649 (t-test)	p-value = 0.04934 (Welch- test)	p-value = 0.00540 9 (t-test)	p-value = 0.00034 42 (t-test)	p-value = 0.6063 (t-test)	p-value = 0.00041 43 (t-test)
Cycles: 300 & 400						
Equality of variances	p-value = 0.8985 (F-test)	p-value = 0.5805 (F-test)	p-value = 0.4924 (F-test)	p-value = 0.2784 (F-test)	p-value = 0.5512 (F-test)	p-value = 0.3181 (F-test)
	p-value = 0.6768 (t-test)	p-value = 0.5426 (t-test)	p-value = 0.1002 (t-test)	p-value = 0.1002 (t-test)	p-value = 0.718 (t-test)	p-value = 0.01308 (t-test)
Cycles: 005 & 500						
Equality of variances	p-value = 0.01635 (F-test)	p-value = 0.05132 (F-test)	p-value = 0.5308 (Mood- test)	p-value = 0.02675 (F-test)	p-value = 0.06053 (F-test)	p-value = 0.2051 (F-test)
	p-value = 3.206e- 10	p-value = 1.679e- 07 (t-test)	p-value = 0.2703	p-value = 0.00015 69	p-value = 0.8237 (t-test)	p-value = 2.778e- 11 (t-test)

	(Welch-test)		(Mann-Whitney-test)	(Welch-test)		
Cycles: 005 & 100						
Equality of variances	p-value = 0.007921 (F-test)	p-value = 0.2536 (Mood-test)	p-value = 0.5921 (Mood-test)	p-value = 0.003344 (F-test)	p-value = 0.926 (F-test)	p-value = 0.1093 (F-test)
	p-value = 1.38e-07	p-value = 0.002516 (Mann-Whitney-test)	p-value = 0.005246 (Mann-Whitney-test)	p-value = 0.9792	p-value = 0.0008148	p-value = 0.01367

B6. Micro-section images of cyclic loading specimen

The effect of the dynamic actuation on the interfaces between the individual layers of the angle-pressure relationship specimens was investigated. For this purpose, parts were taken from an initial specimen that had been produced without the PTFE foil around the pouch and that therefore showed changes in the angle-pressure relationship with increasing cycle number. The specimen was subjected to 1000 load cycles between 0 and 1 bar (4 steps). Micro-section probes from the transition area (middle joint area to stiff component area, 3 cm length) were produced to check for possible delamination of the elastomer layers.

Micro-section probes were produced by embedding specimen probes into a colored or non-colored resin. After the curing of the embedding resin, the micro-section probes were milled down to the specimen and then finely ground and polished to create a very smooth, clean surface for observation under the reflected light microscope.

B7. Manufacturing process GFRP plates with integrated actuation

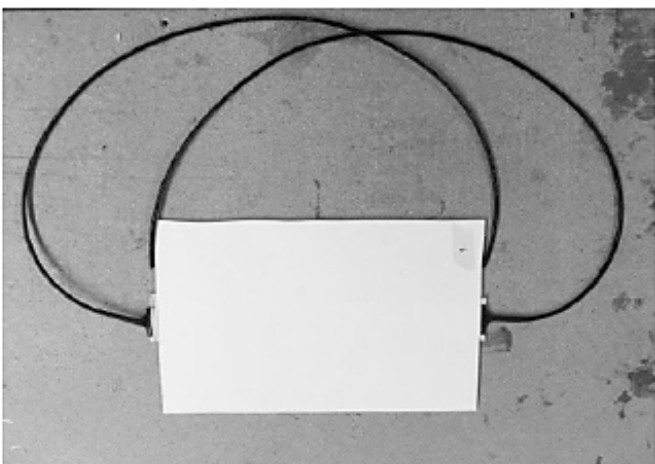
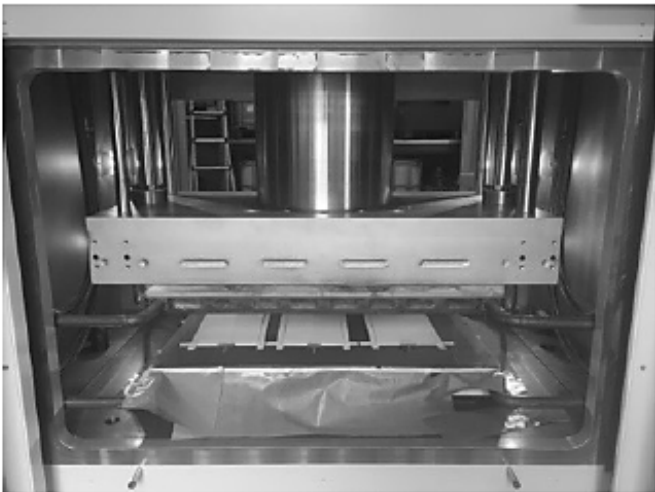
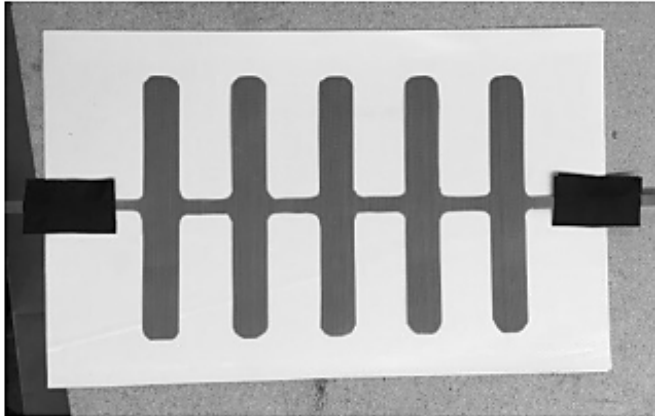


Figure B 1: Fabrication of samples. Top – Placement of the pneumatic pouch within the laminate setup. Middle – Heat pressing. C – Finished sample. Sample size: size of 200 mm x 320 mm. (Fenton 2018)

B8. Initial test on different plate thickness

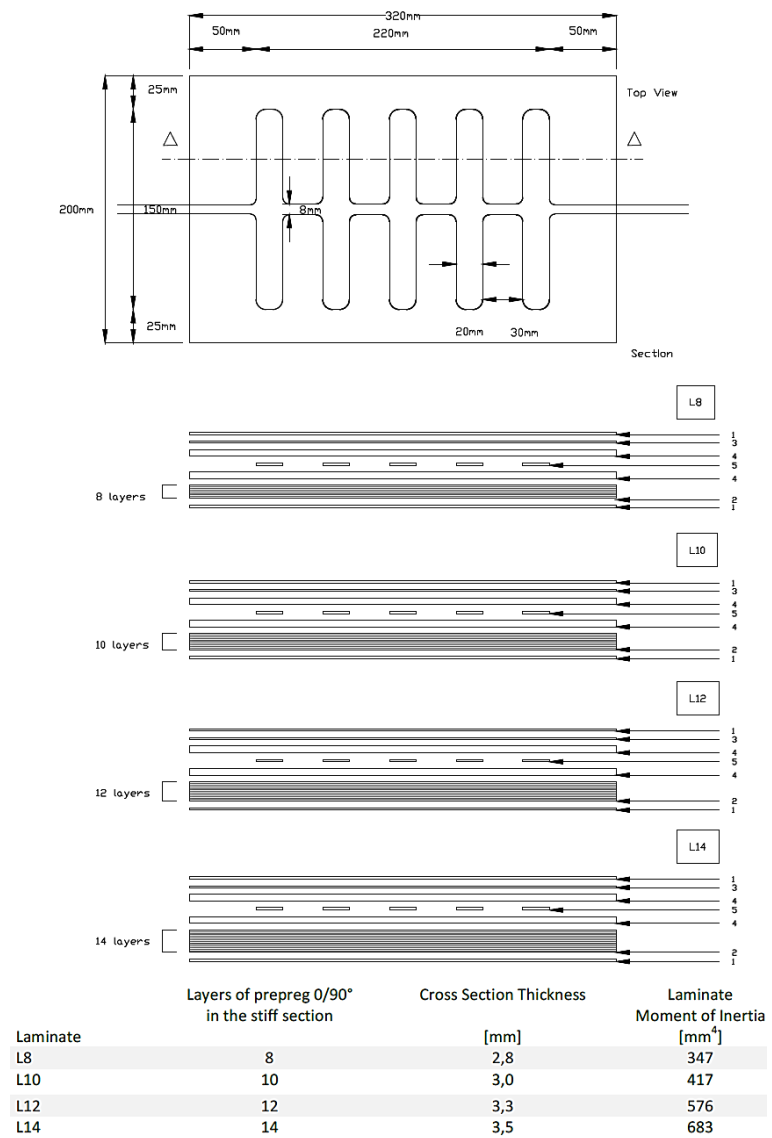


Figure B 2: Pouch geometry and laminate set-up for investigating the influence of plate thickness in the actuation behaviour. (Fenton 2018)

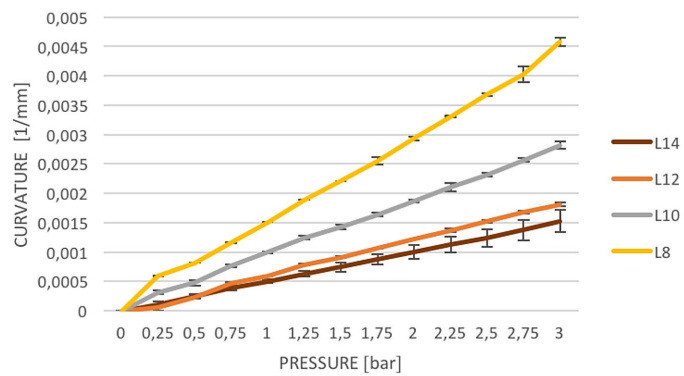


Figure B 3: Results of initial tests on the influence of plate thickness in the actuation behaviour. For experimental details see (Fenton 2018).

B9. Statistical test variable stiffness plates

All statistical tests were conducted by using R (R Development Core Team 2008). The Shapiro-Wilk-test was used as a test of normality followed by the F-test of the equality of two variances, followed by a Student's t-test. $\alpha = 0.05$ for all statistical tests. It needs to be considered that the sample size these calculations are based on are small ($n = 6$ for the reference; $n = 3$ for the `_ov` samples and $n = 4$ for the `_cv` samples).

Table B 3: Results of the statistical test conducted for variable stiffness plates with integrated pneumatic pouches.

	ref	0.6_ov	0.6_cv	1.2_ov	1.2_cv	1.8_ov	1.8_cv
ref	-	p= 0.27	p= 0.27	-	-	-	-
	-	p= 0.00	p= 0.00	-	-	-	-
0.6_ov	-	-	p= 0.80	p= 0.71	-	-	-
	-	-	p= 0.00	p= 0.00	-	-	-
0.6_cv	-	-	-	-	p= 0.80	-	-
	-	-	-	-	p= 0.00	-	-
1.2_ov	-	-	-	-	p= 0.66	p= 0.99	-
	-	-	-	-	p= 0.00	p= 0.00	-
1.2_cv	-	-	-	-	-	-	p= 0.87
	-	-	-	-	-	-	p= 0.00
1.8_ov	-	-	-	-	-	-	p= 0.75
	-	-	-	-	-	-	p= 0.00

B10. Initial test in influence of pouch geometry

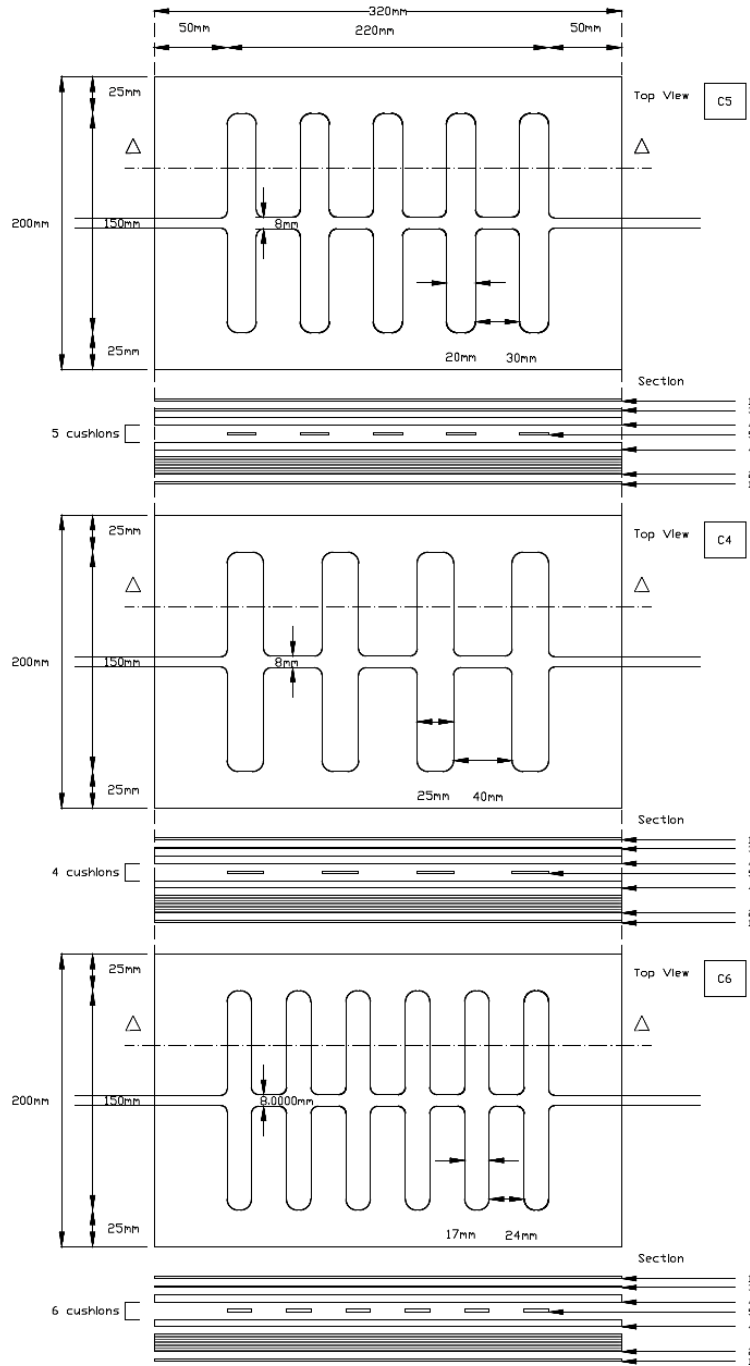


Figure B 4: Pouch geometries used in initial test on the influence of the cushion geometry on the actuation behaviour. (Fenton 2018)

B11. Typical failure of samples at elevated pressures

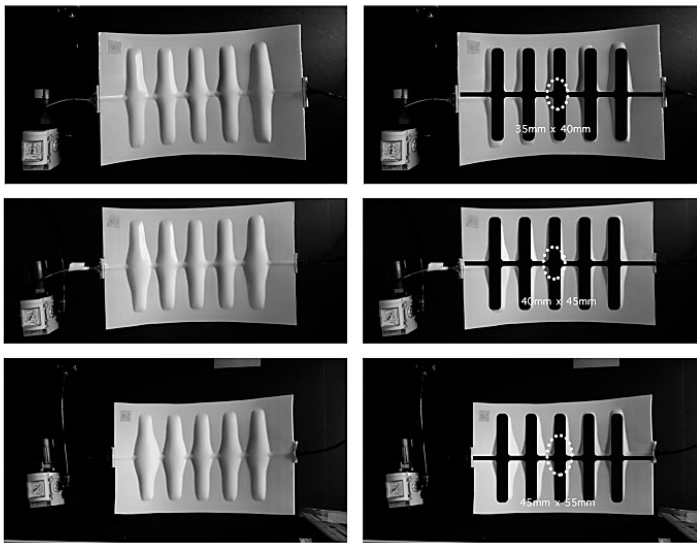


Figure B 5: Typical failure of samples observed at high pressure levels above 2 bar. The images show the clear widening of the pneumatic pouches/chamber with proceeding delamination until eventually a busting point at the plate edges is reached. Top: L10 sample. Middle: L12 sample. Bottom: L14 sample. Specimen size is 200 mm x 320 mm. (Fenton 2018)

6 REFERENCES

- Alvarez, J. M., J. F. Rocha, and S. R. Machado. 2008. "Bulliform cells in *Loudetiopsis chrysothrix* (Nees) Conert and *Tristachya leiostachya* Nees (Poaceae): Structure in relation to function." *Brazilian Archives of Biology and Technology*, 51(1): 113–119. <https://doi.org/10.1590/S1516-89132008000100014>.
- Anderson, E. H., ed. 2004. *Smart Structures and Materials 2004: Industrial and Commercial Applications of Smart Structures Technologies*: SPIE.
- Annunziata, S., and A. Schneider. 2012. "Physiologically Based Control Laws Featuring Antagonistic Muscle Co-Activation for Stable Compliant Joint Drives." *Applied Bionics and Biomechanics*, 9(3): 249–266. <https://doi.org/10.1155/2012/503818>.
- Appel, E., L. Heepe, C.-P. Lin, and S. N. Gorb. 2015. "Ultrastructure of dragonfly wing veins: composite structure of fibrous material supplemented by resilin." *Journal of anatomy*, 227(4): 561–582. <https://doi.org/10.1111/joa.12362>.
- Ashby, M. F. 2013. "Material selection strategies." In *Materials and the Environment*: 227–273: Elsevier.
- Azadi, M., S. Behzadipour, and G. Faulkner. 2009. "Antagonistic variable stiffness elements." *Mechanism and Machine Theory*, 44(9): 1746–1758. <https://doi.org/10.1016/j.mechmachtheory.2009.03.002>.
- Backé, W., and A. Klein. 2004. "Fluidpower Actuators." In *Actuators*, edited by H. Janocha: 155–232, Berlin, Heidelberg: Springer Berlin Heidelberg.
- Balani, K., V. Verma, A. Agarwal, and R. Narayan. 2014. *Biosurfaces*, Hoboken, NJ, USA: John Wiley & Sons, Inc.
- Barrett, R. M., and C. M. Barrett. 2014. "Biomimetic FAA-certifiable, artificial muscle structures for commercial aircraft wings." *Smart Materials and Structures*, 23(7): 74011. <https://doi.org/10.1088/0964-1726/23/7/074011>.
- Bauman, J. T. 2008. *Fatigue, stress, and strain of rubber components: A guide for design engineers*, Munich: Hanser.
- Baumgart, F. W. 2000. "Stiffness — an unknown world of mechanical science?" *Injury*, 31: 14–84. [https://doi.org/10.1016/S0020-1383\(00\)80040-6](https://doi.org/10.1016/S0020-1383(00)80040-6).
- Bent, A. A., N. W. Hagood, and J. P. Rodgers. 1995. "Anisotropic Actuation with Piezoelectric Fiber Composites." *Journal of*

- Intelligent Material Systems and Structures*, 6(3): 338–349. <https://doi.org/10.1177/1045389X9500600305>.
- Bergamini, A., R. Christen, and M. Motavalli. 2007. "Electrostatically tunable bending stiffness in a GFRP–CFRP composite beam." *Smart Materials and Structures*, 16(3): 575–582. <https://doi.org/10.1088/0964-1726/16/3/004>.
- Betts, J. G., P. DeSaix, E. Johnson, J. E. Johnson, O. Korol, D. H. Kruse, B. Poe, J. A. Wise, M. Womble, and K. A. Young. 2017. *Anatomy and physiology*, Houston, Texas: OpenStax College, Rice University.
- Betz, O., A. Birkhold, M. Caliaro, B. Eggs, A. Mader, J. Knippers, O. Röhrle, and O. Speck. 2016. "Adaptive Stiffness and Joint-Free Kinematics: Actively Actuated Rod-Shaped Structures in Plants and Animals and Their Biomimetic Potential in Architecture and Engineering." In *Biomimetic Research for Architecture and Building Construction*, edited by J. Knippers, K. G. Nickel, and T. Speck: 135–167, Cham: Springer International Publishing.
- Binz, H., ed. 2016. *Hybride Intelligente Konstruktionselemente (HIKE) - Abschlusskolloquium der DFG-Forschergruppe 981, Stuttgart, 10.11.2015*, Stuttgart: Universität Stuttgart Institut für Konstruktionstechnik und Technisches Design.
- Bischoff, M. 2015. *Nonlinear Finite Element Analysis: Lecture*, University of Stuttgart.
- Born, L., A. Körner, G. Schieber, A. S. Westermeier, S. Poppinga, R. Sachse, P. Bergmann, O. Betz, M. Bischoff, T. Speck, J. Knippers, M. Milwich, and G. T. Gresser. 2017. "Fiber-Reinforced Plastics with Locally Adapted Stiffness for Bio-Inspired Hingeless, Deployable Architectural Systems." *Key Engineering Materials*, 742: 689–696. <https://doi.org/10.4028/www.scientific.net/KEM.742.689>.
- Briggs, J. P., and P. P. Castaneda. 2002. "Variational Estimates for the Effective Response of Shape Memory Alloy Actuated Fiber Composites." *Journal of Applied Mechanics*, 69(4): 470–480. <https://doi.org/10.1115/1.1464873>.
- Brunner, A. J., M. Barbezat, C. Huber, and P. H. Flüeler. 2005. "The potential of active fiber composites made from piezoelectric fibers for actuating and sensing applications in structural health monitoring." *Materials and Structures*, 38(5): 561–567. <https://doi.org/10.1007/BF02479548>.
- Brusewitz, G. H., Pitt R. E., and Q. Gao. 1989. "EFFECTS OF STORAGE TIME AND STATIC PRELOADING ON THE RHEOLOGY OF POTATO TISSUE." *Journal of Texture Studies*, 20(3): 267–284. <https://doi.org/10.1111/j.1745-4603.1989.tb00439.x>.

- Caliaro, M., F. Schmich, T. Speck, and O. Speck. 2013. "Effect of drought stress on bending stiffness in petioles of *Caladium bicolor* (Araceae)." *American journal of botany*, 100(11): 2141–2148. <https://doi.org/10.3732/ajb.1300158>.
- Campbell, N. A., J. B. Reece, L. A. Urry, M. L. Cain, S. A. Wasserman, P. V. Minorsky, and R. Jackson. 2016. *Biologie: Always learning*, Hallbergmoos: Pearson.
- Capadona, J. R., K. Shanmuganathan, D. J. Tyler, S. J. Rowan, and C. Weder. 2008. "Stimuli-responsive polymer nanocomposites inspired by the sea cucumber dermis." *Science (New York, N.Y.)*, 319(5868): 1370–1374. <https://doi.org/10.1126/science.1153307>.
- Carl, K. 2008. *Technische Biologie des Tasthaar-Sinnessystems als Gestaltungsgrundlage für taktile stiftführende Mechanosensoren*, PhD dissertation, Technische Universität Ilmenau.
- Chen, Y., W. Yin, Y. Liu, and J. Leng. 2011. "Structural design and analysis of morphing skin embedded with pneumatic muscle fibers." *Smart Materials and Structures*, 20(8): 85033. <https://doi.org/10.1088/0964-1726/20/8/085033>.
- Chenal, T. P., J. C. Case, J. K. Paik, and R. K. Kramer. 2014. "Variable stiffness fabrics with embedded shape memory materials for wearable applications." *2014 IEEE/RSJ International Conference on Intelligent Robots and Systems*: 2827–2831.
- Cheng, K. B., and M. Hubbard. 2008. "Role of arms in somersaulting from compliant surfaces: a simulation study of springboard standing dives." *Human movement science*, 27(1): 80–95. <https://doi.org/10.1016/j.humov.2007.05.004>.
- Chillara, V.S.C., L. M. Headings, and M. J. Dapino. 2016. "Multifunctional composites with intrinsic pressure actuation and prestress for morphing structures." *Composite Structures*, 157: 265–274. <https://doi.org/10.1016/j.compstruct.2016.08.044>.
- Cousins, W. J. 1978. "Young's modulus of hemicellulose as related to moisture content." *Wood Science and Technology*, 12(3): 161–167. <https://doi.org/10.1007/BF00372862>.
- Cranford, S. W., A. Tarakanova, N. M. Pugno, and M. J. Buehler. 2012. "Nonlinear material behaviour of spider silk yields robust webs." *Nature*, 482(7383): 72–76. <https://doi.org/10.1038/nature10739>.
- Daerden, F. 1999. *Conception and Realization of Pleated Pneumatic Artificial Muscles and their Use as Compliant Actuation Elements*, PhD dissertation, Vrije Universiteit Brussel.

- Deaconescu, T., and A. Deaconescu. 2018. "Static analysis of a torsion motor generating flexion - extension motions of the elbow." *MATEC Web of Conferences*, 178(3): 7005. <https://doi.org/10.1051/matecconf/201817807005>.
- DIN EN ISO 11339:2010-06. 2010. "Adhesives - T-peel test for flexible-to-flexible bonded assemblies (ISO 11339:2010); German version EN ISO 11339:2010." *DIN EN ISO 11339*, Berlin, Germany.
- DIN EN ISO 14125. 2011. "Fibre-reinforced plastic composites - Determination of flexural properties (ISO 14125:1998 + Cor.1:2001 + Amd.1:2011); German version EN ISO 14125:1998 + AC:2002 + A1:20." *DIN EN ISO 14125*, Berlin, Germany.
- DITF. 2016. "NICHT NUR HEISSE LUFT: Bewegung und Kraft mit pneumatischen Textilien." <https://www.ditf.de/de/index/aktuelles/pressemeldungen/detail/nicht-nur-heisse-luft.html> (Oct. 5, 2021).
- Dumais, J., and Y. Forterre. 2012. "'Vegetable Dynamicks': The Role of Water in Plant Movements." *Annual Review of Fluid Mechanics*, 44(1): 453–478. <https://doi.org/10.1146/annurev-fluid-120710-101200>.
- Erk, K. A., K. J. Henderson, and K. R. Shull. 2010. "Strain stiffening in synthetic and biopolymer networks." *Biomacromolecules*, 11(5): 1358–1363. <https://doi.org/10.1021/bm100136y>.
- Ettema, G.J.C., and P. A. Huijing. 1994. "Skeletal muscle stiffness in static and dynamic contractions." *Journal of Biomechanics*, 27(11): 1361–1368. [https://doi.org/10.1016/0021-9290\(94\)90045-0](https://doi.org/10.1016/0021-9290(94)90045-0).
- Fenton, S. K. 2018. *Biomimetic design based mechanisms in Architecture*, Brussels: Master's Thesis.
- Finckh, V., K. Haigis, C. Riethmüller, and G. Gresser. 2019. *Entwicklung leichter, textiler Druckbehälterarmierungen für Bauanwendungen am Beispiel pneumatischer Linienaktoren (IGF 18587 N)*.
- Finney, E. E., and a. C. W. Hall, JR. 1967. "Elastic Properties of Potatoes." *Transactions of the ASAE*, 10(1): 4–8. <https://doi.org/10.13031/2013.39578>.
- Forterre, Y. 2013. "Slow, fast and furious: understanding the physics of plant movements." *Journal of experimental botany*, 64(15): 4745–4760. <https://doi.org/10.1093/jxb/ert230>.
- Fowler, R. M., L. L. Howell, and S. P. Magleby. 2011. "Compliant space mechanisms: a new frontier for compliant

- mechanisms." *Mechanical Sciences*, 2(2): 205–215. <https://doi.org/10.5194/ms-2-205-2011>.
- Galloway, K. C., J. E. Clark, and D. E. Koditschek. 2013. "Variable Stiffness Legs for Robust, Efficient, and Stable Dynamic Running." *Journal of Mechanisms and Robotics*, 5(1): 100. <https://doi.org/10.1115/1.4007843>.
- Ghorbani-Tanha, A. K., M. Rahimian, and A. Noorzad. 2011. "A Novel Semiactive Variable Stiffness Device and Its Application in a New Semiactive Tuned Vibration Absorber." *Journal of Engineering Mechanics*, 137(6): 390–399. [https://doi.org/10.1061/\(ASCE\)EM.1943-7889.0000235](https://doi.org/10.1061/(ASCE)EM.1943-7889.0000235).
- Gibson, L. J. 2012. "The hierarchical structure and mechanics of plant materials." *Journal of the Royal Society, Interface*, 9(76): 2749–2766. <https://doi.org/10.1098/rsif.2012.0341>.
- Gramüller, B., J. Boblenz, and C. Hühne. 2014. "PACS--Realization of an adaptive concept using pressure actuated cellular structures." *Smart Materials and Structures*, 23(11): 115006. <https://doi.org/10.1088/0964-1726/23/11/115006>.
- Grigore, M., and C. Toma. 2011. "Ecological implications of bulliform cells on halophytes, in salt and water stress natural conditions." *Studia Universitatis Vasile Goldis Arad, Seria Stiintele Vietii*, 21: 785–792.
- Guiducci, L., K. Razghandi, L. Bertinetti, S. Turcaud, M. Rüggeberg, J. C. Weaver, P. Fratzl, I. Burgert, and J. W. C. Dunlop. 2016. "Honeycomb Actuators Inspired by the Unfolding of Ice Plant Seed Capsules." *PloS one*, 11(11): e0163506. <https://doi.org/10.1371/journal.pone.0163506>.
- Haas, F., S. Gorb, and R. Blickhan. 2000. "The function of resilin in beetle wings." *Proceedings of the Royal Society of London. Series B: Biological Sciences*, 267(1451): 1375–1381. <https://doi.org/10.1098/rspb.2000.1153>.
- Haas, F., and R. Wootton. 1996. "Two basic mechanisms in insect wing folding." *Proceedings of the Royal Society of London. Series B: Biological Sciences*, 263(1377): 1651–1658. <https://doi.org/10.1098/rspb.1996.0241>.
- Hagood, N. W., and A. A. Bent. 1993. "DEVELOPMENT OF PIEZOELECTRIC FIBER COMPOSITES FOR STRUCTURAL ACTUATION." In *Proc., 34th Structures, Structural Dynamics and Materials Conference*: 599, Reston, Virginia.
- Ham, R., T. Sugar, B. Vanderborght, K. Hollander, and D. Lefeber. 2009. "Compliant actuator designs." *IEEE Robotics & Automation Magazine*, 16(3): 81–94. <https://doi.org/10.1109/MRA.2009.933629>.
- Hannaford, B., and J. Winters. 1990. "Actuator Properties and Movement Control: Biological and Technological Models." In

- Multiple Muscle Systems*, edited by J. M. Winters, and S. L.-Y. Woo: 101–120, New York, NY: Springer New York.
- Harrington, M. J., K. Razghandi, F. Ditsch, L. Guiducci, M. Rueggeberg, J. W. C. Dunlop, P. Fratzl, C. Neinhuis, and I. Burgert. 2011. "Origami-like unfolding of hydro-actuated ice plant seed capsules." *Nature communications*, 2: 337. <https://doi.org/10.1038/ncomms1336>.
- Heling, B., M. Hallmann, and S. Wartzack. 2017. "Hybrid Tolerance Representation of Systems in Motion." *Procedia CIRP*, 60: 50–55. <https://doi.org/10.1016/j.procir.2017.02.048>.
- Henke, M., J. Sorber, and G. Gerlach. 2012. "Multi-layer beam with variable stiffness based on electroactive polymers." In *Proc., SPIE Smart Structures and Materials + Nondestructive Evaluation and Health Monitoring*, edited by Y. Bar-Cohen, SPIE Proceedings: 83401P.
- Howell, L. L., S. P. Magleby, and B. M. Olsen. 2013. *Handbook of Compliant Mechanisms*, Oxford, UK: John Wiley & Sons Ltd.
- Huber, J. E., N. A. Fleck, and M. F. Ashby. 1997. "The selection of mechanical actuators based on performance indices." *Proceedings of the Royal Society of London. Series A: Mathematical, Physical and Engineering Sciences*, 453(1965): 2185–2205. <https://doi.org/10.1098/rspa.1997.0117>.
- Hübler, M., M. Gurka, S. Schmeer, and U. P. Breuer. 2013. "Performance range of SMA actuator wires and SMA–FRP structure in terms of manufacturing, modeling and actuation." *Smart Materials and Structures*, 22(9): 94002. <https://doi.org/10.1088/0964-1726/22/9/094002>.
- ISO 18458: 2015. "Biomimetics - Terminology, concepts and methodology." *ISO 18458*, Berlin, Germany.
- Jafari, A. 2014. "Coupling between the Output Force and Stiffness in Different Variable Stiffness Actuators." *Actuators*, 3: 270–284. <https://doi.org/10.3390/act3030270>.
- Janke, L., C. Czaderski, M. Motavalli, and J. Ruth. 2005. "Applications of shape memory alloys in civil engineering structures—Overview, limits and new ideas." *Materials and Structures*, 38(5): 578–592. <https://doi.org/10.1007/BF02479550>.
- Janocha, H. 2004a. *Actuators: Basics and applications*, Berlin: Springer.
- Janocha, H. 2004b. "Introduction." In *Actuators*, edited by H. Janocha: 1–17, Berlin, Heidelberg: Springer Berlin Heidelberg.

- Janocha, H. 2004c. "Unconventional Actuators." In *Actuators*, edited by H. Janocha: 233–336, Berlin, Heidelberg: Springer Berlin Heidelberg.
- Kadioglu, A., and R. Terzi. 2007. "A Dehydration Avoidance Mechanism: Leaf Rolling." *The Botanical Review*, 73(4): 290–302. [https://doi.org/10.1663/0006-8101\(2007\)73\[290:ADAMLR\]2.0.CO;2](https://doi.org/10.1663/0006-8101(2007)73[290:ADAMLR]2.0.CO;2).
- Karam, G. N., and L. J. Gibson. 1994. "Biomimicking of animal quills and plant stems: natural cylindrical shells with foam cores." *Materials Science and Engineering: C*, 2(1-2): 113–132. [https://doi.org/10.1016/0928-4931\(94\)90039-6](https://doi.org/10.1016/0928-4931(94)90039-6).
- Kim, S., C. Laschi, and B. Trimmer. 2013. "Soft robotics: a bioinspired evolution in robotics." *Trends in biotechnology*, 31(5): 287–294. <https://doi.org/10.1016/j.tibtech.2013.03.002>.
- Knippers, J., J. Cremers, M. Gabler, and J. Lienhard. 2012. *Construction Manual for Polymers + Membranes: Materials, Semi-Finished Products, Form Finding, Design*, Basel/Berlin/Boston: Walter de Gruyter GmbH.
- Knippers, J., and T. Speck. 2012. "Design and construction principles in nature and architecture." *Bioinspiration & biomimetics*, 7(1): 15002. <https://doi.org/10.1088/1748-3182/7/1/015002>.
- Knippers, J., T. Speck, and K. G. Nickel. 2016. "Biomimetic Research: A Dialogue Between the Disciplines." In *Biomimetic Research for Architecture and Building Construction*, edited by J. Knippers, K. G. Nickel, and T. Speck: 1–5, Cham: Springer International Publishing.
- Konrad, W., F. Flues, F. Schmich, T. Speck, and O. Speck. 2013. "An analytic model of the self-sealing mechanism of the succulent plant *Delosperma cooperi*." *Journal of theoretical biology*, 336: 96–109. <https://doi.org/10.1016/j.jtbi.2013.07.013>.
- Kornbluh, R. D., H. Prahlad, R. Pelrine, S. Stanford, M. A. Rosenthal, and P. A. von Guggenberg. 2004. "Rubber to rigid, clamped to undamped: toward composite materials with wide-range controllable stiffness and damping." In *Proc., Smart Structures and Materials*, edited by E. H. Anderson, SPIE Proceedings: 372.
- Körner, A., L. Born, A. Mader, R. Sachse, S. Saffarian, A. S. Westermeier, S. Poppinga, M. Bischoff, G. T. Gresser, M. Milwich, T. Speck, and J. Knippers. 2018. "Flectofold -a biomimetic compliant shading device for complex free form facades." *Smart Materials and Structures*, 27(1): 17001. <https://doi.org/10.1088/1361-665X/aa9c2f>.

- Kuder, I. K., A. F. Arrieta, W. E. Raither, and P. Ermanni. 2013. "Variable stiffness material and structural concepts for morphing applications." *Progress in Aerospace Sciences*, 63: 33–55. <https://doi.org/10.1016/j.paerosci.2013.07.001>.
- Lambers, H., F. S. Chapin, and T. L. Pons. 2008. *Plant Physiological Ecology*, New York, NY: Springer New York.
- Lan, X., Y. Liu, H. Lv, X. Wang, J. Leng, and S. Du. 2009. "Fiber reinforced shape-memory polymer composite and its application in a deployable hinge." *Smart Materials and Structures*, 18(2): 24002. <https://doi.org/10.1088/0964-1726/18/2/024002>.
- Landkammer, S., F. Winter, D. Schneider, and R. Hornfeck. 2016. "Biomimetic Spider Leg Joints: A Review from Biomechanical Research to Compliant Robotic Actuators." *Robotics*, 5(3): 15. <https://doi.org/10.3390/robotics5030015>.
- Lang, I., S. Sassmann, B. Schmidt, and G. Komis. 2014. "Plasmolysis: Loss of Turgor and Beyond." *Plants (Basel, Switzerland)*, 3(4): 583–593. <https://doi.org/10.3390/plants3040583>.
- Lehmann, M., Schmidt C. M., and E.-M. Hirtz. 2015. "Optimierte Herstellung." *Konstruktion*, 67(07-08): IW 4-IW 5. <https://doi.org/10.37544/0720-5953-2015-07-08-56> (in de).
- Li, L., Z.-Y. Shi, L. Li, G.-Z. Shen, X.-Q. Wang, L.-S. An, and J.-L. Zhang. 2010. "Overexpression of ACL1 (abaxially curled leaf 1) increased Bulliform cells and induced Abaxial curling of leaf blades in rice." *Molecular plant*, 3(5): 807–817. <https://doi.org/10.1093/mp/ssq022>.
- Li, S., and K. W. Wang. 2016. "Plant-inspired adaptive structures and materials for morphing and actuation: A review." *Bioinspiration & biomimetics*, 12(1): 11001. <https://doi.org/10.1088/1748-3190/12/1/011001>.
- Lienhard, J., H. Alpermann, C. Gengnagel, J. Knippers. 2013. "Active Bending, a Review on Structures where Bending is Used as a Self-Formation Process." *International Journal of Space Structures*, 28(3-4):187-196. <https://doi.org/10.1260/0266-3511.28.3-4.187>
- Lienhard, J. 2014. *Bending-active structures: Form-finding strategies using elastic deformation in static and kinetic systems and the structural potentials therein*, PhD dissertation, University of Stuttgart.
- Lienhard, J., S. Schleicher, S. Poppinga, T. Masselter, M. Milwich, T. Speck, and J. Knippers. 2011. "Flectofin: A hingeless flapping mechanism inspired by nature." *Bioinspiration & biomimetics*, 6(4): 45001. <https://doi.org/10.1088/1748-3182/6/4/045001>.

- Lin, H.-T., D. J. Slate, C. R. Paetsch, A. L. Dorfmann, and B. A. Trimmer. 2011. "Scaling of caterpillar body properties and its biomechanical implications for the use of a hydrostatic skeleton." *The Journal of experimental biology*, 214(Pt 7): 1194–1204. <https://doi.org/10.1242/jeb.051029>.
- Lin, T.-T., and R. E. Pitt. 1986. "RHEOLOGY OF APPLE AND POTATO TISSUE AS AFFECTED BY CELL TURGOR PRESSURE." *Journal of Texture Studies*, 17(3): 291–313. <https://doi.org/10.1111/j.1745-4603.1986.tb00554.x>.
- Liu, C.-H., C.-H. Chiu, T.-L. Chen, T.-Y. Pai, Y. Chen, and M.-C. Hsu. 2018. "A Soft Robotic Gripper Module with 3D Printed Compliant Fingers for Grasping Fruits." In *Proc., 2018 IEEE/ASME International Conference on Advanced Intelligent Mechatronics (AIM)*: 736–741.
- Lobontiu, N. 2003. *Compliant mechanisms: Design of flexure hinges*, Boca Raton: CRC Press.
- Luo, Q., and L. Tong. 2013a. "Adaptive pressure-controlled cellular structures for shape morphing I: design and analysis." *Smart Materials and Structures*, 22(5): 55014. <https://doi.org/10.1088/0964-1726/22/5/055014>.
- Luo, Q., and L. Tong. 2013b. "Adaptive pressure-controlled cellular structures for shape morphing: II. Numerical and experimental validation." *Smart Materials and Structures*, 22(5): 55015. <https://doi.org/10.1088/0964-1726/22/5/055015>.
- Mader, A., A. Birkhold, M. Caliaro, O. Speck, O. Röhrle, and J. Knippers. 2017. "Plant-inspired compliant actuation." In *7th GACM Colloquium on Computational Mechanics for Young Scientists from Academia and Industry*, edited by Universität Stuttgart, M. v. Scheven, M.-A. Keip, and N. Karajan: Universität Stuttgart.
- Mader, A., L. Born, A. Körner, G. Schieber, P.-A. Masset, M. Milwich, G. T. Gresser, and J. Knippers. 2020a. "Bio-inspired integrated pneumatic actuation for compliant fiber-reinforced plastics." *Composite Structures*, 233: 111558. <https://doi.org/10.1016/j.compstruct.2019.111558>.
- Mader, A., M. Langer, J. Knippers, and O. Speck. 2020b. "Learning from plant movements triggered by bulliform cells: the biomimetic cellular actuator." *Journal of the Royal Society, Interface*, 17(169): 20200358. <https://doi.org/10.1098/rsif.2020.0358>.
- Mallikarachchi, H. M. Y. C., and S. Pellegrino. 2011. "Quasi-Static Folding and Deployment of Ultrathin Composite Tape-Spring Hinges." *Journal of Spacecraft and Rockets*, 48(1): 187–198. <https://doi.org/10.2514/1.47321>.

- Matini, M.-R. 2007. *Biegsame Konstruktionen in der Architektur auf der Basis bionischer Prinzipien*, PhD dissertation, University of Stuttgart.
- Matschi, S., M. F. Vasquez, R. Bourgault, P. Steinbach, J. Chamness, N. Kaczmar, M. A. Gore, I. Molina, and L. G. Smith. 2020. *Structure-function analysis of the maize bulliform cell cuticle and its role in dehydration and leaf rolling*.
- Mattheck, C. 1998. *Design in Nature: Learning from Trees*, Berlin, Heidelberg: Springer Berlin Heidelberg.
- Mazzolai, B., V. Mattoli, and L. Beccai. 2017. "Soft Plant Robotic Solutions: Biological Inspiration and Technological Challenges." In *Advances in Unconventional Computing*, edited by A. Adamatzky: 687–707, Cham: Springer International Publishing.
- McKnight, G., R. Doty, A. Keefe, G. Herrera, and C. Henry. 2010. "Segmented Reinforcement Variable Stiffness Materials for Reconfigurable Surfaces." *Journal of Intelligent Material Systems and Structures*, 21(17): 1783–1793. <https://doi.org/10.1177/1045389X10386399>.
- McKnight, G., and C. Henry. 2005. "Variable stiffness materials for reconfigurable surface applications." In *Proc., Smart Structures and Materials*, edited by W. D. Armstrong, SPIE Proceedings: 119.
- Mendez, J., P. K. Annamalai, S. J. Eichhorn, R. Rusli, S. J. Rowan, E. J. Foster, and C. Weder. 2011. "Bioinspired Mechanically Adaptive Polymer Nanocomposites with Water-Activated Shape-Memory Effect." *Macromolecules*, 44(17): 6827–6835. <https://doi.org/10.1021/ma201502k>.
- Merriam, E. G., J. E. Jones, and L. L. Howell. 2014. "Design of 3D-printed titanium compliant mechanisms." *Proceedings of the 42nd Aerospace Mechanisms Symposium*, NASA Goddard Space Flight Center, May 14-16.
- Migliore, S., E. Brown, and S. Deweerth. 2005. "Biologically Inspired Joint Stiffness Control." *Proceedings - IEEE International Conference on Robotics and Automation*, 2005. <https://doi.org/10.1109/ROBOT.2005.1570814>.
- Milani, P., M. Gholamirad, J. Traas, A. Arnéodo, A. Boudaoud, F. Argoul, and O. Hamant. 2011. "In vivo analysis of local wall stiffness at the shoot apical meristem in Arabidopsis using atomic force microscopy." *The Plant journal : for cell and molecular biology*, 67(6): 1116–1123. <https://doi.org/10.1111/j.1365-313X.2011.04649.x>.
- Moran, N. 2007. "Osmoregulation of leaf motor cells." *FEBS letters*, 581(12): 2337–2347. <https://doi.org/10.1016/j.febslet.2007.04.002>.

- Müller, L., B. Lehmann, and G. T. Gresser. 2015. "Sandwich Structures: Analysis of Bonding Techniques between Faces and Core and the Effect of Internal Pressure." *MSF*, 825-826: 361–368. <https://doi.org/10.4028/www.scientific.net/MSF.825-826.361>.
- Murray, G., and F. Gandhi. 2010. "Multi-layered controllable stiffness beams for morphing: energy, actuation force, and material strain considerations." *Smart Mater. Struct.*, 19(4): 45002. <https://doi.org/10.1088/0964-1726/19/4/045002>.
- Nasrollahi, F. 2009. *Climate and energy responsive housing in continental climates: The suitability of passive houses for Iran's dry and cold climate*, Zugl.: Berlin, Techn. Univ., Diss., 2009, Berlin: Univ.-Verl. der TU.
- Nelson, L. J. 2002. "Smart piezoelectric Fibre composites." *Materials Science and Technology*, 18(11): 1245–1256. <https://doi.org/10.1179/026708302225007448>.
- Niklas, K. J. 1988. "Dependency of the tensile modulus on transverse dimensions, water potential, and cell number of pith parenchyma." *American journal of botany*, 75(9): 1286–1292.
- Niklas, K. J. 1989. "Mechanical Behavior of Plant Tissues as Inferred from the Theory of Pressurized Cellular Solids." *American journal of botany*, 76(6): 929. <https://doi.org/10.2307/2444549>.
- Nilsson, S. B., C. H. Hertz, and S. Falk. 1958. "On the Relation between Turgor Pressure and Tissue Rigidity. II. Theoretical Calculations on Model Systems." *Physiologia Plantarum*, 11(4): 818–837. <https://doi.org/10.1111/j.1399-3054.1958.tb08275.x>.
- Nultsch, W. 2001. *Allgemeine Botanik: Glossarium mit 803 Stichworten*, Stuttgart, New York: Georg Thieme Verlag.
- Pagitz, M., and E. Kappel. 2014. *Design of Pressure Actuated Cellular Structures*.
- Pagitz, M., M. Pagitz, and C. Hühne. 2014. "A modular approach to adaptive structures." *Bioinspiration & biomimetics*, 9(4): 46005. <https://doi.org/10.1088/1748-3182/9/4/046005>.
- Park, Y.-J., and K.-J. Cho. 2013. "Design and Manufacturing a Bio-inspired Variable Stiffness Mechanism in a Robotic Dolphin." In *Intelligent Robotics and Applications*, edited by D. Hutchison, T. Kanade, J. Kittler, J. M. Kleinberg, F. Mattern, J. C. Mitchell, M. Naor, O. Nierstrasz, C. Pandu Rangan, B. Steffen, M. Sudan, D. Terzopoulos, D. Tygar, M. Y. Vardi, G. Weikum, J. Lee, M. C. Lee, H. Liu, and J.-H. Ryu: 302–309, Berlin, Heidelberg: Springer Berlin Heidelberg.

- Paul, B. 1979. *Kinematics and dynamics of planar machinery*, New Jersey, United States: Prentice-Hall.
- Petit, F., M. Chalon, W. Friedl, M. Grebenstein, A. Albu-Schaffer, and G. Hirzinger. 2010. "Bidirectional antagonistic variable stiffness actuation: Analysis, design & Implementation." In *Proc., 2010 IEEE International Conference on Robotics and Automation (ICRA 2010)*: 4189–4196.
- Philen, M., Y. Shan, C. Bakis, K.-W. Wang, and C. Rahn. 2006a. "Variable Stiffness Adaptive Structures utilizing Hydraulically Pressurized Flexible Matrix Composites with Valve Control." In *Proc., 47th AIAA/ASME/ASCE/AHS/ASC Structures, Structural Dynamics, and Materials Conference*: 51, Reston, Virginia.
- Philen, M., Y. Shan, K.-W. Wang, C. Bakis, and C. Rahn. 2007. "Fluidic Flexible Matrix Composites for the Tailoring of Variable Stiffness Adaptive Structures." In *Proc., 48th AIAA/ASME/ASCE/AHS/ASC Structures, Structural Dynamics, and Materials Conference*, Reston, Virginia.
- Philen, M. K., Y. Shan, P. Prakash, K. W. Wang, C. D. Rahn, A. L. Zydney, and C. E. Bakis. 2006b. "Fibrillar Network Adaptive Structure with Ion-transport Actuation." *Journal of Intelligent Material Systems and Structures*, 18(4): 323–334. <https://doi.org/10.1177/1045389X06066097>.
- Pitt, R. E. 1982. "Models for the Rheology and Statistical Strength of Uniformly Stressed Vegetative Tissue." *Transactions of the ASAE*, 25(6): 1776–1784. <https://doi.org/10.13031/2013.33805>.
- Plaza, G. R., G. V. Guinea, J. Pérez-Rigueiro, and M. Elices. 2006. "Thermo-hygro-mechanical behavior of spider dragline silk: Glassy and rubbery states." *Journal of Polymer Science Part B: Polymer Physics*, 44(6): 994–999. <https://doi.org/10.1002/polb.20751>.
- Polygerinos, P., N. Correll, S. A. Morin, B. Mosadegh, C. D. Onal, K. Petersen, M. Cianchetti, M. T. Tolley, and R. F. Shepherd. 2017. "Soft Robotics: Review of Fluid-Driven Intrinsically Soft Devices; Manufacturing, Sensing, Control, and Applications in Human-Robot Interaction." *Advanced Engineering Materials*, 19(12): 1700016. <https://doi.org/10.1002/adem.201700016>.
- Poppinga, S., and M. Joyeux. 2011. "Different mechanics of snap-trapping in the two closely related carnivorous plants *Dionaea muscipula* and *Aldrovanda vesiculosa*." *Physical review. E, Statistical, nonlinear, and soft matter physics*, 84(4 Pt 1): 41928. <https://doi.org/10.1103/PhysRevE.84.041928>.
- Poppinga, S., J. Smajj, A. S. Westermeier, M. Horstmann, S. Kruppert, R. Tollrian, and T. Speck. 2019. "Prey capture

- analyses in the carnivorous aquatic waterwheel plant (Aldrovanda vesiculosa L., Droseraceae)." *Scientific reports*, 9(1): 18590. <https://doi.org/10.1038/s41598-019-54857-w>.
- Poppinga, S., C. Zollfrank, O. Prucker, J. Rhe, A. Menges, T. Cheng, and T. Speck. 2018. "Toward a New Generation of Smart Biomimetic Actuators for Architecture." *Advanced materials*, 30(19): e1703653. <https://doi.org/10.1002/adma.201703653>.
- R Development Core Team. 2008. *R: A language and environment for statistical computing*, Vienna, Austria: R Foundation for Statistical Computing <<http://www.R-project.org>>.
- Raven, P. H., S. E. Eichhorn, and R. F. Evert. 2005. *Biology of plants*: New York : W.H. Freeman and Company.
- Richfield, D. 2014. "Medical gallery of David Richfield 2014." *WikiJournal of Medicine*, 1(2). <https://doi.org/10.15347/wjm/2014.009>.
- Riemann, B. L., and S. M. Lephart. 2002. "The Sensorimotor System, Part II: The Role of Proprioception in Motor Control and Functional Joint Stability." *Journal of Athletic Training*, 37(1): 80–84.
- Rus, D., and M. T. Tolley. 2015. "Design, fabrication and control of soft robots." *Nature*, 521(7553): 467–475. <https://doi.org/10.1038/nature14543>.
- Saavedra Flores, E. I., M. I. Friswell, and Y. Xia. 2013. "Variable stiffness biological and bio-inspired materials." *Journal of Intelligent Material Systems and Structures*, 24(5): 529–540. <https://doi.org/10.1177/1045389X12461722>.
- Sardellitti, I., G. Palli, N. Tsagarakis, and D. G. Caldwell. 2010. *Antagonistically actuated compliant joint: Torque and stiffness control*.
- Schieber, G., L. Born, P. Bergmann, A. Krner, A. Mader, S. Saffarian, O. Betz, M. Milwich, G. T. Gresser, and J. Knippers. 2017. "Hindwings of insects as concept generator for hingeless foldable shading systems." *Bioinspiration & biomimetics*, 13(1): 16012. <https://doi.org/10.1088/1748-3190/aa979c>.
- Schijve, J. 2003. "Fatigue of structures and materials in the 20th century and the state of the art." *International Journal of Fatigue*, 25(8): 679–702. [https://doi.org/10.1016/S0142-1123\(03\)00051-3](https://doi.org/10.1016/S0142-1123(03)00051-3).
- Schleicher, S. 2015. *Bio-inspired compliant mechanisms for architectural design*, PhD dissertation, University of Stuttgart.

- Schleicher, S., J. Lienhard, S. Poppinga, T. Speck, and J. Knippers. 2015. "A methodology for transferring principles of plant movements to elastic systems in architecture." *Computer-Aided Design*, 60: 105–117. <https://doi.org/10.1016/j.cad.2014.01.005>.
- Schmid, F., and S. Marinitsch. 2017. "Kinetic Lightweight Surface Elements: Composite Actuators." In, edited by A. Bögle, and M. Grohmann, Hamburg, Germany.
- Schubert, B. E., and D. Floreano. 2013. "Variable stiffness material based on rigid low-melting-point-alloy microstructures embedded in soft poly(dimethylsiloxane) (PDMS)." *RSC Advances*, 3(46): 24671. <https://doi.org/10.1039/C3RA44412K>.
- Schumacher, M., O. Schaeffer, and M.-M. Vogt. 2010. *Move: Architecture in motion: dynamic components and elements*, Boston, MA: Birkhaeuser.
- Shi, M. X., B. Liu, Z. Q. Zhang, Y. W. Zhang, and H. J. Gao. 2012. "Direct influence of residual stress on the bending stiffness of cantilever beams." *Proceedings of the Royal Society of London. Series A: Mathematical, Physical and Engineering Sciences*, 468(2145): 2595–2613. <https://doi.org/10.1098/rspa.2011.0662>.
- Sinibaldi, E., A. Argiolas, G. Puleo, and B. Mazzolai. 2014. "Another Lesson from Plants: The Forward Osmosis-Based Actuator." *PloS one*, 9: e102461. <https://doi.org/10.1371/journal.pone.0102461>.
- Skotheim, J. M., and L. Mahadevan. 2005. "Physical limits and design principles for plant and fungal movements." *Science (New York, N.Y.)*, 308(5726): 1308–1310. <https://doi.org/10.1126/science.1107976>.
- Speck, T., and O. Speck. 2008. "Process sequences in biomimetic research." In *Proc., DESIGN AND NATURE 2008*, edited by C. A. Brebbia: 3–11, Southampton, UK.
- Spura, C. 2019. *Technische Mechanik 2. Elastostatik*, Wiesbaden: Springer Fachmedien Wiesbaden.
- Stölting, H.-D. 2004. "Electromagnetic Actuators." In *Actuators*, edited by H. Janocha: 85–153, Berlin, Heidelberg: Springer Berlin Heidelberg.
- Storm, C., J. J. Pastore, F. C. MacKintosh, T. C. Lubensky, and P. A. Janmey. 2005. "Nonlinear elasticity in biological gels." *Nature*, 435(7039): 191–194. <https://doi.org/10.1038/nature03521>.
- Sun, J., M. Ling, W. Wu, B. Bhushan, and J. Tong. 2014. "The hydraulic mechanism of the unfolding of hind wings in *Dorcus titanus platymelus* (order: Coleoptera)." *International*

- journal of molecular sciences*, 15(4): 6009–6018.
<https://doi.org/10.3390/ijms15046009>.
- Sun, X., S. M. Felton, R. Niiyama, R. J. Wood, and S. Kim. 2015. "Self-folding and self-actuating robots: A pneumatic approach." In : 3160–3165, Piscataway, NJ: IEEE International Conference on Robotics and Automation and ICRA.
- Sun, Y., D. Zhang, and T. C. Lueth. 2020. "Bionic Design of a Disposable Compliant Surgical Forceps With Optimized Clamping Performance." *Annual International Conference of the IEEE Engineering in Medicine and Biology Society. IEEE Engineering in Medicine and Biology Society. Annual International Conference*, 2020: 4704–4707.
<https://doi.org/10.1109/EMBC44109.2020.9176027>.
- Takosoglu, J. 2020. "Angular position control system of pneumatic artificial muscles." *Open Engineering*, 10(1): 681–687. <https://doi.org/10.1515/eng-2020-0077>.
- Tsai, L.-w. 1999. *Robot analysis: The mechanics of serial and parallel manipulators*, New York: Wiley.
- van Melick, H.G.H., L. E. Govaert, and H.E.H. Meijer. 2003. "On the origin of strain hardening in glassy polymers." *Polymer*, 44(8): 2493–2502. [https://doi.org/10.1016/S0032-3861\(03\)00112-5](https://doi.org/10.1016/S0032-3861(03)00112-5).
- Vasista, S., and L. Tong. 2012. "Design Considerations of a Pressure Driven Morphing Wing Structure." In : 2174–2183.
- VDI 6220 Blatt 1:. 2012. "Biomimetics - Conception and strategy - Differences between bionic and conventional methods/products." *6220*, Berlin.
- Vos, R., R. Barrett, and A. Romkes. 2011. "Mechanics of Pressure-Adaptive Honeycomb." *Journal of Intelligent Material Systems and Structures*, 22(10): 1041–1055.
<https://doi.org/10.1177/1045389X11412638>.
- Walker, I. D. 2013. "Continuous Backbone "Continuum" Robot Manipulators." *ISRN Robotics*, 2013(1): 1–19.
<https://doi.org/10.5402/2013/726506>.
- Watter, H. 2015. *Hydraulik und Pneumatik: Grundlagen und Übungen - Anwendungen und Simulation*, Wiesbaden: Springer Vieweg.
- Westermeier, A. S., R. Sachse, S. Poppinga, P. Vögele, L. Adamec, T. Speck, and M. Bischoff. 2018. "How the carnivorous waterwheel plant (*Aldrovanda vesiculosa*) snaps." *Proceedings of the Royal Society of London. Series B: Biological Sciences*, 285(1878).
<https://doi.org/10.1098/rspb.2018.0012>.

- Yao, L., R. Niiyama, J. Ou, S. Follmer, C. Della Silva, and H. Ishii. 2013. "PneUI." In, edited by S. Izadi, A. Quigley, I. Poupayrev, and T. Igarashi: 13–22, New York, New York, USA.
- Zarate, J., T. Helbig, and H. Witte. 2019. "Design of a Bioinspired Variable Stiffness Sensor." In *Proc., 2019 IEEE International Conference on Mechatronics (ICM)*: 376–381.
- Zhang, Z. 2016. "Mechanics of human voice production and control." *The Journal of the Acoustical Society of America*, 140(4): 2614. <https://doi.org/10.1121/1.4964509>.
- Zhang, Z., and M. Philen. 2012. "Pressurized artificial muscles." *Journal of Intelligent Material Systems and Structures*, 23(3): 255–268. <https://doi.org/10.1177/1045389X11420592>.
- Zupan, M., M. F. Ashby, and N. A. Fleck. 2002. "Actuator Classification and Selection - The Development of a Database." *Advanced Engineering Materials*, 4(12): 933–940. <https://doi.org/10.1002/adem.200290009>.

6.1 ONLINE IMAGES

FIG. 1.3:

By Annom / CC0. Available from: https://commons.wikimedia.org/wiki/File:Lift_dumperinnerworkingsa320.jpg#file [Accessed 2021/10/09].

FIG. 1.4:

- (A) by Loz Pycock / CC BY-SA 2.0. Left available from: <https://www.flickr.com/photos/99245765@N00/5002172010> [Accessed 2021/10/09]; right available from: <https://www.flickr.com/photos/99245765@N00/5002169660> [Accessed 2021/10/09];
- (B) by Inhabitat / CC BY-NC-ND 2.0. Available from: <https://www.flickr.com/photos/inhabitat/12331374724> [Accessed 2021/10/09];
- (C) upper photo by Dasparag / CC BY-SA 4.0. Available from: https://commons.wikimedia.org/wiki/File:Milwaukee_Art_Museum_evening.jpg [Accessed 2021/10/09]; lower photo by gillfoto / CC BY-SA 4.0. Available from: https://commons.wikimedia.org/wiki/File:Milwaukee_Art_Museum_18.jpg [Accessed 2021/10/09];
- (D) by S.Juhl / CC0 1.0. Available from: [https://commons.wikimedia.org/wiki/File:Syddansk_universitet.Campus_Kolding.Denmark.2014_\(39\).JPG](https://commons.wikimedia.org/wiki/File:Syddansk_universitet.Campus_Kolding.Denmark.2014_(39).JPG) [Accessed 2021/10/09];
- (E) by Rory Hyde / CC BY-SA 2.0. Available from: <https://www.flickr.com/photos/roryrory/2520002205> [Accessed 2021/10/09];
- (F) by Tadeusz Rudzki / CC BY-SA 3.0). Available from: https://de.m.wikipedia.org/wiki/Datei:POL_Stadion_Narodowy_Warszawa_09.jpg [Accessed 2021/10/09].

FIG. 1.11:

- (C) by Pascal Berger / CC BY-SA 4.0. Left available from: https://en.wikipedia.org/wiki/File:Compliant_Iris_mechanism_-_closed.png [Accessed 2021/10/09]; Right available from: https://en.wikipedia.org/wiki/File:Compliant_Iris_mechanism_-_open.png [Accessed 2021/10/09];
- (E) by NASA/Carla Thomas. Available from: <https://www.nasa.gov/sites/default/files/thumbnails/image/ed150076-03.jpg> [Accessed 2021/10/09].

FIG. 1.13:

Redrawn from ADMET (2021). Available from: <https://www.admet.com/wp-content/uploads/2018/12/fig6-S-N-Diagram-for-steel-aluminum-andFRP600x455.jpg> [Accessed 2021/10/09].

FIG. 2.2:

By S.J. de Waard / CC BY-SA 3.0. Available from: [https://commons.wikimedia.org/wiki/File:Rotterdam_Ahoy_Europort_2011_\(14\).JPG](https://commons.wikimedia.org/wiki/File:Rotterdam_Ahoy_Europort_2011_(14).JPG) [Accessed 2021/10/09].

FIG. 2.3:

Upper photo by Giaquini. Available from: <https://pixabay.com/de/photos/zyylinder-pneumatische-kompakt-5263820/> [Accessed 2021/10/09].

Lower image by Cdang / CC BY-SA 3.0). Available from: https://commons.wikimedia.org/wiki/File:Coupe_verin_double_effet_exercice_solution.svg [Accessed 2021/10/09].

FIG. 2.4:

By SKas / CC BY-SA 4.0. Available from: https://commons.wikimedia.org/wiki/File:Excavator_on_the_Aibga_ridge.JPG [Accessed 2021/10/09].

FIG. 2.7:

By Petermaerki / CC BY-SA 3.0. Left available from: https://commons.wikimedia.org/wiki/File:Nitinol_bueroklammer_verbogen.jpg [Accessed 2021/10/09]; right available from: https://commons.wikimedia.org/wiki/File:Nitinol_bueroklammer_heiss.jpg [Accessed 2021/10/09].

FIG. 2.8:

By Pinin / CC0. Available from: <https://commons.wikimedia.org/wiki/File:Perovskite.svg> [Accessed 2021/10/09].

FIG. 2.12:

(A)&(C) by DITF (2016). Available from: <https://www.ditf.de/de/index/aktuelles/pressemeldungen/detail/nicht-nur-heisse-luft.html> [Accessed 2021/10/09].

FIG. 2.13:

By Science and Plants for Schools / CC BY-NC-SA 2.0. Available from: <https://www.flickr.com/photos/71183136@N08/6989068712> [Accessed 2021/10/09].

FIG. 2.14:

By Russell Neches / CC BY 2.0. Available from: <https://www.flickr.com/photos/rneches/2081938105> [Accessed 2021/10/09].

FIG. 2.15:

Photo available from: <https://www.pxfuel.com/en/free-photo-jombq> [Accessed 2021/10/09].

FIG. 2.17:

Based on an image by LadyofHats / CC0. Available from: https://commons.wikimedia.org/wiki/File:Turgor_pressure_on_plant_cells_diagram.svg [Accessed 2021/10/09].

FIG. 2.20:

- (A) by Kohidai, L., Urutseg / CC BY 3.0. Available from: <https://commons.wikimedia.org/wiki/File:Flagellum-beating.svg> [Accessed 2021/10/09];
- (B) by Jonathan Ferrooz, Jean-Jacques Letesson / CC BY-SA 2.0. Available from: [https://commons.wikimedia.org/wiki/File:Brucella_melitensis_flagellum_\(fig._1\).png](https://commons.wikimedia.org/wiki/File:Brucella_melitensis_flagellum_(fig._1).png) [Accessed 2021/10/09].;
- (C) by CNX OpenStax / CC BY 4.0. Available from: https://commons.wikimedia.org/wiki/File:OSC_Microbio_17_02_Cilia.jpg [Accessed 2021/10/09].

FIG. 2.21:

By LadyofHats / CC0. Available from: https://commons.wikimedia.org/wiki/File:Eukaryotic_cilium_diagram_en.svg [Accessed 2021/10/09].

FIG. 2.22:

Upper image by Cymothoa exigua / CC BY-SA 3.0. Available from: https://commons.wikimedia.org/wiki/File:Amoeba_proteus.jpg [Accessed 2021/10/09].

Lower image by Pearson Scott Foresman / CC0. Available from: [https://commons.wikimedia.org/wiki/File:Amoeba_\(PSF\).png](https://commons.wikimedia.org/wiki/File:Amoeba_(PSF).png) [Accessed 2021/10/09].

FIG. 2.24:

By OpenStax / CC BY 4.0. Available from: https://commons.wikimedia.org/wiki/File:1008_Skeletal_Muscle_Contraction.jpg [Accessed 2021/10/09].

FIG. 2.25:

Upper photo by JackMonik / CC BY-SA 4.0. Available from: https://commons.wikimedia.org/wiki/File:Exo_skeleton_Anacridium.jpg [Accessed 2021/10/09].

Lower photo by Postdlf / CC BY-SA 3.0. Available from: https://commons.wikimedia.org/wiki/File:Swordfish_skeleton.jpg [Accessed 2021/10/09].

FIG. 2.27:

(A) by Deepanoffl / CC BY-SA 4.0. Available from: https://commons.wikimedia.org/wiki/File:Indian_elephant_with_raised_trunk.jpg [Accessed 2021/10/09];

(B) by PixelBandit / Pixabay License. Available from: <https://pixabay.com/de/photos/kuh-zunge-tier-wiese-gras-8316/> [Accessed 2021/10/09];

(C) by Anneli Salo / CC BY-SA 3.0. Available from: https://commons.wikimedia.org/wiki/File:Octopus_vulgaris_BCN_0219_Mustekala_C.JPG [Accessed 2021/10/09];

(D) by Inkub0 / CC BY-SA 3.0. Available from: <https://de.m.wikipedia.org/wiki/Datei:Snail.jpg> [Accessed 2021/10/09].

FIG. 2.49:

Upper photo by Ben Freeman / CC BY-NC 2.0. Available from: <https://www.flickr.com/photos/brf/7712721700> [Accessed 2021/10/09].